UNIVERSITÀ DEGLI STUDI DI PADOVA

DIPARTIMENTO DI FISICA E ASTRONOMIA
GALILEO GALILEI

PH.D. COURSE IN PHYSICS
CYCLE XXXVI

DOCTORAL THESIS

Searches for Axion–Like Particles with Very High Energy Gamma Rays

---

Ph.D. Student:
Ivana Batković

Supervisor:
Prof. Michele Doro

Co-Supervisor:
Prof. Marina Manganaro,
University of Rijeka

Coordinator:
Prof. Giulio Monaco

ACADEMIC YEAR 2022/2023

Mojim roditeljima Zvonki i Mariji,
sestri Danijeli i bratu Anti.

Abstract

We introduce the concept of axions and Axion-like particles (ALPs), considering them as promising candidates for Dark Matter (DM) due to their origin in symmetry breaking. The discussion focuses on the interaction of ALPs with photons, particularly the phenomenon of photon-ALP conversion and the calculation of photon survival probability. Photon survival probability is a quantification of photon-ALP conversion, occurring due to their interaction with photons in a two-photon vertex, and resulting in the conversion of photons to an ALP and vice versa in external magnetic fields that are playing mediators for the mixing. As it is mentioned, it is calculated taking into account magnetic fields in the line of sight, as well as the interaction with the Extragalactic Background Light (EBL) in the extragalactic space, and the Cosmic Microwave Background (CMB). As an overview of the state of the art of searches for axion, experiments for ALP detection are categorised based on the type of ALPs they investigate together with the examples and corresponding limits in the ALPs parameter space.

Emphasis is placed on gamma-ray astronomy, using Imaging Atmospheric Cherenkov Telescopes (IACTs) telescopes (Major Atmospheric Gamma Imaging Cherenkov (MAGIC) and Large-sized telescope (LST-1)) to analyse very-high-energy gamma-ray data. The production of gamma rays and their detection, together with a discussion of some principal concepts and the data analysis are explained. The experimental setups, in our case of MAGIC and LST-1 telescopes are described, as it is of a great importance for understanding gamma-ray observations and collection of the data, production of the results and their interpretation. For the analysis of Very High Energy (VHE) data and reconstruction of the source spectrum, we used `gammapy`, an open-source package for gamma-ray astronomy [1]. For the ALP analysis, we used the `GammaALPs`, a python code developed for solving the equations of motion of the photon-ALP system using the transfer matrix method [2].

As mentioned before, ALPs are interacting with two photons, oscillating back and forth in the external magnetic field. In case the conversion occurs, propagation of gamma rays is affected, observable through distinctive signatures in the gamma-ray spectrum of the astrophysical sources reproduced from the IACTs data. ALPs in particular can leave alterations on the observed spectrum at different energies, depending on the point at which the photon-ALP conversion occurred, and the energy of the gamma-ray (photon).

The central study of this thesis explores the impact of ALPs on gamma-ray spectra, providing a detailed analysis of the NGC 1275, an Active Galactic Nucleus (AGN) located in the centre of the Perseus Galaxy Cluster (GC), at the redshift $z \sim 0.0175$. Our dataset includes a strong flare, post-flare and a low activity state of the NGC 1275, combined in a dataset of ~ 41 hours of observations. Methodology involves modelling magnetic fields, considering environmental factors, and using statistical methods to evaluate ALP signatures in the spectrum. To evaluate the hypothesis of the existence of axion-like particles,

[1] https://gammapy.org/

[2] Hosted on GitHub (https://github.com/me-manu/gammaALPs) and archived on Zenodo [1]

we modelled several magnetic fields in the line of sight: the magnetic field of the Perseus GC, the Intergalactic magnetic field (IGMF), the attenuation due to the interaction with the photons of the optical–infrared background light EBL, and ultimately the magnetic field of the Milky Way (MW), in which the conversion of the ALPs back to photons is expected, and hence needs to be considered. While no conclusive evidence for ALPs is found, the study establishes the most stringent limits on ALP models in the range of $40 - 90\,\mathrm{neV}$, reaching the photon-axion coupling down to $g_{a\gamma} = 3.0 \times 10^{-12}\ \mathrm{GeV}^{-1}$.

In the final chapter, preliminary results from studying blazars, particularly Markarian 421 (hereafter Mrk 421), using LST-1 data are discussed. Challenges in investigating magnetic fields in relativistic jets of blazars and combining constraints on ALPs from different sources are highlighted. Our results suggest importance of combination of data from different blazar sources, as well as careful investigation of magnetic fields in the line of sight, in particular the magnetic field of the blazar jet. We conclude by outlining prospects for future studies of ALPs with the VHE gamma-ray data.

Contents

Chapter 1

Introduction

Contents

"Too good to be true", these five words are perhaps the perfect choice to explain one of the most elegant physics theories of our lifetime; the Standard Model (SM) of particle physics [2]. Starting from 1960s and 1970s, the SM narrowed down the explanation for the existence of all the observed particles in a set of a few, called "the elementary particles" (see Figure 1.1) and an elegant scheme for their interactions. Despite being a self-consistent theory from the beginning, the SM has been severely tested down to the precision better than ten parts per billion (e. g., the SM is correctly predicting the fine-structure constant up to 14 decimal places), when applied to the wider scenario of the description of the Universe and its formation, it fails to explain the existence of the Dark Matter (DM) gravity and matter-antimatter asymmetry, leaving the completion of the puzzle of the Universe a challenge. One of the most famous mathematical models confirmed by observations is the ΛCDM, established as the "standard cosmological model". It is based on general relativity as the main theory for the explanation of the Big Bang cosmological model and reconciles the observations of large scale structures such as Galaxy Clusters (GCs), relic background radiation, accelerated expansion of the Universe and chemical composition of the Universe. In the acronym itself, this model reveals its most important postulate: the Universe is constituted of dark energy (for first confirmations of accelerated expansion of the Universe (see [3, 4]), represented by Λ, and cold dark matter (CDM) (for a general review, see [5, 6]).

Baryonic matter, interacting through four fundamental forces, holds only a modest stake in the energy density of the Universe: 4.9% [7]. In Figure 1.2, one can see that most

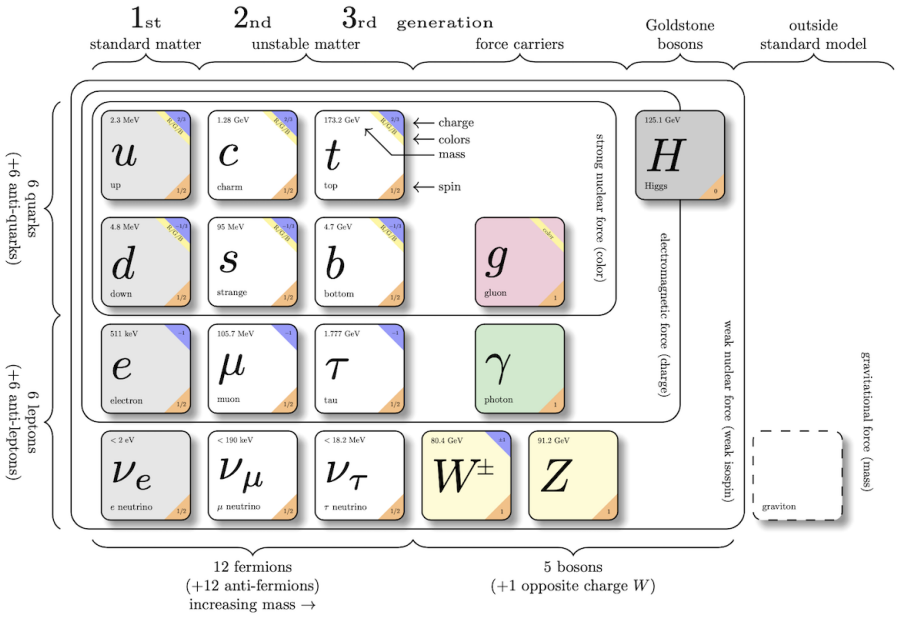

Figure 1.1: Standard model of elementary particles. Obtained using the code developed during the CERN Webfest 2012 by David Galbraith and Carsten Burgard.

of the Universe is permeated by the dark energy, affecting the evolution and accelerated expansion of the Universe.

Second is the DM. 85% of all the matter in the Universe is constituted by DM, and even though its presence has strong gravitational evidences, the real nature of it still remains unrevealed. Its impact on the evolution and dynamics of the Universe is far from negligible, since DM itself was driving the evolution and structure formation. Observations of the gravitational effect of DM lead to conclusions that the areas of higher concentration of the DM are located in galaxies and GCs. Studies up to now indicate its non-baryonic nature, suggesting a missing "box" that would fit outside of the one already including the known SM particles in Figure 1.1. In an effort to unveil these missing pieces, various theories have been proposing massive, Weakly Interacting Massive Particles (WIMPs) and Weakly Interacting Slim Particless (WISPs), that will soon be introduced as the main focus of this work. Among them, the axion particle and Axion-like particles (ALPs), emerge as suitable candidates for DM.

1.1 Axion and axion-like particles (ALPs)

Even though a very self-consistent theory, since its beginning, the SM has been showing some inconsistencies with the observations. Aside of the already mentioned lack of known particles capable of explaining the DM, the inability to explain the asymmetry of matter

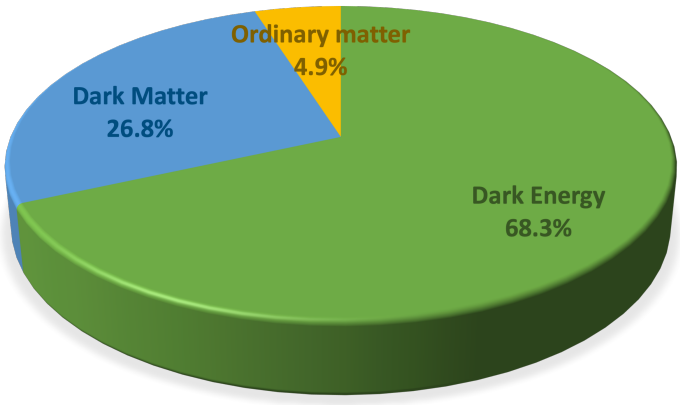

Figure 1.2: The composition of the Universe.

and antimatter in the Universe, neutrino oscillations, and being incompatible with the explanation of gravity within the framework of general relativity, the SM cannot coherently explain all the interactions of fundamental forces. Formed from two fundamental symmetries, conjugation and parity, the CP symmetry assumes the invariance of the system to the simultaneous inversion of the electric charge, through the internal quantum numbers (C, conjugation), and the reversal of the space coordinates (P, parity). So far, no experimental proof of breaking of this symmetry in strong interactions was found, and the CP symmetry remains conserved, even though there is no restrictions from the theory demanding it. To resolve this discrepancy between theory and observations, a new symmetry was introduced in the late 1970s. Spontaneous breaking of this symmetry leads to the existence of a pseudo Nambu-Goldstone boson, a particle named axion [8, 9]. The peculiarity of the axion is its electromagnetic coupling in the interaction with photons, which turned out to be the main asset in searching for it. Studies looking for axions were conducted in the following years, starting from the assumptions of the existence of the so called "QCD axion", envisioned to solve the Strong CP problem. Given that its large mass was accessible to accelerators and particle experiments of the time, the axion was quickly put up to a test. However, this version of the axion was soon dismissed, as none of the studies led to a detection of such a particle. Nevertheless, studies continued searching for axions with lower masses. In this region, axion and Axion-like particles (ALPs) can be identified as particles to constitute DM. The difference between the axion and ALPs is in the nature of the dependence between their mass and coupling to photons, making the axion a specific case of an ALP, with strictly defined relation between its mass and strength of coupling to photons. Axions, ALPs, their interaction with the visible matter, possible detection, and how they can impact the vision of the Universe, will be discussed in Section 2.

1.2 The search for Dark Matter (DM)

The DM has been extensively studied for the past 100 years, starting with its initial proposal by Fritz Zwicky in 1933, who has famously given it the name it has today: "dunkle materie". Zwicky observed and studied the Coma cluster in virial equilibrium, trying to estimate the mass of the cluster needed to maintain a certain speed of the galaxies rotating in it, and compared it to the observable light coming from it, calling this proportion the "mass to light" ratio [10, 11]. What Zwicky concluded was that for keeping such an enormous amount of matter rotating at the measured speed, 400 times more mass should be present than what could be accounted from only the observable light coming from the cluster. Even though Zwicky was a well known astronomer, his conclusions did not trigger the curiosity of the physical society, and his findings were widely confirmed several decades after. A strong interest for DM came only after 1970s, when Vera Cooper Rubin published a work on the systematic measurements of the rotation curves of the Andromeda and many more galaxies [12] (see Figure 1.3). Utilising the virial theorem, the authors proved that the matter in the galaxy is indeed clustered in the centre, but the speed of the rotating matter at greater distances does not decrease as expected, pointing out that there was an additional "invisible" matter present on bigger distances from the centre of the galaxy in the form of spherical halo. With this, the interest for discovering the exact distribution,

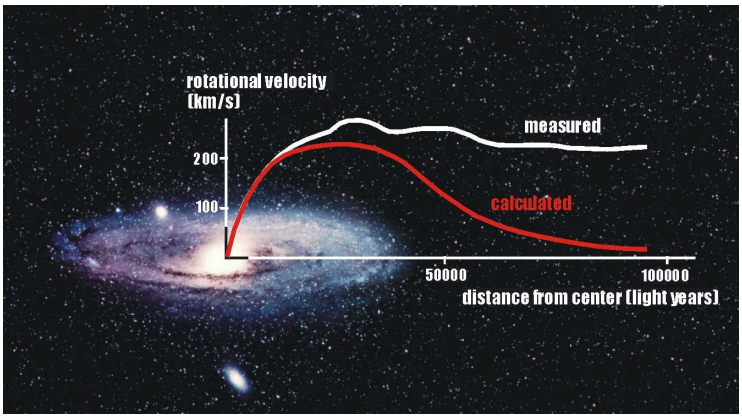

Figure 1.3: Comparison of the measured and calculated rotation curves of the Andromeda galaxy. Reprinted by Queens university.

morphology and the identity of the DM started leading to many new experiments.

Cosmological studies yield us several conditions on the properties that the DM should have: it should be only weakly interacting with the rest of the SM, be electrically neutral, non-baryonic, and able to substantially survive since its production up to today [13], meaning it is long-lived or weakly interacting (for the collection of limits up to date, see [14]. Additionally, since the current observations of the Universe show distinguished areas where matter is clustered, forming galaxies and clusters of galaxies, DM needs to be able to explain the formation and evolution of such objects as well.

Generally, candidates for DM are divided in three main groups depending on their velocity at the moment of their decoupling in the early Universe: the Hot DM (HDM), that was highly relativistic, the Warm DM (WDM) with intermediate velocities and the Cold DM (CDM) that, at the moment when it decoupled, was non-relativistic. In comparison with the data, CDM stands as the candidate that could explain the formation of structures observed today [15].

The entire plethora of the proposed particles and objects as possible building blocks of the DM were studied. They can be grossly divided in few main groups:

- **MAssive Compact Halo Objectss (MACHOs)**, gathering the astrophysical objects such as brown and white dwarfs, neutron stars, black holes or substellar-mass objects [16, 17]. These objects often evade the detection due to being too dim. As such, these "invisible" objects could be forming the DM. Studies searching for them rely on microlensing (e. g. [18–20], the idea envisioned by Albert Einstein, as an effect where a very massive object lying directly on the line of sight to a much more distant star, is lensing the light from the star, which then appears to an observer as portion of a ring around the lens. So far, due to difficulties in the interpretation of the data and small number or such objects detected, it is believed that MACHOs cannot suffice to add up to the predicted amount of the DM in the Universe and have been almost completely discarded as the major contributor to it.

- **Neutrinos**. When the idea of the DM was introduced, one of the first goals was to investigate whether the lightest particle known, the neutrino, can satisfy the conditions [21]. Indeed, neutrinos check all of them: they are non-baryonic, electrically neutral, interact very weakly with the rest of the SM particles and are able to survive the evolution of the Universe from their decoupling up to today. However, due to their relativistic speed at the moment of decoupling, they are a perfect candidate for the HDM, and as such are not able to reproduce the structures that we observe in the Universe. On the contrary, there is still one type of the neutrino that could constitute the CDM, and it is the sterile neutrino, a 4th family of neutrinos [22]. With the mass in the range of keV – MeV, it is a valid candidate for the CDM and is studied up to date.

- **Primordial Black Holes (PBHs)** are black holes created in the early Universe, during the radiation dominated era, and as such, can be of a non-baryonic origin [23]. Due to lack of our knowledge about these stages of the Universe, there are several proposed mechanisms through which the PBHs could have been created. An example are phase transitions of the Universe, when breaking of symmetries occur. It is important to note that the moment of the creation of an PBH has a crucial role in the determination of its mass and the evolution. Up to date, a wide range of PBH masses have been considered, each of which is impacting the evolution and structure formation in a different way (see e. g. [24, 25]).

- **WIMPs** are probably the most scrutinised candidates for DM. These particles, with masses in the GeV - TeV energy range [26, 27], are predicted by several different

theories outside of the SM physics, one of them being the supersymmetry (SUSY) theory [28]. In particular, SUSY is predicting the existence of particles "mirroring" the SM sector, in addition with the change in the quantum spin number by $\pm 1/2$. In this scenario, due to the parity number being opposite to the one of the SM particles, interaction with the SM sector is impossible. As one may conclude, this would perfectly explain the observations and non-detection of any kind of interaction between the visible and dark matter, apart from the gravity. Aside of SUSY candidates, there are many other theories proposing different WIMPs, out of the scope of this work. An example is the super-heavy DM paradigm [29, 30]. Super-heavy DM can be produced at various points during the evolution of the Universe. Based on that, different constraints on its mass are set, varying around $\sim 10^{13}$ GeV, a limit set by inflaton field mass, in case it is produced at the end of inflation [29]. For a broader review, one can consider [31]. Above this, ultra-heavy DM is proposed following the annihilation searches for masses between 30 TeV and 30 PeV [32]. For these thermal relics, annihilation rates are scaling with their mass and depletes the DM abundance once the Universe cools down to temperature below the mass of the DM particle. WIMPs have been investigated in a vast of different experiments, searching for their annihilation and/or decay, concepts that will be mentioned later in greater detail (for review, see e. g. [33, 34].

- **WISPs** are the lightest particles proposed as candidates for DM (see [35] for a review). Most famous are the axion or ALPs, former of which was, and still is, proposed as a solution to the strong CP problem mentioned before, and a good candidate for the CDM as well. Since ALPs are connected with a spontaneous symmetry breaking, they could have been produced in the early Universe via misalignment mechanisms. The misalignment mechanism is proposed by Peccei and Quinn [8] as an effect initiated with the field of a particle having a value different than its potential's minimum. Once the Universe cools down to temperatures around the Quantum Chromodynamics (QCD) energy scale ($\sim$ 200 MeV [14]), the axion obtains mass and its field starts oscillating, converging towards zero. These oscillations of the particle field around the minimum of potential lead to dissipation of the particle energy and decaying into other particles until the minimum is obtained. However, given that the PQ mechanism is not instantaneous, axion oscillations contribute to the Universe's energy density and axion behaves as CDM. [36]. Another example of WISPs, also created through a misalignment mechanism, are dark photons. The key for their detection is the expected kinetic mixing with the SM photons through a new symmetry, which would open a portal to the hidden sector of particles. In case they would have sub – eV masses, these "hidden" photons would be able to constitute DM [37]. A last example of WISP are the so called chameleons, associated with the accelerated expansion of the Universe. As such, they are a candidate for the dark energy, and could interact with the SM particles [38]. Interactions and the nature of chameleons are fairly more complicated that that of an axion, and they will not be discussed in this thesis.

Although there are numerous studies being conducted, DM has eluded a detection so far. Properties of each of the proposed candidates are different, which reflects in different experimental setups needed to search for them. In particular, we have mentioned that in the case of compact objects, such as MACHOs or PBHs, the main method of detection is through the observation and measurement of the effect of gravitational lensing. On the other hand, in case of particle-like DM, the detection can be divided in two to three types: direct and indirect detection, and production at accelerators.

In case of the direct detection, the DM is expected to be produced in collisions of SM sector particles and manifest its presence through the transmission of energy to known particles. Indirect detection studies the product of the annihilation and decay of the DM. In each of these cases, the effect would leave peculiar and unique signatures in the spectra of astrophysical sources, easily distinguished from other astrophysical backgrounds. For example, a spectral cut-off is expected at the DM mass for the annihilating DM, or at its half for the decaying DM [39, 40]. In some cases, even the line-like emission may occur at the termination energy set by the particle mass. For WIMPs, this is expected in the energy range from GeV to $\sim 100\,\mathrm{TeV}$.

In order to search for it, one should have an idea where to look for the DM. Going back to the first discoveries of it, all the evidence are pointing to a few general locations where the overdensities of DM are found: centre of the Milky Way (MW), dwarf spheroidal galaxies (dSphs), clusters of galaxies (GCs), as well as the intermediate massive black holes and globular clusters. Aside of the Fermi Large Area Telescope (Fermi-LAT) at lower, and instruments such as High Altitude Water Cherenkov (HAWC) and Large High Altitude Air Shower Observatory (LHAASO) at higher energies, sensitive in this range are also the Imaging Atmospheric Cherenkov Telescopes (IACTs), offering valid insight into the astrophysics of the Universe, propagation of the particles and their interaction in cosmic regions [34]. Data collected by these instruments was used in the main study of this thesis. As their name might suggest, IACTs are collecting the Cherenkov light coming from gamma rays and charged particles entering the Earth's atmosphere, and creating atmospheric showers of particles. The main objective of IACTs is the characterisation of gamma rays of the astrophysical origin, both galactic and extragalactic.

1.3 Gamma-ray astronomy

Gamma rays are the radiation with shortest wavelengths in the Electromagnetic (EM) spectrum, or highest energies, starting from $\sim 100\,\mathrm{keV}$ and above. Originated in the Universe, gamma rays are keeping the information about an entire zoo of the astrophysical sources and their environments. They are photons, able to cross cosmological distances without being deflected by the magnetic fields permeating the space. This feature allows tracking the gamma ray back to its source, and reconstructing its location and detection. However, gamma rays get absorbed by the background fields of low-energy photons, causing an attenuation of the gamma-ray fluxes: the Extragalactic Background Light (EBL) and the Cosmic Microwave Background (CMB). The EBL is an isotropic background of

photons accumulated through the entire history of the Universe and shifted to μeV energies. Most of this light is emitted during the stellar emission from the nucleosynthesis, stellar evolution or scattered dust in the interstellar space. On the other hand, CMB is a relic background photon field, originated back at the photon decoupling epoch. The impact of these background photon fields on the flux of gamma rays will be described more thoroughly in Section 4.2.2.

The production of gamma rays is mainly through non-thermal processes, connected to the acceleration and interaction of charged particles in the most energetic sites in the Universe. The mechanisms of production include the synchrotron radiation, inverse Compton, and synchrotron self Compton that will be described in Section 4.2.1. Associated to the emission of gamma rays, are the Cosmic Rays (CRs), mostly protons or electrons, hence electrically charged and under the impact of the astrophysical environments and the magnetic fields permeating them. Since the interaction of a CRs with the Earth's atmosphere is very similar to the one of the gamma rays, CRs constitute the major background of gamma-ray astronomy. For this purpose, different algorithms have been developed, with the main objective of distinguishing between the atmospheric showers initiated by a gamma ray vs. a CR.

Instruments calibrated for the detection of the gamma rays from these sources are the aforementioned IACTs, working on the principle of the imaging technique. Imaging technique relies on the characterisation of the image based on the several parameters used to quantify the features of the shower image of in the camera. To obtain such images, IACTs are utilising giant reflectors, tens of meters wide and more smaller mirrors aligned and focused in a way to reflect the incoming light to the photo-multiplier camera on the opposite side of the construction. Currently operating IACTs are distributed over the globe, both Southern and Northern hemisphere. The major IACTs: Very Energetic Radiation Imaging Telescope Array System (VERITAS) [41], High Energy Stereoscopic System (H.E.S.S.) [42] and Major Atmospheric Gamma Imaging Cherenkov (MAGIC). Aside of these, there are also arrays in construction, such as the Cherenkov Telescope Array (CTA)) [43], whose prototype of the Large-sized telescope (LST) is already operating at the Roque de los Muchachos Observatory on the Canary island La Palma. Data of the MAGIC and LST-1 have been used in this work, and their specifications will be described in greater detail in Chapter 4.3.5.

1.4 Modelling the photon-ALP interactions

The main focus of this thesis is study of axion-like particles with VHE gamma-ray data. Once emitted, gamma rays travel through the astrophysical space, interacting with the background photon fields, ambient magnetic fields and once reaching the Earth, entering the atmosphere, creating an atmospheric shower whose Cherenkov light is detected by the IACTs. From that point, a quest to trace back and characterise the gamma-ray which induced the shower begins. We have mentioned the impact of the EBL and CMB in

Section 4.2.2, and that gamma-rays are not suffering the deflection by the magnetic field. Nevertheless, there are effects that can take place and possibly lead to a discovery of a new particle, in this case, an axion (or an ALP). ALPs, as discussed, supposedly take part in the interactions with two photons, oscillating back and forth in the external magnetic field. In case something like that happens, gamma-rays propagation gets disturbed, causing distinctive signatures in the gamma-ray spectrum of the astrophysical sources reprocessed from the IACTs data. ALPs in particular can leave alterations on the observed spectrum in different parts of it, depending on the point at which the photon-ALP conversion occurred. For that reason, the entire path of the gamma-ray propagation needs to be modelled, dividing the entire propagation path in several different regions, depending on the magnetic field present in each of them.

Our study, as it will be revealed in Section 6, investigates NGC 1275, a source located in the centre of the Perseus cluster, at the redshift $z \sim 0.0175$. For our study, we are using the data from a large campaign on the Perseus GC observed with the MAGIC telescopes. This particular dataset includes a strong flare, post-flare and a low activity state of the NGC 1275, combined in a dataset of ~ 41 hours of observations. To evaluate the hypothesis of the existence of axion-like particles, we are modelling several magnetic fields in the line of sight: the magnetic field of the Perseus GC, the Intergalactic magnetic field (IGMF), the EBL attenuation of the photons passing through it, and ultimately the magnetic field of the MW, in which the reconversion of the ALPs back to photons is expected, and hence needs to be considered. In these regions, we are calculating the photon survival probability, the probability that once emitted photons of either polarisation will survive the propagation and be detected as such. For the analysis of the Very High Energy (VHE) data and reconstructing the source spectrum, we are using `gammapy`, an open-source package for gamma-ray astronomy [1][44]. For the ALPs analysis, we are using the `GammaALPs`, a python code developed for solving the equations of motion of the photon-ALP system using the transfer matrix method[2]. We are also considering other effects that could impact the photon flux, for what we have used the models of the EBL absorption, vacuum polarisation and CMB effects, all available in `GammaALPs`.

1.5 Outline of this work

This thesis is structured not only to present the work done (indeed, this will be presented in Section 7.4), but to offer a complete overview of the topic and possibly stimulate the imagination of an interested reader.

To do so, Chapter 2 will discuss the idea about the existence of the axion and his more general relatives, ALPs, their benefits and how they unintentionally became one of the most promising candidates for the elusive DM. Aside of the motivation, we will discuss the mechanism which would allow the detection of an ALP and describe the phenomenology of

[1] https://gammapy.org/

[2] Hosted on GitHub (https://github.com/me-manu/gammaALPs) and archived on Zenodo [1]

the photon-ALP interaction and conversion. This will be done starting from the equations of motion for a generic example of such a system, ultimately obtaining the photon survival probability, the main ingredient in searches for axions and ALPs.

In Chapter 3 we will discuss the state of the art and the experiments in search for axions and ALPs. Starting from the solar axions, we will also introduce the idea of the DM axion and explain the mechanisms that make it so interesting. Finally, we will ponder on the astrophysical axion and studies similar to the one done in this work. In a way, this will be a prelude to what follows in the last chapter of this thesis.

In Chapter 4.2 will be an overview of the gamma-ray astronomy, starting from its inception with the discovery of CRs, continuing to the gamma's and their "life". The production, absorption and detection of gamma rays, together with a discussion of some principal concepts used in the construction of the experimental setups and the data analysis. Chapter 6 will be devoted to the modelling of the propagation of the photon-ALPs system. Most importantly, modelling of the magnetic fields in the line of sight, interaction of the photon-ALP beam with the background photon fields, and in general, all the ingredients for conducting a study of the ALPs using the gamma-rays data.

As important as the data, the experimental setup, in our case MAGIC and LST-1 telescopes, will be described in detail in Chapter 5. This is of a great importance for understanding of gamma-ray observations and collection of the data, production of the results and their interpretation. Chapter 7.4 will discuss the study of the ALPs done using the gamma-ray data of the Perseus cluster collected by MAGIC. We will describe the entire procedure of the study, including the low level data analysis, modelling of the ALPs hypothesis, statistical evaluation of it, and comparison to the conventional descriptions of the source spectrum and ultimately showing the constraints in the ALPs parameter space obtained. In the final Chapter 8, we will discuss the ongoing work with the LST-1 data of blazars. Analysis of only one source, in particular the Mrk 421 will be presented as a first step into obtaining the combined constraints including the data of the LST-1 pool of observed blazar sources. This will be followed by conclusions in Chapter 9 and a critical review of the results and future prospects in the field of ALPs studies.

Chapter 2

The Axion

Contents

2.1 From the Strong CP Problem to a new particle - The Peccei–Quinn mechanism

Encompassing both continuous and discrete forms, symmetries are the central principles in physics. In the field of particle physics, there are three most prominent discrete symmetries: parity transformation (P-symmetry, invariance on the change of space coordinates), charge conjugation (C-symmetry, changing signs of all charges, and transforming a particle in its antiparticle), and time reversal (T-symmetry, symmetry of physical laws under the reversal of time). Extensive studies have been conducted on various processes to test the invariance of each of these symmetries. See [45] for a review of the CPT symmetry tests, and [14] for a full list of tests on the conservation laws. Two primary conclusions have emerged: first, violation of the time reversal, and second, confirmation of the CPT theorem. The CPT theorem combines the symmetries of charge conjugation, parity, and time reversal, and claims it as an exact symmetry of nature. However, conservation of the CPT symmetry also implies the violation of combinations of the individual two symmetries, such as the CP symmetry, considering that the time reversal T is also violated [46]. Indeed, violation of the CP symmetry is shown to take place electroweak interactions, but not the ones mediated by the strong force. For each of the gauge groups corresponding to the respective symmetries, the existence of a θ parameter in Lagrangian terms manifesting the violation can be determined. Indeed, this can be shown for the case of the electroweak

interactions, but given that the discussion is outside of the scope of this thesis, we will not pursue it any further, but rather suggest the interested reader to refer to [47, 48] for a more comprehensive discussion on the Quantum field theory (QFT) concepts, and [36, 49, 50] for more details on the so called $U(1)_A$ problem and its solution. Initially, terms including the θ parameters were expected not to yield any observable effects, but following a deeper consideration of the field vacua, it has been found that such parameters are representing the true state of the gauge vacuum [51, 52]. Their presence in the theory, even though not experimentally identified, had to be taken seriously, because just as the idea of the totalitarian principle states, we may say: "Everything not forbidden is compulsory."

2.1.1 The Strong CP problem

Since its development in 70's of the last century, the theory describing the strong interactions taking place between quarks, the QCD, has been encountering difficulties in reconciling all its predictions with the experimental results. Namely, due to the complex nature of the vacuum, the Lagrangian for QCD allows for a term that violates the CP symmetry:

$$\mathcal{L}_\theta = \theta_{QCD} \frac{g^2}{32\pi^2} G_a^{\mu\nu} \tilde{G}_{a\mu\nu}, \tag{2.1}$$

where θ_{QCD} is the QCD parameter, equivalent to θ parameters mentioned above, related to the vacuum state of the corresponding theory, g^2 is the gauge coupling constant and the $G_a^{\mu\nu}$ and $\tilde{G}_a^{\mu\nu} = \frac{1}{2}\epsilon^{\mu\nu\rho\sigma} G_{a\rho\sigma}$ are the gauge field strength of the SU(3) color symmetry and its dual [53], while $\epsilon^{\mu\nu\rho\sigma}$ is the Levi-Civita symbol, antisymmetric in all indices. As mentioned before, given that this parameter exists in the theory, but the violation of the CP symmetry is not observed in QCD, θ_{QCD} is expected to have a vanishing value. However, experimental results disagree with this assumption. Search for the CP violation in the strong sector can be done with the measurements of the decays of hadrons, neutrino oscillations and electric dipole moments of the electrons, neutrons and more massive nuclei. Given its stability and longer lifetime ($\sim 15\,\text{mins}$), one may use the electric dipole moment of the neutron as an example of a fundamental particle to prove the point that the invariance of the CP indeed can be tested in a simple way. As we noted before, the T symmetry is violated, and in order to assume the violation of the CP, the only thing remaining is to show the violation of the parity P.

Since the neutron is a 1/2 spin particle, with non-zero magnetic dipole moment μ, its electric dipole moment d (in case it exists) is either parallel or antiparallel to it. This assumption on the orientation of the dipole moment follows from the Wigner-Eckart theorem in quantum mechanics requiring the expectation value of any vector operator pointing along the spin quantisation [54, 55]. In Figure 2.1, one can see that the application of P and T symmetries separately leads to a particle with μ and d aligned in the opposite way than it was prior to the transformations. From this, one can conclude that the neutron violates both symmetries and consequently the CP symmetry as well. In contrast to

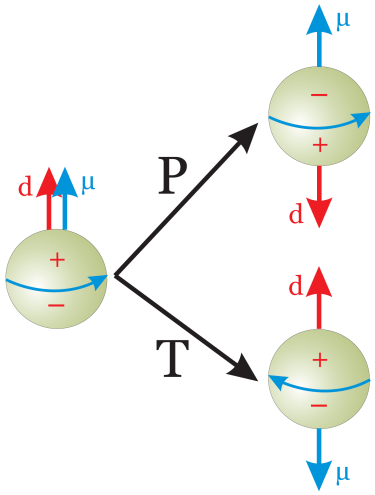

Figure 2.1: The P and T transformations of a particle with parallel magnetic μ and electric dipole d moments. As one can see, the P transformation changes the direction of the electric dipole moment only, while the time reversal T changes the direction of the magnetic dipole moment μ, leaving the electric one unaffected. Comparing the two particles on the right side of the figure, one can conclude that after applying a rotation of 180 deg around the x or y axis, these particles are equivalent. Hence, a particle such as a neutron does not violate the PT symmetry, as well as the charge conjugation C. Image credit: Andreas Knecht.

what is expected, measurements [56] of the decay of a neutron, implicitly measuring the non-vanishing electric dipole moment d_N, require values of θ_{QCD} to be $< 10^{-10}$.

This brings us to a discrepancy between the theory and observations, for more than 50 years known as the Strong CP problem. The CP problem of strong interactions has been found not to be exclusively an issue within the strong, but rather in the weak sector too, more correctly in the impact on quarks that are charged under both gauge groups. As such, the solution for it needs to be searched not only in QCD but the weak and EM sector too.

Several solutions have been proposed, among which the most straightforward was found within the SM itself, and it can be described as the "massless quark" solution. Indeed, in case one of the six quarks is massless (best of which would ideally be the up quark), $\theta_{QCD} = 0$ and consequently the electric dipole moment of the neutron vanishes. However, all experimental studies so far are pointing to a mass of the up quark far from being zero: $m_u = 2.2 \pm 0.5\,\text{MeV}$ [14], directly discarding this proposal.

Another proposed solution is the Nelson-Barr mechanism, an example of a theory utilising the spontaneous breaking of the CP symmetry, such that would make the violation of the CP symmetry not impacting the low energies at which the electroweak interactions may remain unaffected [57–59]. Due to the experimental limitations associated to energies in question, this proposition is still not excluded. Further discussion of this theory is out of the scope of this thesis, but an interested reader is suggested to consider [60] for a review.

In the sea of various solutions to this issue, probably the most promising, dubbed the Peccei–Quinn mechanism, leads us to the existence of a pseudo-Nambu–Goldstone boson, axion.

2.1.2 The Peccei–Quinn mechanism

The Peccei–Quinn (PQ) mechanism [8, 9] solves the Strong CP Problem by introducing a new global symmetry, known as the $U(1)_{PQ}$ symmetry, which makes the CP-violating term (Equation 2.1) in the QCD Lagrangian negligible. In the process of bringing the θ angle to zero, $U(1)_{PQ}$ symmetry is spontaneously broken due to the instantons effects [61] (instantons are the nontrivial gauge field configurations with a finite action). As a consequence, this leads to the existence of a very light pseudoscalar, also called pseudo Nambu-Goldstone boson. At the same time as Weinberg [61], Wilczek [62] was developing a similar idea, and the axion was born. It was proposed as a key piece for the puzzle of an "automatic" solution to the determination of θ parameter [62], the same one that gives a finite value to the dipole moment of a neutron, otherwise expected to be zero. Theories requiring the existence of an axion allow θ to be obtained dynamically [8], as proposed by Peccei and Quinn, or physically insignificant [51, 52], so that all the vacua are physically equivalent, ensuring the CP conservation in strong interactions. In the PQ formalism, the axion is a particle of mass m_a and decay constant f_a, related to the decay amplitude, or in other context, the coupling constant:

$$m_a \simeq 6 \times 10^{-6}\ \text{eV} \left(\frac{10^{12}\ \text{GeV}}{f_a} \right). \tag{2.2}$$

For the original axion proposed by Peccei and Quinn [8], Weinberg [61] and Wilczek [62], known as the $PQWW$, the axion decay constant f_a, associated to the scale of the spontaneous symmetry breaking, is of the order of the electroweak scale ($\nu_{weak} \sim 246\,\text{GeV}$), and the mass of the axion m_a being inversely proportional to it. Its mass was, therefore, expected to be rather large, e. g., of the order of 100 keV. It is worth to mention that both Weinberg [61] and Wilczek [62] provided several ideas following which the existence of such axion was soon experimentally tested and excluded. Even so, these energies were already accessible to accelerators and particle detectors operating at the time. Interested readers are referred to [63–66]. As a logical progression, the quest for axion turned in a different direction, and the condition $f_a \gg v_{weak}$ was set. The PQ mechanism with this implementation yields axions with very low mass m_a, given its inverse proportionality to PQ scale f_a. For this reason, this type of axion is called "invisible". Two main models of such axions are Kim-Shifman-Vainshtein-Zakharov (KSVZ) [67, 68] and Dine-Fischler-Srednicki-Zhitnitsky (DFSZ) [69, 70] models. Up to date, these "generic" models are still under evaluation, given that these axions evade all current experimental studies.

Production of axions includes the interaction with the neutral pions and mesons, hence the axion implicitly inherits their coupling to photons, and takes part in a two-photon

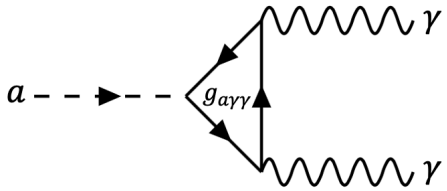

Figure 2.2: Feynman diagram of the axion (a) - 2 photon (γ) interaction.

vertex, shown in Figure 2.2, which offers a favourable opportunity for its detection. This is known as the Primakoff effect [71]. The interaction can be generally expressed as [72, 73]:

$$\mathcal{L}_{a\gamma\gamma} = g_{a\gamma\gamma} \frac{e^2}{16\pi^2 f_a} a F^{\mu\nu} \tilde{F_{\mu\nu}} \tag{2.3}$$

where $g_{a\gamma}$ is a dimensionless coefficient dependent on the axion model, e^2 is the QED coupling, $F_{\mu\nu}$ the strength tensor of the electromagnetic field, $\tilde{F}^{\mu\nu}$ its dual, and a is the axion field with the mass m_a. For any invisible axion model in the presence of an external magnetic field $\vec{B}$, Equation 2.3, can be written as:

$$\mathcal{L}_{a\gamma\gamma} = -\frac{g_{a\gamma}}{4} F^{\mu\nu} \tilde{F}_{\mu\nu} a = g_{a\gamma}\, \vec{E} \cdot \vec{B}\, a, \tag{2.4}$$

where we introduced a physical substitution for the coupling $g_{a\gamma\gamma}$ in units of eV^{-1}. In the second part of the equation, $\vec{E}$ is the electric field of a photon beam, and $\vec{B}$ is the external magnetic field, mentioned before, together with the axion field a. Figure 2.3 is representing the inverse Primakoff effect, which is the interaction of an axion a with a photon from the magnetic field $\vec{B}$, resulting in its absorption and transformation of the axion into a photon γ. The hunt for axions is relying on this particular phenomena,

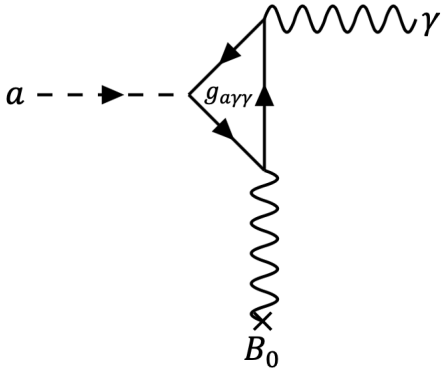

Figure 2.3: Feynman diagram of the axion (a) interaction with a photon (γ) in an external magnetic field $\vec{B}$.

gathering a plethora of experiments that will be described in Section 3. As a relaxation of

the dependence between the two most important axion parameters, the mass m_a and the strength of its interaction with photons $g_{a\gamma}$, the axion model was extended to a wider group of particles, called Axion-Like Particles (ALPs). More interestingly, ALPs emerge not only as a generalisation of the axion but also in many theories beyond the Standard Model, from four-dimensional extensions of the Standard Model [74], to compactified Kaluza–Klein theories [75] and especially string theories [76–78], see e. g., Jaeckel and Ringwald [79] for a review.

Unlike the axion, ALPs do not solve the strong CP problem, but have another interesting property for which they are pursued. Similarly to axion, ALPs have all the pre-requisites to constitute the cold DM. The main reason for this is their small mass, combined with a possibly large decay constant $f_a \simeq 10^{12}$ GeV. In case they are produced via the misalignment mechanisms with $f_a \sim 3 \times 10^{11}$ GeV and corresponding $m_a \sim 20$ μeV, ALPs can constitute the entirety of the DM, giving an axion density parameter close to the one of the dark matter estimated today. Unfortunately, this comparison can only go so far, due to the additional topological effects such as cosmic strings and domain walls that can affect the axion density and will be mentioned later in Section 3.3.

In case one does not find a particular interest in discovering the DM, ALPs are also proposed in models of solar physics where they are produced through processes such as Compton scattering, axion bremsstrahlung and the Primakoff effect. The last one is of a particular interest in the search for solar axions and it will be mentioned later in Section 3. Aside of that, they could contribute to the a possible change in the transparency of the Universe to gamma rays. This effect is particularly interesting for the observational gamma-ray astronomy, given that it impacts the propagation of the VHE gamma rays, otherwise expected to be strongly attenuated by engaging in the pair production with the photons from the background field in the intergalactic space. If ALPs exist, gamma rays can be converted to ALPs and cross the intergalactic space without being absorbed. There are several earlier works that have envisioned experimental search for the ALPs [72, 80–82] and many of which have been followed up to date. Aside from the obvious interest of the particle physics, astrophysics and cosmology, ALPs are also searched for in the experiments in high energy and nuclear physics, reviewed by Kim [66] and Peccei [83].

In the following chapter, we will reflect on the extensive search for axion and ALPs, mentioning some of the most prominent experimental searches up to date. For now, we will discuss the aforementioned interaction of the ALPs with photons in a two photon vertex, used as the main tool in the search for ALPs.

2.2 Phenomenology of the photon-ALP conversion

As anticipated, the main topic of this thesis will be to search for ALPs in their signatures in the gamma-ray spectra. For that purpose, we will dedicate this section on describing the nature of the photon-ALP mixing and the applications in astrophysics.

The existence of axions and ALPs can be probed by their imprints on the spectra of astrophysical sources. This is due to the fact that, in (the presence of) magnetic fields,

the ALPs couple with photons. Therefore, TeV-energy gamma rays can, while travelling over cosmological distances, convert to ALPs due to the presence of strong magnetic fields and, as such, cross the astrophysical distances until they possibly encounter another strong magnetic field, such as that of the MW, in which they can convert back into observable gamma rays. All these conversion/reconversion processes are governed by a probability term for the conversion $P_{\gamma \to a}$, which depends on the actual ALP mass and coupling, as well as the magnetic field characteristics.

Axion - photon conversion in a magnetic field

In order to quantify the effect of the photon-ALP conversion, it is necessary to compute the photon survival probability $P_{\gamma\gamma}$. The Lagrangian of the photon-ALP system can be written as

$$\mathcal{L} = \frac{g_{a\gamma}}{4} F_{\mu\nu} \tilde{F}^{\mu\nu}\, a - \frac{1}{4} F_{\mu\nu} F^{\mu\nu} + \frac{\alpha^2}{90\ m_e^4} \left[(F_{\mu\nu} F^{\mu\nu})^2 + \frac{7}{4} (F_{\mu\nu} \tilde{F}^{\mu\nu})^2 \right] + \frac{1}{2} (\partial_\mu a\, \partial^\mu a - m_a^2\ a^2), \quad (2.5)$$

where the first term relates to the photon-ALP coupling $\mathcal{L}_{a\gamma\gamma}$ term discussed in Equation 2.3, followed by the photon field contribution, term related to the effective Euler–Heisenberg Lagrangian $\mathcal{L}_{EH}$ for corrections of QED loops in photon propagators due to an external magnetic field [84], and the kinetic term of the axion field, $\mathcal{L}_a$. Third term is used to describe the photon-photon interactions in the limit where the photon frequencies are low in comparison with the mass of the electron, being below the threshold for the production of $e^- - e^+$ pairs. In our approximation, this term will be neglected.
Solving the Euler-Lagrangian equations for photon and axion field yields:

$$\partial_\mu F^{\mu\nu} = g_{a\gamma}\, \tilde{F}^{\mu\nu}\, a\, \partial_\mu \quad \text{and} \quad (\Box + m_a^2)\, a = -\frac{g_{a\gamma}}{4}\ F_{\mu\nu}\, \tilde{F}^{\mu\nu} \quad (2.6)$$

In the presence of an external magnetic field, the time-varying part of the vector potential $\vec{A}$ for the axion field is described with:

$$\Box\, A = g_{a\gamma}\, B_T\, \partial_t a \quad \text{and} \quad (\Box + m_a^2)\, a = g_{a\gamma}\, B_T\, \partial_t A, \quad (2.7)$$

where B_T is the transversal component of the magnetic field. The longitudinal component, on the other side, has no impact given that it respects the azimuthal symmetry (same as the longitudinal component of the electric field) and cannot mediate transitions between states of different angular momentum. The impact of the transversal magnetic field component in the photon-ALP system can be explained in analogy with neutrino oscillations; the axion spin is zero, but because the magnetic field component matches the missing quantum number, it can mix with a photon of spin 1.

Coming back to the equations of motion, in this case we will observe a wave of frequency ω, propagating in the z direction and include the plasma frequency of the medium in the equation. After this, equations of motion become:

$$(\omega^2 + \partial_z - {\omega_{pl}}^2)\, A_j = -i\, \omega\, g_{a\gamma}\, a\, B_j \quad ; \quad j = x, y \quad (2.8)$$

$$(\omega^2 + \partial_z - m_a^2)\, a = -i\, \omega\, g_{a\gamma}\, (A_x B_x + A_y B_y) \quad (2.9)$$

For very relativistic axions (ALPs) ($m_a \ll \omega$), short wave approximation can be applied and the equations of motion reduce to the first order equations. Furthermore, assuming that the B field variation in space occurs on much longer scales than the photon or axion wavelengths, using the dispersion relation $k = n\omega$; $|n-1| \ll 1$ and assuming that only magnetic field B is present, we can use:

$$\omega + {\partial_z}^2 = (\omega - i\partial_z)(\omega + i\partial_z) = (\omega - i\partial_z)(\omega + k) \to 2\omega\,(\omega - i\partial_z). \tag{2.10}$$

Respecting this, we can re-write the equations of motion:

$$(\omega - i\partial_z)\,a = \frac{{m_a}^2 a}{2\omega} - \frac{g_{a\gamma}}{2}\,(A_x B_x + A_y B_y) \tag{2.11}$$

$$(\omega - i\partial_z)\,A = \frac{{m_{pl}}^2 a}{2\omega}\,A_j - a\,\frac{g_{a\gamma}}{2}\,B_j. \tag{2.12}$$

These are classical mixing equations in form of the Schrödinger equation with time component replaced by the spatial coordinate z:

$$i\frac{d}{dz}\Psi(z) = (H_0 + H_1)\Psi(z) \quad \text{where} \quad \Psi(z) = \begin{pmatrix} A_x \\ A_y \\ a \end{pmatrix} = \begin{pmatrix} A_\perp \\ A_\parallel \\ a \end{pmatrix}, \tag{2.13}$$

where H_0 and H_1 are free and interaction Hamiltonians, respectively:

$$H_0 = \omega\,\mathcal{I} + \begin{pmatrix} \Delta_\gamma & 0 & 0 \\ 0 & \Delta_\gamma & 0 \\ 0 & 0 & \Delta_a \end{pmatrix}; \quad H_1 = \begin{pmatrix} 0 & 0 & \Delta_x \\ 0 & 0 & \Delta_y \\ \Delta_x & \Delta_y & 0 \end{pmatrix}. \tag{2.14}$$

H_{12} and H_{21} components are neglected because we will not consider polarised sources of photons (even though it is important to remember that the emission from sources such as AGNs is often polarised). These terms are called Faraday terms and they explain coupling of $A_\parallel$ and $A_\perp$. For homogeneous magnetic field B, and y-axis chosen to be along the projection we can substitute:

$$B_x = 0; \quad B_y = |B_T| = B; \quad A_x = A_\perp; \quad A_y = A_\parallel. \tag{2.15}$$

Comparing Equation 2.14 with Equations 2.11 and 2.12, we can write:

$$\left[\omega + \mathcal{M} - i\partial_z\right] \begin{pmatrix} A_\perp \\ A_\parallel \\ a \end{pmatrix} = 0, \tag{2.16}$$

where $\mathcal{M}$ is the photon-ALP mixing matrix:

$$\mathcal{M}_0 = \begin{pmatrix} \Delta_\perp & 0 & 0 \\ 0 & \Delta_\parallel & \Delta_{a\gamma} \\ 0 & \Delta_{a\gamma} & \Delta_a \end{pmatrix}. \tag{2.17}$$

Elements in this matrix are defined considering the plasma condition, the QED vacuum birefringence effect (that we neglect in the simplest case), the axion field, and the photon-ALP mixing:

$$\Delta_\perp = \Delta_{pl} + 2\Delta_{QED}; \quad \Delta_\parallel = \Delta_{pl} + \frac{7}{2}\Delta_{QED}$$

with

$$\Delta_{a\gamma} = \frac{1}{2} g_{a\gamma} B_T; \quad \Delta_a = -\frac{m_a^2}{2\omega}; \quad \Delta_{pl} = -\frac{\omega_{pl}^2}{2\omega}; \quad \Delta_{QED} = \frac{\alpha\omega B_T^2}{45\pi B_{CR}^2}.$$

In the equations above, α is the fine structure constant and $\omega_{pl} = \sqrt{4\pi\alpha n_e/m_e}$ is the plasma frequency, dependent also on the ambient thermal electron density n_e, while term $B_{CR} \sim 4.4\times10^{13}$ G is the critical magnetic field. The factor $\Delta_{a\gamma}$ represents the photon-ALP mixing and depends on the strength of the interaction $g_{a\gamma}$, and the intensity of transverse magnetic field $B_\perp$. By neglecting the effects of vacuum and photon refractive index, the orthogonal component of the axion potential $A_\perp$ decouples and the equations of motion are simplified to the 2×2 mixing problem:

$$\left[\omega + \begin{pmatrix} \Delta_\parallel & \Delta_{a\gamma} \\ \Delta_{a\gamma} & \Delta_a \end{pmatrix} - i\partial_z\right] \begin{pmatrix} A_\parallel \\ a \end{pmatrix} = 0. \tag{2.18}$$

This equation can be solved with diagonalisation by the rotation to primed field, and obtaining the mixing angle θ:

$$\theta = \frac{1}{2} arctan \frac{2Bg_{a\gamma}}{{m_a}^2 - {\omega_p}^2} \tag{2.19}$$

Following the analogy to the neutrino mixing states, one obtains the probability of the photon-ALP conversion [84]:

$$P_{0,\gamma\to a} = \sin^2(2\theta)\sin^2\left(\frac{\Delta_{\rm osc} z}{2}\right) = \left(\Delta_{a\gamma}\, z\right)^2 \frac{\sin^2\left(\Delta_{\rm osc}\, z/2\right)}{\left(\Delta_{\rm osc}\, z/2\right)^2}, \tag{2.20}$$

where z is the size of the magnetic field domain and Δ_{osc} is the oscillation wave number: $\Delta_{osc}^2 = [(\Delta_a - \Delta_{pl})^2 + 4\Delta_{a\gamma}^2]$. This is often written in terms of the critical energy E_{crit} defined as:

$$E_{crit} \sim 2.5\ \text{GeV}\ \frac{|m_{a,neV}^2 - \omega_{pl,neV}^2|}{g_{11} B_{\mu G}}, \tag{2.21}$$

where $\omega_{pl,neV}$ is the plasma frequency in units of neV, $B_{\mu\rm G}$ is magnetic field in μG and $g_{11} = g_{a\gamma} \times 10^{-11}\ \text{GeV}^{-1}$. The critical energy is computed in such a way that, around and above this value, the conversion probability of one photon $P_{0,\gamma\to a}$ in Equation 2.20 becomes sizeable. This will be of a great interest to us later, in Section 3.5. It is the case where $\Delta_{osc} \sim 2\Delta_{A_\parallel}$, and the beam is in the so called "strong mixing regime". For the case of $2|\Delta_{a\gamma}| \gg |\Delta_{pl} - \Delta_a|$, the conversion is energy independent. The last case is considering

$\Delta_{osc} \ll 1$, and the oscillatory term is small (occurs below the critical energy). This is known as the "weak mixing regime"

In order to properly consider the propagation of the photon-ALP beam through a physical B field, we need to consider the exact morphology of the magnetic field, and the hypothesis of having just one single magnetic field domain with a fixed orientation is not plausible. The reason for this is that different polarisation states of axion field can interplay differently in each of the respected magnetic field domains. A common approach is to divide the magnetic field into N different domains. By doing this, the transfer matrix can be reformulated, (for full derivation, see the appendix of [85]) thus providing the total photon conversion probability $P_{\gamma\to a}$:

$$P_{\gamma\to a} = \frac{1}{3}\left(1 - \exp\left(-\frac{3}{2}NP_{0,\gamma\to a}\right)\right). \tag{2.22}$$

If we rewrite Equation 2.20 following the previously introduced substitutions, we obtain:

$$P_{\gamma\to a} = \sin^2(2\theta)\sin^2\left[\frac{g_{a\gamma}Bd}{2}\sqrt{1+\left(\frac{E_c}{E}\right)^2}\right]. \tag{2.23}$$

see from Equation 2.23, $P_{\gamma\to a}$ is dependent on the product of domain length d and magnetic field B. Because of this, it is essential to have a well-defined magnetic field model to account for the oscillations in the spectra of astrophysical objects caused by the photon-ALP mixing.

Chapter 3

Search for Axions and Axion-like particles - The Quest

Contents

Since its birth, the search for axion has attracted a lot of interest. Starting from the 1970s, ideas for detection of axions flooded the scientific journals, proposing the experiments that later discarded the existence of the "heavy" axion, known also as the original PQ axion. On the other side, the search for the "invisible", less massive axion, is still ongoing and it is a very active field [36].

Based on the energy range corresponding to the axion mass, the physics of the experiment varies, and the implications of the existence for such a particle vary as well. The central interest of this thesis is to investigate ALPs with very low masses, reachable by the energy range in which our telescopes are most sensitive. This includes masses in the range of hundreds of μeV to neV. Since these are one of the smallest masses in the ALPs parameter space, this section will start from the experiments in search for the most massive ones, in the range of hundreds of μeV and above. These axions (ALPs), as we will soon reveal,

are very good candidates for DM, but also, in some cases, a solution for aforementioned strong CP problem. These particular ALPs are "positioned" on the "diagonal band" (see Figure 3.1) in the ALPs parameter space, referring to the conventional models of axions, that are envisioned to solve the Strong CP problem.

Continuing with the laboratory searches, we will reflect on light phenomena such as the "light-shining-through the wall" and polarisation, used to explore the axions with meV masses. Advancing towards smaller masses and higher energies, we will encounter solar axions, those produced in the interiors of stars, possibly affecting the stellar evolution.

In the very end of this section, we will mention the limits obtained from the astrophysics, both theoretical and experimental, setting the emphasis on searches done with observations of the VHE gamma rays. Figure 3.1 is showing the ALPs parameter space, filled with the constraints on the photon-ALP coupling up to date. In the following sections this figure will be updated with the experiments of interest and a more detailed explanation will be given.

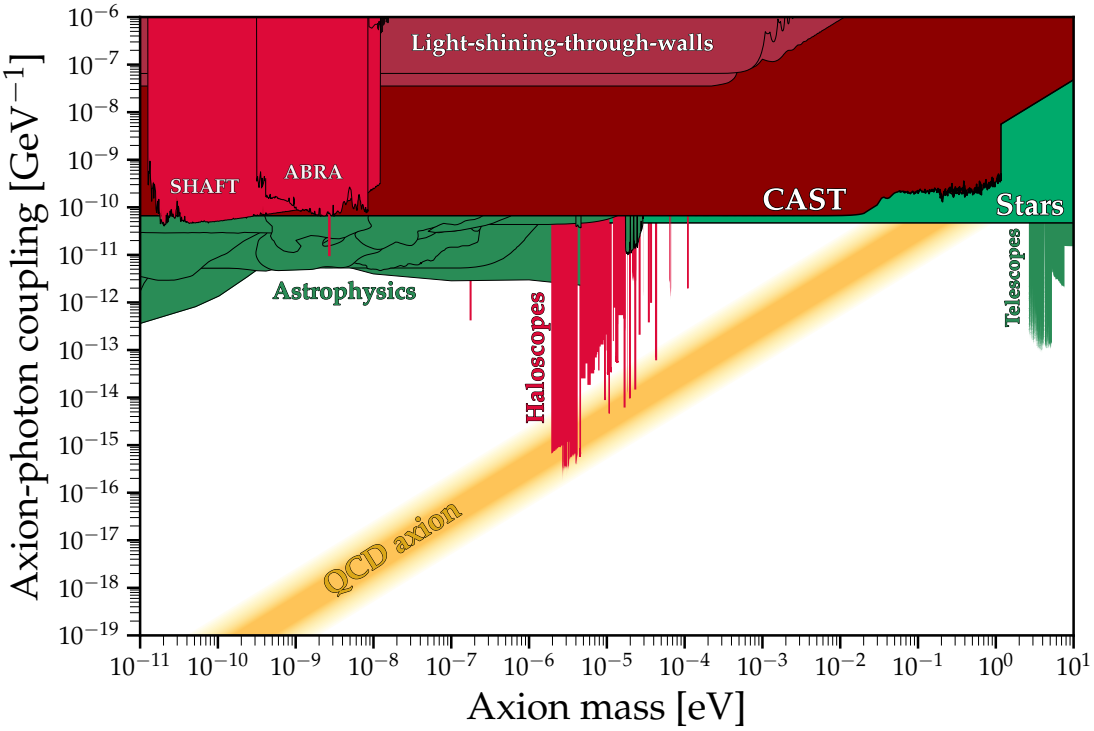

Figure 3.1: ALPs parameter space with general constraints from helioscopes, laboratory experiments, haloscopes and astrophysics up to date. Gathered in [86].

3.1 Solar axions - helioscopes

Solar axions can be detected through the inverse Primakoff effect (see Figure 2.3) in macroscopic B-field inside instruments called helioscopes. Strong magnetic field in the instrument, completed with an X-ray detector at the far end, enables these detectors to search for the reconversion of axions into X-ray photons, as proposed by Sikivie [72]. The first of such experiments in search for axion models fitting the axion QCD paradigm was the CERN Axion Solar Telescope (CAST) [87]. In particular, CAST used a dipole magnet with a strength of $\sim 9\,\mathrm{T}$ and length $L = 9.26\,\mathrm{m}$, previously used at the CERN's Large Hadron Collider (LHC). The helioscope is following movements of the Sun during $\sim 1.5\,\mathrm{h}$ at dawn and dusk, pointing at it with each end of the magnet. The remaining time is used for performing the calibration and background data taking. Conversion of the solar axions occur in the strong magnetic field, enabling the detection of X-ray photons in the solid-state detectors at the energy of the $\mathcal{O}(\mathrm{keV})$. The latest constraint on the coupling of photons to axions obtained with CAST [88] is:

$$g_{a\gamma} < 6.6 \times 10^{-10}\ \mathrm{GeV}^{-1} \text{ for } m_a \lesssim 0.02\,\mathrm{eV} \text{ at } 95\%\ \mathrm{C.L.} \tag{3.1}$$

Scheme of the CAST helioscope is shown in Figure 3.2. Progress in this detection technique

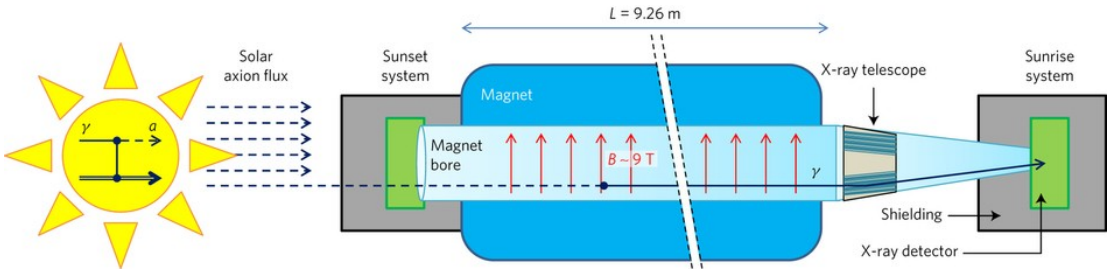

Figure 3.2: Scheme of the experimental setup of the CAST helioscope [88].

is directed towards smaller values of $g_{a\gamma}$, given that due to the limits on the mass set by the cosmic hot DM bound, further pursuit towards larger masses is demotivated. Future improvements are expected from the new-generation axion helioscope International Axion Observatory (IAXO) [89], currently being in the experimental stage named Baby(IAXO) at DESY (Deutsches Elektronen-Synchrotron) [90]. IAXO plans to challenge the current limits for the stellar-losses, under the hypothesis of axion component domination in cooling of the stellar objects such as the white dwarfs and red giants [91]. Exceeding the signal-to-noise ratio (SNR) of CAST by $> 10^4$ and sensitive to $\sim 20\times$ lower $g_{a\gamma}$, IAXO is planned as significantly improved axion helioscope. Projections of the expected constraints in the ALPs parameter space, compared to other helioscopes is shown in Figure 3.3. Solar axions can also be searched for in previously mentioned enhancement of flux through the effects of axion conversion into photons in the electric field. This particular effect occurs when the incident angle of the axion satisfies a Bragg condition with the crystal plane [92]. This type of axion detection is pursued in experiments such as SOLAX [93], DAMA [94], COSME [95]

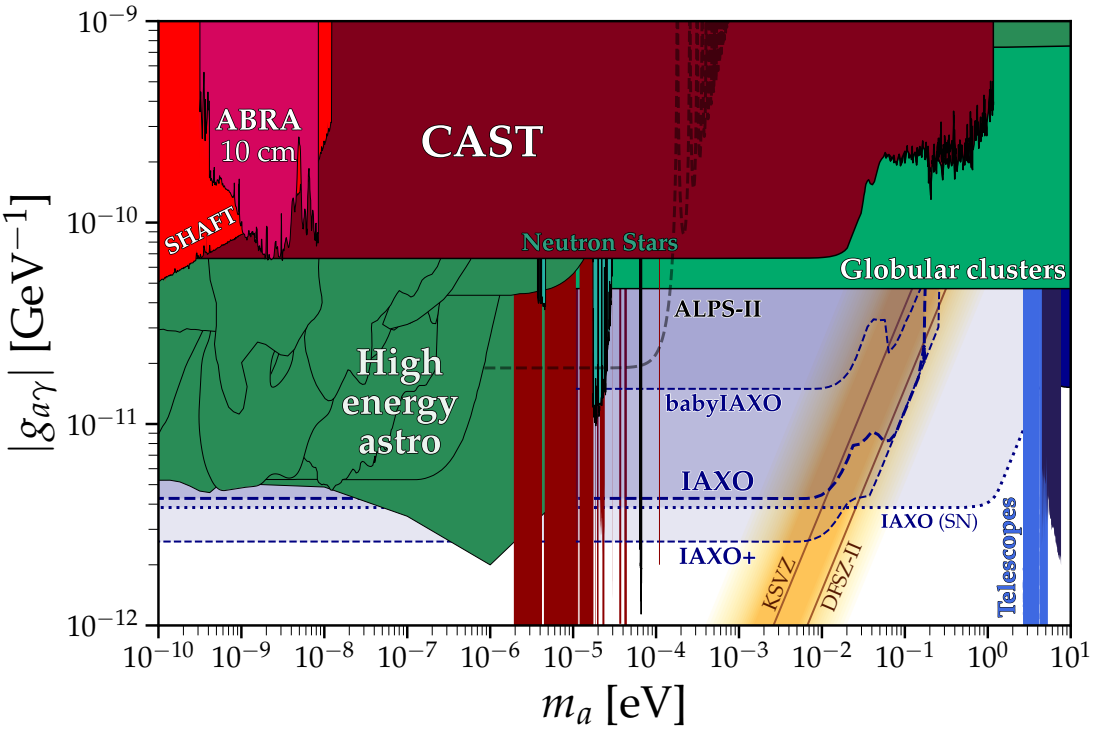

Figure 3.3: Exclusion plot for photon-ALP coupling with closeup on the parameter space accessible to helioscopes. Collected in [86].

and CDMS [96]. However, current limits do not supersede the ones that will be mentioned later, coming from the stellar physics (see Section 3.4).

3.2 Laboratory experiments

3.2.1 Light-Shining-through-Walls (LSW)

LSW is one of the alternative methods used in the laboratory searches for axions. Pursuing the possible conversion of axions into photons in transverse magnetic fields, LSW experiments are using laser beams propagating through a cavity in a superconducting dipole magnet of length L. To test whether the conversion happens, another magnet is aligned with the first, but separated by an optically opaque wall, through which the laser beam cannot cross. In case that the photon-ALP conversion occurs, a regeneration of such axions back in the second magnet is expected, and captured by the detector. A first prototype of such an experiment was operated by the BFRT (Brookhaven-Fermilab-Rochester-Trieste) collaboration [97, 98] and obtained constraints on the photon-ALP coupling:

$$g_{a\gamma} < 6.7 \times 10^{-7}\ \text{GeV}^{-1} \text{ for } m_a < 0.1\,\text{meV at } 95\%\ \text{C.L.} \tag{3.2}$$

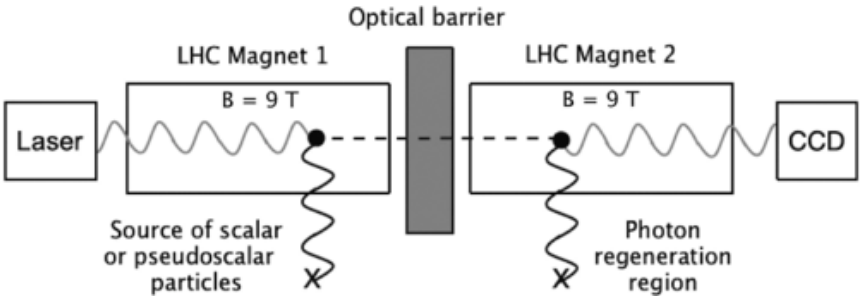

Figure 3.4: Scheme of the experimental setup of the OSQAR experiment [99].

To this date, the most stringent constrain from experiment of this type comes from the Optical Search for QED Vacuum Birefringence (OSQAR) at CERN [99]:

$$g_{a\gamma} < 3.5 \times 10^{-8}\ \text{GeV}^{-1} \text{ for } m_a \lesssim 0.03\,\text{meV at } 95\%\ \text{C.L.} \tag{3.3}$$

OSQAR is an experiment utilising a decommissioned 9 T magnet with a laser emitting at ∼532 nm (see Figure 3.4). Although the magnet is very similar to the one used in CAST, one can notice that the results by OSQAR are significantly less constraining. This can be explained with the argument that the flux of solar axions is higher than the ones artificially produced in magnetised cavities using a laser. This is followed by the fact that these axions have energies around eV, unlike keV axions produced in the Sun.

In the previous years, there have been developments and improvements on the instrumentation in goal of increasing the sensitivity of the detection. Firstly, to increase the flux of possibly generated axions, the optical cavity is installed on both ends of the generating cavity before the wall. In this way, before converting to axions, photons have several opportunities to convert, having in mind that they are bouncing back and forth in the generating cavity [97]. In addition to this, as explained by [100–102], the photon regeneration can be boosted by inserting both the production and regeneration cavities inside of two tuned Fabry-Pérot cavities and detectors installed on both sides of the regeneration cavity. As demonstrated in [101, 102], this setup allows for improvement in sensitivity in the axion-photon coupling. Following this idea, ALPS II (Any Light Particle Search 2) experiment [103] was envisioned. As an improvement of already existing ALPS I [104] experiment, ALPS II is targeting $g_{a\gamma} > 2.0 \times 10^{-11}$ GeV^{-1}, which would indicate above three times better sensitivity compared to the current LSW experiments.

3.2.2 Light polarisation

As proposed by et al. [105] and Raffelt and Stodolsky [73], the axion can affect the propagation of a photon beam through a magnetic field. This is explained through the effects of birefringence and dichroism. Due to the axions mixing with the parallel component of the magnetic field, linearly polarised light gets slightly rotated (birefringence) and elliptically polarised (dichroism). The effort for measuring the vacuum magnetic birefringence is lasting for the past 25 years and it was started with the experimental studies

by the aforementioned BFRT [98] collaboration, yielding constraints on ALPs coupling to photons: $g_{a\gamma} < 3.6 \times 10^{-7}$ GeV^{-1} for $m_a \lesssim 0.05$ meV at 95% C.L. In 2006, Polarisation of the Vacuum with Laser (PVLAS) experiment, Zavattini [106] reported an observation of a change in light polarisation in a vacuum filled with a magnetic field. This claim was refuted by a following publication two years later [107]. Nevertheless, these were the results that motivated some of the studies of ALPs using the very-high-energy gamma rays, as it will be repeated later in Section 3.5.

3.3 Dark Matter (cosmological) axions

The inspiration for the extensive searches for axions and ALPs is coming mainly from the fact that they are good candidates for the DM. In some cases, even for its entirety. Axions and ALPs can be produced thermally and non-thermally. Thermal axions are produced in processes including quarks, gluons, and in some cases, pions [14]. So far, they have been considered as "problematic", due to the argumentation similar to the massive neutrinos and their ability to evade the detection. Just as neutrinos, if produced in the early Universe through thermal scatterings, axions would constitute hot dark matter (HDM) with masses $m_a \sim$ eV, and as such, they would affect structure formation. HDM leads to primary creation of superclusters, which subsequently gravitationally collapse into smaller fragments, galaxies, encompassed under the "top-down" hierarchy of structure formation [15]. This scenario is in contrast with the observations that are supporting the opposite, "bottom-up" scenario [108] asserting the creation starting from the primordial seeds forming bigger structures, galaxies, and finally clusters. Following from this scenario, limits on the QCD axion mass $m_a \sim$ eV are obtained [109]. Further constraints are set from limits on the possible fraction of the HDM, and for higher masses, by cosmological observations related to big bang nucleosynthesis, EBL, galactic gamma-ray spectra and more (e. g. see [110, 111]).
The non-thermally produced axions and ALPs on the other side, are the main goal in searches for these evasive particles. Non-thermally produced axions and ALPs can constitute CDM. The main mechanism of the CDM axions and ALPs production is the vacuum misalignment. Assuming a homogeneous axion field, at the critical time in the early Universe, when $H \sim m_a$, where H is the Hubble parameter, the axion field starts oscillating. This is the moment when the axion field obtains mass. Soon after, when $H \ll m_a$, these oscillations of the axion field become adiabatic, allowing axion to decouple, behave as non-relativistic particles, move slowly, accrete, create structures of matter and possibly constitute what we call the CDM.

Under the assumptions of the CDM density today, it is possible to approximate the expected axion abundance. Considering the standard cosmological model, in order to explain the energy density of DM today, one arrives to the constrain on the axion mass [112]:

$$g_{a\gamma} < 10^{-12} \left[\frac{m_a}{1 \text{ neV}} \right]^{1/2} \text{GeV}^{-1}. \tag{3.4}$$

Following from this equation, the mass of the axion should be $m_a \gtrsim \mu$eV. This is the case for the QCD axion, one that was initially proposed as the solution of the strong CP problem [8, 9, 61, 62]. In the case of ALPs, mass is independent of the moment of their creation in the Universe, and correspondingly its temperature, impacting the strength of their coupling to photons, $g_{a\gamma}$. Hence, models and corresponding predictions of ALPs parameter space for which they could be accounted as the CDM, partially or in its completeness, is a lot wider than in the case of axions. This can be also concluded from the ALPs parameter space, such as the one in Figure 3.1.

To consider the interesting case of axionic DM, we need to differentiate two options:

1. PQ symmetry is broken **before** the inflation. We are going to address this as the pre-inflation scenario.

2. PQ symmetry is broken **after** the inflation. We are going to address this as the post-inflation scenario.

The PQ phase transition, an event at which the $U_{PQ}(1)$ symmetry becomes spontaneously broken, occurs at the temperature when the axion is still massless and all values of the axion field are possible [113].

In the pre-inflation scenario, the topological effects, caused by oscillations of the axion field before inflation, would affect the fluctuations of the temperature in the CMB and could be observed in post-inflation times, and today [114].

On the contrary, post-inflation scenario assumes the breaking of the PQ symmetry after the inflation concludes. For this reason, there are separated regions in the Universe where the axion field is present, and the energy density can be calculated simply as an average value of all the separated regions. Same as in the previous case, topological defects are present, but now they are not blown away by the inflation, and can contribute to the total axion DM density. These additional contributions could come from the axion strings, radiating the axions from the time of the PQ transition to the moment when the axion field acquires mass, as well as from the axion domain walls and vacuum realignment at later times. These contributions have been widely discussed and studied (in. e. g. [115–118]), but so far they seem to be subdominant [119], or in some cases, too large [120] in comparison to the contribution coming from the misalignment mechanism.

As mentioned above, post-inflation scenario supposes spatially separated regions in the Universe with higher abundance of axions. These particular regions in the Universe, where the "clumps" of axions form after the Universe enters the matter-dominated era, serve as a perfect object for studies of the cosmological and astrophysical observations in search for the CDM. Morphology, spatial and temporal coherence of the expected axion clumps, halos, and in general, regions of higher density, are very important asset in the axion dark matter searches. In particular, the two coherences are important for determining the size and quality factors of the resonant cavities experiments searching for massive axions, respectively.

3.3.1 Experimental searches for DM axions

Depending on the assumed mass of the axion/ALP, different detection methods have been used and exploited in the axion DM searches. Given that the expected mass range for the DM axion is between 10^{-6} – 10^{-4} eV, the best modality of detection is through the resonant photon-ALP conversion inside an electromagnetic cavity, as initially proposed by Sikivie [72]. The idea of detection is as follows: photons are produced through the conversion from axions that is enhanced by tuning the microwave cavity modes to match the angular frequency of the axion signal. The signal is picked up by an antenna, amplified by a low-noise receiver, sampled and analysed. Using the frequency-mass conversion (see Equation 2.2 and have in mind the $0.25\,\mathrm{Hz} \approx 10^{-15}\,\mathrm{eV}$ conversion), it is easy to conclude that GHz frequencies are the best for detecting the DM axions with masses of the order $\mathcal{O}\,(10^{-5}\,\mathrm{eV})$. Having in mind that the axion mass is unknown, cavity needs to be tuneable, though there are examples of non-tuneable ones as well. Tuning is achieved by using the mobile metal and/or dielectric posts inside of the cavity [121]. The first of such experiments were RBF (Rochester-Brookhaven-Florida) and UF (University of Florida). Limits were set in the $4.5 < m_a < 16.3\,\mu\mathrm{eV}$ range, significantly less sensitive to models of the DM axions expected [122, 123].

Currently one of the most sensitive experiments is the ADMX (Axion Dark Matter eXperiment). The experimental scheme of ADMX is shown in Figure 3.5. The initial version of this experiment was the first of that kind to achieve the DSFZ line in the axion parameter space. The latest results by the ADMX set unprecedented constraints in the axion parameter space for axion masses $3.3 < m_a < 4.2\,\mu\mathrm{eV}$, more stringent than any instrument of this kind up to date [125] (see Figure 3.6). More recently, ADMX introduced a novel cavity design, tuned to higher frequencies using a piezoelectric actuator, capable of searching for more massive axions, called ADMX Sidecar [126].

Less constraining, but working with with same principle, is The Haloscope At Yale Sensitive To Axion CDM (HAYSTAC) experiment [127]. In comparison with ADMX, HAYSTAC is searching for heavier axions, with masses $m_a \sim 20\,\mu\mathrm{eV}$. In their latest publication, HAYSTAC set the constraints on the axion masses in the range of $18.44 - 18.71\,\mu\mathrm{eV}$, down to $g_\gamma^{KSVZ} = 2.06$ at a 90% C.L, where g_γ^{KSVZ} stands for the KSVZ benchmark coupling [67, 68] [1]. For comparison with the other constraints from the cavity searches, see Figure 3.6.

One of the most perspective laboratories in search for axionic DM is The Center for Axion and Precision Physics Research (CAPP). Since 2018, following his construction, CAPP has conducted several haloscope experiments utilising the high-temperature superconducting cavities. First results published by CAPP were obtained with the CAPP-8TB experiment [128], constraining the photon-ALP coupling for masses $6.62 - 6.82\,\mu\mathrm{eV}$ at a 90% C.L, reaching the parameter space of the KSVZ models. Improving the experimental setup by introducing the multi-cell cavity setup, they achieved the sensitivity to constrain the photon-ALP coupling for axion masses between $13.0 - 13.9\,\mu\,\mathrm{eV}$ [129]. Another axion

[1] KSVZ benchmark is defined as the coupling for the original KSVZ model axion with a neutral quark.

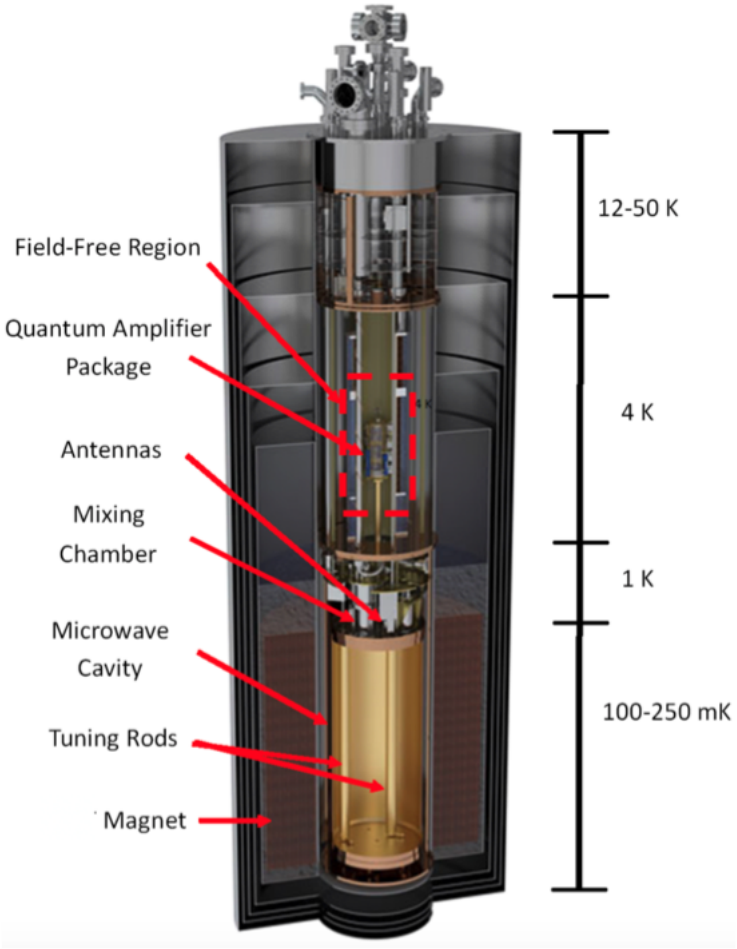

Figure 3.5: Experimental setup of the ADMX experiment [124]. The detector composed out of several parts and placed within bore of a superconducting solenoid magnet. Top part of the detector contains a field-free region within which the quantum amplifiers, antennas, switches and circulators, cooled down with a pulse tube cooler on the top. Below field-free region, tanks containing liquid helium are placed, together with mixing chambers and another set of amplifiers. Microwave cavity with tuning rods are located on the bottom, where the magnetic field is applied and cavity frequency is changed by positioning tuning rods.

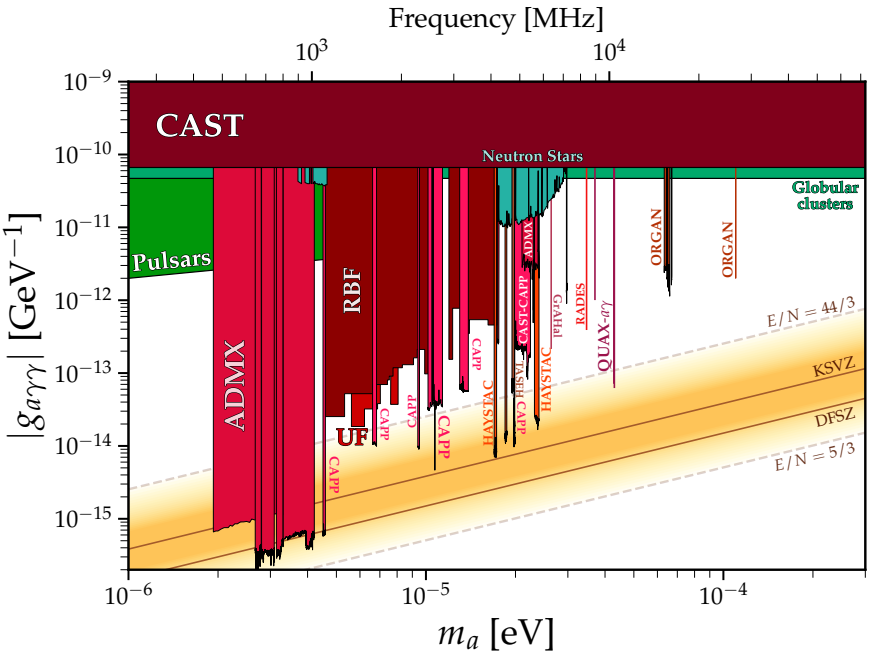

Figure 3.6: Exclusion plot for photon-ALP coupling with closeup on the parameter space accessible to haloscopes. Gathered in [86].

experiment at CAPP is the CAPP-PACE, "the coldest" DM axion experiment so far, operating at 38 mK. CAST-PACE also improved the scanning speed and covering the available axion mass range in less time. Their results are setting the constraints on axions with masses around 10.7 μeV, for couplings around g_γ^{KSVZ}, and up to 9 times above g_γ^{KSVZ} in the mass range $10.16 - 10.37\,\mu$eV, at a 90% C.L. Their main experiment, CAPP-MAX, operates with a 12 T superconducting magnet, and collects the data with the sensitivity to DSFZ models around 1 GHz frequency. Their latest published results are setting the constraints on the axion masses around 4.55 μeV [130].

Leaning towards higher masses of axions is the QUAX experiment at Laboratori Nazionali di Legnaro in Italy. QUAX-aγ haloscope is an un-tuneable haloscope composed of an oxygen-free high thermal conductivity cavity, equipped with a 8 T magnet and exploring the galactic axions with masses $\simeq 43\,\mu$eV. Around these masses, QUAX set constraints on the photon-ALP coupling $g_{a\gamma} \lesssim 0.766 \times 10^{-13}\,\text{GeV}^{-1}$ [131]. Recently, the results have been improved down to $g_{a\gamma} \lesssim 0.731 \times 10^{-13}\,\text{GeV}^{-1}$ through re-assessing the data analysis and significantly improving the system noise temperature to improve the axion's signal estimation-efficiency [132].

Another example of a non-tuneable cavity, but covering wider range of axion masses, going from $60 - 210\,\mu$eV, is The Oscillating Resonant Group AxioN (ORGAN) experiment [133]. In 2022, ORGAN set limits on the axions in energy mass range $63.2 - 67.1\,\mu$eV, limiting the photon-ALP coupling $g_{a\gamma} \gtrsim 3 \times 10^{-12}\,\text{GeV}^{-1}$. These results are excluding the models predicting the ALPs in the SM that would simultaneously explain the observed

baryon and dark matter densities in the early Universe, so called ALPs cogenesis models [134].

As a part of the experimental setup at previously mentioned CAST, the Relic Axion Dark-Matter Exploratory Setup (RADES) detector is searching for axion DM around 34.67 μeV As it can be seen in Figure 3.6, RADES sets the exclusion limit with a 95 % C.L. for photon-ALP coupling of $g_{a\gamma} \gtrsim 4 \times 10^{-13}\,\mathrm{GeV}^{-1}$.

Aside of the conventional microwave resonant cavity principle, there are other, novel concepts for detecting the axion DM. One of them is the MAgnetized Disc and Mirror Axion eXperiment (MADMAX), currently under construction [135]. MADMAX is an open

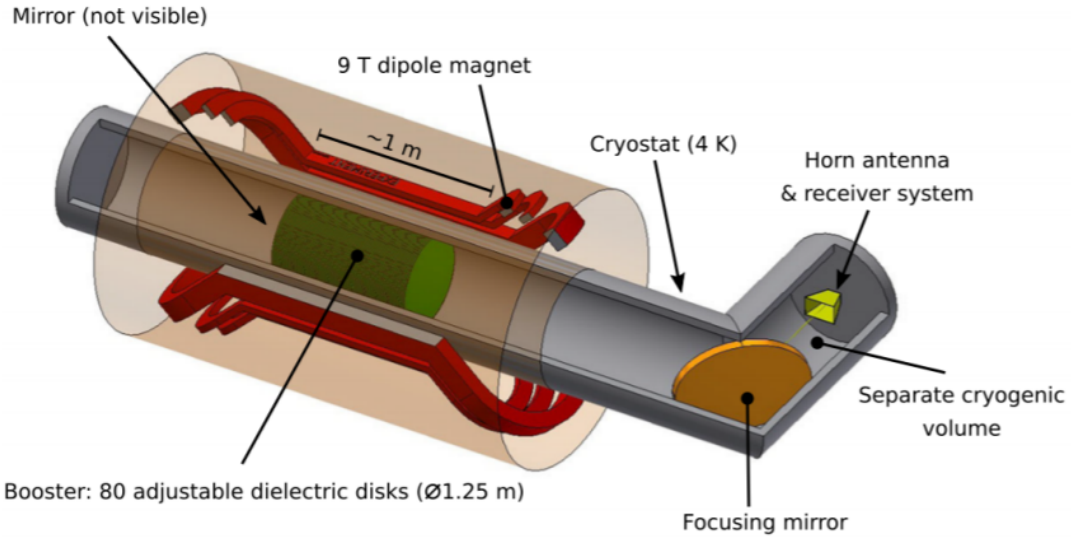

Figure 3.7: Preliminary base design of the MADMAX experiment. The experiment can be divided into three parts: magnet, booster and the receiver – consisting of the horn antenna and the cold preamplifier [135].

tuneable dielectic haloscope, capable of scanning the axion masses in the range $40-200\,\mu$eV. It is consisted of several parallel dielectric discs located in a strong magnetic field, aligned in way that they can be adjusted to resonantly enhance the photon signal. The experimental scheme of MADMAX is shown in Figure 3.7.

Other examples of DM axion searches include experiments searching for axion with masses smaller than μev. These experiments necessitate the cavity detector of length of $\mathcal{O}$ (10 m). For this purpose, the conventional resonant cavity is replaced by a cooled LC circuit. The ABRACADABRA experiment is designed following this idea and it searches for an AC magnetic flux in a toroidal magnet, expected in case of existence of axion DM [136]. The SHAFT is a similar experiment as well, but in this case using a ferromagnetic core of a toroidal magnet [137].

3.4 Stellar limits

Axions can be produced in the interior of the Sun by the Primakoff conversion of thermal photons in the fluctuating electric field of the plasma [138]. The solar flux of axion has been previously calculated by Raffelt [139]:

$$\frac{d\Phi_a}{dE} = \frac{6.0 \times 10^{10}}{\mathrm{cm^2\,s\,keV}} \left(\frac{g_{a\gamma}}{10^{-10}\,\mathrm{GeV^{-1}}} \right)^2 E^{2.481} \exp\left(-\frac{E}{1.205} \right), \tag{3.5}$$

where E is the energy of a photon that is converted into an axion of the same energy. An integration over a standard solar model (Sun core temperature $T \sim 10^7\,\mathrm{K}$) gives the average energy of axions arriving to the Earth, being 4.2 keV. In case these axions also have a non-negligible coupling to electrons, this flux can be enhanced through the Compton-like scattering.

Following the idea of the axion emission from the stars, constraints on the axion coupling to photons, and in some cases electrons or nucleons can be set. Initial constraint comes from the solar age limit. Having in mind that the Sun is halfway through its hydrogen burning phase (following the standard solar model), the luminosity of the Sun ($L_\odot$) should not be exceeded by the solar axion luminosity. This condition can be checked with models of the helioseismology leading to $L_a \lesssim 0.20\ L_\odot$ [140]. Axion emission, as an additional component in the solar cooling, requires the accelerated nuclear burning, increased temperature in the Sun, and consequently enhanced flux of solar neutrinos. Studies done by combining the helioseismology models and solar neutrino observations placed upper limits on the axion coupling to photons [141]:

$$g_{a\gamma} \lesssim 4.1 \times 10^{-10}\,\mathrm{GeV^{-1}}. \tag{3.6}$$

The same principle can be expanded to other populations of stars as well. Different stages of stars evolution can be determined by comparing the surface brightness to the surface magnitude, obtaining the color-magnitude diagram, known as the Hertzsprung-Russell Diagram [142]. Depending on the evolution stage, different processes are dominating the life of the star. The so called "horizontal branch" (HB) stars are in the burning-helium stage which would be shortened in case of the significant Primakoff energy loss rate. Comparison of the number of HB stars and red giant branch (RGB) stars (with significantly lower rate of Primakoff conversion) offers the estimation of the HB lifetime and direct constraint on the coupling of axions to photons [143, 144]:

$$g_{a\gamma} < 6.6 \times 10^{-11}\ \mathrm{GeV^{-1}}\ \text{at } 95\%\ \text{C.L.} \tag{3.7}$$

Prior to the ignition of the helium core, mid-sized stars ($0.6-10\ M_\odot$), spend their evolution in the red-giant branch, during which the hydrogen is still burning, in now already thin shell, and the helium core is increasing in size. The critical mass of the helium core before its ignition depends on the cooling processes, where axion production can be relevant. In case significant, it could delay the ignition of the core and increase the lifetime of the star in the RGB phase. Due to the interplay of bremsstrahlung effects, de-excitation and

recombination, this effect can be used to set constraints on the axion-electron coupling. Most sensitive constraints up to date are set in [145]:

$$g_{aee} \lesssim 1.6 \times 10^{-13}\ \text{GeV}^{-1} \text{ and } g_{aee} \lesssim 1.3 \times 10^{-13}\,\text{GeV}^{-1} \text{at } 95\%\ \text{CL}, \tag{3.8}$$

respectively. Once it burns all its fuel, star similar to our Sun proceeds in the stage of a white dwarf (DW). This evolutionary phase is characterised by the remaining hot core at a temperature higher than 10^5 K, cooling through the neutrino emission from the core and photons from its surface. Being in the agreement with the expectations, studies of the WD emission also give the constraints on the axion-electron coupling [146]:

$$g_{aee} \lesssim 3.0 \times 10^{-13}\,\text{GeV}^{-1}. \tag{3.9}$$

Other constraints from different stages of stars evolution, such as supernova explosion, also offer constraints on the axion coupling, in most cases the one with nucleons [147], which will not be thoroughly discussed here. For further discussion on the limits, and probably most detailed collection of constraints set by these, see [14].

3.5 Astrophysical axions

The photon survival probability, as mentioned before (see Figure 2.23), depends on the strength of the axion coupling to the photon, the intensity, and the coherence scale l_{coh} of the magnetic field in the medium in which the photon/ALP beam (gamma ray converting to an ALP and back) is propagating. While the first term is governed by the microscopic nature of the ALP, magnetic fields through the Universe vary and depend on the environment through which the photon/ALP beam is propagating. Therefore, one needs to consider all the different magnetic field environments on its path from the source to the detector, also taking into account the position and type of the source. As a general example, we will consider an Active Galactic Nucleus (AGN) with a relativistic jet aligned to the line of sight, called blazar. For the case of a blazar, an emitted gamma ray passes through at least four different magnetic fields during its propagation to our detector:

- Magnetic field at the source itself.
- Magnetic field of the relativistic jet, in which the particles are accelerated and/or emitted.
- Magnetic field of the GC in which the blazar is residing.
- IGMF, in which gamma rays are also interacting with the ambient fields of particles, e. g. the EBL and CMB.
- Magnetic field of the MW.

The propagation of the photon/ALP beam from the source to the Earth is illustrated in Figure 3.8. Blazar is a type of a broader family of sources, called AGNs. AGNs are the most studied sources in searches for ALPs, located in cores of GCs. Here, once generated, gamma rays from the AGN would encounter strong magnetic fields in the cluster core and have a sizable probability of being converted to ALPs. Such ALP could travel unimpeded over intergalactic distances, whose magnetic field is extremely low, thus allowing only a moderate photon reconversion. Finally, the ALP, when entering the MW magnetic field, could (or not) be reconverted back to gamma rays.

Therefore, there are several kinds of imprints in the original gamma-ray spectrum. In the first case, if an ample fraction of photons is converted at the source into ALPs that do not later convert back in the MW, a signal depletion would be observed. In the second case, if an ample conversion happens in the source but then a back conversion happens in the MW, one could also observe an ampler signal than expected; for example, if the ALP travelled through regions of space that are opaque to gamma-rays (for example, regions with strong particles or radiation fields). One should mention that the above signatures would be observed on top of the well-known gamma-ray extinction due to the interaction with the EBL [53, 148–152] which strongly limits the observation of TeV emission above redshift $z \sim 1$.

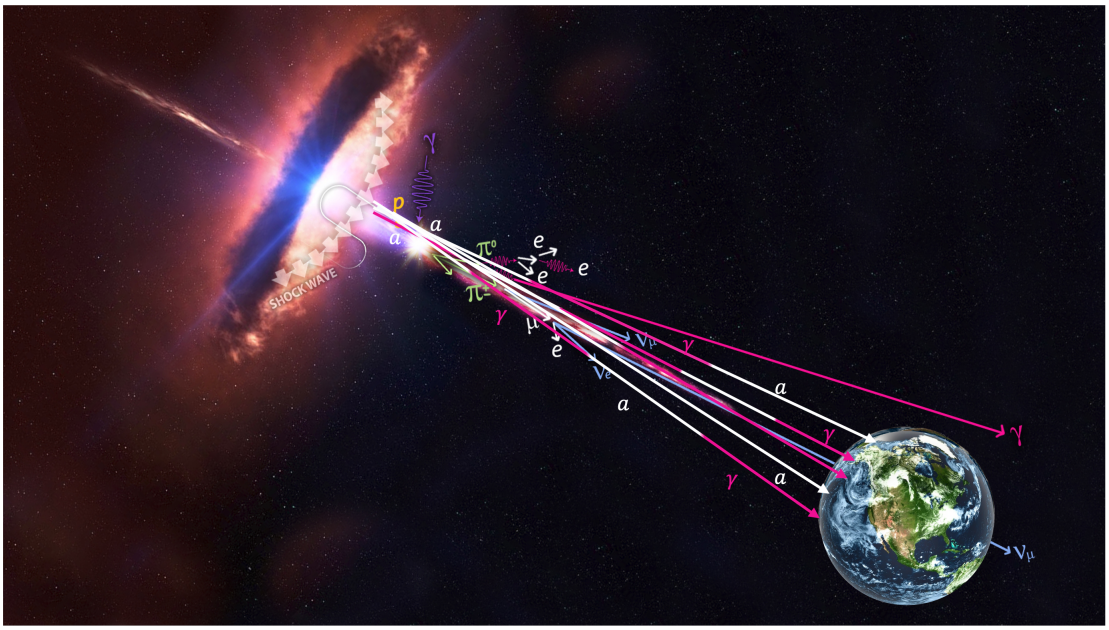

Figure 3.8: Propagation of the photon/ALP beam through the Universe. Credit: IceCube & NASA.

The propagation of VHE photons is affected by pair production with the EBL. There are uncertainties around the true value of the EBL. From one side, it is subject to uncertainties when assuming different emission models, due to the interplay of several factors, and on the other side subject to bias when estimated experimentally due to the presence of the strong optical foreground from our galaxy. However, during the past decade, models have been converging to a higher level of agreement. Protheroe and Meyer [153] and de Angelis et al. [148] suggested that the observation of TeV photons was implying an EBL intensity lower than previously expected. This first motivated the introduction of ALPs as a way to escape or soften this tension [53, 148, 150, 153–158]. Depending on the photon energy, HE photons interact with the EBL or the CMB, producing an electron–positron pairs ($\gamma\gamma_{EBL} \rightarrow e^+ + e^-$). The relativistic pairs produced in these interactions can upscatter the CMB photons and initiate creation of secondary, lower-energy electromagnetic showers. In this interplay of processes, attenuation of flux can occur due to the photon absorption, which being converted to $e^+ + e^-$ pairs, avoid detection. The flux attenuation caused by these processes is dominant for photon energies around $E_\gamma \approx 500\,\mathrm{GeV}$ (EBL) and $E_\gamma \approx 10^6\,\mathrm{GeV}$ (CMB), respectively [148]. In that way, the greater part of photons is absorbed and evades detection: the Universe becomes opaque to VHE gamma rays. The above-mentioned cases of the ALP signatures are possible in a regime above the critical energy E_{crit} of Equation 2.21, where the photon-ALP mixing is maximum. A different occurrence is possible at around E_{crit}. In this regime, the oscillatory behaviour in Equation 2.23 would create "wiggles" in the spectrum, modulated by the probability term. These wiggles would be hardly misinterpreted as being of astrophysical origin and

would, therefore, constitute a clear detection. Such a case is extensively discussed in, e. g. [53, 150, 155, 156].

3.5.1 Astrophysical Targets for ALP Searches with IACTs

In the attempt to maximise the ALP signatures, it is possible to select the best target of observation. These are astrophysical emitters, where both ample, high-energy gamma-ray photons fluxes are produced, and where the gamma-ray radiation encounters extended regions with significantly intense magnetic fields, which extend over much larger distances than their coherence length [159]. These conditions guarantee that the probability of the interaction is maximal (see Equation (2.20)). Recently, the authors of [160] quantified the importance of intensity of the magnetic field and the source brightness, showing that, for example, a factor of 2.5 more intense magnetic field could result in significantly stronger constraints on the ALP coupling ([160], Figure 7). This is however a point that will be discussed again later in Section 7.4. In the gamma-ray TeV sky, sources often display a flaring state, as opposed to a baseline emission state. If possible, flaring states are then preferred in searches for ALP. The best candidates for observations are, therefore, AGNs, where particle acceleration and subsequent gamma-ray emission are found in the region around the central supermassive black holes (SMBHs). AGNs are the largest population of TeV targets. An optimal situation is an AGN located in the central core of GCs, especially in a cool core one, in which extended and intense magnetic fields permeate the region around the central galaxies. In this condition, magnetic field is more intense (tens of μG) with respect to that in the intergalactic space. One of the best examples of this is the AGN NGC 1275 at the centre of the Perseus GC, presented above and used in this work. Another class of objects of interest for ALP searches is that of compact objects, namely, pulsars and neutron stars, which are also present in binary systems. Here, the magnetic field is more localised, but significantly more intense.

In Figure 3.9 one can see the distribution of possible acceleration sites, in our case sources of gamma rays, depending on the size and strength of the magnetic field at their position.

In order to make a prediction of the photon-ALPs interaction pattern, one has to define both the microscopic nature of the ALP (mass and cross-section) as well as the magnetic field. For the former, one has to build a model of the interaction, as done, for example, in the aforementioned, open-source `GammaALPs` code, and scan the available parameter space. This is, at present, mostly done with grid sampling. For the magnetic field, used procedure is the computation of several random realisations, as we will show later.

Other targets have been explored for ALPs searches. In case of a supernova explosion, ALPs would be emitted via the Primakoff process and could be observed with gamma rays after a possible re-conversion in the magnetic field of the MW. Following the observation of the supernova SN1987A, constraints due to the non-observation of gamma rays, coincidental with the neutrino observations, were set [162, 163], but affected by strong uncertainties. Due to this, [164] revisited these papers using a more detailed analysis. Additionally, neutron stars are another possible candidate for ALP searches. Considering radiative decays of axions produced by nucleon–nucleon bremsstrahlung in neutron stars [165, 166], Berenji

et al. [167] have set constraints on the axion mass m_a using the Fermi-LAT data of four neutron stars. This phenomenon was investigated in previous works with X-ray [168] and gamma ray data from a supernova [169].

3.5.2 Critical Energy and Parameter Space for gamma-ray Studies

The interest in ALP searches in the gamma-ray range was firstly encouraged by the unexplained observation of a change in light polarisation in a vacuum filled with a magnetic field detected by the Polarization of the Vacuum with Laser (PVLAS) experiment [106], that was mentioned in more detail in Section 3.2.2, offering an explanation based on the existence of a light axion. The results of the PVLAS experiment were in tension with the astrophysical limits. In order to reconcile the signal obtained with PVLAS, the authors theorised an ALP with mass $m_a = 1.3\,\text{meV}$ and coupling $g_{a\gamma} = 3 \times 10^{-6}\,\text{Gev}^{-1}$.

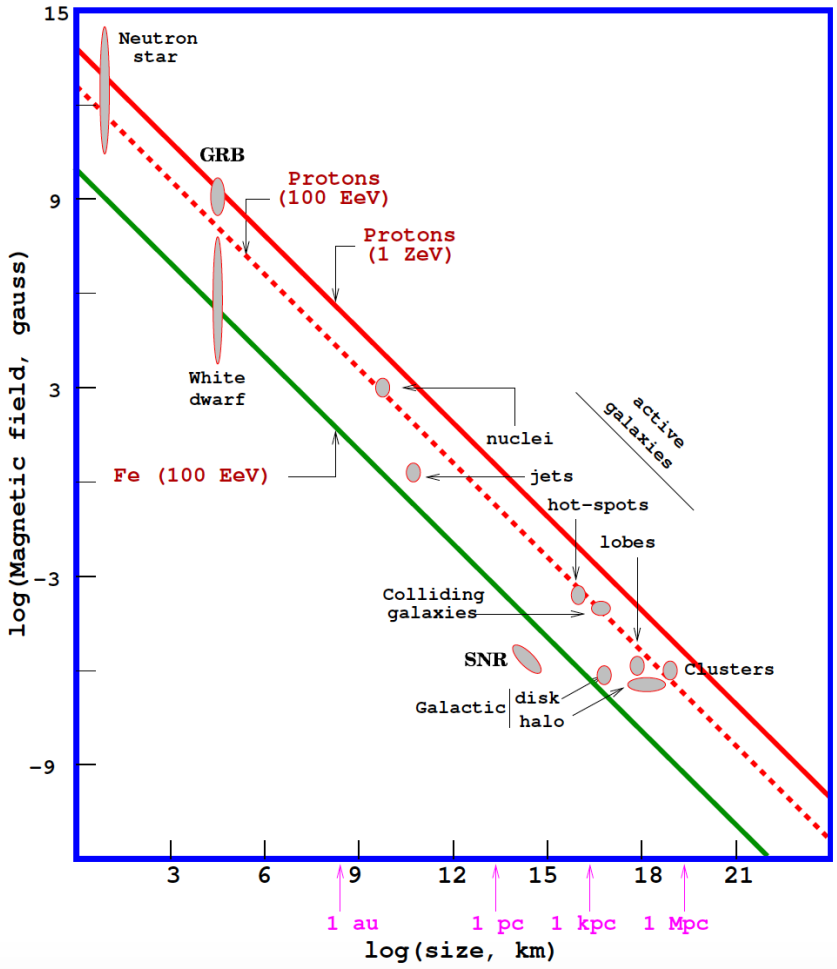

Figure 3.9: The Hillas diagram showing the possible acceleration sites, distributed in the parameter space of the size and strength of their magnetic fields from [161].

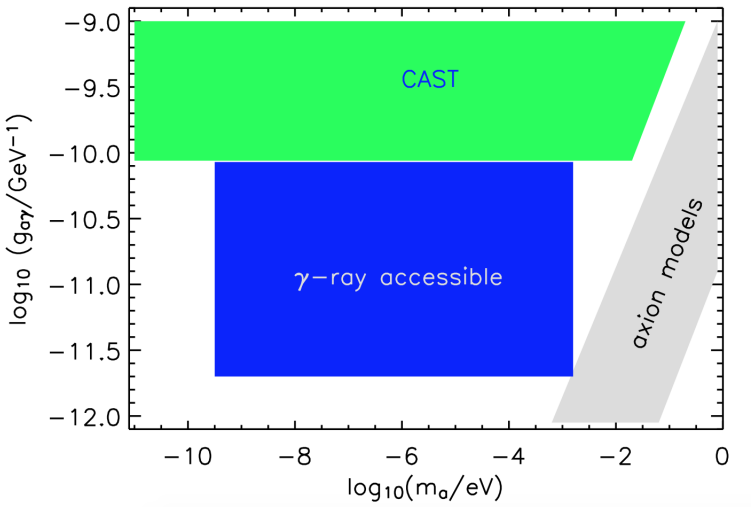

Figure 3.10: ALPs parameter space available for gamma-ray observations. Reprinted from Hooper and Serpico [155].

Following this interpretation, Mirizzi et al. [154] included photon-ALP conversion in the magnetic field of our galaxy and, taking mentioned parameters into account, presented possible distortions in the photon spectra above the energies $E_\gamma \geq 10\,\mathrm{TeV}$. A few months later, de Angelis et al. [170] and Hooper and Serpico [155] extended this approach. Taking into account the possibility of the photon-ALP conversion in and around the gamma-ray source, as strong astrophysical accelerators, they showed that the critical energy in Equation 2.21 falls directly in the gamma-ray range. The photon-ALP conversion then depends on the condition

$$g_{a\gamma} B\, s/2 \geq 1 \tag{3.10}$$

where B is the magnetic field component aligned with the photon polarisation vector and s is the size of the magnetic field domain. If the photon–axion conversion happens at the source, product Bs in Equation 3.10 is directly connected to the Hillas criterion [171] for the maximum possible acceleration energy of CRs, and taking into account that CRs with energies up to 10^{20} eV have been observed [172], it follows that sources with $B_G s_{pc} \geq 0.3$ should exist [155] (in case that the CR acceleration is electromagnetic). Hooper and Serpico [155] showed that IACTs such as H.E.S.S., MAGIC and VERITAS could probe the range of masses of $m_a = (10^{-9} - 10^{-3})\,\mathrm{eV}$ with sensitivities stronger than CAST, as shown in Figure 3.10. The best candidates for observation were identified with AGNs located in the cores of GCs. One can now compare Figure 3.10 with Figure 3.1 to see how Hooper and Serpico [155] were right in their predictions.

The first works by de Angelis et al. [148, 170] are based on the observed, yet unexpected transparency of the Universe: EBL observations at the time showed higher transparency at higher redshifts than anticipated by the available models [153, 173]. Following the idea that, if converted to ALPs, photons could travel through the extragalactic space without interaction with the EBL or CMB photons, be converted back to photons in the Galactic

magnetic field (GMF) and be detected as such, the photon-ALP conversion could reduce the opacity of the Universe to VHE gamma rays, as discussed above. In order to explain the possible detection of TeV photons from 3C 66A, a source located at $z = 0.44$, which was not expected by conventional physics of photon propagation at the time, Sanchez Conde et al. [150] laid out a similar model. They built a model combining both the mixing near or in the source and mixing in the intergalactic space, stressing the importance of observations, both in the lower and highest energies in order to better constrain the intrinsic spectra of the sources, the EBL attenuation and explore the morphology of the considered magnetic fields. The photon flux attenuation was investigated by varying and combining the photon energy, magnetic field intensity, source redshift and ALPs parameters, showing that these effects could be observed in the spectra of AGNs at the higher energies, $E_\gamma \geq 1\,\mathrm{TeV}$, especially if combined with the Fermi-LAT energy regime [150]. After MAGIC detected the surprising rapidly varying emission from the Flat Spectrum Radio Quazars (FSRQ) PKS 1222+216 [174], Tavecchio et al. [157] performed a combined ALPs study using the MAGIC and Fermi-LAT data. The aim of [157] was to present the emission model, including the photon-ALP oscillations mechanism, and explain the mentioned detection. The results showed an agreement with the previously introduced De Angelis, Roncadelli and Mansutti (DARMA) scenario that includes photon-ALP oscillations triggered by large-scale magnetic fields to effectively reduce the EBL attenuation at the energies above 100 GeV [53, 156]. These results showed the possibility of explaining such emissions with photon-ALPs oscillations by applying them to the other detected FSRQs. A dedicated paragraph on a very recent study by the Fermi–LAT collaboration will be presented later in the end of Section 3.5.3.

The challenge related to the detection of spectral features induced by ALPs in the gamma-ray spectra is due to the number of statistical and systematics fluctuations that shape the spectrum, even in the case of no ALP effect. First of all, the intrinsic spectrum is shaped by the absorption by the EBL, as discussed above. Such an effect is non-negligible for targets farther than $z \sim 0.1$, but many models have been created based on EBL observations in the Ultraviolet (UV)-Infrared (IR). Therefore, it is possible to correct the spectra for EBL absorption at different redshifts. The effects of Lorentz Invariance Violation (LIV) on the flux in photons could also compete with ALPs conversion, but the power of a given source to constrain LIV increases with its variability in time, the hardness of its energy spectrum, even the redshift z since the effects of LIV accumulate (paying attention to the effects of EBL which causes softening of the spectrum), so not all the considered targets are necessarily good targets for studying LIV. For a review of LIV studies with IACTs, readers are advised to consider Terzić et al. [175]. The energy reconstruction is generally performed with IACTs at about $10-20$ % precision, depending on the energy. Finally, the data are affected by a variety of systematics due to the instrument itself (e. g., telescope mirror reflectivity) as well as external factors (atmospheric optical depth). While the former are estimated more accurately, less accurate results were obtained for the latter. Observing irregularities in the spectrum, such as those caused by the ALPs—see Figure 3.13—is, therefore, challenging.

In the following, we will discuss some of the most important studies of the ALPs with

the VHE gamma-ray data, entering in details about the data and statistical analysis, and the constraints they set in the ALPs parameter space.

3.5.3 20 years of ALP studies with HE and VHE gamma rays

This section will be dedicated to a broader overview of the experimental searches for ALPs with the IACTs and other telescopes in the HE and VHE gamma-ray regimes. Over past 20 years, studies for ALPs have always been drawing the attention, offering unique explanation to discrepancies between the observations and theory. These will be mentioned and explained here, followed with studies that gave exclusions in the ALPs parameter space around neV range of the ALPs masses.

H.E.S.S. results with PKS 2155-304 After the first predictions of Hooper and Serpico [155], one of the first attempts to constraint ALP with gamma rays was made by H.E.S.S., using the data from the BL Lac object PKS 2155-304 [159]. In this work, a search for irregularities induced by the photon-ALP mixing in the spectrum was performed, and schematically shown in Figure 3.11.

The problem is in searching for ALP-induced spectral patterns on top of a spectrum generated by the main astrophysical processes at the source. Normally, these generate rather smooth and featureless spectra, such as power-laws with or without a cutoff, or of a log-parabolic shape. H.E.S.S. Collaboration in [159] assumed a Power-Law (PWL) function as a local spectral model, justified by the processes explaining the acceleration and radiation in the extreme astrophysical sources, such as BL Lacs [176]. For an estimation of the irregularities, Wouters and Brun [177] proposed a reduced χ^2 test with the null hypothesis build without the ALP ($\phi_{w/oALP}(\vec{\theta})$):

$$I = \frac{1}{d}\sum_{k}^{N}\frac{\left(\phi_{w/oALP}(\vec{\theta}) - \phi_k\right)^2}{\sigma_k^2} = \frac{\chi^2}{d}, \tag{3.11}$$

where d is the number of degrees of freedom, k runs over the N bins, and $\phi_{w/oALP}(\vec{\theta})$ is a global fit without ALPs with spectral parameters $\vec{\theta}$. This method relies on the accuracy of the assumed shape of the spectrum, and is, therefore, subject to possible bias, but can be used in the case when the global fit represents a good estimate on the spectrum [178]. Expanding on this, H.E.S.S. Collaboration [159] searched for irregularities avoiding a global fit and using only a spectral shape over three adjacent points in the energy spectrum (a triplet i):

$$\mathcal{I}^2 = \sum_i \frac{\left(\tilde{\phi}_i - \phi_i\right)^2}{\vec{d}_i^T C_i \vec{d}_i}, \tag{3.12}$$

where $\left(\tilde{\phi}_i - \phi_i\right)^2$ is the residual of the middle bin in the triplet, ϕ_i the measured flux, $\tilde{\phi}_i$ the flux in the median bin expected from the PWL fit to the side bins, C_i covariance matrix for the triplet and $\vec{d}_i^T = \left(\frac{\partial\tilde{\phi}_i}{\partial\phi_{i-1}}, -1, \frac{\partial\tilde{\phi}_i}{\partial\phi_{i+1}}\right)$.

Although both methods showed consistent results, H.E.S.S. Collaboration [159] evaluated that, due to its independence of the global spectral model assumption, the sum of residuals over three adjacent spectral bins is preferred for this kind of analysis. This estimator is calculated for each set of ALPs parameters and 1000 spectra are simulated in order to take the randomness of both the IGMF and the GC magnetic field into account. The distribution of values of the spectral irregularity estimator for both the observed spectrum and spectra folded with photon-ALP oscillations for different ALPs parameters are compared, and exclusions of the ALPs parameter space were obtained at 95% confidence level. The results (Figure 3.12) yielded constraints on the photon–ALP coupling value $g_{a\gamma} < 2.1 \times 10^{-11}$ GeV^{-1} for masses of the ALPs m_a in the range (15–60) neV [159].

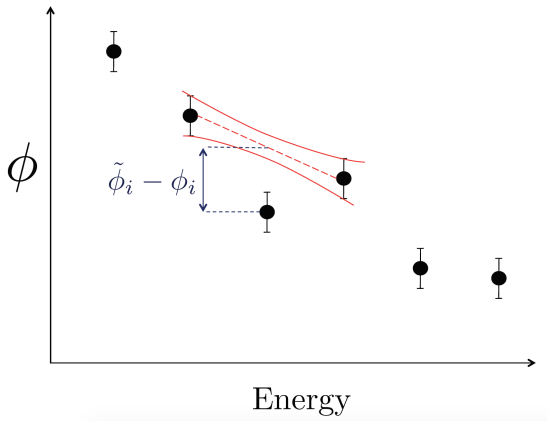

Figure 3.11: Schematic view of spectral irregularity quantification. Reprinted from the H.E.S.S. Collaboration [159].

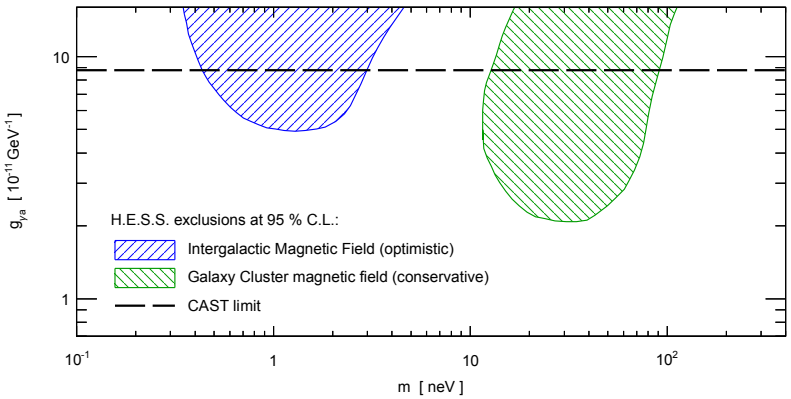

Figure 3.12: Constraints set in the ALPs parameter space with the PKS 2155-304 data from H.E.S.S. telescopes. Reprinted from the H.E.S.S. Collaboration [159].

Observations of astrophysical sources and their spectra have put constraints on a sizable part of the ALP parameter space, as seen in Figure 3.1. In the gamma-ray astronomy

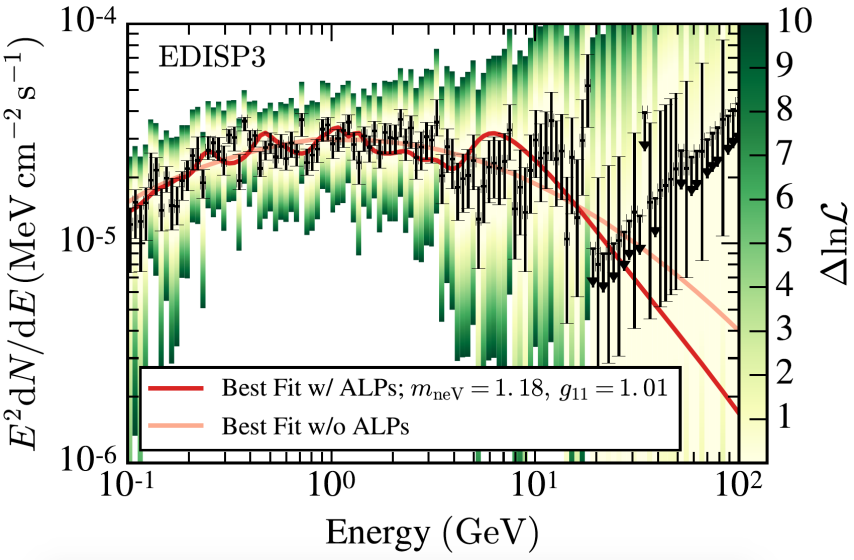

Figure 3.13: Likelihood curves for one event type and best spectral fits with and without ALPs. Reprinted from [179].

domain, taking the strength of astrophysical magnetic fields and the considered energy range into account, the mass of axions m_a relevant for studies is $m_a \leq 10^{-6}\,\mathrm{eV}$, and part of the ALP parameter space available for study is shown and discussed in Figure 3.10 from Hooper and Serpico [155].

As previously mentioned, photon-ALP coupling is expected to leave a signature in otherwise smooth astrophysical spectra through spectral irregularities, reduced photon absorption, or flux enhancement at the TeV energies. Current constraints set on the ALPs parameter space by observing such effects were obtained using the Fermi-LAT data of the active galaxy NGC 1275 in the centre of the Perseus GC [179].

Studies on Spectral Irregularities of NGC 1275 The IACT results were completed at lower energies, making use of the Fermi-LAT instrument data. In [179], Fermi-LAT Collaboration analysed 6 years of NGC 1275 data, collected with Fermi-LAT, using the `Pass 8` event analysis, and produced ALP predictions by including the photon-ALP conversion in the Instracluster magnetic field (ICMF) and in the GMF of the MW. A fit of the time-averaged spectrum of NGC 1275 and ALPs models was made, and a likelihood analysis was performed. In Figure 3.13, one can see the likelihood of one of the event types, together with the best spectral fit with and without ALPs. To evaluate the ALPs hypothesis, they exploited a likelihood ratio test statistics. In the procedure, a time-averaged spectrum is modelled by a smooth function, and likelihood is extracted for each reconstructed energy bin k', $\mathcal{L}(\mu_{k'}, \theta | D_{k'})$, where $\mu_{k'}$ is the expected number of photons in the photon-ALP conversion scenario, θ are the nuisance parameters of the fit, and $D_{k'}$ is the observed photon count. For each set of ALPs parameters and magnetic field, the joint likelihood of all reconstructed energy bins k' is maximised and the best-fit parameters are determined.

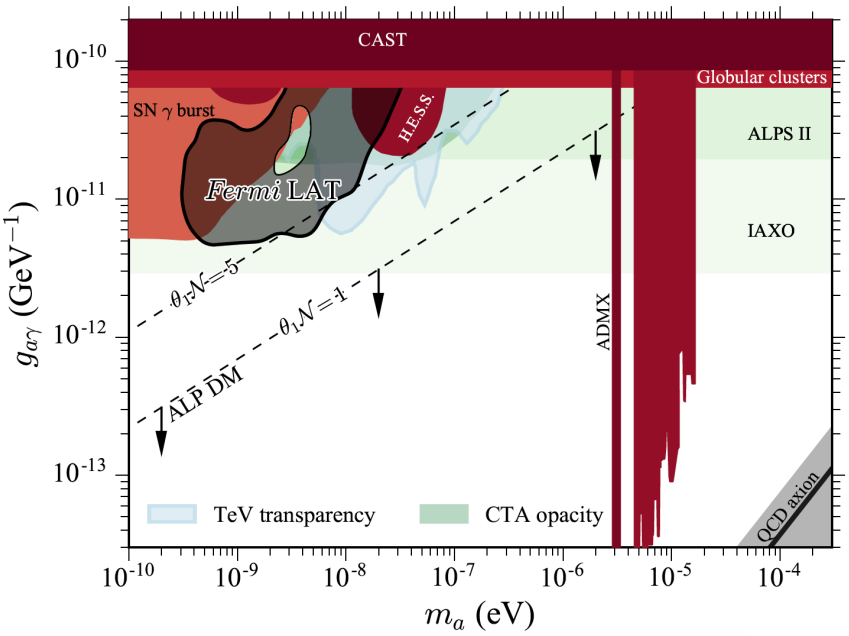

Figure 3.14: Projected limits on the ALPs parameter space obtained with the Fermi-LAT study of the NGC 1275 data, compared with the results from other experiments at the time. Reprinted from [179].

Among the different turbulent magnetic field realisations, simulated by accounting for its randomness, the one corresponding to the 0.95 quantile of the likelihood distribution is chosen. The likelihood ratio test is performed as

$$TS = -2\ ln\left(\frac{\mathcal{L}(\mu_0, \hat{\hat{\theta}}|D)}{\mathcal{L}(\hat{\mu}_{95}, \hat{\theta}|D)}\right), \tag{3.13}$$

where the null hypothesis is the no-ALP scenario (including the EBL attenuation) with expected photon count μ_0 and nuisance parameters $\hat{\hat{\theta}}$, and the alternative hypothesis of ALP, shows an expected photon count μ_{95} and nuisance parameters $\hat{\theta}$ [179]. Aside from the degeneracy of the photon-ALP conversion in coupling and magnetic fields, and non-linearly scaled irregularities considering the ALPs parameters, in comparison with the ALP hypothesis, the null-hypothesis is independent of the realisations of the magnetic field. Considering this, the test statistic distribution of the null hypothesis needs to be derived from Monte Carlo (MC) simulations [179]. From it, the exclusion threshold value, above which the set of ALPs parameters can be excluded with the 95% confidence level statistics, is also calculated. The result of this research was the exclusion of the ALP coupling values in the range 0.5×10^{-11} GeV$^{-1} \leq g_{a\gamma} \leq \times 10^{-11}$ GeV^{-1} for ALPs masses 0.5 neV $\leq m_a \leq$ 5 neV and $g_{a\gamma} \geq\ 1 \times 10^{-11}$ GeV^{-1} for 5 neV $\leq m_a \leq$ 10 neV [179], as seen in Figure 3.14.

Combined Fermi-LAT and H.E.S.S. Observations of PKS 2155-304 Another study using the Fermi-LAT data from the PKS 2155-304 was carried out by Zhang et al. [180]. The data were taken from Fermi-LAT observations in the energy range of 100 MeV–500 GeV. Photon-ALP oscillations in the inter-cluster magnetic field and the GMF of the MW are included. For different sets of couplings in the range of 10^{-12} GeV$^{-1} \leq g_{a\gamma} \leq \times 10^{-10}$ GeV^{-1} and mass of ALPs 10^{-1} neV $\leq m_a \leq 10^2$ neV and 800 different realisations of the ICMF, a binned likelihood analysis similar to [179] was performed. The best fits with and without ALPs were compared to the observed spectrum, and the result is shown in Figure 3.15. A joint likelihood was calculated; parameter space regions

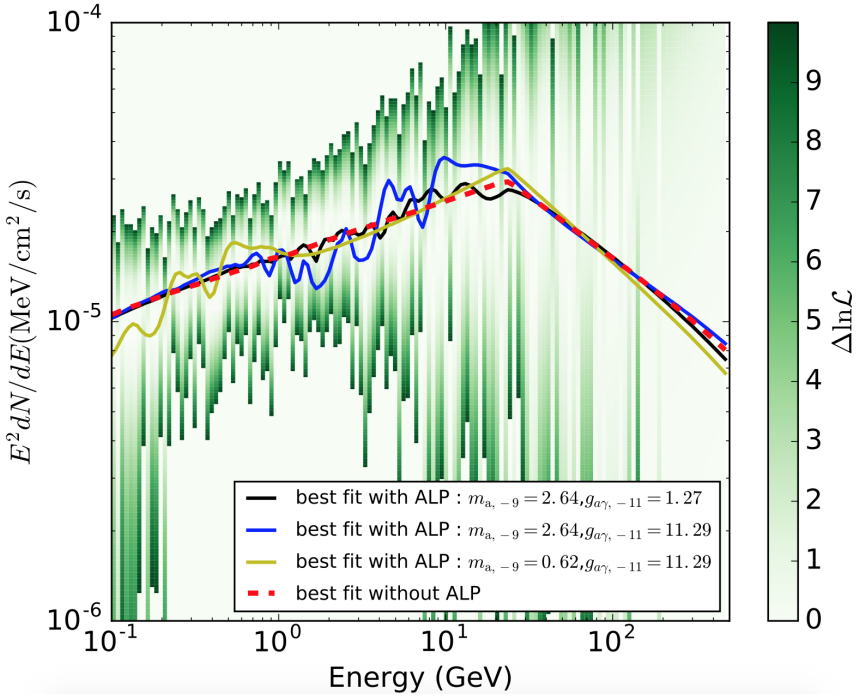

Figure 3.15: Likelihood curves for the observed spectrum of PKS 2155-304. Solid lines represent best fits including the photon-ALP oscillations, while the dashed red line is showing the best spectral fit without ALPs. Reprinted from [180].

were excluded with 99.9% confidence level and compared with the previous results from H.E.S.S. [159] and with the Fermi-LAT observations of NGC 1275 [179] in Figure 3.16.

H.E.S.S. Study with Galactic Sources In 2019, H.E.S.S. data of galactic TeV gamma-ray sources were used to search for the ALP oscillation effects [181]. Ten sources, mainly supernova remnants and pulsar wind nebulae studied by H.E.S.S., were utilised. By using sources in the galactic plane, one can probe the ALPs parameter space with higher ALP mass, $m_a > 10^{-7}$ neV. This is due to the strength of the GMF, an important factor for the photon-ALP oscillation, as seen in Equation 2.21. The ALP model was obtained by multiplying a spectral fit without ALPs with the $P_{\gamma\gamma}$ for a certain parameter set $(m_a, g_{a\gamma})$, and

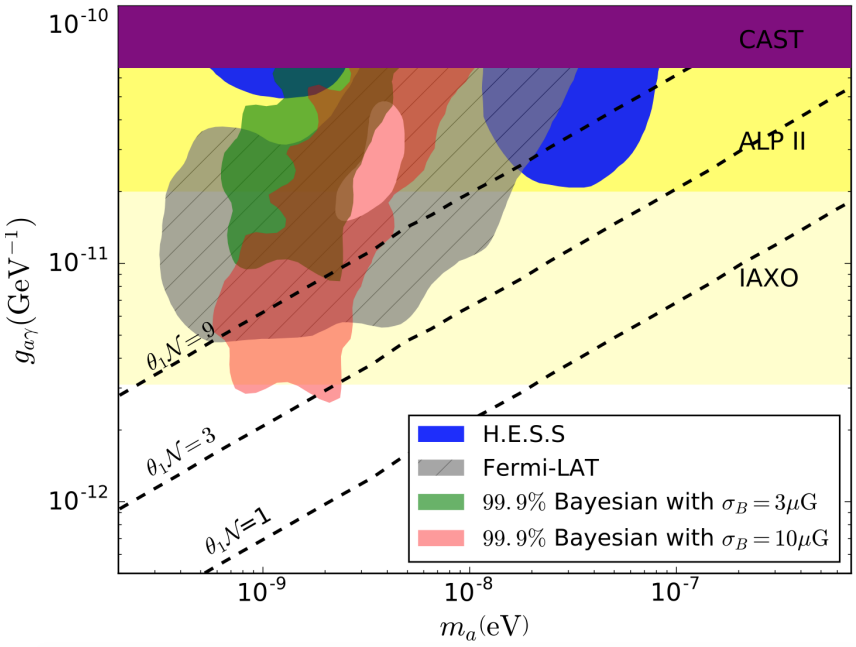

Figure 3.16: Comparison of exclusion regions derived in [180], compared with exclusion regions from H.E.S.S. observations of PKS-2155-304 [159] and Fermi-LAT observations of NGC 1275 [179]. Reprinted from [180].

including the instrument energy resolution. As above, for each set of parameters $(m_a, g_{a\gamma})$ the ALP model was fitted to the observed spectrum, and a χ^2 value was calculated and compared to the best fit over the whole parameter space. The best parameters were deduced from the calculation of the χ^2; however, as the photon-ALP conversion is degenerate in the coupling and magnetic field, and that the induced irregularities are not linearly scaled with the ALPs parameters, a threshold value for excluding the ALPs parameters was derived using the MC simulations. For example, in [181], the threshold value is reconstructed from MC simulations and compared to the difference in χ^2 values for each set of ALPs parameters and the best fit over the whole parameter space. Since a scan of the whole parameter space is not feasible [179], it is assumed that the overall shape probability distribution of the alternative hypothesis (with ALPs) can be approximated with the null distribution (no ALPs). It has been shown that such an approach yields conservative limits [179]. The results of Zhang et al. [181] were consistent with other limits, but were uniquely sensitive towards the higher mass range. This showed that using galactic observations of TeV sources can improve and further constrain the high-mass part of the ALPs parameter space.

Other studies using Fermi-LAT observations combined with IACTs results have been carried out, using the MAGIC [182] and the H.E.S.S. [183] data. In [182], both signatures induced by the photon-ALP oscillations and step-like flux suppression at the energies $E_\gamma > E_{crit}$ in the spectrum of NCG1275 were investigated.

As can be seen, the irregularity estimator in Equation 3.11 is the reduced-χ^2. For its

general applicability in testing fits to the observed data, and simplicity of calculation, the χ^2 test has been used in several works [181, 182]. For each set of the considered ALPs and each magnetic field realisation, and photon survival probability is calculated and multiplied by the best fit of the time-averaged spectrum, not including the ALPs effects. χ^2 values for each of these fits are calculated. Testing of the ALPs hypothesis is performed using the $\Delta\chi^2$ test statistics, defined as $\Delta\chi^2 = \chi^2_{wALP} - \chi^2_{w/oALP}$. Based on the distribution of these values for each set of ALPs parameters, the exclusion region is evaluated under specific criteria and ALPs parameters are excluded. Malyshev et al. [182] considered 1000 different random realisations of the cluster magnetic field (modelled as in [179]) for a range of ALP parameters, coupling 10^{-14} GeV$^{-1} \leq g_{a\gamma} \leq 10^{-9}$ GeV^{-1} and mass of ALPs 10^{-2} neV $\leq m_a \leq 10^2$ neV. By combining observations of Fermi-LAT and MAGIC, available energy range is extended, and by observing the patterns of the spectrum, a higher sensitivity to the photon-ALP coupling values is reached, reaching down to $g_{a\gamma} \sim 10^{-12}$ GeV^{-1}.

The result was the exclusion of a broader part of ALPs parameter space, compared to the previous analysis of the Fermi-LAT data alone. The excluded region also included the part of the ALPs parameter space which can be assigned to the possible ALP DM. This showed the potential of combining data obtained by different instruments for the purpose of increasing part of the available ALPs parameter space and increasing the sensitivity. Following previous interest in the effects that ALPs oscillations could impose on the BL Lac spectra [184, 185], recent works investigated the same using the simulations for the upcoming experiments and showed that BL Lac could be used for future studies of the ALPs oscillations [186].

Supernova Remnants In case of a supernova explosion, ALPs would be emitted via the previously discussed Primakoff process and be observed with gamma rays after a possible re-conversion in the magnetic field of the MW. Following the observation of the supernova SN1987A, constraints due to the non-observation of gamma rays in coincidence with the neutrino observations were set [162, 163], but affected by strong uncertainties. Because of that, Payez et al. [164], revisited these works using a more detailed analysis. Simulations of the core-collapse SN explosions were used to calculate the expected ALP flux taking into account the nucleon-degeneracy effects and the reduction of the nuclear masses in the hot and dense nuclear medium of the supernova, alternatively including the photon survival probability calculated for the scenario of the MW magnetic field [164]. An estimation of the uncertainties showed that the greatest effect on the results comes from the change of the magnetic field model, where out of two probed models, [187, 188] (versions from 2012 and 2011, respectively), more recent, constrained model resulted in more conservative limits. This gave following constraints in the ALPs parameter space: $g_{a\gamma} \leq 5.3 \times 10^{-12}$ GeV^{-1} for masses of the ALPs $m_a \sim 10^{-1}$ neV. The results were additionally tested for different supernovae and GMF models. It was shown that the greatest effect on the constraints have modifications in the model of the magnetic field, which are still one of the most important remarks in the astrophysical searches for ALPs.

More recently, expanding their previous work, Xia et al. [189, 190] performed a search for spectral irregularities in three galactic supernova remnants, combining GeV data from Fermi-LAT and TeV data from IACTs (H.E.S.S., MAGIC and VERITAS). The broadband spectra were fitted with models with and without photon-ALP conversion in the GMF. The ALP hypothesis was tested using the χ^2 analysis and combined limits were again shown to be inconsistent with limits already set by CAST in [88]. The authors speculated that a possible reason for this result could be the uncertain connection between the Fermi-LAT spectrum and observations of IACTs, which are not easily calibrated in energy, and also the systematic uncertainties of the instruments that were not taken into account [190]. This approach is likely to be revisited once CTA starts observing.

Constraints Obtained Comparing Data from Different Blazars In [183], the Fermi-LAT and H.E.S.S. data of two BL Lacertae (BL Lac) are analysed. Two different EBL models are also probed. The ALP model included mixing in the ICMF modelled as a Gaussian turbulent field with zero mean and variance σ_B, as in [191], and the GMF [187, 192]. The ALPs hypothesis was evaluated in a similar way, as in [179], using a likelihood ratio test. The results showed the improvement of the fit when ALP models are included and set constraints on the ALPs parameter space consistent with the previously obtained ones.

In [158] the highest energy spectra of AGN studied by Fermi-LAT and IACTs are compared, showing that the inclusion of proton-ALPs oscillation effects improves the agreement of the standard AGN model with the data.

Recently, the analysis of the Fermi-LAT Collaboration [179] was revisited by Cheng et al. [178] using a different analysis method, calculating the irregularity of the spectrum of NGC 1275.

Aiming to measure the irregularity of the spectrum, an estimator needs to be chosen. Looking back to the article by the HESS Collaboration [159], one could decide to use the estimator from Equation 3.12. A possible problem arises in the case of a large number of energy bins (∼100) (as in [178]), since ALPs signatures might become wider than the bin size, making this kind of estimator insensitive to rapid alternations. Using the method of energy windows, instead of triplets of spectral points, and following the assumption of a PWL model in those energy windows, Cheng et al. [178] proposed an alternative version of the estimator,

$$\mathcal{I}_{alt} = \sum_i \sum_j \frac{\left(\phi^{pl}_{i,j} - \phi_{i,j}\right)^2}{\sigma^2_{i,j}}. \tag{3.14}$$

where i and j represent the energy window and bin, respectively, while ϕ^{pl} is the flux assumed by the PWL spectral fit in each energy window, and ϕ and σ are the measured values of the flux and uncertainty, respectively [178]. Each of the simulated ALPs models were fitted assuming a baseline log parabola. From the assumption that the observed irregularity can be explained by the photon conversion connected to a given set of ALPs parameters, exclusion limits were set. This study included mixing in the ICMF and in

the GMF of the MW. Excluded couplings are $g_{a\gamma} > 3 \times 10^{-12}$ GeV^{-1} for masses of the ALPs $m_a \sim 1$ neV at a 95% confidence level. The results of this search show the possibility of further improvements of the constraints by combining NGC 1275 observations with observations of PKS 2155-304 [178].

Projection of limits using the CTA simulated data of NGC 1275 CTA is expected to probe the energies up to $E_\gamma \sim 300$ TeV, which directly improves the possibility of studying ALPs manifestations. Abdalla et al. [160] created simulations of the observation of the radio galaxy NGC 1275. The magnetic field of the Perseus cluster is modelled following Jansson and Farrar [187, 192], with a morphology modelled as a random field with Gaussian turbulence. The conservative value of the central magnetic field strength was set to 10 μG, along with the other parameters listed in [160]. Using three different sets of ALPs parameters with 100 different magnetic field realisations, $P_{\gamma\gamma}$ was calculated using the `GammaALPs` code[2]. Considering other effects that could impact the photon flux, `GammaALPs` includes the EBL/CMB absorption and vacuum polarisation. Observations in both the quiescent and the flaring state are included in a ~ 300 h exposure. The authors included the systematic uncertainties of the instrument, and fits are performed both with and without ALPs effects. As the energy binning has a great importance for observing wiggles in the spectrum, three different sets of parameters are used, and fits for each of them are performed by maximising the likelihood and summing over 40 energy bins. For each set, 100 different magnetic field realisations are computed and likelihood values corresponding to quantile $Q = 0.95$ of the distributions are chosen. To obtain the confidence intervals of 95% and 99%, MC simulations are used.

The results showed that, in contrast to the quiescent state, the flaring state of the source provides stronger exclusions in the ALPs parameter space, reaching the sensitivity to exclude models of ALPs that could explain the entirety of DM. A probable reason for this is a strong background cut on the quiescent data, which causes the exclusion of the low energy bins from the analysis. On the other side, flaring state observations extend to lower energies. As concluded by the authors, this shows the great importance of observing the high activity states of this and other sources that are yet to be studied. Changes in the magnetic field parameters are also tested and the projected exclusion parameters are presented in Figure 3.17. It is important to note that the constraints on the ALPs parameter space are sensitive to changes in the assumed parameters' values in the model of the magnetic field of the Perseus GC. Moreover, results show that finer energy binning gives stronger constraints, as the analysis becomes more sensitive to sudden oscillations in the spectrum, caused by the photon-ALP oscillations. What remains to be studied is the choice of optimal binning as dependent on limitations due to the systematics.

The projected limits obtained in [160] can be seen in Figure 3.18. Compared to future laboratory experiments, CTA exclusions of the ALPs parameter space will be dominated by the systematic uncertainties of the model [160].

[2] https://github.com/me-manu/gammaALPs.

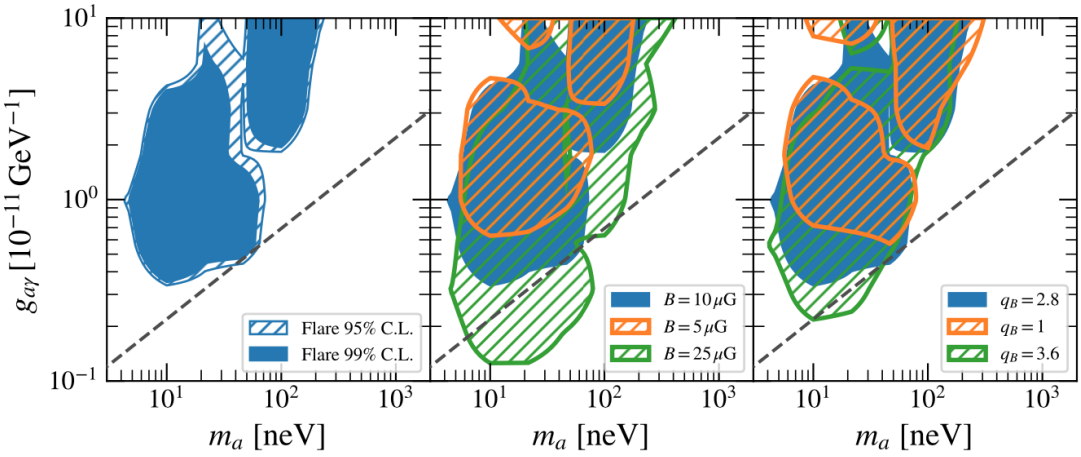

Figure 3.17: Projected CTA exclusions on the ALPs parameter space for different assumptions on the ICMF parameters. Reprinted from [160].

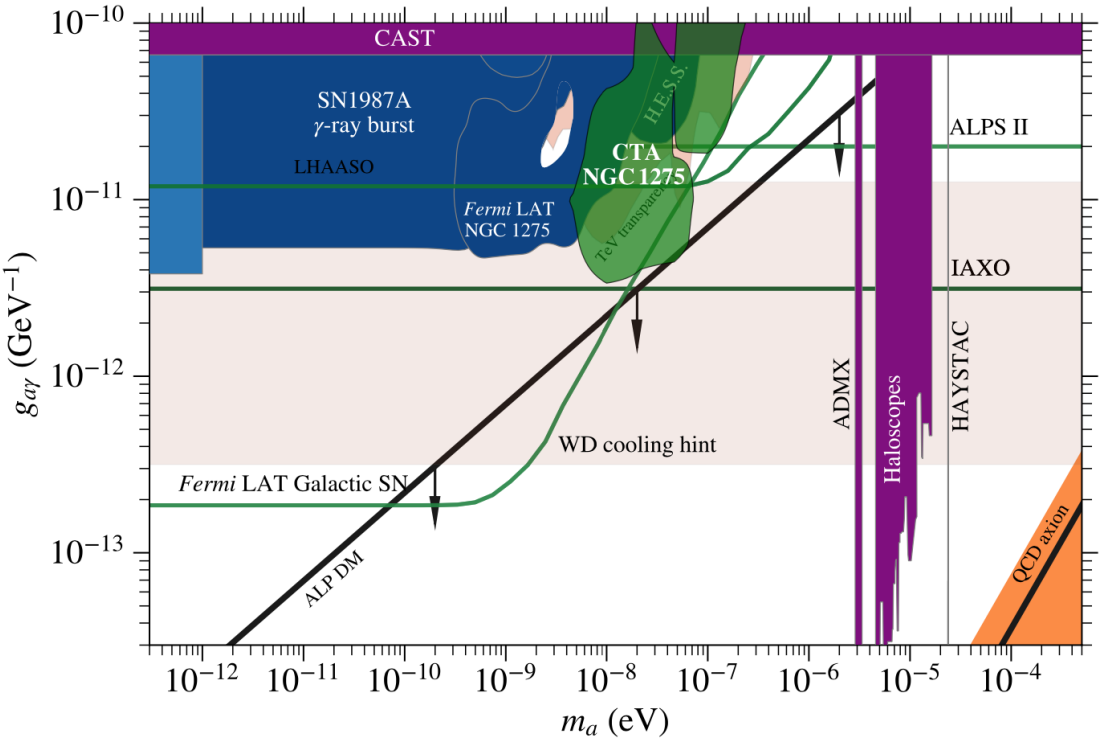

Figure 3.18: Projected limits from the CTA simulations marked with green shaded area, compared to constraints on the ALPs parameter space with Fermi-LAT and H.E.S.S.. Reprinted from [160].

Relevance of the jet magnetic field and study of the Fermi FSRQs In [193], authors have investigated the relevance of the jet magnetic field modelling in the studies of ALPs using the balzars data. Studies up to now have considered merely simple models

of the jet magnetic fields, mostly because if its unknown nature, but yet great importance in the modelling of the gamma rays propagation. Models so far explained the jet as either random domain-like structure, or a completely ordered transverse field. For this purpose, Davies et al. [193] simulated data of Mrk 501 and used a leptonic model of the jet by Potter and Cotter [194], assuming an accelerating parabolic jet base, evolving into a decelerating conical jet. The magnetic field was modelled correspondingly, assuming both helical and tangled components, in order to describe the two regions and the transition between them. As it turns out, the effect of the jet magnetic field dominates in comparison to the mixing in the IGMF and MW, while for the case where the GC magnetic field is included in the assumption, its effect can be negligible. This comes from the fact that the GC magnetic field, in comparison to the jet one, even though quite weaker (10 μG compared to the $\sim$ 10 mG in the jet) is expanded over longer distances, and it can produce both small- and large-scale oscillations in the energy spectra. Furthermore, they show that the strength of the magnetic field at the transition region is crucial for discussing the impact that inclusion of the jet magnetic field in the photon survival probability calculation might have. The results show that in the case where the jet magnetic field is weaker than ~ 0.05 G, its effect in the mixing is negligible. In comparison to rather strong jet magnetic field in BL Lacs, this can be safely assumed for the FSRQs.

In accordance with these results, Davies et al. [195] published a very recent study on the ALPs searches in the spectra of three FSRQs. In this study, considered in the ALPs hypothesis are the mixing in the blazar jet together with the GMF of the MW. On top of this, for the first time, a complete consideration of the photon fields is taken into account. This includes the photon fields in the accretion disk, broad line region and the dusty torus of the FSRQ, CMB and the synchrotron protons in the jet plasma. The statistical analysis is quite similar to the ones in [160, 179], assuming 100 realisations of the magnetic field and simulating 100 datasets to compute the exclusions in the ALPs parameter space. A novelty in the analysis is including the magnetic field strength B as a free parameter in the likelihood analysis. This is done by including a prior factor $p(B_0)$ in the likelihood function, determined in a form of a Gaussian distribution obtained by varying the values of B_0:

$$p\left(B_0\right) = \exp\left(-\frac{1}{2}\left(\frac{B_0 - \overline{B_0}}{\sigma_B}\right)^2\right) \tag{3.15}$$

where B_0 is the strength of magnetic field, $\bar{B}_0$ is its initial value, and σ_B is the error, in each case $\sim 20\%$. The likelihood function used is then:

$$\mathcal{L}_{ALP}(m_a, g_{a\gamma}, \mathbf{B}_j, \boldsymbol{\theta}) = p\left(B_0\right) \prod_i \mathcal{L}(\mu_i(m_a, g_{a\gamma}, j)), \tag{3.16}$$

where $\mathcal{L}(\mu_i)$ are the likelihood curves for the SEDs of the corresponding sources, dependent on the mass of the ALP m_a, its coupling to photons $g_{a\gamma}$, spectral parameters θ and the expected counts μ_i. Details on the computation of the expected counts one can see in [195]. Furthermore, the scan of the ALPs parameters was done in 56 steps, corresponding to the 56 pairs of mass and coupling, for each of which the test statistic, similar to the one in

Equation 3.13 is computed. Unlike in the study of Abdalla et al. [160], 3 to 8 points of the ALPs parameter space are used for calculating the coverage and obtaining the exclusion region, for each of the three FSRQs, respectively. The results obtained show slight preference towards one of the ALPs models, in particular the one with $m_a = 100.8\,\text{neV}$ and $g_{a\gamma} = 4.64 \times 10^{-12}\,\text{GeV}^{-1}$, at the level of 2σ. With the further analysis and by combining the constraints from three source, this hint disappeared. Finally, as it can be seen in

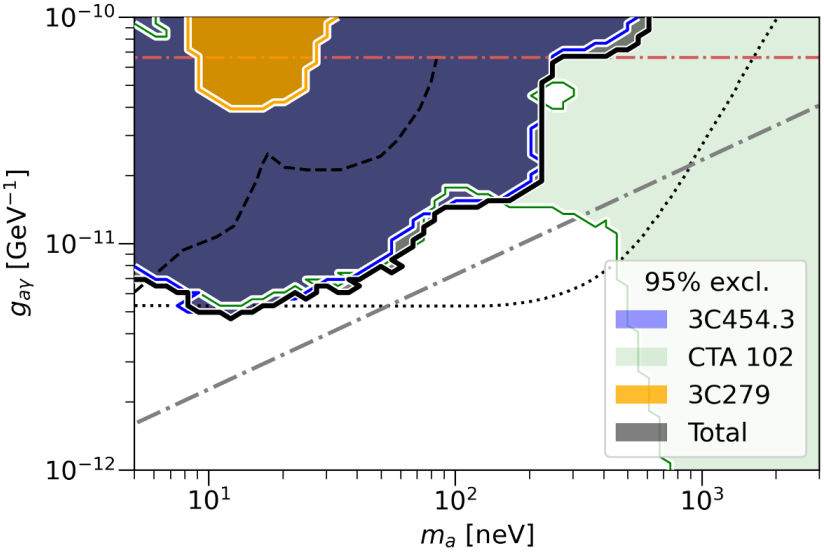

Figure 3.19: 95% exclusion contours for each FSRQ and a combined dataset obtained in [195].

Figure 3.19, the constraints obtained are excluding the ALPs models for $m_a \lesssim 200\,\text{neV}$ and $g_{a\gamma} \gtrsim 5.0 \times 10^{-12}\,\text{GeV}^{-1}$.

Photon-ALP Back Conversion in the Galactic Magnetic Field (GMF) As investigated by Long et al. [196], new observations of VHE gamma-ray sources could lead to the detection of the flux enhancement due to the ALP-photon back-conversion in the GMF. This enhancement is expected at energies $E_{crit} \sim 100\,\text{TeV}$ [196] and could be detected by the existing HAWC [197], LHAASO [198], and CTA experiments, and by the planned The Southern Wide-field Gamma-ray Observatory (SWGO) [199]. Long et al. [196] analysed HE and VHE gamma-ray data from three promising AGNs (M 87, IC 310 and Mrk 510) and the spectra were extrapolated to the energies $E \sim 100\,\text{TeV}$. Further on, the assumed intrinsic spectra were folded with the $P_{\gamma\gamma}$, assuming the photon-ALP conversions in the source magnetic field and the back-conversion in the magnetic field of the MW. These spectra were compared to the ones obtained only by including the EBL and CMB attenuation. The results showed that, in the respective energy range (above $E \sim 100\,\text{TeV}$), predicted flux enhancement is above one order of magnitude and higher than the sensitivity of the instrument, which will allow for the constraints to be set on

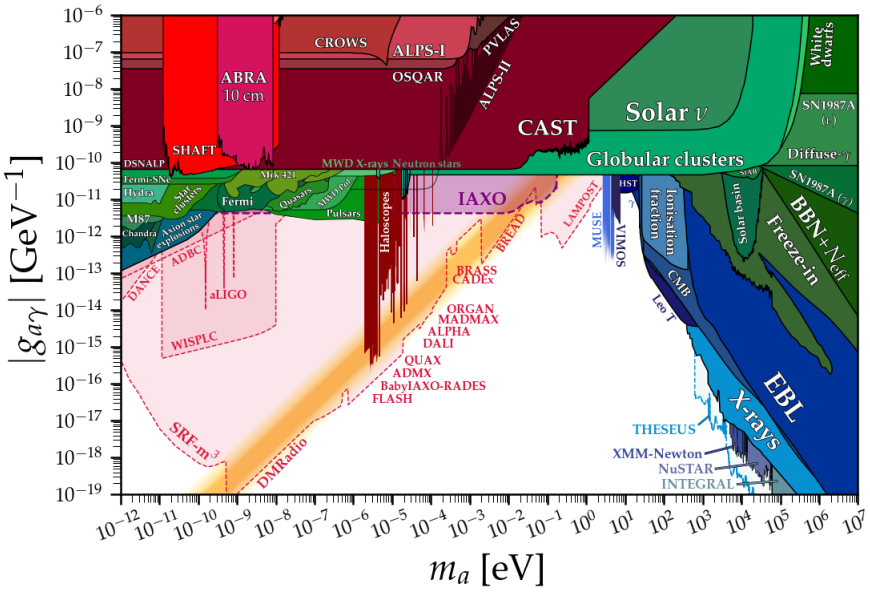

Figure 3.20: Complete constraints in the ALPs parameter with the projections of the upcoming experiment up to date. Gathered in [86].

the ALPs parameter space [196]. It is also emphasised that, to set stringent constraints, a better estimation of the intrinsic spectra, magnetic fields and EBL attenuation needs to be established, all of which are expected with the upcoming experiments in HE and VHE gamma-ray astronomy.

The collection of the current constraints on the photon-ALP coupling and many more that are not mentioned here, together with the projections from the upcoming axion experiments can be seen in Figure 3.20. Since the main topic of this thesis is to discuss the photon-ALP interaction and the constraints set on this particular coupling, we will not mention the enormous effort on searches implementing and exploiting the axion couplings to nucleons or electrons, the maiden fruits of the axion theory itself. The interested reader is advised to see [14] for a short review, and [86] for a collection of limits up to date.

Chapter 4

Gamma-Ray Astronomy

Contents

In this chapter, astroparticle physics will be brought in the picture. Imagined as a bridge between the particle physics discussed in the first two sections, and astrophysics that will soon come into our consideration, we will try to connect the two, just as it was done more than a century ago, when the ground-based, laboratory experiments started to be insufficient to explain the observed phenomena.

Starting from the CRs, we will investigate their origin, mechanisms of acceleration and propagation in order to discover that their evolution through the space gives us the main protagonist of this work (after the axion, of course), gamma rays. After that, the ground based astronomy can be introduced, presented by the MAGIC and the LST-1 telescopes.

4.1 Cosmic rays (CR)

The birth of the astroparticle physics started in the early 20th century with the discovery of CRs. Observations of spontaneous electrostatic discharge starting by Coulomb in 1785, motivated studies in search for the cause of this phenomena. Closely connected to the spontaneous radioactivity discovered by Becquerel in 1895, and discovery of the radioactive elements by Curie in 1911, whose presence was proven to cause discharge of the electroscope, search for the origin of the natural radioactivity began. Explanations offered were including the emission from the Earth's core, Sun or the extraterrestrial sources. A part was proven to come from the Earth, but not in amount big enough to explain the results of experiments conducted in vacuum conditions, big heights or depth. After years of ground-based experiments and elevated measurements by Theodor Wulf [200], the underwater ones by Domenico Pacini [201], and the balloon excursions by Albert Gockel [202, 203] and Victor Hess in 1912 [204], one was sure: the origin of this, still unexplained radiation, was mostly extraterrestrial. Wulf decided to perform measurements on top of Eiffel tower, at the altitude of 300 m, using an improved version of the electroscope, obtaining undetermined conclusions, but a conclusion that on those heights the radiation comes mostly from the soil [200]. His model of electroscope served as the instrument for performing the following measurements. Only two years after, in 1911, Pacini performed series of experiments on different latitudes, over lakes and the sea, and a final one, on 3 m of depth in the sea, leading to the observation that the level of radiation does not increase, but is rather decreasing, and concluding that there is a radiation from the outside that is in fact absorbed by the water [201]. In attempt to test the change in the amount of the radiation with height, Gockel performed balloon flights in 1909, reaching the maximum of 4500 m (out of planned 7000 m) and even though measuring the increase of radiation, had to cancel the last, and highest planned flight [202, 203]. Instead, two years later, Hess performed balloon flights up to the altitude of 5200 and laid out four main conclusions [205]:

- "Immediately above ground the total radiation decreases a little."
- "At altitudes of $1000 - 2000$ m there occurs again a noticeable growth of penetrating radiation."
- "The increase reaches, at altitudes of 3000 to 4000 m, already 50% of the total radiation observed on the ground."
- "At 4000 to 5200 m, the radiation is stronger [more than 100%] than on the ground."

However, even though detected, the explanation of the composition of CRs came later. Only in 1926, Robert A. Millikan, following his many measurements of the radiation at various heights and depths, concluded that these particles are coming from space and all the directions equally. These conclusions lead to the name we use today: "cosmic rays".

CRs are charged particles of extraterrestrial origin, composed mostly of protons (87%), helium nuclei (12%), some positrons, electrons and heavier nuclei ($\sim 1\%$). The remaining

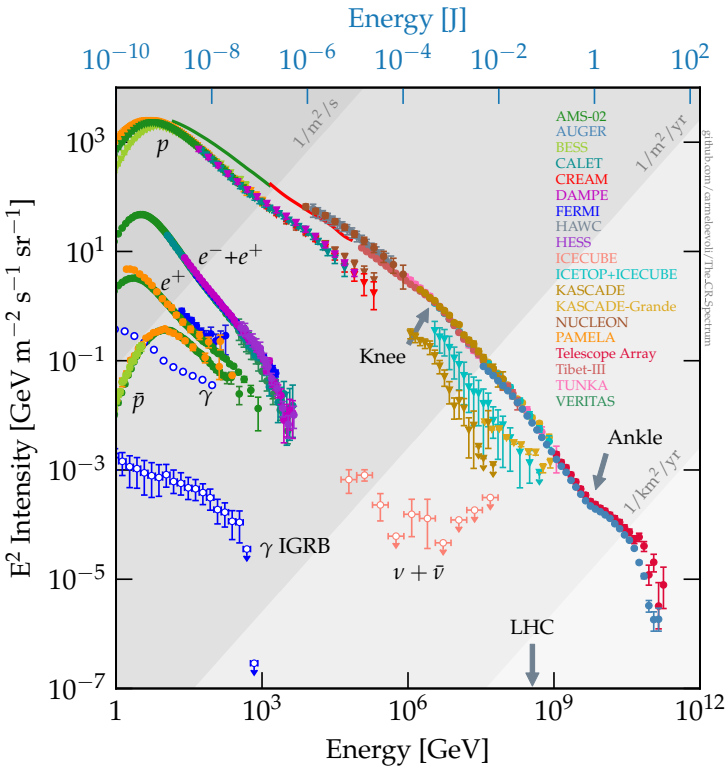

Figure 4.1: The CR energy spectrum. The data is collected at [207].

fraction are the neutral particles, such as photons, neutrons and neutrinos. Their spectrum can be roughly divided in three parts, while in reality it is more complex due to the rigidity of particles that we will further discuss (see Figure 4.1). Each of the spectrum components are associated to a different origin and acceleration mechanism [206]. We have to emphasise some difficulties in characterisation of Cosmic-ray (CR) spectrum. First of all, charge that these particles carry makes them sensitive to astrophysical magnetic fields, meaning that during their propagation, they are deflected, interacting with the surrounding medium, and ultimately covering traces to their source, while distinguishing the charge is also problematic. Second issue is that the energy spectrum of CRs extends over more than 12 orders of magnitude, from around 10^9 eV to 10^{21} eV, making it difficult to make a characterisation of the entire spectrum using only one type of detector. In this case, advanced methods of their detection and characterisation have been developed and will be introduced in the following sections. The energy spectrum of CRs is distributed from 10^9 eV to 10^{21} eV, divided based on the main process of acceleration, used to describe the production of the CRs with the corresponding energy (for a review on CR searches, see [208]).

Flux and the composition of CRs up to energies $\sim 10^{14}$ eV is fairly known and it consists mostly of light elements: hydrogen and helium nuclei, as well as some heavier nuclei. Approaching the energy of 3×10^{15} eV is characterised by change in the slope,

called the *knee*, above which particles are exhibiting a rather smooth spectrum, compatible with a PWL model with γ index steepening from 2.7 to 3.1. They are believed to be of galactic origin, produced in supernova (SN) explosions of dying stars, or even in pulsar wind nebulae (PWN), objects powered by a highly magnetised neutron star rotating in a centre of wind of relativistic plasma. Above the *knee*, CR spectrum exhibits flattening on energies from $E > 10^{18}\,\text{eV}$ up to $E = 10^{19}\,\text{eV}$ [209]. This observable feature is called the *ankle*, characterised by the change of spectrum index to $\gamma \sim 2.6$. Sources of CRs with emission up to these energies are still unknown today, with several possible candidates. An example are Gamma Ray Bursts (GRBs), highly energetic explosions in the sky, capable of accelerating particles to energies of the *knee*, divided in two groups, high and low-luminosity GRBs. Out of the two, low-luminosity population seems to be providing higher CRs production rate and favours the survival of highly energetic CR nuclei in comparison with the high-luminosity GRBs [208]. Recently, more and more focus is being set on different sources, such as energetic supernovae explosions (see e. g. [210]), pulsars [211], remnants of Galactic neutron star mergers [212], AGNs and their subgroups, blazars and radio galaxies as leading contributors to the CR production, with an addition also coming from low-luminosity AGNs and quasars. For a broader review, readers are advised to consider [208]. From the spectrum in Figure 4.1 we can see above the *ankle*, number of the detected particles is extremely low: about 1 particle per square kilometer per century for particles with the energy of $E = 10^{20}\,\text{eV}$. Particles with these energies are additionally suppressed due to the interaction with photons of CMB and EBL, and it depends closely on the energy and composition of CRs [208].In case of protons, strong suppression is expected around the threshold energy for the photo-pion production, resulting in production of charged/neutral pion - neutron/pion pairs, for the two most represented channels respectively. This is known as the Greisen-Zatsepin-Kuzmin (GZK) cutoff and occurs at energies $\sim 6 \times 10^{19}\,\text{eV}$ [213, 214]. For nuclei heavier than proton, this energy threshold depends on the atomic number, and leads to the process of photo-disintegration at energies around $E > A \times 10^{18}\,\text{eV}$, where A is the atomic mass number [209]. Consequently, one can conclude that even in the case of iron nuclei, cut-off due to the photo-disintegration occurs at energies lower than $E \sim 10^{20}\,\text{eV}$. Composition and origin of CR spectrum around this energies, particularly the *knee* and *ankle* are greatly investigated by KASCADE Cosmic Ray Data Centre (KASCADE)-Grande [215], Pierre Auger [216, 217] and Telescope Array (TA) [218] observatories, that will be also mentioned later in Section 4.3.6.

Acceleration mechanisms of the CRs are still under the discussion, but those up to date are offering satisfying predictions in accordance to the observations. Two most famous mechanism proposed for an explanation of acceleration of these particles are Fermi mechanisms of first and second order [219]. Particles are believed to be accelerated in regions with strong magnetic fields (also called magnetic clouds) exhibiting variations leading to creation of variable electric fields that can accelerate particles. General scenario is assuming shockwaves produced due to a gravitational collapse associated with irregularities in a magnetic field, so called "magnetic mirrors" inside of which the charged particle can be scattered several times in random directions and with a collision probability dependent of relative velocities of the particle and shockwave [206]. In this way, particles gain energy

stochastically due to "reflections" from the mirrors. This scenario is called the Fermi acceleration mechanism of second order, since the particle energy gain ΔE has quadratic dependence on the velocity v_{cloud} of the shockwave [209]:

$$\frac{\Delta E}{E} \propto \left(\frac{v_{cloud}}{c}\right)^2. \tag{4.1}$$

Having in mind that the shockwave velocity is usually small, $v_{cloud}/c \leq 10^{-4}$, this mechanism is not very effective, and the final velocity of the particle is far below the energy of cosmic rays observed at the *knee* level. In the case a locally plane shockwave front is passing through the cloud with a supersonic speed, like it is the case e. g. during supernova explosions, particles can undergo several acceleration cycles, passing through the front and back, colliding with the surface and gaining energy ΔE proportional to the velocity of the front and escaping the shock region [209]:

$$\frac{\Delta E}{E} \propto \frac{v_{cloud}}{c} \tag{4.2}$$

Following this mechanism, called the second order Fermi mechanism, detection of cosmic rays with energies up to the *knee* can be explained with a PWL spectrum with index $\gamma \sim 2.7$, a reason why today it is believed to be the main acceleration mechanism for high-energy cosmic rays. Assuming general supernova conditions in a GMF of a strength of $\mathcal{O}(\mu\text{G})$, maximum energies to which particles can be accelerated is hundreds of TeV, depending on the particle type (its nuclear charge), up to the energies around the *knee*. To reconcile the maximum energies to which the CRs are accelerated at the acceleration sites, one may refer to Figure 3.9, where the dependence of the magnetic fields and the size of the source is shown. In order to accelerate particles to certain energies, source needs to be positioned above the corresponding line.

4.2 Gamma rays

Gamma rays are the most energetic radiation in the electromagnetic spectrum. Unlike charged CRs, gamma rays are photons, travelling through the space and keeping the information about their direction of arrival, pointing to their source. Among many other messengers, such as aforementioned CRs or neutrinos, first being impossible to back-track, and second very difficult to detect due to their extremely weak interaction with the visible matter, gamma rays turn out to be another very useful asset in the astrophysical observations.

Known gamma rays span over 9 orders of magnitude in energy, from MeV to PeV energies. As we previously saw in Hillas diagram in Figure 3.9, depending on the energies, different sources can emit in different energy ranges, specially if we strictly refer to the maximum possible energies. Based on the energy, we can roughly characterise them in three corresponding groups:

- High Energy gamma rays (HE), with energies 0.1 MeV to 100 GeV.
- Very High Energy gamma rays VHE, with energies from 100 GeV to 100 TeV.
- Ultra High Energy (UHE) gamma rays, with energies from 100 TeV and above.

For the main study of this work, we will focus on the VHE gamma rays, emitted by the galactic and the extragalactic sources. Before proceeding with the characterisation of these two distinctive groups of sources, we will focus on the mechanisms of the production. Gamma rays are produced from more energetic particles through the non-thermal emission processes. They include interactions with charged particles, heavier nuclei, and magnetic fields.

4.2.1 Production of gamma rays

Production processes of the gamma rays can be divided it two groups based on the parent particle type, hence, we are distinguishing leptonic and hadronic processes.

Leptonic processes are including the synchrotron radiation and inverse-Compton scattering. Synchrotron radiation is occurring when a highly energetic electron or a positron emits energy due to its accelerated motion in the magnetic field and effects of the Lorentz force. Similarly to this, protons, pions and muons can undergo the same effect, even though, due to the inverse quadratic ($dE/dt \propto m^{-2}$) dependence of the emitted energy on the mass of the particle, contribution of the synchrotron component is more significant in case of electrons and positrons. For that reason, synchrotron radiation of protons is considered to be an inefficient process.

On the other side, inverse Compton scattering, same as the Compton scattering, turns out to be more efficient in terms of energy gain for the scattered particle. In particular, inverse Compton scattering occurs when a relativistic electron is scattered of a low energy photon, which is then up-scattered to higher energies. In case the same relativistic electrons that are emitting the energetic photons through the synchrotron radiation, are also up-scattering them through the Compton scattering, we are witnessing the process of the self-synchrotron Compton scattering.

Hadronic processes, on the other hand, are including only hadrons and gamma rays, and mediating the interactions between them.

An example is the synchrotron radiation of charged hadrons due to the presence of a magnetic field as mentioned above. Moreover, the aforementioned population of accelerated charged particles can interact with photons emitted in synchrotron processes, or with electrons that underwent the brehmsstralung due to the presence of magnetic fields. On top of this, gamma rays can also be produced through the interaction of CRs with interstellar gas, such as in molecular clouds, where they interact with other hadrons or photons, producing subsequent, less energetic particles. Furthermore, these particles, e. g. pions, can decay into two gamma rays (in 99% of cases) or a gamma ray and an electron-positron

pair (1%):

$$\pi^0 \rightarrow \gamma + \gamma \tag{4.3}$$
$$\pi^0 \rightarrow \gamma + e^- + e^+ \tag{4.4}$$

Threshold energy of an initial proton for neutral pion decay to occur is $E_{thr} \simeq 280\,\mathrm{MeV}$, producing neutral pion with rest mass of $m_{\pi^0} = 134.97\,\mathrm{MeV}$ and the remaining energy in the form of momentum. Subsequently, neutral pions decay and produce two gamma rays. Their energy is equal to half of the energy of the original pion at rest [206]:

$$E_\gamma = \frac{m_{\pi^0} c^2}{2} \simeq 65.7\,\mathrm{MeV} \tag{4.5}$$

In case the initial pion is moving, energy of the produced gamma-ray is given by:

$$E_\gamma = \frac{1}{2}\, m_{\pi^0}\, c^2\, \frac{1 + \frac{v}{c}\cos\theta_\gamma}{\sqrt{1 - (\frac{v}{c})^2}}, \tag{4.6}$$

for a neutral pion travelling with the velocity v, in a direction closing θ_γ angle with the direction of the emitted photon. In comparison to photons emitted from the synchrotron radiation, photons from hadron decay generally have higher energies since electrons cool down more efficiently than hadrons. Detection of these gamma rays provides a unique insight into production and propagation of charged CRs. Prior to their detection, entering the Earth's atmosphere, these particles are producing the so called "atmospheric showers", used in detection methods and reconstruction of the evolutionary path of a cosmic/gamma ray. More details on this will be discussed in Section 4.3.3.

4.2.2 Absorption of gamma rays

Production and all the processes during the history of the Universe are leaving traces, encrypted in the background fields of photons. Even though most of the components of the photon background of the Universe are understood as we will soon discuss, exact details on their quantitative description, and the effects on the rest of the radiation are not yet completely known. Photon backgrounds present in the Universe are shown in Figure 4.2.

Gamma-ray background is a component mainly attributed to the radiation coming from the extragalactic sources, star-forming galaxies and AGNs. Lesser part, almost negligible, comes from the millisecond pulsars, Type Ia supernovae and GCs. Moreover, around 20% of photon background radiation in the energy range of 0.1 – 50 GeV can be explained by the observations of blazars. Above that energy, almost entirety can be attributed to blazars, dominated by the Fermi-LAT sample [221]. The most sensitive measurement of the gamma-ray background up to date was done by Fermi-LAT collaboration, covering energy range of 100 GeV to 800 GeV, and showing a cutoff at around 280 GeV [222]. Remaining part of the gamma-ray background is possibly of the galactic origin, possibly coming from

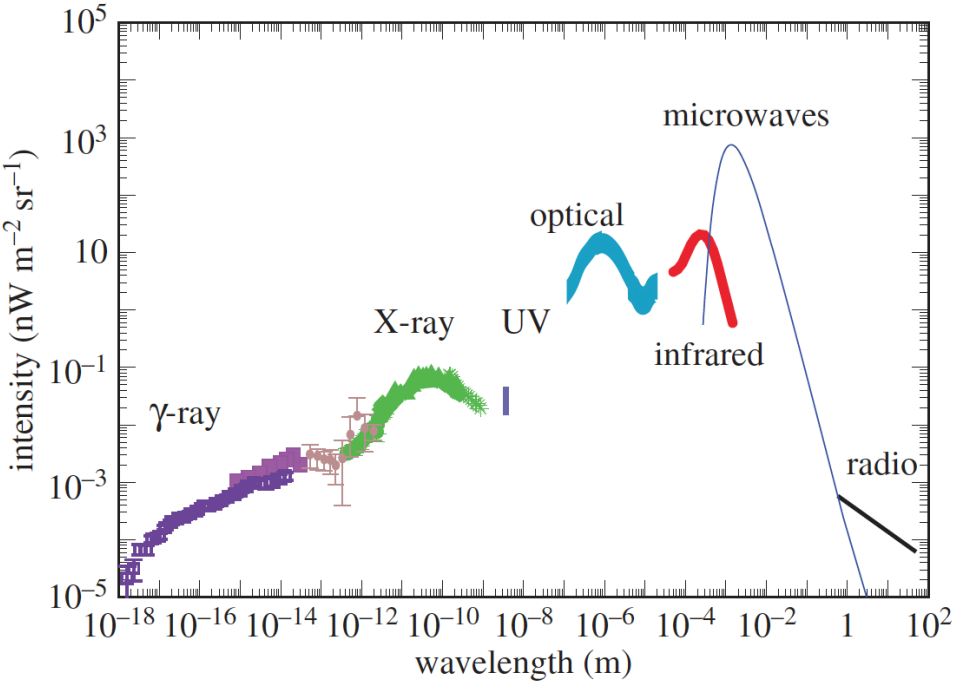

Figure 4.2: Intensity of the extragalactic background as a function of the wavelength in meters. Figure is reprinted from [220] where the full list of references can be found.

the interaction of the CRs with the interstellar medium. For a complete review of the gamma-ray background and contributing factors, readers are advised to consider [223]. Aside from these, there are also many efforts in unveiling the DM induced signatures coming from its decay and/or annihilation in our galaxy, that in case detected, would contribute to this component as well.

X-ray background can in general be divided into two parts; contribution coming from the thermal emission of hot gas associated with the interstellar medium or the Galactic halo, resolved with the observations with ROSAT (ROentgen SATellite), and the second contribution coming from extragalactic sources, mainly AGNs, all accompanied with lower fractions attributed to starburst galaxies [224] and GCs [225], obtained with the Chandra X-ray observatory and the XMM-Newton survey.

Ultraviolet background has been the most scarcely detected background in the EM. This is due to large statistical and systematic uncertainties of the current measurements in this range. It is believed that the strongest impact on the extragalactic photons in this energy range have the neutral hydrogen in our Galaxy and the intergalactic medium causing the absorption at wavelengths below 91.2 nm [220]. However, there are notable contributions and planned observations in goal to further constrain this component of the photon background by attributing it to galactic, as well as the extragalactic sources.

Optical and near-IR background is mainly dominated with the stellar emission from the nucleosynthesis. Aside of this, photon background in this energy range carries the information about the emission of the primordial sources, high-shifted to near-IR wavelengths.

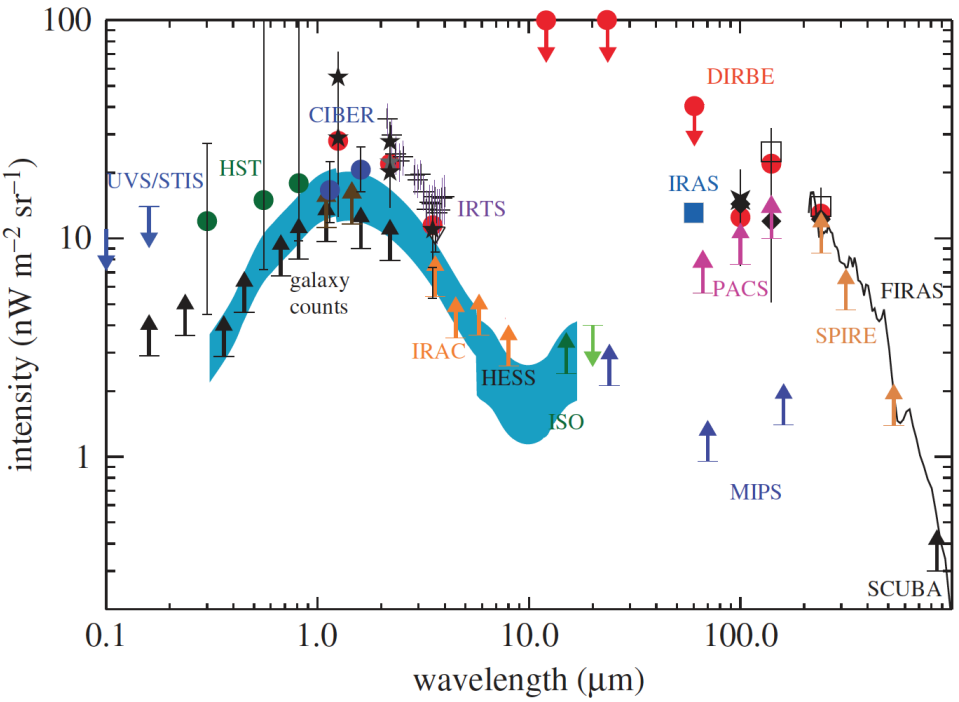

Figure 4.3: The cosmic optical and IR background light components of photon background in the Universe. Figure is reprinted from [220] where the full list of references can be found.

Interestingly so, accompanied by direct radiation coming from stars and mini-quazars, this component of the photon background offers a complete coverage of the Universe's history. Wide range of this contribution, particularly in between 5 μeV – 100 μev, is limited by the Zodiacal inter-planetary dust emission. Zodiacal light is the solar light scattered from the inter-planetary dust particles in the Solar system, mainly in the Earth's orbit. Constraints of this component are obtained by combining the measurements using the absolute photometry, the integrated galaxy light counts and the fluctuation-based estimates of the EBL that can be seen in Figure 4.3.

Most promising constraints are offered by combining the aforementioned with the constraints obtained from observations of the absorbed GeV – TeV spectra, uniquely probed by the IACT, constraining the optical and IR background by evaluation of the pair production causing the photon attenuation (see e. g, [226, 227]. In particular, this effect will be discussed in the following, as well as in Section 6, dedicated to the modelling of the photon/axion propagation through the astrophysical environments.

Far-IR background, similarly to the previous component, can be constrained by VHE observations at energies above several TeV. Dedicated to these searches are also the IR space telescopes, which are unfortunately suffering from the detection of diffusive radiation and limited angular resolution. Radiation in this range is mainly re-processed short-waved radiation coming from the galaxies or AGN accretion, spanned in the energy range of 5 μeV – 300 μeV.

Microwave background is the dominant component of the photon background uniquely describing the Universe from the moment in which the first photons decoupled close enough to be able to reach us. This radiation is uniformly permeating the whole Universe uniformly, and offering a unique opportunity to explore its earliest periods. Well known distribution of the co called CMB is represented by a blackbody spectrum, peaking at the wavelength of 1.9 mm with the temperature of 2.725 K [7]. Studies of the CMB are an interesting topic in the cosmology, focusing on the spatial anisotropies and polarisation.

Radio background is representing the longest wavelengths of the photon background in the Universe. It is also the least contributing component, also suffering from the lack of experimental improvements, as well as the poor understanding and modelling of the Galactic radio foreground.

Extragalactic background light (EBL)

Once combined, the optical, near- and far-IR backgrounds are forming probably the greatest nemesis of VHE gamma rays: the EBL. Propagation of the VHE gamma rays with energies above 100 GeV is greatly impacted by pair production, an interaction of the gamma ray photon with photon from the background population, creating an electron-positron pair:

$$\gamma_{VHE} + \gamma \rightarrow e^- + e^+, \tag{4.7}$$

which occurs above a threshold on energy of the VHE photon:

$$E_{thr}(E, \theta) = \frac{2\ {m_e}^2\ c^4}{E\ (1 - cos\theta)}, \tag{4.8}$$

where E is the energy of the background photon, E_{thr} energy of the incident VHE photon, θ the scattering angle, and m_e the electron mass. Pair production causes the attenuation of the VHE gamma-ray spectra, exhibiting exponential cut-offs at high energies dependent on the energy of the photon E_γ and redshift of the source z, affecting the observed spectrum of the source defined as:

$$\Phi_{obs} = \Phi_{em} \times e^{-\tau(E_\gamma, z)}, \tag{4.9}$$

where Φ_{em} is the emitted flux, $\tau(E_\gamma, z)$ is the optical depth, also dependent on the energy of the VHE photon and the redshift z of the source. In Figure 4.4 one can see the evolution of optical depth depending on different photon energies for sources located on different redshifts z. Having in mind the expansion of the Universe and that all the radiation emitted at a particular distance is shifted in wavelength, hence we have the light coming from different sources distributed over the same energy range:

$$\lambda_{obs} = (1 + z)\ \lambda_{em}, \tag{4.10}$$

where λ_{obs} and λ_{em} are the observed and emitted wavelengths, respectively. EBL is in particular showing two distinctive peaks, one at optical wavelengths $\sim 10\ \mu$m, attributed to the stars emission from the thermonuclear burning, and the second at $\sim 100\ \mu$m due

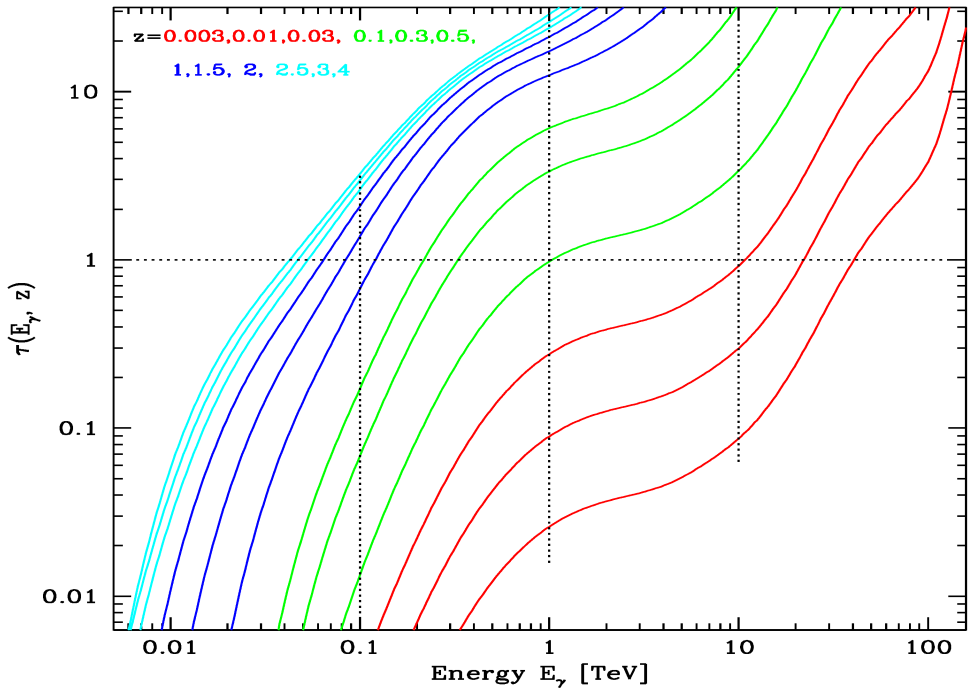

Figure 4.4: Dependence of the optical depth $\tau(E_\gamma, z)$ on the photon photon energies for sources located on different redshifts z. Figure is reprinted from [228].

to the re-emission of the same light by the interstellar dust (see Figure 4.3). Aside from these, an important role is also played by the non-thermal emission of AGNs, diffuse emission of GCs or first stars. Observations of the attenuated VHE spectra can then set constraints on the EBL, which in the other hand is crucial in cosmological studies exploring the evolution of the Universe.

As such, EBL is an important factor in the evaluation of the photon propagation while assuming the existence of axionlike particles, both for the correction of the observed VHE gamma-ray spectra and the possible resurrection in the GMF of the MW. Since the aforementioned is the main interest of this thesis, further consideration and discussion about the EBL will be addressed again in Section 6.

4.2.3 VHE gamma-ray sources

A skymap of the VHE sky counts over 240 sources, both galactic and extragalactic, detected over the past 30 years. Figure 4.5 is showing the map (September 2023.) above 100 GeV. In the case of galactic observations, high brightness of the centre of the galaxy is obstructing the observations of other sources in the line of sight. Consequently, the majority of yet unidentified sources are located in the galactic plane. This drawback is expected to be overcome with the upcoming ground- and space-based experiments. The ones already detected, are divided between the few most common types, such as supernova remnants (SNRs), pulsars, pulsars wind nebulae (PWNs), etc.

Extragalactic sources are e. g., already mentioned AGNs, the afterglow emission of GRBs and starburst galaxies (SBGs).

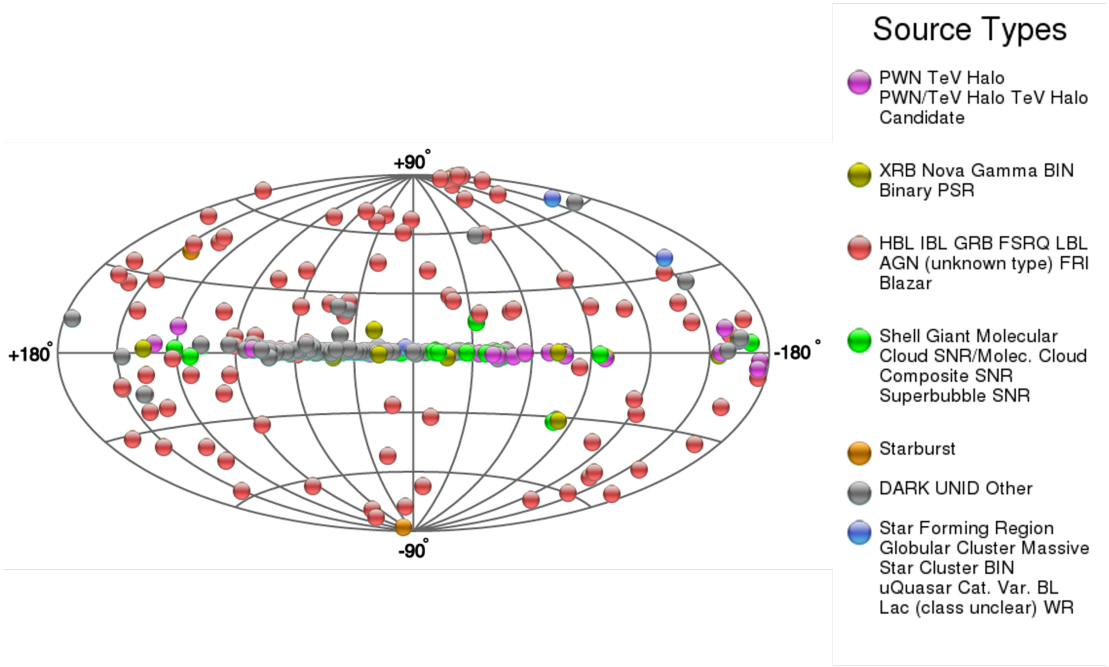

Figure 4.5: Map of the VHE sources detected by the ground based instruments [229] (accessed in October 2023).

Most active instruments in detection and observation of the HE and VHE sky are the Fermi-LAT telescope and the ground-based IACT arrays.

In the following sections we will discuss the principles and methods for the detection of VHE gamma rays, together with an overview of the current instrumentation in space and ground-based VHE gamma-ray astronomy.

4.3 Detection of gamma rays

The Earth's atmosphere is dense with molecules, atoms and other particles, essentially behaving as a "curtain" to protect the Earth itself, and blocking the path for the majority of the EM radiation. As it can be seen in Figure 4.6, the only exceptions are a very narrow

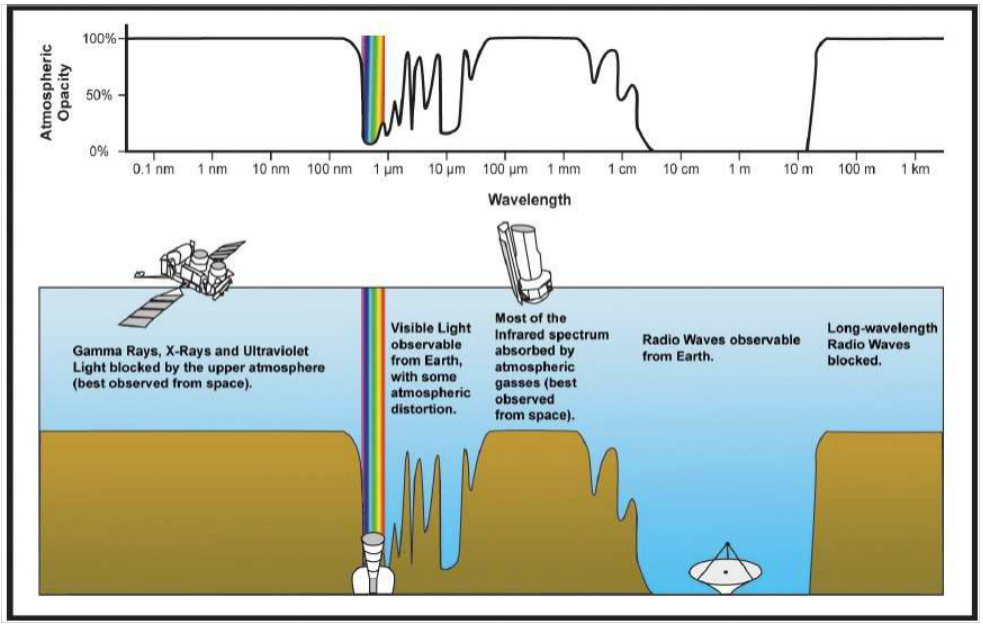

Figure 4.6: Transparency of the atmosphere to the Electromagnetic (EM) radiation in dependence of the wavelength. Image credit: NASA/IPAC.

interval of wavelengths in the optical range and part of the radio wavelengths. Just as the rest of the EM spectrum, gamma rays are not an exception. For that reason, their detection with the ground based instrument seemed impossible in the past, and the leading experiments in the direct observations of gamma rays have been space-based instruments. Nonetheless, difficulties encountered in the attempts of direct detection have been overcome with the development of the ground-based observatories. These observations rely on the interactions of gamma rays with particles in the atmosphere, allowing for reconstruction of their energy and arrival direction.

In the following two sections, we will briefly discuss direct and indirect detection of gamma rays, and explain the methods utilised by the experiments representing state of the art.

4.3.1 Direct detection of gamma rays

As mentioned before in Section 4.2, gamma rays are covering a wide range of energies and for simplification are divided in few groups. Direct detection of gamma rays with the satellite experiments is targeting the HE gamma rays with energies from 0.5 MeV

to 100 GeV. In this energy range, there are two most dominant processes on which the detection is based: Compton scattering, strongly affecting gamma rays in the energy range from 0.5 MeV to 20 MeV, and the aforementioned pair production, dominant on energies starting from 30 MeV. These two demand slightly different detectors, both of them facing certain limitations. A representative of the first type of detectors is the Imaging COMPton TELescope (COMPTEL), composed of a two-part detector: one for inducing the Compton scattering and the other for absorption of gamma rays [230].

In the other case, Fermi-LAT [231] telescope is an instrument based on the detection of the pair production, mounted on the Fermi satellite, orbiting the Earth at the altitude of ~ 565 km, with a period of 1.5 hours. It covers the energy range of 20 MeV to 300 GeV. The detector is structured in two parts, the tracker where the pair production happens and the calorimeter that measures the energy of the produced particles [231]. Overall, as it will soon become evident, a great asset of this instrument is its long duty cycle, given their independence on the day-night differences and the ability to do a full-sky coverage every three hours. Unfortunately, due to the limitations in the size of the detector and the big number of the pair productions that can superimpose and saturate the detector, Fermi-LAT is characterised by sub-optimal energy and angular resolutions, respectively. Observations done by Fermi-LAT in the past few decades have been strongly supporting and contributing to the gamma-ray astronomy, yielding numerous scientific discoveries and enriching the soil for the growth and expansion of new physics. Some of the studies are done on the searches for axion-like particles as we have seen in the previous sections.

4.3.2 Indirect detection of gamma rays

Unlike the direct detection of gamma rays, once located within the Earth's atmosphere, experiments are suffering issues in reconstructing the exact energy and the arrival direction of the gamma ray due to its interaction with other particles during the propagation from the emission site to the detector. As we saw in Figure 4.6, Earth's atmosphere is opaque to gamma rays, due to their interactions with the particles of the atmosphere and decay into less energetic ones, causing the phenomenon called atmospheric showers. During their evolution in the atmosphere, ambient particles are emitting Cherenkov light, detected by the (IACTs), whose data was used in the main study of this work of thesis [232]. Once the HE particle, such as a proton, $e^{\pm}$, or a gamma ray enters the atmosphere, it interacts with ambient particles, creating an Extensive Air Shower (EAS), that is subsequently developing into a typical shape, distinguishable for hadrons and leptons. The first detection and a comprehensive explanation of the extensive air showers was given by Pierre Auger and his collaborators back in 1939 [233]. They reported and proved the coincidence between the particles detected by an array of detectors mutually separated up to 300 m on the ground and the nucleonic cascades created upon the interaction with the CRs of energy exceeding 10^{15} eV at the top of the atmosphere.

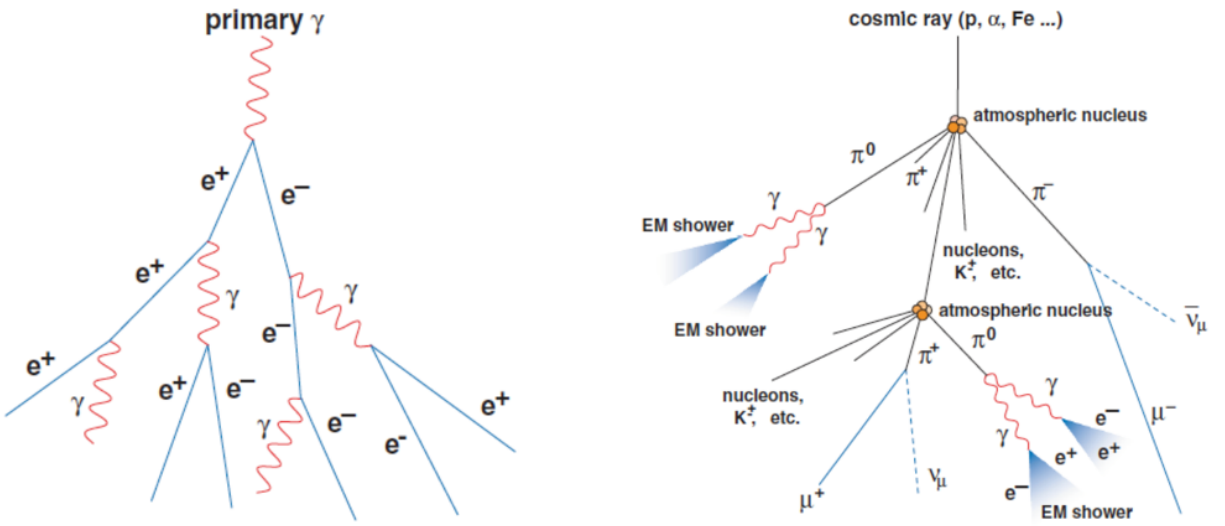

Figure 4.7: Scheme of the development of the extensive air showers for the case of a gamma ray (left) and a charged particle (right). Reprinted from [234].

4.3.3 Extensive air showers

Depending on the type and the energy of the incident particle, created atmospheric shower has a different shape, as it can be seen in Figure 4.7.

Electromagnetic shower shown on the left side of the figure is caused by the primary gamma ray or an electron/positron entering the atmosphere, and interacting with the atmospheric particles. Once the interaction occurs, $e^{\pm}$ pairs are produced at the mean free path of $\frac{7}{9}X_0$, where $X_0 = 36.6$ gcm^{-2}, being the atmospheric radiation length [206]. Further on, created particles are loosing the energy due to the bremsstrahlung, emitting the photons and creating an extensive air shower. This continues until the ionisation losses do not overcome the cooling through the process of the bremsstrahlung. The threshold for this process is reached when the energy of the last produced photon decreases down to $\sim$ 80 MeV (for standard atmosphere conditions), called the critical energy E_c. A simple model by Heitler [235] in this case predicts the maximum of the shower X_{max} at:

$$X_{max} = X_0 \, ln \, \frac{E}{E_c}, \tag{4.11}$$

where E is the initial energy of the incident photon (gamma ray). Given that the height on which the first interaction occurs varies between 5 and 30 km, it is worthy noting that the probability of the gamma ray travelling through N atmospheric radiation lengths is given as:

$$P(N) = exp\,(-9/7N). \tag{4.12}$$

More about the specifics of the shower development and simulations will be discussed in Chapter 5, dedicated to the MAGIC and LST-1 telescopes.

Hadronic showers, on the other hand (right side of Figure 4.7), are created once a highly energetic charged particle, such as a proton, enters the atmosphere and starts interacting with the ambient particles. Unlike more "centered" and "narrower" electromagnetic showers, hadronic showers suffer from larger fluctuations, resulting in a wider transverse profile. Since the shower is induced by a charged particle or a nuclei, development of the shower is more complex than in the case of a gamma ray. Strong interactions are now governing the majority of interactions, while only one third of the shower is electromagnetic, attributed to the almost instantaneous decay of neutral pions into pairs of photons.

Accordingly, we can say that the hadronic showers have three components: **hadronic**, **electromagnetic** and **muonic**. Hadronic component is consisted of charged pions $\pi^{\pm}$, making the $\sim$ 90% of the total count of produced particles, and the remaining $\sim$ 10%, attributed mostly to kaons $K^{\pm}$. These are subsequently decaying into lighter particles: muons, $\mu^{\pm}$ and muon neutrinos ν_{μ} $\bar{\nu}_{\mu}$, constituting the last, muonic component of the shower. In case of very energetic muons, the probability of their decay is low, and most of them reach the ground. Otherwise, they are decaying, producing the $e^{\pm}$ pairs and neutrinos ν $\bar{\nu}$. Similarly, as in the case of the EM showers, the hadronic interactions also continue down to a certain energy threshold, this time until the one for the production of the lightest hadron (also a meson), a pion $\pi^{0,\pm}$, being $E_{thr} \sim$ 1 GeV. Aforementioned atmospheric interaction length in this case, specifically a for a proton, is $X_0 \sim 70.0\ \mathrm{g\,cm^{-2}}$, resulting in shallower shower than in the case of leptons.

4.3.4 Cherenkov light

Extensive air showers, as we noted, are produced from energetic particles entering the Earth's atmosphere and interacting with the particles in it. Given that the energy of the incident particle is very high, speed of the produced particles is as well. For some of the produced particles, the speed can even exceed the speed of light in the air. This is the phenomenon leading to the Cherenkov radiation [236]. The passage of a charged particle through a dielectric medium, in this case the atmosphere, induces the polarisation of the surrounding atoms and molecules emitting coherent radiation, and causes the creation of a light shockwave, one as in Figure 4.8. With $n(z)$ being the refractive index of the air, dependent on the height of the atmosphere z and β the superluminal speed of the particle, $\beta > 1/n$, and the opening angle θ_z of the Cherenkov cone, is:

$$cos(\theta_c(z)) = \frac{1}{\beta n(z)}. \tag{4.13}$$

The refractive index scales in dependency to the height of the atmosphere as: $n(z) = 1 + \eta_0\ exp(-z/h_0)$, where $\eta_0 = 2.9 \times 10^{-4}$ and $h_0 = 7250$ m. Correspondingly, development of the Cherenkov cone depends on the height at which the particles start emitting the Cherenkov radiation, hence the cone angle increases with the decrease of the height above the sea level. Ultimately, the emitted radiation illuminates an area with the radius $\sim$ 120 m

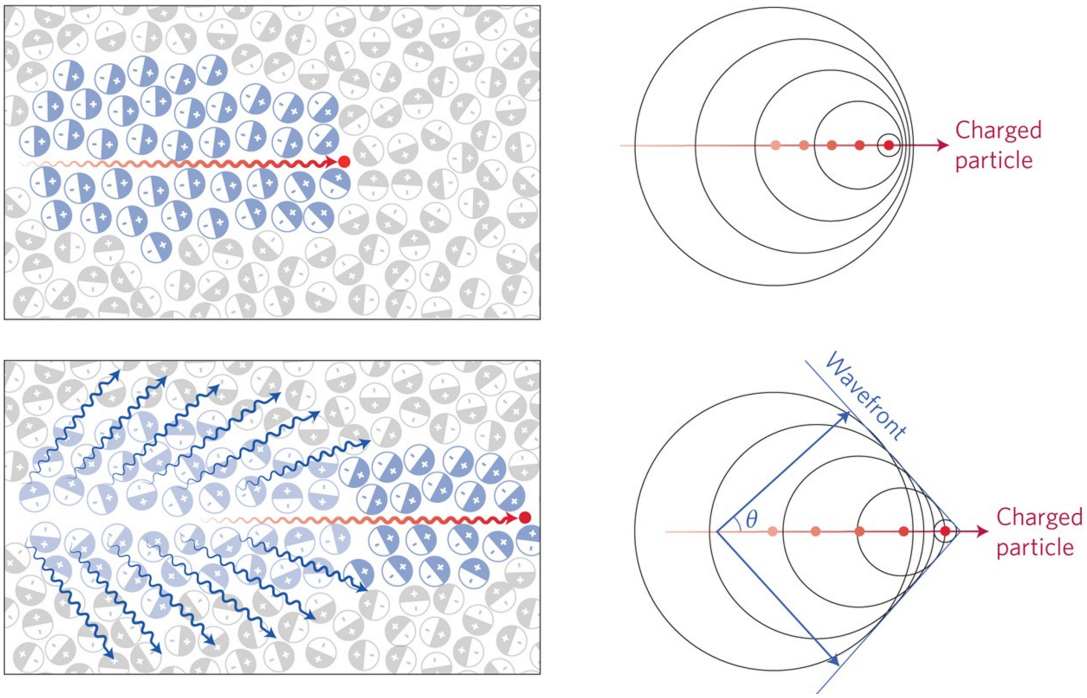

Figure 4.8: Comparison of subluminal and superluminal motion. The figure on right is representing an example in which Cherenkov radiation occurs. Reprinted from [237].

on the ground. The spectrum of the emitted Cherenkov radiation is [206]:

$$\frac{d^2N}{dEd\lambda} = \frac{2\pi\alpha}{\lambda^2}\, sin^2\theta\, c = \frac{2\pi\alpha}{\lambda^2}\left(1 - \frac{1}{\beta^2\, n^2(z)}\right), \tag{4.14}$$

where α is the fine structure constant. Important to note is that the refractive index also varies with the wavelength λ, and as a consequence, Cherenkov spectrum is peaked in the UV and the optical range of the EM spectrum. Also, photons from the outskirts of the shower are not arriving to the ground at the same time as the ones in the core, causing a small delay in the arrival time. The conclusions are the same when comparing the photons emitted at higher altitudes to those emitted closer to the ground. Overall, this results in a duration of the shower being $\sim 2\,\text{ns}$, too fast to be observed by a naked eye [238]. Henceforth, techniques like imaging technique are developed and utilised in the experiments dedicated especially to this purpose, called the IACTs.

4.3.5 Imaging Atmospheric Cherenkov Telescopes (IACTs)

IACTs are usually constructed in arrays of reflectors with range from few meters to tens of meters, used to focus the incoming light into a high performance camera, constructed of a large number of PMTs. More detailed explanation of the design of the IACTs and all

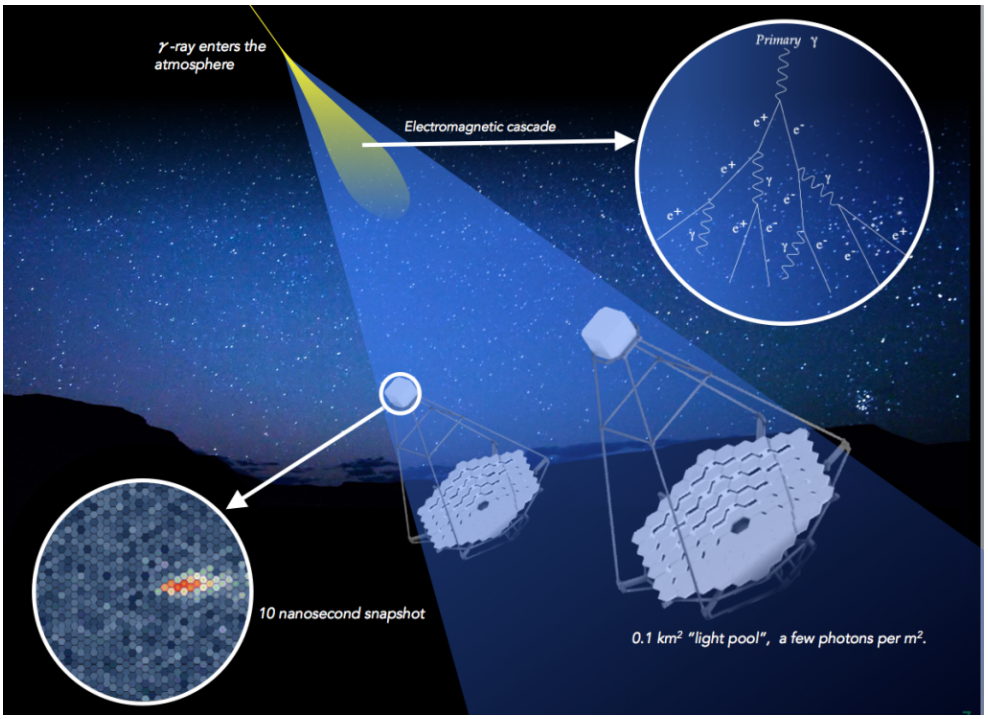

Figure 4.9: Scheme of the imaging technique for the detection of Cherenkov light with IACTs. Credit: CTA Observatory.

the components missing from this very brief description will be mentioned later, giving an example of two particular IACT arrays.

IACTs measure the energy and direction of a gamma ray indirectly: during its passage through the atmosphere, gamma ray interacts with the atmospheric nuclei and produces a shower of particles, as explained in Section 4.3.3. Based on the nature of primary particles, we distinguish between hadron and gamma-ray induced showers. Due to their similarities and large number, exceeding the number of gamma-ray showers by several orders of magnitude, hadronic showers are the main background for detection of the Cherenkov radiation caused by the VHE gamma rays. For example, Cherenkov radiation caused by a muon will be detected in the camera as a ring or an arc, seen by one telescope only, in comparison to an elliptical shape image from a Cherenkov shower caused by a gamma ray. On the contrary, Cherenkov radiation originating from other charged particles creates wide and irregular shapes in the camera. To distinguish this background radiation from the gamma rays, training algorithms are used in the data analysis to classify the collected data in one of the two groups. We will discuss this method, the so called "random forest", in Section 5. The faint Cherenkov light is collected by the mirror dishes of the telescopes and reflected to the camera positioned on the opposite side (see Figure 4.9). The energy threshold of IACTs is inversely proportional to the signal-to-noise ratio, so it is convenient to maximise the mirror area and throughput of the optical system to minimise the threshold for the particle detection. The shape of the shower image is described with Hillas parameters [239] that will

be discussed in more detail later. The flux of gamma rays is reconstructed using the MC simulations trained with data collected from regions of the sky with no gamma-ray emission (so called OFF regions), taking the collection area of telescopes and the effective time of the observations into account. The analysis of the data for the existing IACTs differs at the high level of analysis, when different methods to correct (unfold) the energy spectrum are used. The need for correcting the spectrum comes from the fact that the obtained number of events assigned to each energy bin is subject to $\sim 15\%$ spread of reconstructed energy, hence not perfectly overlapping with true energy of the events. For that reason, the unfolding procedure has to be performed, taking into account the effective collection area corresponding to the true energy of the gamma ray. The unfolding methods can be based on different algorithms in order to assign its true energy to each gamma ray, and to calculate the intrinsic spectrum of the source. Overall, all the mentioned specifications of an IACT, limited or enhanced by its instrumental setup and the analysis, gather into a collective parameter able to judge on telescope's performance, the sensitivity. Sensitivity of an IACT telescope or an array is defined as the minimum flux from point-like targets that it is able to detect with a 5 σ significance in a given time, with additional constraints on the number of excess events and signal-to-noise ratio.

While there have been several early attempts to detect gamma rays at the ground starting from the 1950s [240], rise of the ground-based gamma-ray astronomy officially kicked-off with the detection of the Crab Nebula with the Whipple telescope in 1989. Number of the new TeV emitters populating the gamma-ray sky increased, allowing the insight into one of the last unexplored windows in the electromagnetic radiation from the Universe. IACTs are suitable for detection of VHE gamma rays, highly energetic photons produced in the environments of astrophysical objects such as AGNs, supernovae, binary stars, pulsars, etc., as a result of highly accelerated (TeV-PeV) CRs such as electrons and protons. The energy range where the IACTs are most sensitive is $\sim$ 50 GeV $-$ 50 TeV. At present, Whipple is decommissioned, and there are three major IACT arrays currently operating:

- VERITAS [41] is an IACT array, consisting of four, 12 m diameter telescopes, located in the F. L. Whipple Observatory in southern Arizona, USA on 1268 m. VERITAS is operating since 2004 and its Field of View (FoV) is 3.5 °.

- H.E.S.S. [42] consists of 5 telescopes since 2012 when the central, 28 m diameter reflector was installed. Since then, the energy threshold for the detection is improved down to $\sim$ 30 GeV. FoV of the four smaller telescopes is 5 °, while the central, big reflector has the FoV of 3.2 °.

- Major Atmospheric Gamma Imaging Cherenkov (MAGIC) [241] are two 17 m diameter telescopes, located in the Observatory Roque de los Muchachos, at the altitude of $\sim$ 2200 m. The energy threshold for the particle detection is 60 GeV, accompanied by the FoV of 3.5 °.

In particular, each array of IACTs possesses a different configuration and asset so the instrument response function, used to obtain the final spectra of the source, is different.

Despite a build-up of successes from the early Crab Nebula detection, the technique became really mature in the first decade of 21st century, when not only an increasing number of targets was detected, but the results also reached a level of precision and significance never achieved before. As an example, in [242], MAGIC reports the spectrum of the Crab Nebula over three orders of magnitude in the energy and four orders of magnitude in intensity, able to detect the source in less than 1 min. Along with this ramp-up of performance, the attention moved from purely astrophysical interests to more fundamental questions, such as the possibility of observing the signature of ALPs in gamma-ray spectra. The first decade of the 21st century brought the interest for the imprints and modifications that the conversion of photons to ALPs and vice versa could leave on the spectra of astrophysical objects [53, 150, 154, 155, 243, 244].

Expectations and the excitement have been reaching their peeks in these years, following the final planning stages and the construction of the CTA. CTA will be the most advanced IACT array up to date, covering energies from 20 GeV − 300 TeV. This will be achieved utilising three specific configuration of telescopes, each specified to cover a dedicated energy range [43]: Small-Sized Telescope (SST), constructed with two mirrors, one with 4.3 m and the other with 1.8 m diameter, covering the highest energies in the range from 5 TeV − 300 TeV, Medium-Sized Telescope (MST), with a 12 m diameter reflector and covering energies from 150 GeV−5 TeV, and the LST-1, with a design similar to MAGIC telescopes, but with a slightly larger reflector of 23 m diameter, reaching the highest sensitivity in the energy range from 20 GeV − 200 GeV.

As such, CTA is expected to surpass all the current IACT arrays in terms of the sensitivity, energy and angular resolution, collection area and FoV. In Figure 4.11, one can see the comparison of sensitivities of all the current IACTs, Fermi-LAT telescope, and upcoming instruments, alongside both CTA subarrays.

Great improvement in the energy coverage, collection area, but also the background estimation and the direction reconstruction will be also achieved by careful positioning of the array, which is planned to be divided in two subarrays, one located on the northern and the other on the southern hemisphere. The Northern hemisphere array will be located, as it is already being built and has one operational telescope that we will discuss later, in the vicinity of the MAGIC array, in the Observatory Roque de los Muchachos on the Canary island of La Palma. It will be consisted of 4 LSTs and 9 MSTs. On the other hand, Southern array will exploit the advantages of smaller telescopes, detecting higher energies and it will be configured out of 14 MSTs and 37 SSTs.

In Chapter 5, we will make an overview of an IACT array, the MAGIC telescopes and one standalone IACT, prototype of the future upcoming CTA observatory, the LST-1.

4.3.6 Extensive air shower (EAS) arrays

Aside from the imaging technique, utilized by the Cherenkov telescopes for the detection of VHE gamma rays, there is also another technique, relying on particle detection, the particle sampling technique. This technique is directly measuring secondary charged particles arriving to the ground and is used by the EAS arrays. In order to improve the performance,

these arrays are built in a very large area in comparison to the IACTs, $\sim 10^4 - 10^5$ m^2, ensuring a large effective area and FoV of ~ 2 sr. Another advantage is gained by the location of the array itself, high altitudes at which they are constructed ensure more statistics, highly important since only particles with energies TeV and higher can reach the ground. For that reason, energy threshold of EAS arrays is higher, making them most sensitive instruments in the energy range from few TeV to ~ 100 TeV. Detection of theses particles is somewhat robust, and there is more than one type of detectors, hence, we have examples of water Cherenkov tanks, scintillator counters and resistive-plate chambers. Working principle of a water Cherenkov particle detector is shown in Figure 4.10.

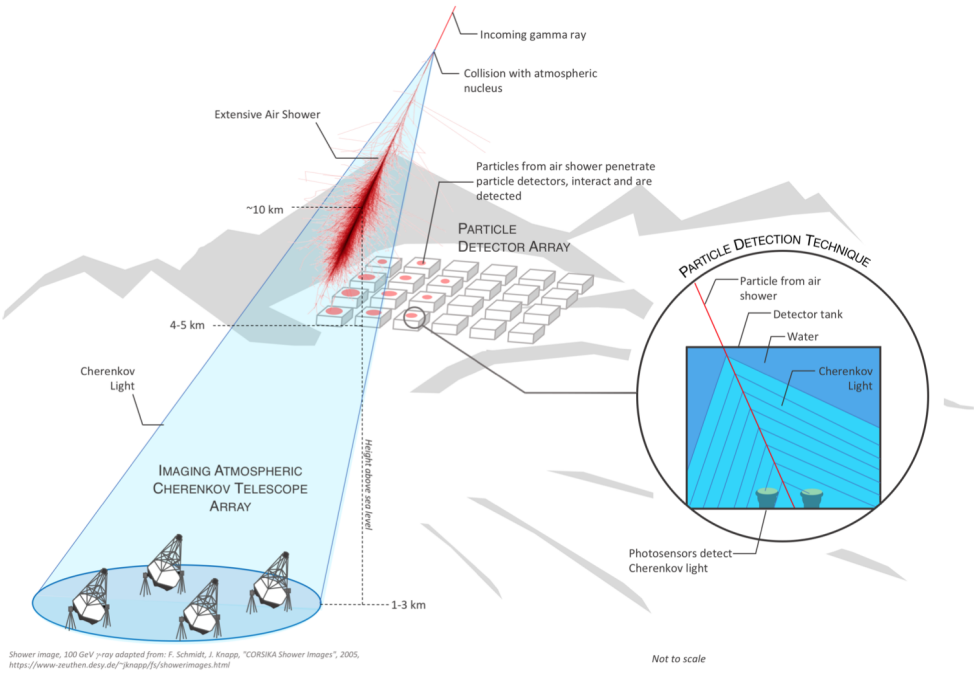

Figure 4.10: Scheme of the direct detection of particles from atmospheric air showers, along with the imaging technique utilised by IACTs. Image credit: F. Schmidt, J. Knapp, "CORSIKA Shower Images", 2005, https://www-zeuthen.desy.de/~jknapp/fs/showerimages.html.

Neither of these have any restrictions regarding the Sun light, enabling the EAS arrays to have a duty cycle of almost 100%. For that reason, we may also call them all-sky monitors. There are two currently operating EAS arrays. The HAWC telescope [197], located in the state of Puebla, Mexico on the mountain Sierra Negra, at the altitude of 4100 m contains an array of 300 Cherenkov tanks each with three PMTs, distributed over ~ 20000 m^2. Due to its configuration, HAWC monitors two-thirds of the sky every 24 hours, and has the duty cycle ~ 90 %.

A new era of the direct detection of VHE gamma rays started with the construction of the most recent EAS LHAASO, located in Sichuan, China. Just as its predecessor, it is located at high altitude of 4410 m. Superiority of LHAASO in comparison to other EAS

arrays, lays in its particular configuration and four different types of instruments. It is a composite detection array, designed to detect gamma rays from sub – TeV to beyond PeV energies [245]. It is divided in detector arrays, first being the WCDA (Water Cherenkov Detector Array), a 78000 m^2 array for detection of gamma rays in the energy range from sub – TeV to few TeV [198]. LHAASO-WDCA consists of 3210 5 m $\times$ 5 m water Cherenkov pools, equipped with two upward-facing PMTs. Overlapping outer array is the KM2A, built on 1.3 km^2, designed for gamma-ray detection from 10 TeV to $\sim$ 1 PeV energies. It consists of 5195 electromagnetic detectors and 1188 muon detectors, distributed around the central WCDA array and spaced 15 m and 30 m, respectively. Third array is positioned in the outskirts of the area, called Wide Field-of-View Cherenkov Telescopes Array (WFCTA) and it currently has 18 wide FoV IACTs. This subarray is dedicated mainly for studying cosmic-ray astronomy. Being composed in this way, LHAASO possess versatility to gather and combine the data over a wide range of energies and offer complete overview of the gamma-ray spectrum. One of the main goals is to complete and obtain a complete measurement of the *knee* region of the CR spectrum, details on the effects of spectral hardening, steepening and cutoffs, but also reach the highest energies and investigate the physics of sources emitting on PeV energies, the so called pevatrons [198].

Having in mind that no matter the dominance that LHAASO asserts over the other currently operating IACTs or EAS arrays, being located on the northern hemisphere means it has certain limitations in observations of the sources on the south sky, most importantly, the Galactic centre. However, this aspect will not wait long to be explored. Currently in planning, is the SWGO [199], based also on the ground-level particle detection, with $\sim$ 1sr FoV and almost 100% duty cycle. SWGO will be located in South America at the altitude of 4400 m or higher. Idea is to build a core detector similar, but larger than HAWC and an outer array with more spaced water Cherenkov detectors [199]. Due to its planned large effective area and duty cycle, SWGO has a potential to exceed the sensitivity in the energy range of the gamma-ray spectrum around 30 TeV. This will offer an insight into yet not studied sources of the PeV energy gamma rays located in the Galactic plane [199]. One of the main goals of SWGO is to, combined with the HAWC and LHAASO, obtain an all-sky mapping of the gamma-ray regions and improve the background estimation which is crucial for the observation of the sources with faint emission extended over several angular degrees. Aside of this, there is a long list of possibilities for the usage of the SWGO data, one of them being the exploration of the DM regions, especially those located in the centre of our galaxy. Furthermore, from the perspective of this thesis, ability of SWGO to reveal and probe TeV energies with high sensitivity, offers the possibility of studying the aforementioned effect of the photon resurrection, expected at the energies in question. Up to date, there are several studies on this topic, in particular one previously mentioned in Section 3.5.3, performed with LHAASO data [196].

Extending into higher energies, above the ones shown in Figure 4.11, there are three observatories dedicated to constraining the ultrahigh-energy photons: KASCADE-Grande, Pierre Auger observatory and TA. KASCADE-Grande studies the $10^{16} - 10^{18}$ eV energy range. Even though it stopped the active data acquisition in 2013, its data has been published through KASCADE Cosmic Ray Data Centre (KCDC) [252] and continues to provide

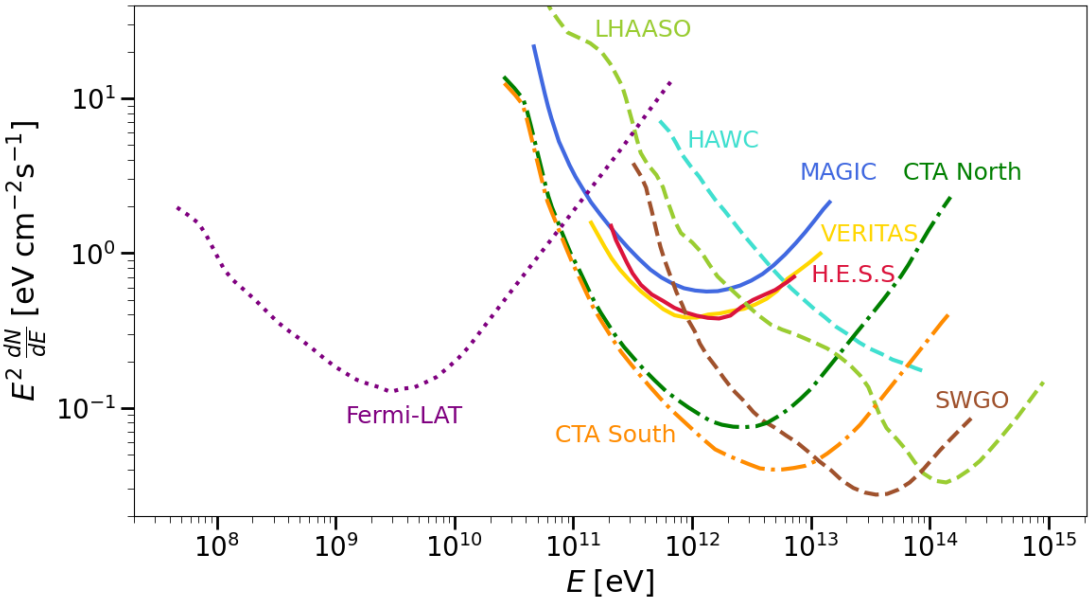

Figure 4.11: Sensitivity curves for the point sources of different gamma-ray instruments, both space and ground based. VERITAS [246], H.E.S.S. [247], MAGIC [248] and both CTA [43] curves are obtained for 50 h of observations. For HAWC [249], the curve is obtained for 507 days, while those for LHAASO [198] and SWGO [250] are obtained for 1 and 5 years, respectively. Fermi-LAT sensitivity is obtained for different sources in the sky, located at different positions [251].

scientific results in the field of extensive air showers, cosmic ray primary composition and the hadronic interactions at the aforementioned energies.

Pierre Auger observatory is an EAS array located in west Argentina, at the altitude $\sim$ 1400 m, observing cosmic rays with energies up to 10^{20} eV [217]. The observatory combines two different methods and types of detectors: 1600 water surface tanks distributed over 3000 km^2, each containing 3 Photomultiplier Tubes (PMTs) detecting Cherenkov light from atmospheric showers, and 24 fluorescence detectors, observing ultraviolet light produced by atmospheric nitrogen upon its interaction with charged particles in air showers. Combining data from both detectors, the observatory is provided with information on the trajectories and energy of cosmic rays from which, among others, information on their composition and origin can be extracted [217]. Similarly to the Pierre Auger observatory, TA is an experiment combining ground array and air-fluorescence techniques. It is located in Utah, USA, since 2007 and it consists of 507 scintillator detectors distributed over a 1.2 km^2 area. As fluorescence detectors, there are 3 telescope stations surrounding the array in a 30 km triangle. Together with the aforementioned two arrays, it investigates the CR spectrum at the highest energies, above $E > 10^{18}$ eV [253].

Chapter 5

MAGIC & LST

Contents

MAGIC is an array of two Cherenkov telescopes located at the *Observatorio del Roque de los Muchachos* (ORM) on the Canary island La Palma in Spain. It is residing at an altitude of $\sim$ 2240 m, surrounded by neighbouring telescopes, including the LST-1 that will be introduced later.

MAGIC I (M1), as the first telescope is named, started operating in 2003, initially in standalone mode, until 2009, when MAGIC II (M2) was inaugurated. Since then, the telescopes are operating mostly in stereoscopic mode. MAGIC underwent a major hardware upgrade in 2011 and 2012, when the camera and trigger systems of M1 were upgraded, and

both telescopes were provided with a new readout system. After the upgrade, a study on the performance was conducted [248]. For reconstructing the image of the shower, MAGIC is utilising the aforementioned imaging technique, based on the parameterisation of the shower image (see Section 4.3.5). At a respective distance of $\sim$ 85 m, MAGIC telescopes are working in stereoscopic mode.

On the contrary, LST-1 is currently a standalone telescope, as the expansion and construction of rest of the North CTA site is ongoing. LST-1 is a prototype of the Large Sized Telescope of the CTA array, inaugurated in 2018 and since few months concluded the commissioning phase. Given its proximity to the MAGIC telescopes, being placed only 100 m away, and working on the same principle and the imaging technique, LST-1 and MAGIC are regularly performing joint observations using the software stereo trigger system. As a confirmation of a well established cooperation, a study of the performance on the Crab Nebula observations was performed, and yielded results that overall surpass the sensitivity of MAGIC alone for 30 % [254].

In this chapter we will explain the hardware, structure and supporting subsystems necessary for performing the observations and the datataking with MAGIC and LST-1 telescopes, shown in Figure 5.1. As a bond between the instrument and science, we will discuss the software of MAGIC, but also a more general overview of the analysis of data analysis, as used for the LST-1 data, followed by the analysis pipeline used to obtain the final products of the observations, used also in the first step of our study.

Figure 5.1: Cherenkov telescopes at the *Observatory Roque de Los Muchachos*. From left to right, M1, M2 and LST-1.

5.1 Hardware

5.1.1 Structure and drive

MAGIC telescopes are envisioned and constructed with the intention of being lightweight instruments, fast in repositioning and tracking desired target of interest. The frames of the MAGIC telescopes are built out of carbon fibre space tubes joint with aluminium knots, as it can be seen in Figure 5.2. The reflectors of the telescopes are at $\sim$ 17 m distance from the camera mounted on an arc. The telescopes are placed on a rail of $\sim$ 19 m in diameter, able to turn $\sim$ 450 ° in azimuth, and up to $\sim$ 150 ° in zenith. For this purpose, total of 7 motors are used, along the railway and on the back of the reflector for movements in azimuth and zenith, respectively. The structure of the entire telescope with all the equipment, including the camera and its counterweights, reflector, frame, access towers, and carriages sums to 67 tons, so it is quite impressive to state that the repositioning angular speed of the telescope, in order to rapidly respond to a transient event, is 7 $^\circ/s$, while for the standard repositioning is 4 $^\circ/s$ [255]. Generally, it is valuable to mention that the telescopes have three operational modes in the sense of the structure: parking position, standard position during the day when the camera is resting on the supporting structure of the tower, lid is closed and the telescope drive is locked with the bolts in the rail (as seen in Figure 5.2), second, the repositioning mode, when the telescope is changing the position between pointing towards different sources during the night, as mentioned before, and lastly, the tracking mode, used during the observations of a source, when the telescope is following its trajectory on the sky.

Similarly to MAGIC telescopes, LST-1 is also designed as a lightweight instrument, targeting fast repositioning in case of a transient event. The comparison of the structures of the two can be made by using almost a single word: "enlarged".

LST-1 is the largest of the three telescope types of the future CTA. The rail on which the frame of the telescope is placed, including the reflector and the camera, has 23.3 m diameter and width of 0.5 m [256]. Similarly to MAGIC, frame of the telescope placed on it is able turn $\sim$ 408 ° in azimuth, and up to 95 ° in zenith. Most of the frame, including the dish structure and the camera supporting arch and frame, are made out of carbon-fibre reinforced plastic [256]. The base structure is made out of steel tubes, more stable and heavier than the rest of the structure but not problematic, given that it is static and does not require zenith-azimuth movements. On the other side, small weight of the space-frame enables fast repositioning, necessitating less than 20 seconds for 180 ° turn in azimuth. The camera is placed in a frame that is a part of an almost-parabolic arch on a focal distance of 28 m from the reflector, shown in Figure 5.3. Same as MAGIC telescopes, LST-1 has also three modes of operation, tracking, repositioning and the parking mode, during which the camera is rested on a platform, located at the 95 ° in zenith and 13 m above the ground on the access tower.

Figure 5.2: M1 telescope in parking position.

5.1.2 Reflector dish

The reflector dishes of MAGIC telescopes are built containing mirrors with different layering and dimensions. Parabolic dishes have a total diameter of 17 m and $\sim$ 236 m^2 area. M1 contains mostly 1 m $\times$ 1 m mirrors of different production, aluminium sandwich configuration originally from 2004, and glass-aluminium 1m $\times$ 1 m mirrors added later. On the other hand, reflector of M2 is assembled of 143 all-aluminium sandwich mirrors of 0.985 m $\times$ 0.985 m and a combination of 96 0.985 m $\times$ 0.985 m square like and 8 square angle-cut mirrors with glass plate around the aluminium sandwich produced with the cold slumping technique. Reflector dishes and mirrors of MAGIC telescopes can be seen in Figure 5.4.

An interesting peculiarity noticeable on the reflector of M1 is the so called "chessboard" layout of mirrors. This was a solution to a flaw in mirror surface planning due to which mirrors were touching during the focusing procedure. The process of focusing mirrors to assigned points on the camera is performed using the Active Mirror Control (AMC) [257]. AMC is using the lasers located at the centre of each mirror to correctly position light emitted by each of them in correct point in the camera plane. This correction is repeated directly after every repositioning of the telescope, due to the sensibility of the structure of the telescope which, affected by the weight of the camera and itself, gets slightly deformed. The correction necessitated for each of the combinations of the zenith and azimuth angles is stored in the look up tables from which AMC is adjusting the mirrors. Once per night, usually before the start of the observations, AMC is also estimating the Point Spread

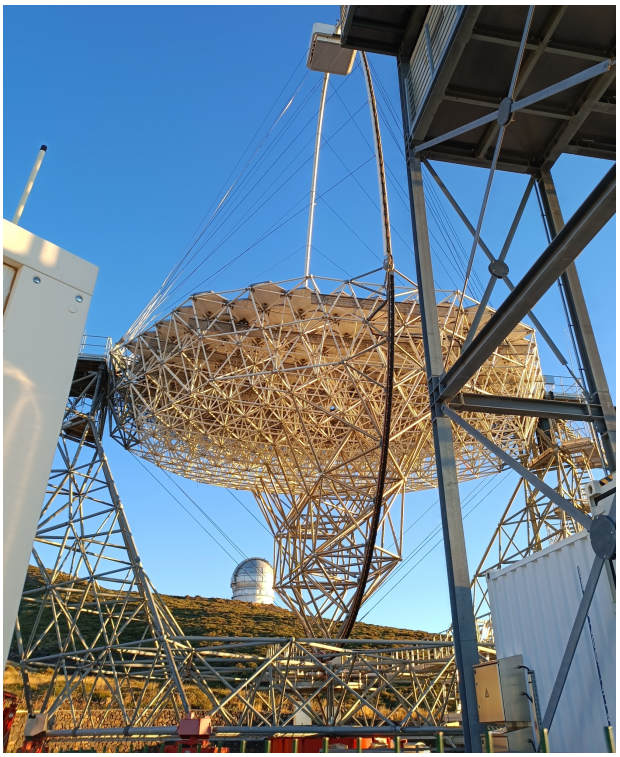

Figure 5.3: LST-1 telescope pointing $\sim 0\,^{\circ}$ in zenith, revealing the back of its reflector and the carbon-fibre pipes structure.

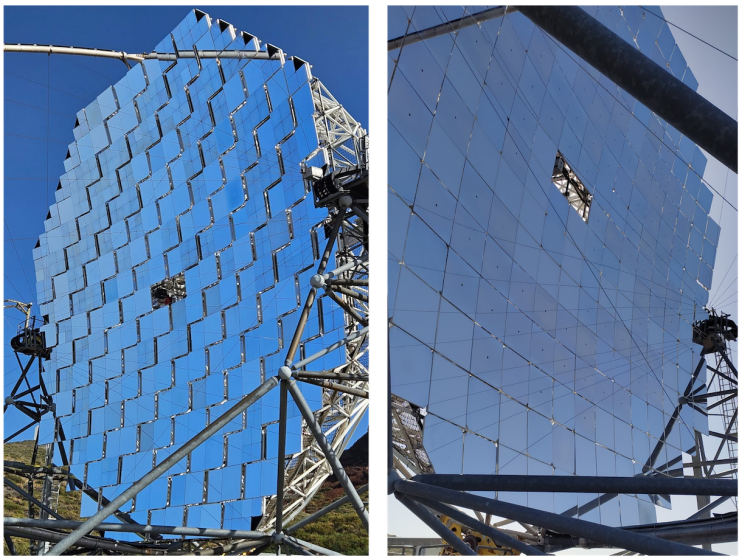

Figure 5.4: M1 (left) and M2 (right), showing differences between the layouts of their mirrors.

Function (PSF) of the reflector. This is done using the SBIG camera, a CCD (Charge-

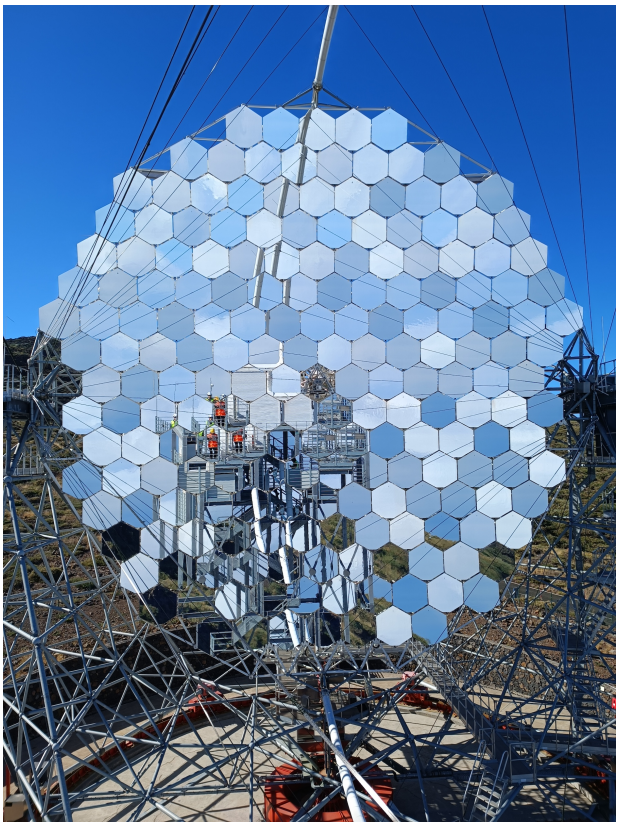

Figure 5.5: Reflector dish of LST-1 made out of hexagonal mirrors.

Coupled Device) camera that measures the PSF of each mirror separately and provides the input for calculating the total reflectivity of the reflector at different wavelengths.

As mentioned before, reflector of the LST-1 telescope has diameter of 23 m, composed of 198 individual, hexagonal mirrors, each of 2 m^2 surface area, seen in Figure 5.5. Similarly to mirrors of M2 reflector, mirrors of LST-1 are produced using the cold slum technique and they are made of soda-lime glass sheet in an aluminium honeycomb box, on top of which there is another glass sheet, resulting in a sandwich-like structure [256]. AMC is operating utilising a camera in the central point of the mirror, and 2 motors on the back of each mirror, located in the actuators that are attaching mirrors to the space frame of the telescope.

5.1.3 Camera and readout system

Main cameras of MAGIC telescopes weigh $\sim$ 600 kg, and they are mounted on an aluminium arc in the focal point of the reflector. Cameras are equipped with 1039 Photomultiplier Tube (PMT) pixels of 2.54 cm diameter [255]. PMTs are divided in groups of 7 pixels, in total of 169 clusters. In order to fill the entire plane, light collectors of hexagonal shape are placed on top and coupled to PMTs. The purpose of the light collectors is to

filter the Night Sky Background (NSB) light arriving to a PMT at large angles. The signal produced by the PMTs is amplified. To reduce the dispersion and allow the transmission of the analogue signal to the readouts system located in the facility called the Counting House (CH), the signal is converted to optical. Using fibre cables, the optical signal is travelling $\sim 160\,\mathrm{m}$ to the readout and trigger systems. Once the signal arrives to CH, the receiver boards, based on the Domino Ring Sampler 4 (DRS4) chips, are converting the optical signal back to electrical one, and splitting it into two branches for further processing: analogue readout branch, for storing the digitised signal and the second part, evaluated in the digital trigger branch.

The MAGIC trigger system is divided in several steps. Initially, the signal is being evaluated for the Discrimination Threshold (DT) defined as ~ 4.25 photoelectrons (phe) for the extragalactic sources and somewhat higher, by $\sim 15\%$ for the galactic sources and moon observations due to the NSB contamination. This is the Level 0 Trigger (L0). Once and if the signal passes the L0 trigger, it is further on tested in a camera grid, divided in 19 macrocells containing 37 pixels to detect groups of active pixels, as it can be seen in Figure 5.6. This is so called Level 1 Trigger (L1) trigger, searching for neighbouring pixels passing the AMC trigger within a window of 5 - 9 ns for an individual telescope [255]. Once

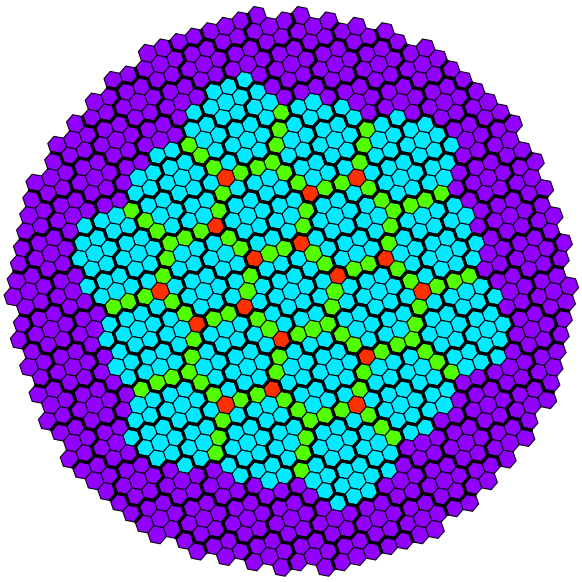

Figure 5.6: Layout of MAGIC cameras containing 1039 channels, divided in clusters. Cyan hexagons represent 19 macrocells. Green and red represent pixels covered by two or three macrocells, respectively. Each of the hexagonal macrocells contains 36 pixels. Reprinted from [255].

"categorised" by each telescope readout system, signal is tested by the conditions set for the stereoscopic Level 3 Trigger (L3). Here the time window is extended to 100 ns width in order to enable correction for the corresponding time delay due to the position of the telescopes. In this way, the signal obtained by the PMTs is assigned to matching events.

If the signal successfully passes the trigger levels, it is stored in the DRS4 and forwarded to the Data AcQuisition system (DAQ). DAQ systems, one for each of the telescopes, are based on the `C++` language, and dedicated to further processing of the signal, reading, online analysis and storing. Furthermore, calibration of the camera is performed, for which there is a developed calibration system. For that purpose, a laser ($\sim$ 355 nm wavelength) is installed in central points of the telescope's dish (one for each of them), and is illuminating the camera with flashes of light of duration similar to the Cherenkov shower, $\sim$ 1 ns, with adjustable intensity up to 1000 phe and frequency of 25 Hz. This procedure enables to define the High Voltage (HV) in the PMTs and ensure the uniform gain for the readout process, useful for calculation of the conversion factor between Flash Analog-to-Digital Countss (FADCs) and number of phe. Lastly, it is used for estimation of the signal time delay in the DRS4 chip to apply the corrections on the readout signal [255].

The LST-1 camera, on the other hand, is significantly larger, with the area of $\sim 9\text{m}^2$, composed of 1855 PMTs divided in 265 modules, each with 7 chambers [256]. Each PMT in the LST-1 camera is equipped with photo-sensors with optical light concentrators and DRS4 chips for the readout of the signal. The analogous signal created in the PMTs is further divided into low and high gains branch. Similarly to the MAGIC telescopes, further passing a certain DT conditions. Given that LST-1 is soon going to leave the standalone operations and be accompanied with three new LSTs, plans are to combine the operations of the cameras and form a synchronised hardware trigger.

5.1.4 Weather monitoring

MAGIC telescopes, as well as the LST-1 telescope are located at high altitude, $\sim$ 2200 m above the sea level, where the weather conditions are subject to fast changes. For that reason, there are several instruments installed at the site, used to measure and determine the state of the atmosphere.

The pyrometer is an instrument mounted on the dish of M1, used for measuring the reflectivity of the base of clouds in the atmosphere and determining the value of the so called "cloudiness" parameter. To calculate the cloudiness, pyrometer is measuring the temperature of the sky in different directions, subject to changes due to the presence of clouds which reflect the thermal radiation from the Earth.

LIght Detection And Ranging (LIDAR) [258] is an instrument measuring the transmission of the atmosphere at different heights using the extinction method. For that purpose, it is using a 532 nm wavelength laser, emitting electromagnetic pulses into the atmosphere, specifically targeting clouds or aerosols within the visible spectrum. Subsequently, it records the distribution of arrival times for the back-scattered photons and estimates the transparency of the atmosphere.

Aside of the two, weather station located on the roof of the CH is measuring the air temperature, humidity, wind speed and orientation. All information is gathered under the supervision of the weather monitoring subsystem, together with some data outsourced from the other telescopes and their auxiliary instruments, i.e Dust Particle Counter by the Telescopio Nazionale Galileo (TNG) telescope, that measures the presence of the dust in

the air, as it is the case during the Calima, strong wind carrying the dust and sand from Sahara. Continuous monitoring of the atmosphere and weather conditions at the site is necessary for maintenance of safety and high-quality of the observations.

LST-1 is, on the other hand, using the weather station located on the LST camera access tower, while other instruments are in development.

5.1.5 Online subsystems

In compliance with its ability to respond to the extraordinary and fast events in the sky by rapid telescope movements, MAGIC is equipped with the GRB monitoring alert system, allowed to overtake the operations with the telescope in case of an alert from the General Coordinates Network (GCN), if the observational criteria are met, of course.

During the standard stereo observations, as well as the exceptional ones, MAGIC On-Line Analysis (MOLA) program is performing real-time fast analysis and providing basic information on the flux and the significance of the signal from the observed source. All data is momentarily processed by the On Site Analysis (OSA) and reduced to the data level easy to transfer to the data cluster. With the given pipeline, data becomes available to analysers during the following day, which is very useful in case of detection of new sources, flaring states, or special events such as GRBs.

5.2 Observation mode and datataking

As previously mentioned, Cherenkov telescopes are limited to the observations during the night, called *dark time* observations, significantly constraining their duty cycles. In the case of MAGIC telescopes, on a yearly basis, this gives $\sim 18\%$ duty cycle, given that there are ~ 1600 night hours in a year. It is noticeable that this percentage is really low, for which reason MAGIC modified PMTs by reducing their gain to accommodate for NSB levels up to 20 times higher than it is the case during the dark time. This modification is enabling the observations during the moon presence. Furthermore, by applying additionally moon filters, limits on the NSB levels extend up to 100 times higher than of those expected during the dark nights. As a result, the duty cycle increases up to $\sim 40\%$. Unfortunately, due to adverse weather conditions like rain, clouds, high humidity, strong wind ($> 50\,\mathrm{km/h}$) or high dust concentration, the duty cycle is additionally decreased.

MAGIC telescopes are conducting two different modes of observations. Initially, all the IACTs have been working in the so called ON-OFF pointing mode. In this approach, observational time, hence the dark time, is divided between observations of two different pointings on the sky; ON stands for the observations of the source directly, with the exact coordinates of the source being in the centre of the camera and tracking its position, while OFF pointing stands for the observation of a patch of sky where the VHE emission is not expected, and following the same zenith-azimuth path as during the corresponding ON pointing run. The OFF observations are however of a great importance for the background

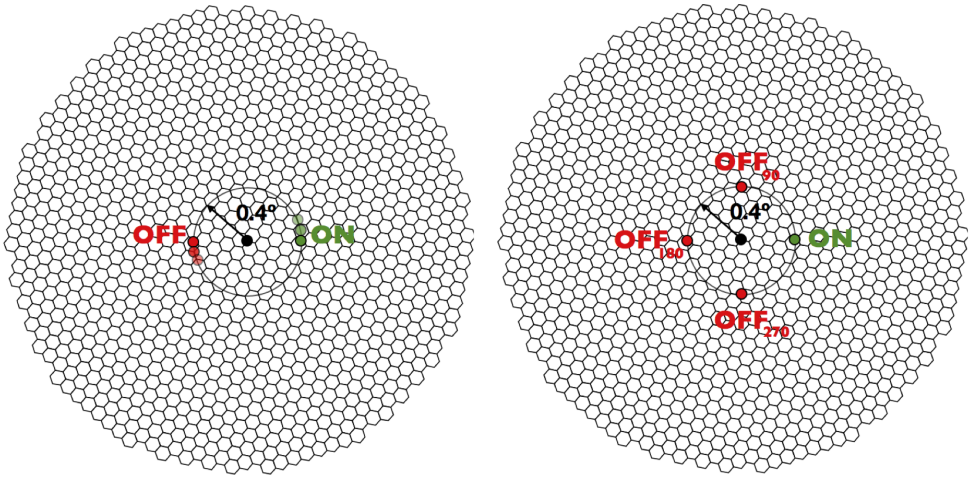

Figure 5.7: The wobble pointing modes with 1 (left) an 3 (right) OFFs. Reprinted from [260].

estimation, used later in the data analysis. Obvious disadvantage of such a method is losing a significant amount of the dark time, for which reason, a new technique was encouraged.

For that reason, in 1994, Fomin et al. [259] introduced a new method used today, called the *wobble* mode. In this mode, the source is not being observed and tracked directly, but through a rather witty configuration of different pointings. To be precise, camera centre is not positioned in such a way that the source is in its centre, but with an offset of 0.4 deg in right ascension (RA) from the nominal position. Pointings are configured symmetrically around the position of the source, starting from the first, called the ON position and then rotated by 90 ° or 180 °, depending on the requirements of the observations, keeping the shift in RA by already mentioned 0.4 °. This is the standard offset but there are more examples that can be used based on the needs of the observations and the morphology of the patch of the sky around the source. Usually four wobble positions are used, labelled as W1, W2, W3 and W4. One of exemplary configurations of a wobble mode observations can be seen in Figure 5.7. Main advantage of this approach is simultaneous observation of the source and estimation of the background, the main flaw of the standard ON-OFF method. Standard observations are operated in the wobble mode, although there are special situations where only ON observations are requested, such as in the case of the observations of dark patches for estimation of the hadronic background or observations of some extended sources.

5.3 IACT data analysis

Once the data is collected, forwarded to DAQ and processed for general use, members of MAGIC collaboration and external scientists with access to data are performing the analysis. Starting from raw data files, containing the information about charge and arrival

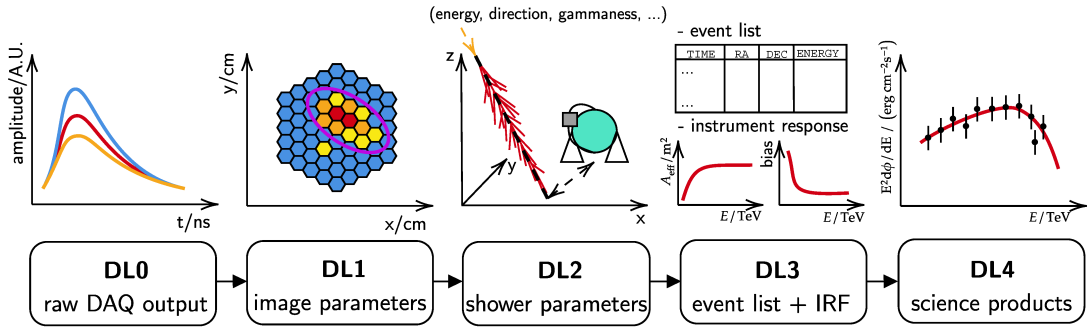

Figure 5.8: Schematic overview of the reduction process of the IACTs data. Reprinted from [265].

time, analysis of the data is performed using the proprietary software, made as a collection of programs and scripts written in `C++` language and based on `ROOT`, named MAGIC Analysis and Reconstruction Software (MARS) [261]. MARS is used for the analysis of data in several steps, each of which is adding a particular component and extracting information about the gamma-ray spectrum of the observed source. Finally, the high level science products, such as the Light Curve (LC) or Spectral Energy Distribution (SED) are reconstructed. Apart from only reproducing the observed spectrum of the source, same can be studied further by applying the unfolding methods and unveiling the intrinsic spectrum by confronting different unfolding methods and mathematical functions. For the analysis of LST-1 data, currently still under development, is the `cta-lstchain` [262], python-based analysis framework, heavily dependent on `ctapipe` [263] developed for the analysis of future CTA data. `cta-lstchain` includes all the tools for processing the LST data from raw level up to files containing list of events and parameters of reconstructed direction, energy and arrival time. Higher level analysis, used for obtaining the binned data products like SEDs, sky maps, or LCs curves, along with associated data (source models, fit results...) is performed with high-level gamma-ray analysis package `gammapy`.

Having in mind that so far we concentrated on two different arrays/telescopes, one of which being the MAGIC array and other the LST-1 telescope, we will try to keep the following section more general. For that purpose, we will introduce different levels of data and steps of reduction, following a scheme for IACT data levels as presented in [264]. Step by step, a comparison with an equivalent level in MARS will be described as well, while in Figure 5.8, an overview of levels and data files content can be seen.

Before proceeding with the data levels, one has to emphasise the importance of the atmospheric showers simulations mentioned in Section 4.3.3.

5.3.1 Monte Carlo simulations

Characterisation and recognition of VHE gamma rays can be problematic due to different background process and similar events that can be misidentified as gamma rays. For that reason, MAGIC and other IACTs use MC technique to produce simulations of

atmospheric showers originated by the incident CR, both charged or neutral, as it is the case with gamma rays. They are produced with COsmic Ray Simulations for KAscade (CORSIKA) [266], program for simulation of the atmospheric showers, their propagation and evolution in the atmosphere, along with subsequent particles decays and interactions. General pipeline of CORSIKA provides simulations including the information about the position of the shower, type of the incident particle, its energy, arrival time and direction. More dedicated version for analysis of MAGIC data also includes particular programs for reconstruction of the response functions of mirrors and entire reduction chain, providing the so called MC files analysed in parallel with the raw data files. Once choosing the particular production of MC files, one needs to pay attention to match the observational and hardware conditions to the ones of the data planned to be analysed, meaning the same zenith distance and pointing mode.

For the analysis of the sources investigated in this work, standard MC simulations of gamma rays were used, dubbed *ringwobble*, as a combination of previously mentioned *wobble* mode accompanied with 0.4 deg pointing offset from the tracked source position.

5.3.2 Data Level 0 - Raw data produced by DAQ

Data of level 0 is the raw data produced during the night of the observation and it is a direct product of DAQ. For the case of MAGIC analysis, performed with MARS software, program `merpp` (MERging and Preprocessing Program) does this step of processing. In particular, it converts the files into `ROOT` format and merges the data files with reports from the MAGIC subsystems. These files contain ~ 1 TB of data per MAGIC telescope, including the charge from the DRS4 capacitors for all the pixels in camera, and cover all events triggered by L3, including interleaved pedestal and calibrated events. LST-1 data is currently being saved only in the raw format, called R0, which consists mainly of digitised waveforms for every pixel, sampled at ~ 1 GHz. To enhance the telescope's dynamic range, each pixel signal is divided in two gains, representing high and low signal amplification. This setup effectively records two separate "events", each lasting approximately 40 ns, corresponding to telescope's observations, e. g. Cherenkov light emitted from extensive air showers.

As of now, LST-1 directly preserves the R0 data without implementing any data volume reduction methods that might result in information loss, such as discarding one gain setting or pixels that do not show an apparent signal. Goal in the future is to make level 0 data the first data level permanently stored.

5.3.3 Data level 1 - Image calibration and cleaning

Once the raw data is ready in `ROOT` format, calibration is performed. In MAGIC analysis pipeline, program `sorcerer` does this step and computes the integrated charge and arrival time. To estimate the baseline of the signal, several pedestal events are binned in a same way and fitted with a Gaussian function in order to obtain the baseline value. Once the pedestal is subtracted, *sliding window* algorithm is used to estimate the signal.

While charge is taken to be the maximum value between sums of charges in groups of 5 subsequent time slices, the arrival time is taken as an average over all 50 slices weighted with the sampled charge. Calibration of the signal is done using the previously mentioned conversion factor between the FADCs and number of photoelectrons. Image of a shower after the calibration is shown in Figure 5.9. Once the signal is extracted and calibrated, it

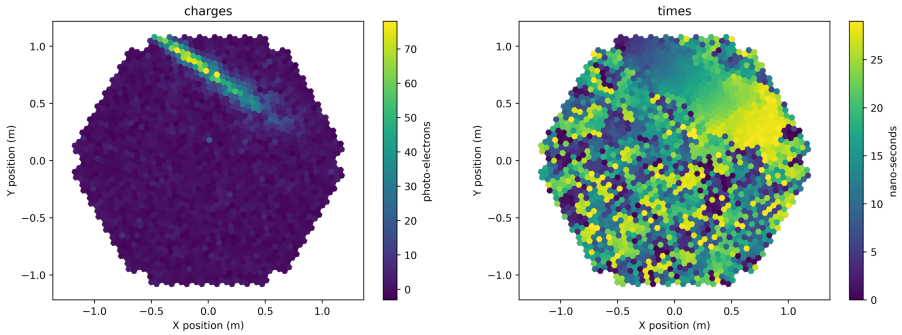

Figure 5.9: Calibrated signal with extracted charge and arival times. [267].

is important to reduce the number of pixels used for the further processing by excluding pixels that contain NSB photons. Further on, pixels are tested by searching for groups of 2, 3 or 4 neighbouring pixels whose total charge count exceeds a certain threshold, both charge and arrival time based. Pixels grouped in "islands" and passing the so called sum cleaning are onward tested with the charge threshold individually. Pixel whose charge

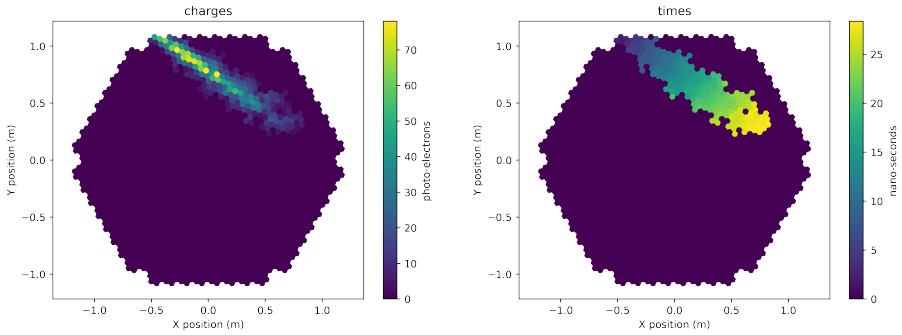

Figure 5.10: Cleaned image of an air shower [267].

surpasses the *core* threshold and at the same time is neighbouring another pixel of such kind, is determined to be part of the *core*. Furthermore, all pixels whose arrival time is not within the fixed time constraint of 4.5 ns with respect to mean arrival time of the *core* pixels are being rejected. Surrounding pixels are being tested by a weaker threshold on the charge value and time arrival error of 1.5 ns in respect to the arrival time of their neighbouring *core* pixel/s. In MARS framework, calibration and cleaning is performed by the program `star` (STandard Analysis and image Reconstruction).

Once the charge is calibrated and signal is cleaned, image of the shower assimilates to the one shown in Figure 5.10. Main set of parameters used to describe the shower image are

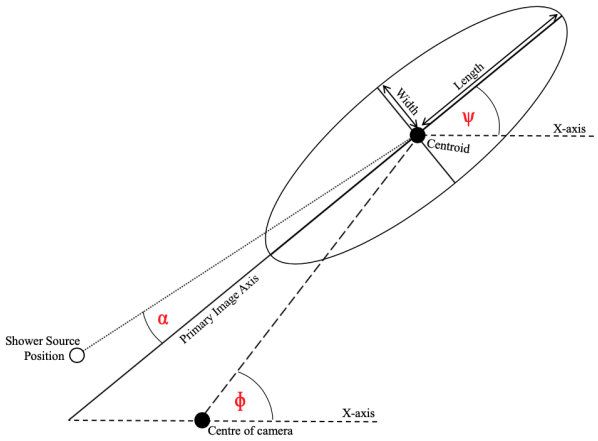

Figure 5.11: Shower image parameterised with an ellipse and corresponding Hillas parameters. Image credit: Jason Watson.

size, *width* and *Center of Gravity (CoG)*, introduced by Hillas [239]. *Size* is given by the total number of photoelectrons in the image. For the obtained ellipse, the *length* and *width* are indicators of the root mean square (RMS) distribution of the light in directions parallel and perpendicular to the major axis of the island, respectively. The centroid represents the *CoG* of the image, determined by the signal detected by the respective pixels. Ψ is the rotation angle of the ellipse with the X-axis, while Φ is the polar coordinate of the centroid, as it can be seen in Figure 5.11. Along with α which denotes the orientation of the main axis, *distance* of the centroid from the source position represents source-dependent parameters. Aside of them, there are several other types of parameters, related to time, image quality or direction, used to discriminate between the head and tail of the shower. In particular, one must note that the ellipse is not necessarily symmetrical, in which case the centroid is not positioned in the pixel with the peak of the signal. In that case, additional parameters for quantifying the asymmetry have to be included. In Figure 5.12 one can see a resulting image of the shower obtained after calibration, cleaning and Hillas parameterisation.

5.3.4 Data level 2 - Estimation of energy and direction and γ/hadron separation

Parameterised images of showers at this stage need to be joined for the stereoscopic reconstruction. This is applicable for the case of MAGIC telescopes, while LST-1 is still operating as a single telescope and this step is simplified. Computation of the stereoscopic parameters and joining the independent `star` files from both MAGIC telescopes is performed using the `superstar` program. By building a three-dimensional image of the shower, estimating the direction of its axis, and the height at which its development was

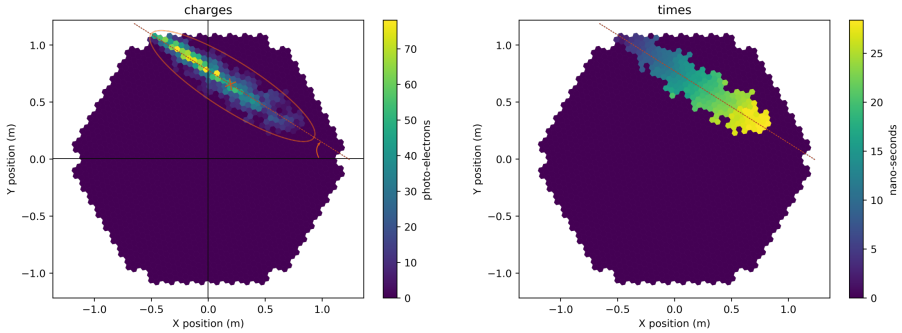

Figure 5.12: Reconstructed image shower with Hillas ellipse and parameters in red. [267].

initiated h_{max}, impact parameters $M1$ and $M2$ for both of the telescopes, and quantifying the distance on the ground where the shower falls in respect to the telescope position, Cherenkov radius of the shower, r_{Cher} can be reconstructed. These parameters are particularly important for the energy reconstruction.

In case of standard MAGIC data analysis, `superstar` files can be a starting point, for that reason, there is an executable, named `quate`, using which the data quality selection can be performed, testing the quality of the data and selecting the desired subset satisfying certain requirements of the analysis. So called "cuts" with `quate` can be performed on parameters like the zenith or azimuth angle of the telescope during the observations, direct current of the telescope or simply by setting a threshold on weather conditions or clouds transmission on a desired height, going from 3 to 12 km. `Quate` can perform checks on `star`, `superstar` (data level 2), or even higher level data that will be introduced next (data level 3).

However, parameterisation of recorded and cleaned images is not enough. For the same reason as mentioned in Section 4.3.5, since most of showers generated in the atmosphere and detected by the telescopes are of hadronic origin, classification of showers needs to be performed. Aside of hadrons, other charged particles can create similar showers, in particular leptons as electrons and muons, or even accidental triggers caused by the NSB.

Identification of γ-ray induced showers is performed using sets of parameters that can distinguish them from showers of different origin. For the separation between events of γ and hadron origin, estimation of their energy and reconstruction of their direction, there is an algorithm called Random Forest (RF).

On average, 75% of recorded events during the observations are coming from hadron events surviving the cleaning, rather than gamma rays emitted by the observed source. For that reason, this step is of a high importance for the analysis. As mentioned above, procedure of dividing the sample of events into the gamma rays and on the other side hadronic ones can be described in a natural way, like growing a tree and its branches. To train an RF, two samples of data are needed. One containing the events of gamma-rays and the other with events of hadronic nature. For gamma-ray events, MC simulations are used, while hadron part of the sample is taken from the data of observations with no gamma-ray

signal present. For the latter, patches of sky with no gamma-ray sources or simply with no gamma-ray signal can be used. In MARS terminology, this sample is called *OFF data*. Important to mention is that the *OFF data*, as well as the MC simulations have to be taken/simulated with the similar characteristics as the data to be analysed, meaning the same zenith pointing distribution and even the weather and hardware conditions (meaning the same analysis period), latter of which is being applied while choosing the *OFF data* sample. Process of the "training" is based on the minimisation of the Gini index, defined based on the number of gamma N_γ and hadron N_h events:

$$G \simeq \frac{N_\gamma N_h}{{N_\gamma + N_h}^2} \tag{5.1}$$

Given that the `star` and `superstar` files contain calculated Hillas parameters, their values are used for determination of the cuts minimising the Gini index. Smaller Gini index indicates better separation. Gini index equal to 1 indicates a sample with equal number of events of each class, while 0 index is marking a branch with events of only one class. Starting from only one sample, each cut is dividing it in two branches, until one branch is left with minimum number of events that is set in advance, but most usually equals to 3. This process is repeated for a large number of the so called "trees" (~ 100) and forming the RF. The last units of RF, called *leaves*, contain the final parameter describing the nature of the particle, *hadronness*.

In MARS, RF training is performed using the executable named `coach`. In `cta-lstchain` pipeline, parameter for γ/hadron separation is called *gammaness*. As the name suggests, is provides the information opposite from hadronness, estimating how much one event "resembles" to a gamma-ray event.

After the so called training, RF is ready to be applied to the dataset of the interest, the *test* sample. MARS program used in this step is called `melibea`. Processing of the data with this program is providing the `melibea` files of the data and the corresponding MC simulations. In `lstchain`, DL2 files of MC simulations processed with RF provide Instrument Response Functions (IRFs), while in MARS this step is performed later, simultaneously with computing the high level products like spectrum or LC. Similarly as in the training procedure, events in the test sample are being divided in groups and each of them are assigned a value of the *hadronness* parameter. Along with the γ/hadron separation, energy estimation and arrival direction are also determined using different methods within the RF algorithm.

Energy estimation of the MAGIC data is performed using two different methods. Both methods are implemented into the MARS pipeline and both can be used in the `coach` executable. In this case, methods do not significantly differ, having in mind that the second is introduced with the goal of improving the estimation of the energy for the events with true energy above tens of TeVs. This method is called *stereoRF* and it is most often used in cases when additional checks and comparisons with results of the first method want to be performed. Standard method used are the Look Up Tabless (LUTs). In this method, two-dimensional tables are built giving the grid of two Hillas parameters for each event. Parameters in question are the *size* parameter, epitomising the number of

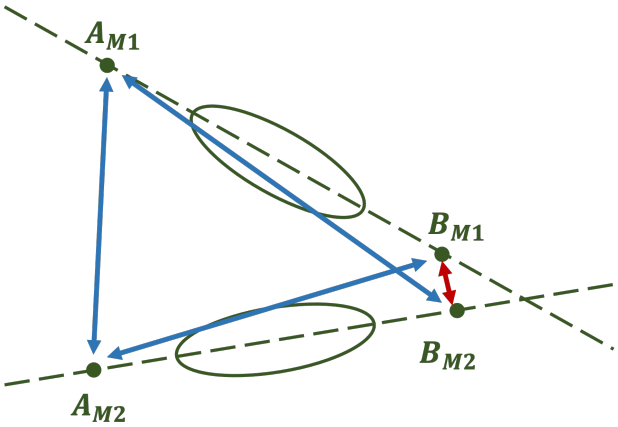

Figure 5.13: Scheme of the DISP method for estimation of the arrival direction. Four different coordinates are identified, two for each of the shower images on distance equal to impact parameters for two respective telescopes. Double-arrowed lines are representing possible distances, out of which the red, shortest one, is selected as the correct one.

Cherenkov photons produced by gamma rays, and ratio of the impact parameter (M_1, M_2) and r_{Cher}. Aside of determining these two parameters, additional corrections are applied to take into account parameters such as zenith angle and geomagnetic field, also affecting the amount of detected light. Finally, average energy of each table is weighed and the final estimated energy E_{est} is given.

Lastly, the **arrival direction** of the gamma-ray is computed. In case of mono observations, the Distance between the Image centroid and the Source Position (DISP) method is used for estimating the Hillas parameters such as the aforementioned *impact* parameters and the maximum height of the shower, and yields the position of the incident gamma ray, laying on the main axis and distance DISP from the centroid of the reconstructed ellipse. Analysing data of a stereoscopic array such as MAGIC requires an adjusted version of the method, the DISP-RF. As the name suggests, method is used within the RF training, hence implemented in `coach`. In summary, it computes DISP parameters for both of the telescopes and calculates four possible arrival directions of the gamma ray, as it can be seen in Figure 5.13. Furthermore, the final distance chosen is the minimal distance between the four respective points given by the four possible arrival directions. For achieving greater power for rejection of hadronic showers images, the event is being rejected in case the angular distance $B_{M1} - M_{M2}$ is greater than 0.22 °. Finally, the reconstructed direction is obtained as the average of the pair of selected points weighted with the number of pixels in each image.

5.3.5 Data level 3

At this stage, analysis pipelines of MAGIC and LST-1 start to diverge. For the case of MAGIC, high level products can be produced directly using the `melibea` files of the

data sample and MC simulations, while in the `lstchain` pipeline, the remaining step of processing simulated MC DL2 level data and providing IRFs, needs to be performed.

For that reason, we will first explain the process concerning the LST-1 data, describing the content of data level 3 (DL3) files, later used in `gammapy` to obtain the high level results. They will be mentioned in the following section, in comparison with the final part of the MARS pipeline.

As mentioned before, DL3 files, originating both from the data and simulations, contain the information about the surviving gamma events: estimated values of their *hadronness/gammaness*, energy and position. Second component of the DL3 files are the IRFs. Used as an inclusion of realistic conditions of the instrument, IRFs are used for embodying the response of the instrument and reconstruction of the estimated values of the parameters stored in DL3 files into their "true" values.

Three main ingredients of IRFs are:

- **Effective area**, defined as the correction of the telescopes' collection area with an energy dependent efficiency, subject to requirements of the analysis:

$$A_{eff}(E, \vec{P}) = \frac{N_{MC,final}(E, \vec{P})}{N_{MC,sim}(E, \vec{P})} \times A_{MC,total}, \tag{5.2}$$

  where $N_{MC,final}(E, \vec{P})$ and $N_{MC,sim}(E, \vec{P})$ are numbers of survived and total simulated events, respectively, and $A_{MC,total}$ is the area on which MC events are simulated.

- **PSF**, dependent on the energy E of the event, as well as the estimated direction $\hat{P}$ and true direction $\vec{P}$ of the events, obtained with the DISP method. PSF is defined as the spatial distribution function of the estimated coordinates of the photons coming from a source otherwise detected as point-like.

- **Energy dispersion**, being the probability distribution function of the estimated energy stored in LUTs, computed with `coach`.

In the `lstchain`, two types of IRFs are produced. *Full enclosure* IRFs, appropriate for analysis of any source within the FoV, given that they take into account the dependence of the direction parameter on the coordinate system of the camera. *Point-like* IRFs, on the other hand, are applicable to data taken with a fixed offset from the camera centre, as it is the case with MAGIC data. *Point-like* IRFs are produced by fixing the offset value applied on simulated events, resulting in a ring around the camera centre. For that reason, only sources laying in one of the points on the ring can be analysed with the IRFs in question. For simplicity, acceptance α can be assumed as uniform within the given offset value, leading to an effective area and energy dispersion independent on the event direction.

With the goal of estimating the performance of the LST-1 telescope, variations in IRFs as functions of the true energy were compared for different values of the efficiency of *gammaness* cuts and zenith distance, concluding with the overall superiority of the IACTs arrays over the standalone telescopes and anticipating the construction and observations

with the upcoming CTA [268]. This conclusion comes from the evaluation of the sensitivity on lower energies ($\sim$ GeV), where arrays dominate due to the stereoscopic reconstruction of the shower images and background rejection.

5.3.6 Data level 4 - High level products

This stage represents the very end of the analysis pipeline, both in MARS and `lstchain`. For the case of MARS, this stage incorporates few programs and executables for computing the number of signal counts and significance plots (`odie`), sky-maps (`caspar`), and other high level products, such as SED, LC, etc. LST-1 analysis is from this point performed with `gammapy`, where DL3 files, together with tables containing the information about the data, hardware and observations conditions can be imported and scientific results can be obtained.

Evaluation of the gamma-ray signal is done through calculation of the significance of the signal, expressed in number of standard deviations, computed with the likelihood ratio test under the hypothesis that the signal is not present. In order to compute the significance, several ingredients are needed. For the reasons connected to the background rejection and usage of the *wobble* pointing mode explained in Section 5.2, observations are performed pointing to regions around the source, most often defined by the angular distance of 0.4 deg from the centre of the source. They are playing a crucial role in determination of the background OFF counts used in the analysis. In particular, parameter α is defined as the ratio of the OFF and ON exposures, called acceptance α. ON region is the region enclosing the observed source, and it counts the total number of detected events. In order to estimate the number of excess events N_{exc}, assumed to come directly from the source, one can calculate:

$$N_{exc} = N_{ON} - \alpha\, N_{OFF}, \tag{5.3}$$

where N_{ON} is the number of *ON* events and N_{OFF} is the number of OFF events. In MARS, executable `odie` is performing the signal extraction, computing the histograms of the events coming from the respective sky regions described and the *excess* events as functions of their squared angular distance θ^2 from the centre of the respective ON/OFF region, as it can be seen in Figure 5.14. Distribution of the events in the histogram can easily be distinguished; excess events are localised mostly around the minimal values of θ^2, peaking around 0, while background events are uniformly distributed in all regions observed. The significance of the signal can then be computed using all the ingredients in the Li and Ma [269] equation:

$$\mathcal{S} = \sqrt{2\left[N_{\text{on}} \ln\left(\frac{(\alpha+1)N_{\text{on}}}{\alpha(N_{\text{on}}+N_{\text{off}})}\right) + N_{\text{off}} \ln\left(\frac{(\alpha+1)N_{\text{off}}}{N_{\text{on}}+N_{\text{off}}}\right)\right]}, \tag{5.4}$$

where N_{on} and N_{off} are N_{ON} and N_{OFF} events from Equation 5.3 selected for $\theta^2 < \theta^2_{max}$ (in this case 0.02°), respectively. In this case, considering the Gaussian distribution, values of $\sigma > 5$ are considered inconsistent with the background and indicating a detection.

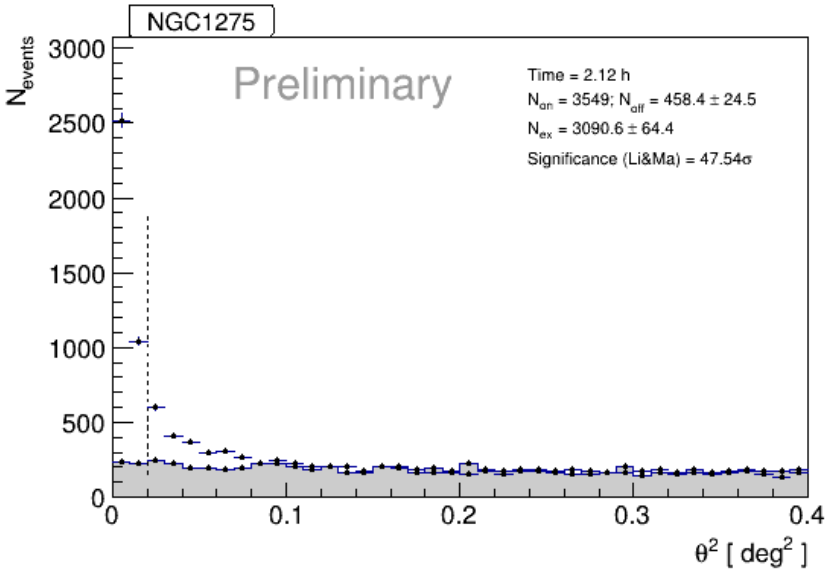

Figure 5.14: An example of a θ^2 plot, in this case representing the flaring state of the AGN in the centre of Perseus cluster, detected on 1st of January 2017. θ^2 plot is showing a histogram of events coming from the centre of ON region, accumulated around the centre, meaning small values of θ angle, and events coming from centre of OFF regions (area under which is shaded in grey) scaled with acceptance α, resulting in a flat distribution over all values of θ^2 angle.

Additional checks on the sky regions observed and the events detected can be provided by sky-maps. In MARS, executable `caspar` creates skymaps of both the ON and OFF regions and computes the significance of the signal through a modified version of the Li and Ma [269] significance, accounting for the background and the IRFs of the telescope, namely the PSF. An example of a sky-map produced with `caspar` is shown in Figure 5.15.

Most of the data analysed under the scope of this thesis was processed with the MARS pipeline, and cross-checked with the `gammapy`, hence there is a direct comparison between the high level results produced with both. Extraction of the spectrum is similar in both cases. The calculation of the spectral flux $\frac{d\phi}{dE}$ $(E, \mathbf{\Lambda})$ dependent also on the parameters of the assumed spectral model $\mathbf{\Lambda}$, requires several ingredients:

- **Number of detected gamma rays**, as well as the counts coming from other observed sky regions, namely ON and OFF regions. This information is provided by the previous executable, `odie` and weighted based on the cuts on the θ^2, *hadronness*, and *size* parameters, depending on the energy range considered and the efficiency, optimised for each energy bin.

- **Effective time** t_{eff}, different from the total observational time, considering the realistic dead time, during which the detector is not able to process any other incoming event. For MAGIC telescopes, dead time has changed in the past, and the most recent value (since the latest major hardware update in 2012) is set to 26 μs.

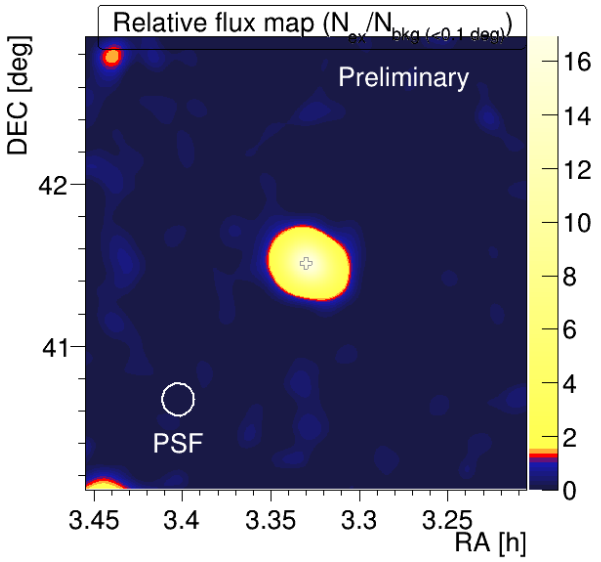

Figure 5.15: Relative flux map of the NGC 1275 flaring state on January 1st 2017. Color code represents the excess events relative to the background density.

- **Effective collection area**, which in the case of LST-1 data is one of the computed IRFs in the step right before the DL3 production. In the case of MAGIC, it is directly computed with the `flute` executable, and incorporated extraction of spectral points. While computing the effective collection area, dependencies on the energy of the incident gamma ray, coming from the dependence on the zenith and azimuth angles are taken into account. The effective collection area is computed from MC simulations of gamma rays, and it inherits the dependence on the tentative spectrum and energy binning. Hence the A_{ff} from Equation 5.2 is weighted with the spectrum of the observed source:

$$\langle A_{eff} \rangle_{E_1<E<E_2} = \frac{\int_{E_1}^{E_2} \frac{d\Phi}{dE} A_{eff}(E)\, dE}{\int_{E_1}^{E_2} \frac{d\Phi}{dE}\, dE} \tag{5.5}$$

  Since binning of the real data includes the entire range of zenith angles, A_{eff} needs to be integrated over the zenith range Z_d of data sample:

$$\langle A_{eff} \rangle_{Z_{d1}<Z_d<Z_{d2}} = \int_{E_1}^{E_2} A_{eff}(Z_d)\, f(Z_d)\, d(Z_d), \tag{5.6}$$

  where $f(Z_d)$ is the fraction of the observation time spent at Z_d. Finally, dependence on the azimuth angle, coming from the impact of the geomagnetic field on the particles of the shower and the change in the effective distance between the telescopes, is accounted by averaging with the azimuth angle.

In `flute`, spectrum is evaluated using the maximum likelihood method, binned in estimated energy. The likelihood is by definition given as the probability of observing the data $\boldsymbol{D}$

(in this case ON and OFF counts), while assuming the spectral model parameters $\mathbf{\Lambda}$ to be true:

$$\mathcal{L}(\mathbf{\Lambda}|\boldsymbol{D}) = \prod_{i=1}\prod_{k=1} \mathcal{P}\left(N_{\text{on}}^{i,k} \mid s_{i,k}(\mathbf{\Lambda} + \alpha\, b_{i,k}\right) \times \mathcal{P}\left(N_{\text{off}}^{i,k} \mid b_{i,k}\right). \tag{5.7}$$

Indexes i and k are denoting observations, divided in runs or samples, as we will see in Section 7.4, and bins in estimated energy E'. $\mathcal{P}$ is the Poisson probability mass function for observing n counts with expected count rate r: $\mathcal{P}(n|r) = r^n e^{-r}/n!$, while $s_{i,k}$ is the expected signal counts in the energy bin ΔE_k in the ON region for the i–th run/sample:

$$s_{i,k} = \int_{\Delta E_k} dE\ \Phi_{obs}^{i}(E; \mathbf{\Lambda}), \tag{5.8}$$

and $b_{i,k}$ being the expected background counts in the OFF region. In Equation 5.8 we have introduced the observed flux for the i–th sample

$$\Phi_{obs}^{i} = T_{eff,i} \int_{\Delta E'_k} dE'_k \int_0^\infty \frac{d\Phi}{dE}(E; \mathbf{\Lambda})\ A_{eff,i}(E)\ f_{E,i}(E'|E) \tag{5.9}$$

Including all the ingredients, *differential energy spectrum*, quantitatively describing the flux per interval in gamma-ray energy, given in units of $\text{cm}^{-2}\,\text{s}^{-1}\,\text{TeV}^{-1}$ is defined as:

$$\frac{d\Phi}{dE} = \frac{dN_\gamma(E)}{dE\ dA_{eff}(E)\ dt}. \tag{5.10}$$

Important to mention is that the energy spectrum obtained in this step is evaluated in estimated energy, which doesn't necessarily match the true one. If this is the case, possible *spillover* can occur, making the reconstructed events binned in an incorrect way. A solution for this issue is offered by the *unfolding* procedure. Information about the most likely fraction of events moving from bin of estimated energy E' to bin of true energy E due to the finite energy resolution of the experiment is stored in the migration matrix. Goal of the unfolding procedure is to obtain the true distribution of events in energy bins, for which the inversion of the migration matrix is needed. However, the migration matrix is not necessarily squared and the simple inversion is not possible, and "reshuffling" of the events from estimated energy bins to true energy bins with the unfolding is needed. In MARS pipeline, there are two different unfolding procedures available. First is performed by re-scaling the $\langle A_{eff}\rangle$ by assuming the spectral shape of the source spectrum. Using the spectral shape, source redshift, effective observational time and the matrix giving A_{eff} vs. true energy for each of the E' bins, one can perform *forward-folding* using the executable `fold`. `Fold` is calculating the Poissonian likelihood of the spectrum, maximising the likelihood given the excess values in each E' bin, while leaving the background counts as nuisance parameters. In that way, background in each E' bin is independently obtained to maximise the likelihood. Aside of obtaining spectral parameters and their uncertainties, `fold` also calculates spectral points using the re-calculated A_{eff}, now taking into account possible *spillover* of events calculated using the "best fit" model. These points are statistically independent, but their flux values are connected by the assumption of the global fit

function. A second program for performing the *forward-folding* in MARS is the `ROOT` macro called `combunfold`. Aside from forward-folding, `combunfold` can also be used for proper unfolding with the regularisation methods setting the requirements on the smoothness of the unfolding solution. Regularisation is used to reduce the large errors of the unfolding solution (matrix representing the distribution of the events in true energy bins), reflected in its covariance matrix [270]. Valuable to mention is that in the case of LST-1, whose high-level data is analysed with `gammapy`, standard unfolding methods are not yet implemented. This will be of special importance in Section 7.4, where high-level products of the MARS analysis and `gammapy` will be confronted and evaluated. Once unfolded, *differential energy spectrum* of the source is given in true energy E and from it, the evaluation of the LC can be computed by integrating over the range of selected energies:

$$\Phi(E > E_{thr}) = \int_{E_{thr}}^{\infty} \frac{d\Phi}{dE} dE, \tag{5.11}$$

that can be numerically estimated from the observations:

$$\Phi(E > E_{thr}) \approx \frac{N_{excess}(E' > E_{thr})}{t_{eff}\ A_{eff}(E > E_{thr})}. \tag{5.12}$$

5.4 Systematic uncertainties

Aside of the statistical uncertainties, evaluated through analysis, observations of IACTs suffer from systematics, emerging from many fairly unknown effects, such as limited precision, day/night changes, NSB, atmosphere, reflectivity of mirrors, as well as the conversion of the signal and in general during the data reduction. In conclusion, estimated uncertainty on the energy scale is $\lesssim 15\%$, 11 – 18% on the flux normalisation and $\pm$ 0.15 on the spectral slope of the observed source spectrum. More recently, LST-1 performance was evaluated in [268]. Reported uncertainties strongly depend on the energy and cuts on the data applied in the analysis, resulting in angular resolution ranging from 0.12 – 0.40 °, and energy resolution from 15 – 50 %. As a novelty, and outcome of successfully collaboration of two neighbouring observatories, MAGIC and LST collaborations published a combined study on the observations of Crab Nebula, and as it is mentioned in Section 4.3.5, due to the increase in the collection area and stronger background rejection, up to 20% more events are reconstructed. Those events would otherwise be rejected in the stereoscopic reconstruction including images of MAGIC telescopes only. Moreover, energy threshold has been lowered by 15 % with respect to the energy threshold in MAGIC-only observations. Overall sensitivity has been improved by 30 % (40 %) in case of the detection of flux in the energy range between 200 GeV and 3 TeV [254] for independent MAGIC (LST-1) observations. In case of other systematics, such as angular and energy resolution, improvements are minor in comparison to performance of MAGIC telescopes alone. In the following sections, we will discuss analysis results of the main study of this thesis, including the comparison of MARS and `lstchain` high-level products of the observations of

NGC 1275 located in the Perseus GC. Given that our main interest is setting constraints on ALPs parameter space, we will first discuss the modelling of magnetic fields present on the propagation path of gamma rays travelling towards the Earth. Correct and precise modelling of magnetic fields is crucial for calculation of photon survival probability, the main ingredient for ALP models. For this reason, we will dedicate time to evaluate state of the art models and their impact on final results.

Chapter 6

Modelling of astrophysical magnetic fields for the photon/ALP beam propagation

Contents

The importance of magnetic fields in studies of ALPs has been argued in previous sections; however, we can summarise it in a few points:

- Photon-ALP mixing is strongly dependent on the presence of an external magnetic field, given that the transverse component of the magnetic field enables mixing between the photon with spin one and spin-zero axion [73]. For that reason, magnetic fields have to be carefully modelled for the calculation of the photon conversion (survival) probability.
- Astrophysical sources are located in fairly unknown magnetic fields. These fields are observed but rather difficult to measure precisely, both in strength and morphology.
- VHE gamma rays are crossing astronomical distances prior to detection. Along the way, they are encountering several magnetic fields, each with particular strength and morphology.

In the following sections we will discuss the magnetic fields that the gamma ray encounters, starting from the source, and briefly outline currently available models. After that, we will discuss the importance and their implementation in ALPs studies considering different astrophysical targets.

6.1 Magnetic field of the AGN relativistic jet

AGNs are the most explored targets regarding the ALPs searches with VHE gamma rays [150, 151, 157, 159, 178–181, 183, 195, 196]. They represent the majority of VHE gamma-ray emitters, located in centres of galaxies, accreting surrounding matter, and emitting radiation. Although they are usually assimilated with the presence of relativistic jets, only ~ 10 % of AGNs host them, observed as outflows of relativistic particles extending into the surrounding environment up to Mpc scales.

Studies so far have not revealed the exact details of the acceleration and creation of the jet, with the most popular theories being recollimation shocks and magnetic reconnection [271–273]. In addition to the origin of relativistic jets, there is a debate on the overall model of AGNs. Morphologically, they have been divided in two groups: Fanaroff-Riley type-I (FR-I) and Fanaroff-Riley type-II (FR-II). The difference is in the presence of large lobes in the former ones, created by strong and focused jets, and latter, whose jets manifest as rather unstable. Furthermore, 10% of total population of jetted AGNs are pointing towards us, collectively called blazars [274].

Observations so far are suggesting bimodal distribution of these sources into BL Lacs and Flat Spectrum Radio Quasars FSRQs. In comparison, FSRQs are recognisable by strong emission lines and a spectrum dominated by the radiation from the torus of gas and dust, unlike weak emission lines observed in case of BL Lacs.

Due to their strong flaring activities and being sources of VHE photons, AGNs are excellent candidates for ALPs studies. The debate on the importance of modelling the magnetic field of the relativistic jet is ongoing [186, 193, 195, 243, 275]. The mere presence of the jet is not a sufficient argument to include its effects in the calculation of photon survival probability. In particular, the inclusion of additional parameters, describing the magnetic field of the jet, could introduce additional uncertainties on the final results. An argument for neglecting the jet is that gamma rays spend a small fraction of their total path passing through it, justifying its exclusion from calculations of photon survival probability. However, in the case of blazars, where detected particles cross almost the entire length of the jet, its inclusion can be crucial. Nevertheless, most of studies done so far, have: a) neglected the magnetic field of the relativistic jet, e. g. [179], b) used a simple random domain-like structure, e. g. [150] or, c) used a completely transverse field model, e. g. [186].

Random domain-like structure models rely on the assumptions of many magnetic field cells, with an overall averaged photon survival probability akin to the one discussed in Section 2.2. On the other hand, transverse field models, as in [186], utilise only the toroidal part of the magnetic field, transverse to the jet axis and relevant for the photon-ALP conversion [186]:

$$B_{T,jet} = B_{T,VHE}\left(\frac{y_{VHE}}{y}\right), \tag{6.1}$$

where $B_{T,jet}$ and $B_{T,VHE}$ are the strength of the magnetic field in the jet and the VHE gamma-ray emission region within the jet, respectively, while y and y_{VHE} are the corresponding distances from the central black hole.

Regarding this topic, a study was done by Potter and Cotter [194], fitting a sample of 38 blazars detected by Fermi-LAT, and proposing an alternative approach. The magnetic field of the blazar's jet is modelled in two parts: a parabolic base and a conical jet. The scheme of the model can be seen in Figure 6.1. The model in question uses the observations of

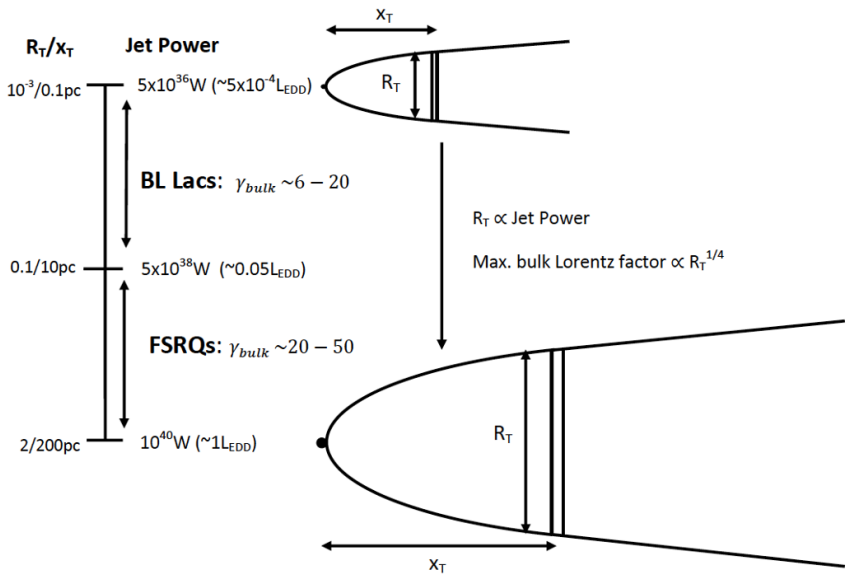

Figure 6.1: Schematic representation of the relativistic jet model by Potter and Cotter [194] and main conclusions of the fitting procedure done for a sample of 38 blazars detected by Fermi-LAT.

M87 AGN to determine the distance at which the parabolic base transitions into a conical-shaped jet. The jet is modelled as a 1D time-independent relativistic fluid flow, starting as an accelerating and magnetically dominated parabolic base, and transitioning to a conical jet, slowly decelerating as it distances from the transition region at distance r_t defined by $r_t = 10^5\ r_s$, where r_s is the Schwarzschild radius of the black hole. This particular model is based on observations, but is in agreement with general relativistic magnetohydrodynamic simulations [276]. It is a leptonic model, depending on 12 parameters, fewer than most of state-of-the-art models of relativistic jets [194], while accounting for the emission down the entire jet. In addition to the magnetic and particle component, it also includes adiabatic losses, as well as those from synchrotron and inverse Compton processes. The main source of the jet power is the conversion of radial kinetic energy into internal non-thermal particle energy through recollimation shocks. Varying the test source, in this case, blazars, different emission regions are modelled, referring to the accretion disk, broad and narrow line region, as well as starlight and CMB. Results of this study, providing the parameters of jets of various blazars will be used later in `GammaALPs`, as input for the model of the magnetic field of the relativistic jet in calculations of photon survival probability.

This model was also used by Davies et al. [193] who showed the importance of including the jet magnetic field model in ALPs searches, particularly in studies of blazars located

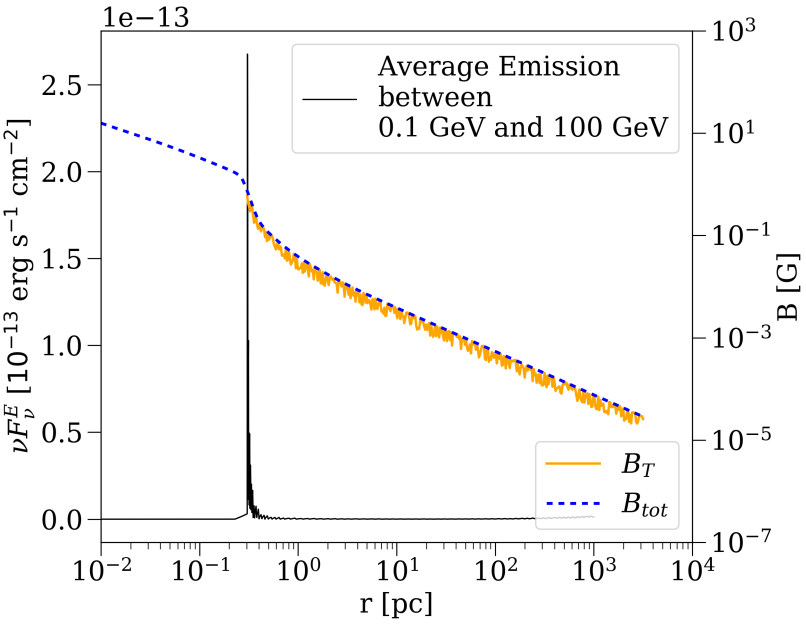

Figure 6.2: Strength profile of the jet magnetic field as dependent on the distance from the centre of the source. Figure shows total magnetic field strength (dashed blue line) and transverse field strength calculated starting from the distance of the emission region from the centre (orange line). Flux axis is taken from the PC model of Potter and Cotter [194] is also shown on the y-axis. Figure is reprinted from [193].

in fairly poor GCs, as magnetic field of their jets can out-power the one of the GC and significantly impact the photon-ALP mixing. In particular, it is composed of a tangled and helical component, turning from poloidal to helical as it propagates down the jet [193]. Figure 6.2 shows the dependence of the strength of the jet magnetic field in dependence on the distance from the centre of the source.

For that reason, this model will be mentioned and described in light of photon survival probability calculations in the results of the preliminary study done on data of blazars observed by LST-1 that will be discussed in Chapter 8.

6.2 Magnetic field of the GC - Intracluster magnetic field (ICMF)

Despite being briefly discussed in Section 3.5.3, where results from ALPs studies with VHE gamma-ray data where presented, and the importance of magnetic fields of GCs was emphasised, it is worthwhile to discuss their origin and nature in more detail. Observations of radio synchrotron and inverse Compton emission and Faraday rotation measurements Rotation Measure (RM) of polarised radio sources within and behind the GCs have es-

tablished the well-accepted existence of ICMFs [277]. The overall strength of ICMFs can be derived from analytical evaluation of the observed synchrotron emission or the inverse Compton emission. At the same time, a more experimental approach investigates the Faraday RM effect. It occurs as an impact of magnetised plasma on propagating electromagnetic waves, making it a great indicator of the presence of magnetic fields and their structure. The existence of magnetic fields within some GCs is supported by observations of large regions emitting diffuse synchrotron emission and thus proving the presence of relativistic electrons and $\sim \mu$eV magnetic fields.

These regions are classified into radio halos, relics and mini-halos, depending on their size and position within the cluster. Observations of these fairly vague sources offers an insight into mechanisms of the creation of relativistic particles originating from magnetic fields, generally separated in two scenarios: primary electrons injected into the ICMF during star formation or from AGN activity, and secondary electrons produced in interactions of relativistic and thermal protons in the ICMF. From an observational point of view, especially for radio halos, the first option is more supported, inferring the connection between the X-ray properties of a cluster and processes of cluster mergers. On the other hand, radio relic are found to be located in the outskirts of GCs, offering a direct insight into the radial development of the magnetic field profile, and unlike radio halos, they are strongly polarised. Lastly, mini-halos are located outside the central galaxy of the cluster, but exhibiting strong synchrotron emission unrelated to merger processes. Interestingly so, they are found to be located in cool core clusters, one of which is the Perseus GC, the main observational target in this thesis.

While estimations of the strength of the magnetic field from these three types of targets can be reconciled through magnetohydrodynamic simulations, all coming down to the range of $0.1 - 10\,\mu$G [277], the origin of magnetic fields is not yet clear. Possibilities include the primordial production of ICMFs before the recombination period [278] or later, in phase transitions of the early Universe, and lastly, the injection of galactic material into the ICMF [279]. Although all the mechanisms are relatively different, ultimate solution to the creation of ICMFs is most probably a combination, additionally altering them through the aforementioned mergers of clusters. During mergers, magnetic fields can be enhanced due to the created shocks and turbulence, resulting in locally stronger and structurally altered magnetic field in the entire cluster [277, 280] (consider also [281] for a more elaborated review on the topic).

Cool core GCs studied in the main work of this thesis have shown good agreement with assumptions of the magnetic field profile to be dependent on the electron density, directly connected to thermal and dynamical properties of the cluster, estimated to $\sim 10\,\mu$G, unlike weaker magnetic fields in merging clusters of galaxies mentioned before. Through surface brightness observations, the Perseus GC has been found to be undergoing a merging process with a smaller galaxy subcluster, exhibiting the presence of a cool core in the centre. The core is separated from hotter, outer horseshoe-like region by a bright edge surface [282]. Additionally, the RMs of Taylor et al. [283] found to be significantly high, in accordance with the lack of observed polarisation from the centre of the cluster, estimating the strength of the magnetic field to be $15\,\mu$G. Studies performed by MAGIC collaboration on ~ 85 hours

of Perseus GC observations on energies above 630 GeV have set an independent limit on the strength of the magnetic field in Perseus to be $4 < B < 9\,\mu$G [284].

Aforementioned studies, their results and assumptions have been used in the development of the divergence-free homogeneous and isotropic Gaussian turbulent magnetic field model for Perseus GC implemented in the `gammaALPs` code used in calculation of photon survival probability in our study. The model employed here assumes radial dependence of the magnetic field B^{ICM} on the electron density n_{el} [191]:

$$B^{ICM}(r) = B_0^{ICM} \left(\frac{n_{el}^{ICM}(r)}{n_0^{ICM}(r)} \right)^{\eta_{ICM}}, \tag{6.2}$$

where n_0^{ICM} is the electron density normalisation in the cluster and electron density $n_{el}^{ICM}(r)$ is modelled as a double distribution, accounting for different structure of the magnetic field in the core and outskirts of the cluster:

$$n_{el}^{ICM}(r) = n_{0,1}^{ICM} \left(1 + \frac{r}{r_{core,1}} \right)^{-3\beta_{ICM,1}/2} + n_{0,2}^{ICM} \left(1 + \frac{r}{r_{core,2}} \right)^{-3\beta_{ICM,2}/2}. \tag{6.3}$$

Here $n_{0,1}^{ICM}$ and $n_{0,2}^{ICM}$ are normalisations of the electron density in the core and outskirts respectively, r_{core} represents the extension of the cluster core, while η_{ICM} and β_{ICM} are scaling parameters describing the magnetic field dependence on electron density. The strength profile of the ICMF model implemented in `gammaALP` is plotted in Figure 7.14.

In Chapter 7.4, we will discuss the impact of different parameterisation of the GC magnetic field models imposed on the photon survival probability calculations in studies with VHE gamma rays coming from AGNs. We will explore their effects on the final results and constraints in the ALPs parameter space.

6.3 Intergalactic magnetic field (IGMF)

Magnetic fields permeating galaxies and filaments connecting them fill only a small fraction of the entire Universe, with volume filling factors being $\lesssim 10^{-3}$ and $\sim 10^{-3} - 10^{-1}$ respectively, while in comparison, with the volume filling factor of $\gtrsim 10^{-1}$ voids are dominating the Universe [285]. In that sense, vast voids between galaxies have a great importance on large scales. Given their prevalence over smaller, but stronger magnetic fields in galaxies ($\sim 1\,\mu$G) and filaments ($\sim 0.1 - 1\,$nG), IGMF is believed to be the main clue for unveiling the secret of the creation of cosmic magnetic fields and the propagation of particles in general. Depending on the origin of IGMF, one could set constraints and draw conclusions about the production and enhancement of magnetic fields mentioned in previous subsections of this chapter.

As we will discuss soon, only constraints on the IGMF strength and coherence length were set so far, in contrast to actual measurements done, e. g. for the magnetic fields of GCs, where the strength is constrained using the Faraday RMs, e. g. [286, 287]. Most recent and constraining limits have been set by CMB [288]. Fairly important for large-scale

magnetic fields in general, given that their homogeneity cannot be assumed over arbitrarily large distances, is to constrain the coherence length. Neronov et al. [289] proposed to use measurements of the slope of the extended emission by the electromagnetic cascades and/or their light curves to obtain a measure of the IGMF coherence length. First constraints [290] yielded upper bounds $L_{coh} \lesssim 300\,\mathrm{Mpc}$, while lower bounds, dependent on the EBL model, are set to $L_{coh} \gtrsim 30\,\mathrm{kpc}$ in general case, and $L_{coh} \gtrsim 300\,\mathrm{kpc}$ for a case of weaker EBL absorption. Otherwise, the origin, strength and structure of the IGMF are fairly unknown. Two main ideas for the creation of what is now known as the IGMF are explained by the time of their creation, making it either of cosmological or astrophysical origin.

From the cosmological perspective, most of constraints are set with studies of the CMB, as some scenarios predict the creation of IGMF in pre or post-inflation periods, as well as during phase transitions, similar to the case of GCs, which would then impact our knowledge about the Universe during those early evolutionary stages. From observations of the CMB, constraints set on IGMF strength by the Planck collaboration have resulted in an upper limit set around $\mathrm{B}^{\mathrm{IGMF}} \sim 4\,\mathrm{nG}$ [291]. The majority of other cosmological constraints are set through theoretical considerations, in which case the strength of IGMF is constrained from above [285].

On the other side, astrophysical scenario assumes that this magnetic field was created during the formation of galaxies and stars or through the ejection of galactic material into the void, "feeding" it with magnetic fields. Another viable option is the battery effect, where the misalignment of temperature and changes in density in the early stages of the Universe lead to the creation of magnetic field. Regardless of the creation mechanism, in order to reconcile observations with theory, enhancement of the magnetic field is needed, enabled through dynamo mechanisms capable of increasing the strength of the magnetic field up to several times. For a thorough overview of the topic, reader is suggested to consider reviews by [292] and [285].

Furthermore, observations of polarised emission, previously mentioned as Faraday RMs of extragalactic sources such as blazars, can be used for disentangling the effect of IGMF from the effects of GCs and our own galaxy. Unfortunately, such observations have only provided broad constraints on the strength of IGMF. More recently, constraints have been derived using the observations from IACTs and Fermi-LAT telescopes, utilising the electromagnetic cascades of VHE gamma rays. Blazars emit into extragalactic space, leading to creation of electromagnetic cascades through the interaction of gamma rays with the EBL, generating $e^- e^+$ pairs. These pairs are then deflected by IGMF and observed as effectively larger halos around blazars, increasing their brightness at lower gamma-ray energies. Several studies based on gamma-ray observations have been done, setting constraints on the strength of IGMF [293–295]. Depending on the assumed duration of blazars' activity, the IGMF strength is constrained to $B^{IGMF} > 7.1\ 10^{-16}\,\mathrm{G}$ ($B^{IGMF} > 3.9\ 10^{-14}\,\mathrm{G}$) for a 10-year ($10^7$-year) duty cycle, assuming $l_{coh} \sim 10\,\mathrm{Mpc}$ in the most recent study [296]. Regarding the ALPs studies, IGMF effect is most often neglected due to its weak effect on the photon-ALP mixing in the studied range of ALP masses. With the given strength and coherence length, masses accessible through the observed energies in astrophysical measurements are deemed too high, as indicated in [179]. Nevertheless, some studies have considered the

effect of IGMF, modelling it as a randomly oriented, domain-like magnetic field [150, 193] or a turbulent magnetic field [191, 244]. These studies demonstrated that the uncertainties introduced by the latter can be avoided, since the results of two approaches do not differ. For that reason, IGMF strength profile is usually taken as [297]:

$$B^{IGMF}(z) = B_0^{IGMF}(1+z)^2, \tag{6.4}$$

depending on the strength of IGMF B_0^{IGMF} at redshift $z = 0$.

Overall conclusion is that the IGMF causes large scale oscillations in photon survival probability, a consequence of its large coherence scale. This effect is readily distinguishable from the influence of other magnetic fields acting on smaller scales, such as the blazar jet magnetic fields ($l_{coh} \sim$ pc) or GC magnetic fields ($l_{coh} \sim 10\,$kpc) [193], but given that the IGMF coherence length can acquire wide range of different values, it needs to be examined carefully. This of course can also change considering different ALPs parameters, as the photon-ALP oscillation length depends on them.

6.4 Magnetic field of the Milky Way (GMF)

The magnetic field of our galaxy has been extensively studied over the years (e. g. [188, 298–300]), with the model proposed by Jansson and Farrar [187, 192] used in majority of ALPs studies. Jansson and Farrar [187] are using the Faraday RM and synchrotron emission maps to combine the data and determine the best parameters for a turbulent magnetic field model, including components for the galactic disk, halo, and X component.

Given the complexity of MW, model incorporates three different structures: regular, striated, and small-scale random fields. The latter is believed to result from galactic outflows, such as supernovae, assumed to be randomly oriented fields ($l_{coh} \lesssim 100\,$pc) [301, 302]. Striated fields, on the other hand, compensate for effects caused by the differential rotation of the ambient medium. Determining values of 36 different parameters, this model predicts the strength of MW magnetic field to be of $\mathcal{O}(\mu\text{G})$. To properly incorporate this model into calculation of the photon survival probability, the coherence length of the turbulence scale needs to be assumed. Furthermore, the magnetic energy spectrum of the field is modelled to follow:

$$\frac{\langle |B|^2 \rangle}{8\pi^2} = B_{rms}^2 \left(\frac{s}{s_{max}} \right)^{\alpha - 1}, \tag{6.5}$$

where s is the scale for the integration, s_{max} being the limit of it, and α being the slope of the spectrum. More details on the exact modelling can be found in [297]. Following the findings of Meyer et al. [297], turbulent component is subsequently neglected, given that its impact is found to be several orders of magnitude weaker than that of the regular component. The original model of Jansson and Farrar [187] was revisited, incorporating results from the Planck collaboration [303], and addressing uncertainties that were neglected in previous works [304]. An improvement of this model was done in [305], followed by the latest update by Unger and Farrar [306]. This emphasises the fact that the thorough modelling of the GMF requires extensive studies and is subject to future changes.

Efforts have been made in recent years to improve the GMF model, particularly focusing on the central region of the galaxy and local magnetic fields [307]. However, such models consider important, but overall insufficient region of the galaxy, lacking information about the GMF at large distances from the centre, important for the calculation of the photon survival probability. In our context, importance of the GMF modelling is crucial for the possible back-conversion of ALPs to photons. The full potential of this phenomenon is expected to be explored with the newest and upcoming generation of IACTs and EAS arrays, anticipated to obtain significant statistics on energies above several TeV, where this effect is expected.

Chapter 7

Constraining the Axion-Like particles parameter space using the VHE data of Perseus GC with MAGIC

Contents

This section is dedicated to discussion of the results and findings from the MAGIC collaboration publication "Constraints on axion-like particles with the Perseus GC with MAGIC", whom of which I am a corresponding author [232]. My role was to lead the data and statistical analysis, as well as write the original draft of the manuscript. In the study we are constraining the ALPs parameter space using 41.3 hours of observational data from the Perseus GC collected with the MAGIC telescopes. Propagation of the photon-ALP beam is calculated assuming the photon-ALP conversion in magnetic field of Perseus GC, impacted by the photon attenuation due to the interaction with EBL photons in IGMF, and allowing for back-conversion in the magnetic field of MW. By searching for distinctive spectral signatures and introducing a new approach the statistical analysis of the data, we confirmed constraints on ALPs with masses in the neV $-$ μeV range and established the most stringent limits for ALPs with masses around 40 neV. This section will also include additional checks and calculations performed during the evolution of this project, some of which were also presented in the publication.

7.1 MAGIC observations of the Perseus GC - data selection

Perseus is the brightest X-ray GC, displaying a dense population of electrons and a strong magnetic field at its core [282, 283]. Also known as Abell 426, Perseus has been observed with MAGIC for a long time, being an important source with dataset including over 400 hours of data [308–316]. Furthermore, data of Perseus GC has been used in searches for DM [316] and studying its energy density [308, 311]. Aside of extensive dataset collected by MAGIC, Perseus is an interesting target for ALPs searches due to the strong magnetic field permeating the cluster over large distances (in order of hundreds of kpc), as well as for its proximity to Earth which allows to minimise the discrepancies that arise from different choices of the EBL model. Preceding this publication, there are ALPs studies published by Fermi-LAT collaboration [179] and independent studies using the data from Fermi-LAT and MAGIC telescopes [178, 182]. In its center, at the redshift of $z = 0.01759$, Perseus hosts a strong AGN called NGC 1275, also known as 3C 84. NGC 1275 is characterised as FR-I galaxy as revealed by radio observations of its morphology. FR-I sources are roughly corresponding to BL Lacs, hosting strong relativistic jets. Majority of blazars are exhibiting a relativistic jet visible under a viewing angle of few degrees from the line of sight, while radio interferometry observations [317] of NGC 1275 in the centre of Perseus estimated it to be $65° \pm 15°$ on the scale of one parsec.

For our study, we have selected a period of observations corresponding to a flaring state and preceding/following period of NGC 1275, spanning from September 2016 to February 2017. Corresponding to the day of flare is January 1st of 2017, peaking with 61.3 σ significance, as defined by Li and Ma [269] and in Equation 5.4. This dataset has been already published and analysed by Ansoldi et al. [315] in a MAGIC publication about the detection of this flaring state. Additionally, in Section 7.5.6 we introduced

a set of observations of IC 310, a radio galaxy located in the vicinity of NGC 1275, in particular its flaring state detected in November 2012. Interest for flaring states of the sources is motivated by the fact that the spectral distortion introduced by ALPs is small and only observable in firm detections, which occur during the highest states of the source. The NGC 1275 data are further classified into three datasets, including the strong flare activity detected by MAGIC in Jan 2017, the post-flaring state in two following days, and the baseline emission over two consecutive years. The whole dataset of MAGIC includes 41.3 hours of data. Datasets of corresponding periods are listed in Table 7.1, including the dataset of IC 310, also used in the analysis to evaluate the possible impact that addition of this dataset could impose on the final constraints in the ALPs parameter space. In the table, we also give the zenith range of the data, important for choice of proper MC simulations for the low-level data analysis performed with MARS. For our analysis, we have used the data/MCs taken/simulated in the wobble mode at a fixed offset of 0.4°.

Target	Date	Observation time [h]	Zenith range [°]
NGC 1275	1 Jan 2017	2.5	12 - 50
	02-03 Jan 2017	2.8	12 - 38
	Sep 2016 - Feb 2017	36.0	12 - 50
IC 310	13 Nov 2012	1.9	12 - 35

Table 7.1: The datasets of NGC 1275 and IC 310 used in the study. For each dataset we report the observation date, the duration in hours and corresponding zenith range of observations.

7.2 Data analysis

Datasets were analysed using the MARS software, following the previously published analysis [313, 315]. Upon this, it was converted from `melibea` format into DL3 fits files, and prepared to be analysed with the cross-platform, multi instrument[1], open-source software `gammapy` [44]. In the following section, we will present the results of the validation of the data conversion from MARS `melibea` format into DL3 fits files, described in Nigro et al. [265]. To perform the conversion, energy dependent cuts on *hadronness* and $theta^2$ parameters are used and applied to conversion of `melibea` files with appropriate MC simulations.

[1] `gammapy` is an open-source `python` package for gamma-ray astronomy https://gammapy.org/ It is used as core library for the Science Analysis tools of CTA and is already widely used in the analysis of existing gamma-ray instruments, such as H.E.S.S., MAGIC, VERITAS and HAWC.

7.2.1 DL3 conversion and gammapy analysis validation

Validation of the converted NGC 1275 DL3 files and `gammapy` analysis was performed in three steps. To perform the comparison between the datasets, reference point was the dataset and SED points previously published in [315].

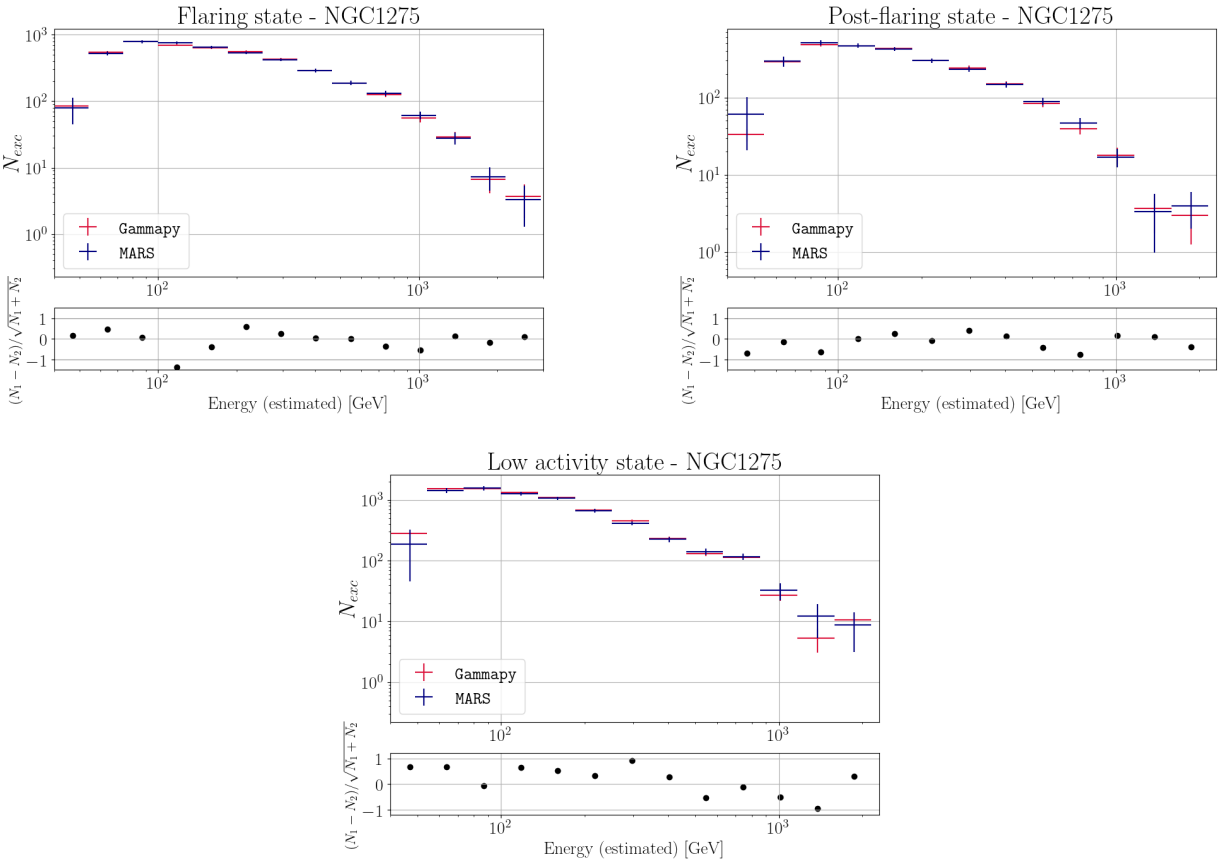

Figure 7.1: Comparison of excess counts extracted from MARS proprietary `melibea` files and DL3 files converted using the `magicDL3` [318] converter.

Excess event counts We extracted excess event counts from the proprietary `Flute` files of the data analysis published in [315]. For comparison, we did the same by extracting the number of excess counts (see Equation 5.3) from DL3 files of our data. In Figure 7.1, one can see the comparison between excess counts from these two datasets for all three activity states of NGC 1275, extracted from the same respective energy bins. Similarly as in published data (marked as "`MARS`"), excess extracted from DL3 files are exhibiting larger errors in energy bins with poorer statistics, especially in two bins at highest energies in the plot. Overall, the datasets are proved to be compatible, despite using different analysis software.

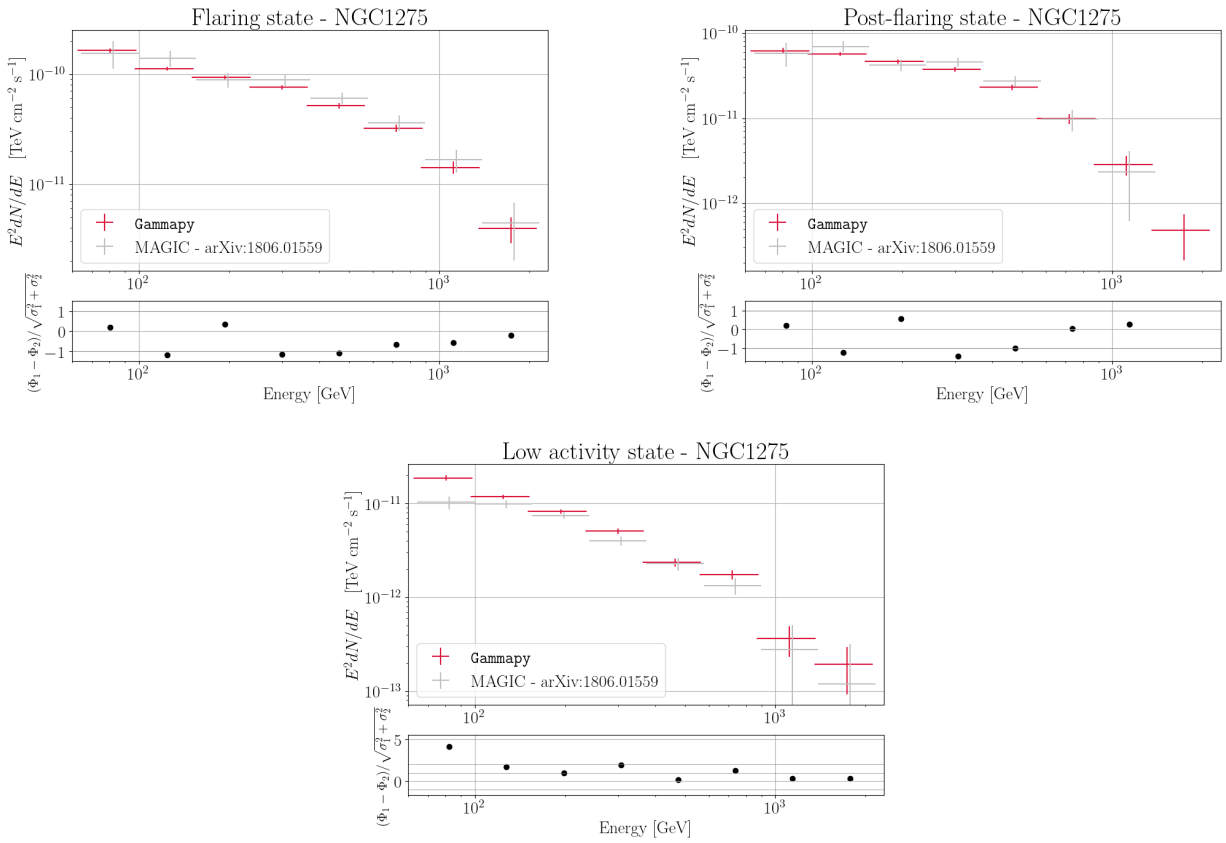

Figure 7.2: SEDs for three activity states of NGC 1275 computed with MARS executable `Flute` using `melibea` data and corresponding stereo MC simulations of MAGIC IRFs, compared to SEDs computed from corresponding DL3 files using `gammapy`. Both spectra are fitted using the EPWL spectral model (see Equation 7.1) [232].

Spectral energy distribution (SED) The second check is performed upon the extraction of flux point and computation of SED. In this case, as defined in Equation 5.9, the flux points depend on the IRFs of the telescope, combined with `melibea` files on the `flute` level, and during the conversion to DL3 files in case the high-level analysis is done with `gammapy`. In case one follows the pipeline of, e. g. `lstchain`, IRFs are added to DL2 files to create DL3 files, but in our case, since we started from `melibea` files obtained with MARS, files are processed with `magicDL3` [318]. `magicDL3` is MAGIC-proprietary pipeline containing classes and executables for conversion of `melibea` data and producing standardised gamma-ray data files [265] complying with the specifications of the future Data Formats for Gamma-ray Astronomy (GADF)[2]. Produced with it, DL3 files of MAGIC contain IRFs of the instrument and can be used for computing the spectrum of the source using `gammapy`. Same as in the original publication [315], we have performed fitting of our data (spectrum)

[2]https://gamma-astro-data-formats.readthedocs.io/en/latest/general/index.html

to the Power-Law with an Exponential Cut-off (EPWL) function:

$$\Phi^i_{int}(E') = \Phi^i_0 \left(\frac{E'}{E_0}\right)^{\Gamma^i} e^{E'/E^i_c}, \tag{7.1}$$

for each $i-$th dataset, where E' is the reconstructed energy, Φ_0 is the normalisation flux computed at the energy scale E_0. Γ_i is the photon index and E_c is the cutoff energy for the EPWL. Discrepancy between points is coming from the fact that MAGIC publications featured unfolded SED (as explained in Section 5.3.6), while `gammapy` SED is not unfolded. For that reason, SED points published in [315] are lower in flux, but still compatible with SED from `gammapy` given the weak effect of EBL on redshift $z = 0.01759$ where NGC 1275 is located. This can be seen in Figure 7.2, confirming the validity of `magicDL3` conversion tools used for our analysis.

Parameters of the fit In Figure 7.3 one can see comparison plots for all the three best-fitting parameters of the EPWL models for three activity states of NGC 1275. Here we performed unfolding of the spectrum with MARS analysis of our dataset, prior to conversion into DL3 files. The unfolding procedure is performed in the same way as by Ansoldi et al. [315], using the EPWL fit, defined in Equation 7.1. The compatibility factor plotted in the second column is defined as the ratio of the difference of the parameters divided by the square root of the quadratic sum of errors. Same as above, discrepancy between results obtained for two datasets processed with MARS and the one processed with `gammapy` comes from the fact that current version of `gammapy` does not support the unfolding of gamma-ray spectra. Best values of the parameters obtained by fitting data to an EPWL are given in Table 7.2.

Dataset NGC 1275	Φ_0 [10^{-10}cm^{-2} s^{-1} TeV^{-1}]	Γ	E_c [TeV]
Flare	12.8 ± 1.10 (16.1 ± 2.3)	-2.26 ± 0.07 (-2.11 ± 0.14)	0.67 ± 0.10 (0.56 ± 0.11)
Post-flare	10.9 ± 2.00 (15.4 ± 4.5)	-1.83 ± 0.13 (-1.61 ± 0.25)	0.30 ± 0.05 (0.25 ± 0.05)
Low state	0.89 ± 0.14 (1.14 ± 0.32)	-2.70 ± 0.11 (-2.28 ± 0.22)	0.64 ± 0.18 (0.36 ± 0.11)

Table 7.2: Comparison of best parameters of the EPWL function fit applied to all three activity states of NGC 1275 and for two analyses; DL3 files from our analysis, processed with `gammapy` and best-fit parameters of analysis published in [315].

7.2.2 Modelling of the intrinsic spectra of NGC 1275

The SEDs of the three activity states can be seen in Figure 7.4 (see also Table 7.2). In the figure, solid lines represent the best fit of the spectral points assuming no–ALP (null hypothesis) and the shaded areas represent the statistical uncertainties on the best fit function. In agreement with [309, 315], best fit curves for the intrinsic energy spectrum are modelled with an EPWL function, and the results for each of the three NGC 1275

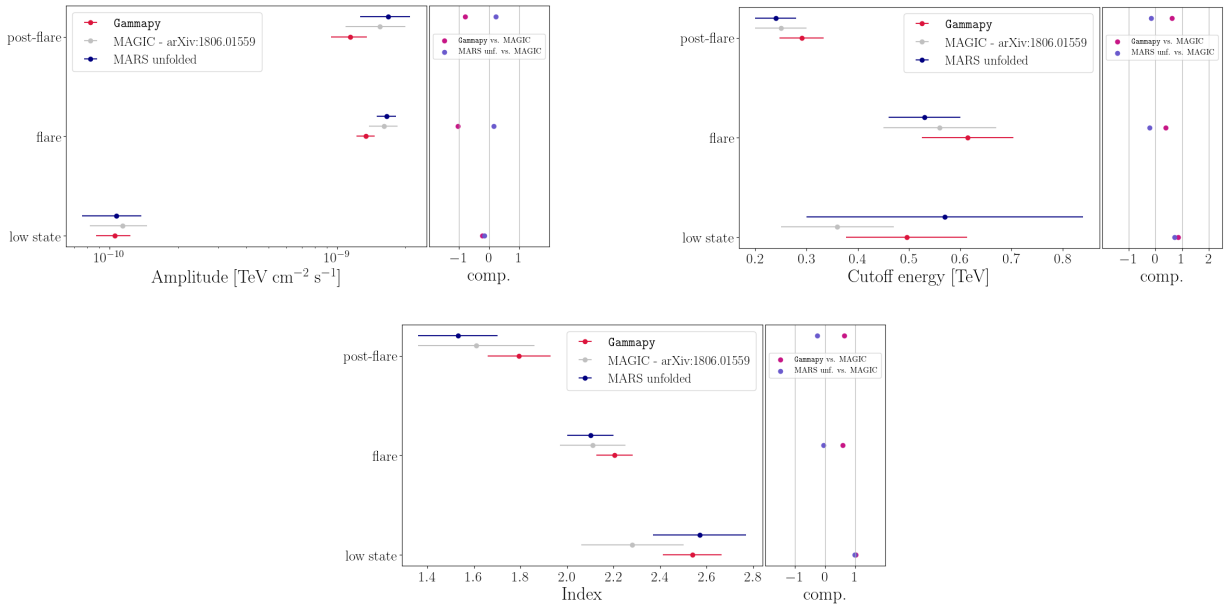

Figure 7.3: Comparison plots with parameters of EPWL function used for fitting NGC 1275 spectra of three different activity states and for three datasets obtained with `gammapy` and MARS software, compared with already published results by MAGIC collaboration in [315]. Second column is showing the comparison of compatibility factors for `gammapy` and MARS results with already published MAGIC results.

datasets are reported in Table 7.3. Differences in the spectral variations between different activity states of NGC 1275 are obvious.

Target NGC 1275	Date	Duration [h]	N_{on}	N_{off}	N_{exc}	$\mathcal{S}$	Spectrum	Γ	$\Phi_0/10^{-10}$ [cm^{-2} s^{-1} TeV^{-1}]	E_c [TeV]
Flare	1 Jan 2017	2.5	6632	6703	4397	61.3	EPWL	-2.31 ± 0.06	12.2 ± 1.0	0.72 ± 0.11
Post-flare	02-03 Jan 2017	2.8	4376	6060	2356	37.8	EPWL	-1.79 ± 0.14	11.4 ± 2.1	0.29 ± 0.04
Low state	Sep 2016 - Feb 2017	36.0	28830	68943	5849	31.8	EPWL	-2.54 ± 0.13	1.1 ± 0.2	0.5 ± 0.12
Total		41.3	39838	81706	12602	60.8	–	–	–	–

Table 7.3: The three datasets used for the analysis. For each dataset we report the observation date, the duration in hours, the global number of events in the ON and OFF region ($N_{\text{on}}, N_{\text{off}}$ respectively), number of excess events (N_{exc}), and the significance of the excess signal in the dataset $\mathcal{S}$ (Equation 5.4). We report the spectral features corresponding to the null hypothesis (no ALP), namely EPWL, including the photon index Γ, the normalisation flux Φ_0 computed at a normalisation energy $E_0 = 0.3\,\text{TeV}$ in all cases, and the cut-off energy E_c [232].

EBL absorption A high-energy gamma ray interacts with two main diffuse ambient radiation fields during its propagation through the Intergalactic Medium: the CMB in the mm range and the UV-optical-IR photons ($10^{-2} - 10^{4}$ μm) of the EBL. If the interaction is

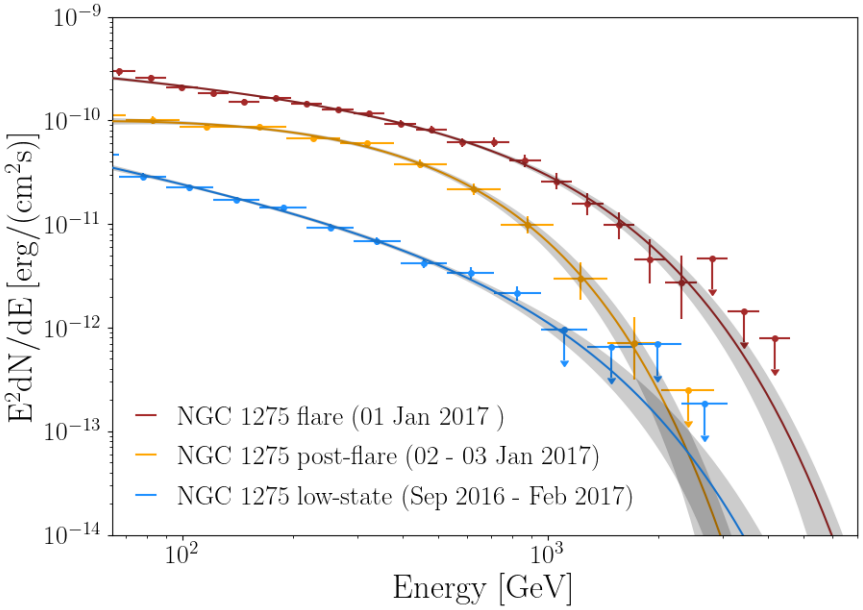

Figure 7.4: SED of NGC 1275 (different states) obtained with `gammapy` for the three brightness periods (activity states) in consideration [232].

efficient, such high energy gamma-ray radiation is lost through the process of pair production. The UV-optical EBL photon field is the result of the optical-IR direct star light around 1 μm and the light reprocessed into 100 μm-range IR light by surrounding dust throughout the evolution of the Universe. This interaction is particularly strong for TeV photons, with optical depths of $\tau\ (z = 0.5, E_\gamma = 1\ \text{TeV}) \simeq 4$ and $\tau\ (z = 0.5, E_\gamma = 10\ \text{TeV}) \simeq 30$ [319, Figure 12]. In our study, the target is in relative proximity with $z \simeq 0.01759$. As a result, the EBL absorption plays a role at this distance, but with a dependence on the energy of gamma ray, with an optical depth of $\tau\ (300\ \text{GeV}) \simeq 0.03$ and $\tau\ (10\,\text{TeV}) \simeq 0.4$ [319, Figure 12]. We model the optical depth due to EBL following Dominguez et al. [320]. However, there are several other well-motivated models in the literature such as the aforementioned Franceschini and Rodighiero [319]. Importance of the EBL absorption is however emphasised in the modelling of the expected ALPs signal, given that it impacts the photon-ALPs conversion in the intergalactic medium. For our study, the specific choice of the model of Franceschini and Rodighiero [319] does not have a sizable impact on the ALP limits, as discussed also by Abdalla et al. [160]. For that reason, we decided to keep the choice of Dominguez et al. [320] model.

Data binning and significance We have divided the $i-$th dataset in $k-$energy bins both in the ON and OFF regions. The ON region is the Region Of Interest (ROI) in which the signal is expected. Events from the ON region are comprised of both signal and irreducible signal-like background events. To estimate this number of signal events we use three background control OFF regions in which no signal is expected. The signal is then

estimated using the Equation 5.3. In Table 7.3 we report the total number $N_{\rm on}, N_{\rm off}, N_{\rm exc}$ events for the three datasets, as well as the significance $\mathcal{S}$ of $N_{\rm exc}$, computed both for the individual datasets and a joined one, following Equation 5.4.

7.2.3 Modelling of ALP induced signal

The presence of ALPs represents our *alternative hypothesis*. According to Equation 2.21, we are sensitive in the sub-μeV, so we prepare a scan of a parameter space with 154 models of ALPs, logarithmically spaced between 4×10^{-9} eV and 1×10^{-6} eV in mass m_a, and $5 \times 10^{-13}\,\mathrm{GeV}^{-1}$ and $5 \times 10^{-10}\,\mathrm{GeV}^{-1}$ in coupling $g_{a\gamma}$. This choice encompasses the region in which we expect to be sensitive to the putative signature of ALPs. For curiosity, tested region also includes the part of the parameter space already excluded by CAST experiment [88]. We computed $P_{\gamma\gamma}(E_\gamma; \boldsymbol{B})$ using `gammaALPs` for each of these points, as a function of different magnetic fields.

Magnetic fields modelling Specific studies for the magnetic field of Perseus B^S are found in Churazov et al. [282] and Taylor et al. [283]. A recent comparison between magnetic field models in Perseus was also made by the CTA Consortium [321]. Given the large extension of the core and the present magnetic field, the number of domains N crossed by the photon beam is very large and therefore the effective magnetic field encountered $\langle B(r) \rangle = 0$, while the RMS can be computed as the average B-field intensity of $\langle B_0 \rangle$ following the recipe of Meyer et al. [191]. Further parameters defined in `gammaALPs` for the magnetic field of Perseus are taken from [179]: the electron spatial indices of Churazov et al. [282, Equation 4] set at $n_0 = 3.9 \cdot 10^{-2}$ cm^{-3} and density parameter $\beta = 1.2$ at 80 kpc, $n_2 = 4.05 \cdot 10^{-3}$ cm^{-3} and $\beta_2 = 0.58$ at 280 kpc, the extension of the cluster $r_{Abell} = 500$ kpc, and the scaling of the B field with the electron density parameter $\eta = 0.5$. The turbulence is modelled in accordance with the A2199 cool-core cluster with maximum and minimum turbulence scale $k_L = 0.18$ kpc^{-1} and $k_H = 9$ kpc^{-1} respectively and turbulence spectral index $q = -2.8$ following Vacca et al. [322]. These parameters are summarised in Table 7.6 (upper row).

As for the strength of $B^{\rm IGMF}$, there are still large uncertainties (as we discussed in Section 6.3), with upper limits at the $\sim 10^{-11}$ G [288], and lower limits at the 10^{-8} nG scale [323]. Furthermore, Inserting such values in Equation 2.23 leads to resolution that, at TeV-scale energies, the photon-ALP beam is in the weak mixing regime, with negligible contributions to the photon-ALP mixing. Following those conclusions, we excluded the modelling of IGMF and leaving only the EBL background when computing the effect of intergalactic medium in our ALP hypothesis.

Finally, the modelling of $B^{\rm MW}$ is based on the work of Jansson and Farrar [187]. The magnetic field is modelled with a turbulent component, with 10^{-2} pc domain size, and a regular component that varies between $1.4 - 4.4$ μG from the Sun vicinity to the exterior.

7.3 Statistical framework

The primary objective of the analysis in this study is to evaluate the hypotheses of the existence of signatures of ALPs in the observed gamma-ray spectra. These signatures are derived by setting the coupling constant $g_{a\gamma}$ and mass m_a to the values that can be tested by our data. To do so, we defined the null hypothesis, assuming that no–ALP effects are present, and that only EBL absorption occurs. For this purpose, we are employing a likelihood maximisation method.

We define a binned likelihood as follows:

$$\mathcal{L}(g_{a\gamma}, m_a, \boldsymbol{\mu}, \boldsymbol{b}, B|\boldsymbol{D}) = \prod_{i,k} \mathcal{L}_{i,k}(g_{a\gamma}, m_a, \boldsymbol{\mu_i}, b_{i,k}, B|\boldsymbol{D}_{i,k}), \tag{7.2}$$

where $\boldsymbol{\mu_i}$ are the SED nuisance parameters (flux amplitude Φ_0, spectral index Γ and cut-off energy E_c, see Table 7.3) for the i–th sample in our dataset, $b_{i,k}$ are the expected background counts in the OFF region, and $\boldsymbol{D}_{i,k} = (N^{i,k}_{\rm on}, N^{i,k}_{\rm off})$ are the number of ON and OFF events observed in the k–th energy bin from the i–th sample (see Section 7.2.2). With B we indicate one possible magnetic-field realisation. The likelihood is by definition the probability of observing the data $D_{i,k}$ assuming the model parameters $g_{a\gamma}$ and m_a to be true:

$$\mathcal{L}_{i,k} = \mathcal{P}\left(N^{i,k}_{\rm on} \mid s_{i,k} + \alpha\, b_{i,k}\right) \times \mathcal{P}\left(N^{i,k}_{\rm off} \mid b_{i,k}\right) \tag{7.3}$$

with $\mathcal{P}$ being the Poisson probability mass function for observing n counts with expected count rate r: $\mathcal{P}(n|r) = r^n e^{-r}/n!$. The parameter α is the exposure ratio of the ON and OFF region (see Section 7.2.2), while $s_{i,k}$ is the expected signal counts in the energy bin ΔE_k in the ON region for the i–th sample:

$$s_{i,k} = \int_{\Delta E_k} dE\ \Phi^i_{obs}(E;\ g_{a\gamma}, m_a, \boldsymbol{\mu_i}, B, z). \tag{7.4}$$

In Equation 7.4 we have introduced the observed flux for the i–th sample:

$$\Phi^i_{obs} = \int dE'\ \Phi^i_{int}(E'; \boldsymbol{\mu_i}) P_{\gamma\gamma}(E') \cdot \mathrm{IRF}^i(E|E'). \tag{7.5}$$

Thus, in order to perform the integrals in Equation 7.5 and Equation 7.4, and get the likelihood expression from Equation 7.3 and Equation 7.2, we need to determine the following quantities:

- the $\mathrm{IRF}^i(E|E')$ for the i–th sample, e. g. the probability of detecting an event with true energy E' and assigning it an energy E;
- the total photon survival probability $P_{\gamma\gamma}(E'; m_a, g_{a\gamma}, B, z)$ in which both ALPs induced absorption in GC and MW, together with EBL attenuation in the IGMF, are taken into account.

- The intrinsic energy spectra Φ^i_{int} described in Section 7.2.2 for each dataset. See also Table 7.3.

We have therefore 9 nuisance parameters $\boldsymbol{\mu_i}$ coming from the intrinsic spectrum: 3 for each of the EPWLs of the 3 states of NGC 1275. Further nuisance parameters of the analysis are the magnetic-field realisation B, as discussed in Section 7.2.3, and the expected background counts $b_{i,k}$ which are fixed to the values $\hat{b}_{i,k}$ that maximise it for a fixed $s_{i,k}$, as shown by Rolke et al. [324]:

$$\hat{b}_{i,k} = \frac{N + \sqrt{N^2 + 4(1+1/\alpha)\ s_{i,k}\ N_{\rm off}}}{2(1+\alpha)}, \tag{7.6}$$

with $N \equiv N^{i,k}_{\rm on} + N^{i,k}_{\rm off} - (1+1/\alpha)\ s_{i,k}$.

Given the likelihood in Equation 7.2, the statistic $\mathcal{TS}$ is defined as:

$$\mathcal{TS}(g_{a\gamma}, m_a) = -2\Delta \ln \mathcal{L} = -2 \ln \frac{\mathcal{L}(g_{a\gamma}, m_a, \hat{\boldsymbol{\mu}}, \hat{\mathbf{b}}, \hat{B}|\boldsymbol{D})}{\hat{\mathcal{L}}}, \tag{7.7}$$

where $\hat{\mathcal{L}}$ is the maximum value of the likelihood over the parameter space, while $\hat{\boldsymbol{\mu}}$ and $\hat{B}$ are obtained from profiling the likelihood, e. g. by fixing them to the values that maximise the likelihood for a given coupling $g_{a\gamma}$ and mass m_a.

For the nuisance parameter B instead, given the limitations of computational power, it is improbable that the magnetic-field realisation B which maximises the likelihood function $\mathcal{L}$ is included among the simulated magnetic-field realisations. Thus, instead of profiling over B, we sort the likelihoods $\mathcal{L}$ in each ALP grid point in terms of the magnetic-field realisation. At this point, for each ALP grid point we use the likelihood value that corresponds to a specific quantile $Q = 0.95$ of the obtained distribution of $\mathcal{L}$.[3]

The statistic defined in Equation 7.7 is known as the likelihood ratio. According to the Neyman-Pearson lemma [325], it is the goodness-of-fit test with maximum *power*, and according to Wilks' theorem [326] it follows a χ^2-distribution with 2 degrees of freedom. This is because the log-likelihood defined in Equation 7.7 is a function of only two parameters, m_a and $g_{a\gamma}$.

In our analysis, however, the primary conditions necessary for a direct application of Wilks' theorem are not satisfied. For example, one prerequisite stipulates that two distinct points within the parameter space should yield two unique predictions. Unfortunately, this condition does not hold up when considering values of the couplings $g_{a\gamma}$ close to zero (e. g., there is no ALP effect). In such cases, any variation in the mass m_a will inevitably lead to identical predictions, thus violating this essential criterion. Therefore assuming a χ^2-distribution with two degrees of freedom for the statistic $\mathcal{TS}(g_{a\gamma}, m_a)$ would lead to a

[3] If one could have been sure about the presence of the B field that maximises $\mathcal{L}$ in the simulations, then a proper treatment of the nuisance parameter B would correspond to putting $Q = 1$, e. g. profiling over B. This procedure for the treatment of the nuisance parameter B is the same adopted in [160] in which it was found (and confirmed by our analysis) that putting $Q = 0.95$ and not to 1 is insensitive to the *ad-hoc* choice of number (100 in our analysis) of realisations.

wrong coverage. For this reason, we have computed the correct coverage by getting the effective distribution of the statistic from MC simulations.

In previous works [160] this was done by computing these distributions for few ALP points. Generally 2 or 3 points that produce the most pronounced features in the energy flux, e. g. one that yields no mixing, one where the mixing is maximal, and another model in which case oscillations in the spectrum would be observed. Upon computation of the same procedure and obtaining the 95th quantiles of the distributions for each of the points, the most conservative one, e. g. the one with larger 0.95 (or 0.99) quantile, would be taken as the reference point for the exclusions. This was motivated also by the computing power needed to extract these distributions for different points. This approach was one of the starting points of our analysis, as we followed it and obtained exclusions by using the data at hand. These results will be presented in Section 7.5.2. In continuation of our study, we developed and applied a more accurate approach that consists of computing the distribution of the statistic $\mathcal{TS}(g_{a\gamma}, m_a)$ for each of the 154 points in the ALP parameter space [232]. In this way, we can now directly translate a certain $\mathcal{TS}(g_{a\gamma}, m_a)$ into a significance for excluding the ALP hypothesis $(g_{a\gamma}, m_a)$, expressed in standard deviation of the corresponding Gaussian or the $z-$score.

7.4 Results

Using the datasets of Table 7.3 and following the prescription described in detail in Section 7.3, we computed the statistic $\mathcal{TS}(g_{a\gamma}, m_a)$ in Equation 7.7 for each of the 154 points in our ALP parameter space. As described in further details in Section 7.5.1, these observed statistics are used to compute the rejection significance of the ALP hypotheses. The rejection significance is shown in Figure 7.5 for each point (smoothed for graphical purposes) expressed in numbers of the 1-dimensional-Gaussian equivalent standard deviations $\sigma = \sqrt{2}\,\mathrm{erf}^{-1}(\mathrm{CL})$, where erf^{-1} is the inverse of the error function and CL is the confidence level for excluding the hypothesis (see Section 7.5.1 for more details).

The dark red area corresponds to ALP models that are excluded above 5 standard deviations. Dark blue area corresponds to ALP models that are better in agreement with the data, e. g. they have a low significance rejection. The model that better agrees with the observation is the one corresponding to $m_a = 1.0 \times 10^{-7}\,\mathrm{eV}$ and $g_{a\gamma} = 2.71 \times 10^{-10}\,\mathrm{GeV}^{-1}$. The null hypothesis of no–ALP effect is disfavoured with a $\sim 2\sigma$ confidence level in favour of the alternative hypothesis, which is not enough to claim any discovery of ALP effects. As further discussed in Section 7.5.5, the spectral points of Figure 7.4 are nicely fit with simple dependency as in Equation 7.1 and the null hypothesis yielded:

$$-2\ln\mathcal{L}(g_{a\gamma} = 0\,\mathrm{GeV}^{-1}, \mathrm{m_a} = 0\ \mathrm{eV}, \hat{\boldsymbol{\mu}}, \hat{\mathrm{B}}|\mathrm{D}) = 62.2, \tag{7.8}$$

which is an expected value considering the total number of degrees of freedom[4], indicating a good fit to the data. However, the alternative hypothesis corresponding to $m_a = 2.15 \times 10^{-8}$

[4]The total number of degrees of freedom are given by the difference between the number of energy bins and the number of free parameters used in the model, summed over all datasets. Such a value corresponds

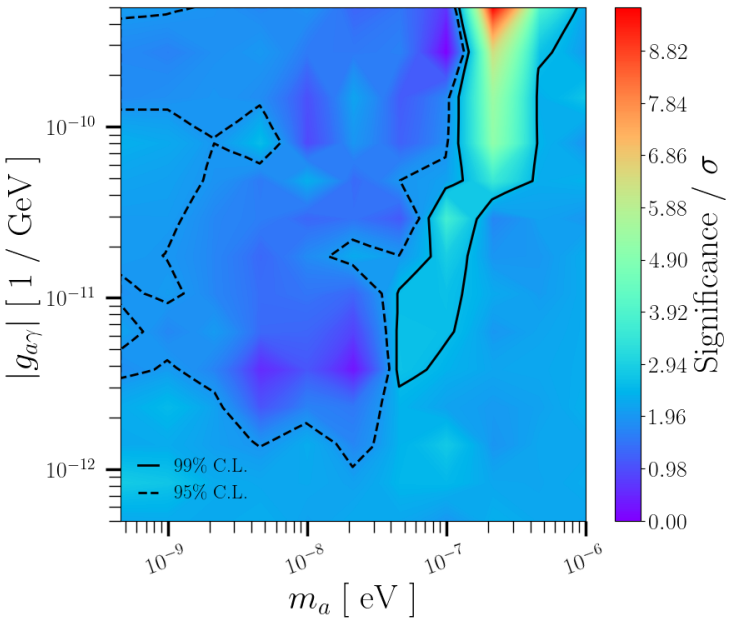

Figure 7.5: The likelihood-ratio statistic $\mathcal{TS}$ of Equation 7.7 is computed over 154 ALP points with m_a and $g_{a\gamma}$ using the data in Table 7.3. For each point, the obtained statistic is then compared to the distribution of $\mathcal{TS}$ one would get assuming the corresponding ALP hypothesis m_a and $g_{a\gamma}$ to be true. The obtained p-value is converted in the 1-dimensional-Gaussian equivalent standard deviations σ (also known as $z-$scores). See Section 7.5.1 and for more details. The black dashed line shows a significance of 1.96 σ while the black solid one a significance of 2.58 (corresponding to a 95% and 99% confidence level, respectively) [232].

eV and $g_{a\gamma} = 3.81 \times 10^{-12}\,\mathrm{GeV}^{-1}$ demonstrated an even better agreement with:

$$-2\ln\mathcal{L}(g_{a\gamma}, m_a, \hat{\mu}, \hat{B}|\boldsymbol{D}) = 55.4. \tag{7.9}$$

Following Equation 7.7 we obtain for the null hypothesis a statistic of $\mathcal{TS} = 6.8$. As discussed in Section 7.5.1, assuming the null hypothesis to be true a more extreme value of 6.8 would have been observed only 4.2% of the times, which corresponds to a rejection significance for the null hypothesis of $2.03\,\sigma$. Since the null hypothesis is already excluded at 95.8% CL in favour of the alternative hypothesis, the exclusion region of the ALPs parameter space obtained here will be shown at 99% CL.

Lastly, in Figure 7.6, we juxtapose the limits established by MAGIC with the currently accessible limits [159, 160, 178–180, 183] within the corresponding range of the ALPs parameter space. Our constraints are consistent with limits obtained using similar astrophysical data analysis techniques, and represent the most competitive constraints for ALP masses m_a in the range of $40 - 90\,\mathrm{neV}$.

for this analysis to 60.

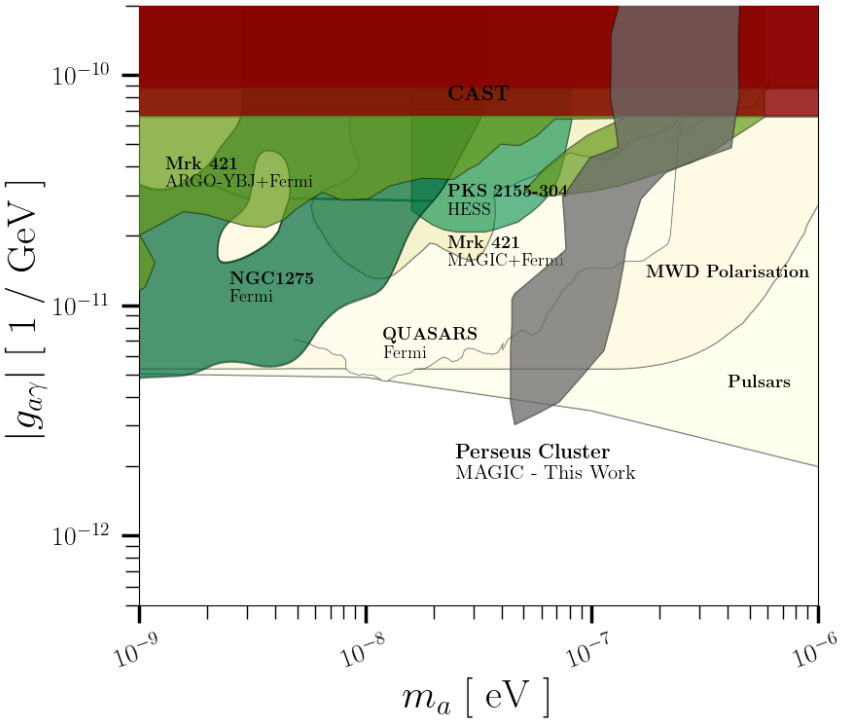

Figure 7.6: The 99% CL limits obtained with this work ([232]) in comparison with current 95% CL limits in similar part of the parameter space, gathered in [86].

7.5 Discussion

7.5.1 Point by point coverage computation

The likelihood ratio statistic, as described in (Equation 7.7), is expected to follow a χ^2 distribution with a number of degrees of freedom equal to the number of independent parameters, according to Wilks' theorem [326]. In our case, there are two independent parameters: the ALP mass (m_a) and the axion-photon coupling ($g_{a\gamma}$). However, Wilks' theorem is not applicable for this analysis, necessitating the determination of proper coverage through MC simulations. We perform this assessment on a point-by-point basis, in contrast to the approach taken by Abdalla et al. [160], where the most conservative point among the few investigated was selected. In Figure 7.7, we present the Cumulative Distribution Functions (CDFs) of the statistic $\mathcal{TS}(m_a, g_{a\gamma})$ obtained from MC simulations, considering various axion masses (m_a) and two distinct axion-photon couplings: $g_{a\gamma} = 5.0 \times 10^{-13}\,\mathrm{GeV}^{-1}$ (left plot) and $g_{a\gamma} = 1.7 \times 10^{-11}\,\mathrm{GeV}^{-1}$ (right plot). It is noteworthy that, for the lowest coupling considered in this analysis ($g_{a\gamma} = 5.0 \times 10^{-13}\,\mathrm{GeV}^{-1}$), the CDFs of the statistic exhibit minimal variation across different m_a values. This observation is consistent with expectations, as the ALP effects on the observed SED are relatively subtle for such a low coupling value, leading to only minor changes in the statistic's distribution when the ALP

mass is altered.

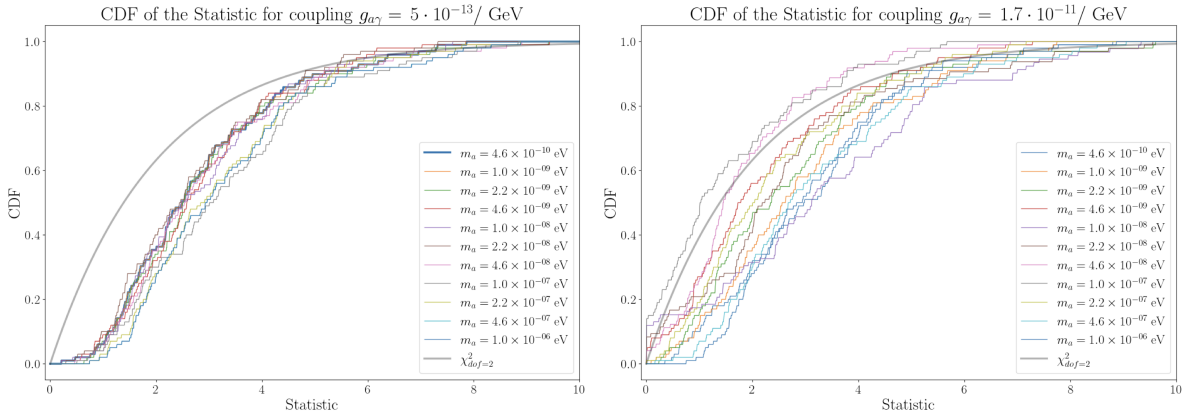

Figure 7.7: Cumulative Distribution Functions (CDFs) of the statistic $\mathcal{TS}(m_a, g_{a\gamma})$ (see Equation 7.7) obtained from MC simulations for different axion masses (m_a) and two axion-photon couplings: $g_{a\gamma} = 5.0 \times 10^{-13}\,\mathrm{GeV}^{-1}$ (left plot) and $g_{a\gamma} = 1.7 \times 10^{-11}\mathrm{GeV}^{-1}$ (right plot). The thicker blue line in the left plot highlights the CDF for the lowest ALP mass and coupling considered, which aligns with the null hypothesis. The grey line in both plots represents the χ^2 CDF for comparison, illustrating that using the χ^2 CDF with 2 degrees of freedom would lead to undercoverage [232].

On the left plot of Figure 7.7, we emphasise (using a thicker line) the CDF for the lowest ALP mass (m_a) and coupling ($g_{a\gamma}$) considered in this analysis. Taking into account the telescope's energy resolution, the expected counts under this hypothesis align with those under the null hypothesis (no ALP effect). Indeed both the observed statistic and the CDF obtained from MC simulations are identical for the null hypothesis and for the hypothesis with $m_a = 4.6 \times 10^{-10}$ eV and $g_{a\gamma} = 5.0 \times 10^{-13}\,\mathrm{GeV}^{-1}$ [232].
Finally, each distribution of the statistic for each of the 154 ALP points considered is fitted using the gamma distribution G:

$$G(x; \alpha, \beta) = \frac{\beta^\alpha}{\Gamma(\alpha)} x^{\alpha-1} e^{-\beta x}. \tag{7.10}$$

Here, α represents the shape parameter, while β denotes the rate parameter. The function $\Gamma(x)$ is defined as:

$$\Gamma(x) = \int_0^\infty t^{x-1} e^{-t} dt. \tag{7.11}$$

The χ^2 distribution with k degrees of freedom is a special case of the gamma distribution G, characterised by a shape parameter of $k/2$ and a rate parameter of $1/2$. The fitted gamma distributions are subsequently employed to compute the confidence level (CL) at which each of the 154 ALP hypotheses can be excluded:

$$\mathrm{CL} = \int_0^{\mathcal{S}_{\mathrm{obs}}} \mathrm{G(x; \alpha, \beta)\, dx}, \tag{7.12}$$

with $\mathcal{TS}_{obs}$ the observed statistic for a given ALP point derived from Equation 7.7. In order to obtain Figure 7.5 each CL is converted to the Gaussian equivalent deviation σ through the inverse of the error function: $\sigma = \sqrt{2}\text{erf}^{-1}(\text{CL})$.
Lastly, it is worth noting that if we had uncritically applied Wilks' theorem and utilised the χ^2 CDF with 2 degrees of freedom (displayed as a reference in grey in Figure 7.7), this would have led to undercoverage. The reason for this is that the χ^2 distribution results in a lower threshold for rejecting a given hypothesis, thereby increasing the likelihood of Type I errors (false positives).

7.5.2 "3 point coverage" approach

The computation of the rejection significance is done through the likelihood ratio test statistic of Equation 7.7, the Wilks' [326] theorem for the nested hypothesis cannot be blindly applied. For this reason, for each point of the ALP parameter space the correct coverage is obtained through MC simulations. In our work we have managed to compute the coverage for each point, which allowed us to calculate the $z-$score reported in Figure 7.5. This is a relevant improvement with respect to earlier similar computations such as done in Abdalla et al. [160] where it is explicitly mentioned that the coverage of the test statistic is not computed point by point but only for 3 points, among which the one that yields the most conservative exclusion is used. This approach was thereafter needed due to the substantial computational resources required to generate MC simulations for all ALP points. CDF distribution for 3 different points in the ALPs parameter space and χ^2 distribution are shown on the left side of Figure 7.8.
In Figure 7.8 we compare our method with the assumption of Abdalla et al. [160]. This is shown in the significance inlay of Figure 7.15 were, besides our 99% CL excluded region, we also report the 99% CL region that we would have obtained using the previous, more conservative coverage-computation method of Abdalla et al. [160]. It is clearly visible that the conservative coverage method computation significantly reduces the strength of the limits.

7.5.3 Comparison with CTA projections

Our limits displayed in Figure 7.5 show the highest significance for expected ALP masses $\sim\ m_a = 200\,\text{neV}$ for couplings to photons between $g_{a\gamma} = 5.0 \times 10^{-11}\,\text{GeV}^{-1}$ and $g_{a\gamma} = 5.0 \times 10^{-10}\,\text{GeV}^{-1}$. However, similar limits obtained with H.E.S.S. [159] or expected with CTA [160] are also sensitive to lower ALP masses around 10 neV. We decided to further investigate this discrepancy. In particular, the results from the CTA were obtained by extrapolating a portion of the NGC 1275 dataset that we are using to generate this result: Abdalla et al. [160] consider that during the lifetime of CTA Perseus could be observed for 260 hours, during which NGC 1275 would be in the baseline emission state for 250 hours and in flaring state for 10 hours. The authors model the baseline and flaring state with the values measured by MAGIC and reported here [309, 315].

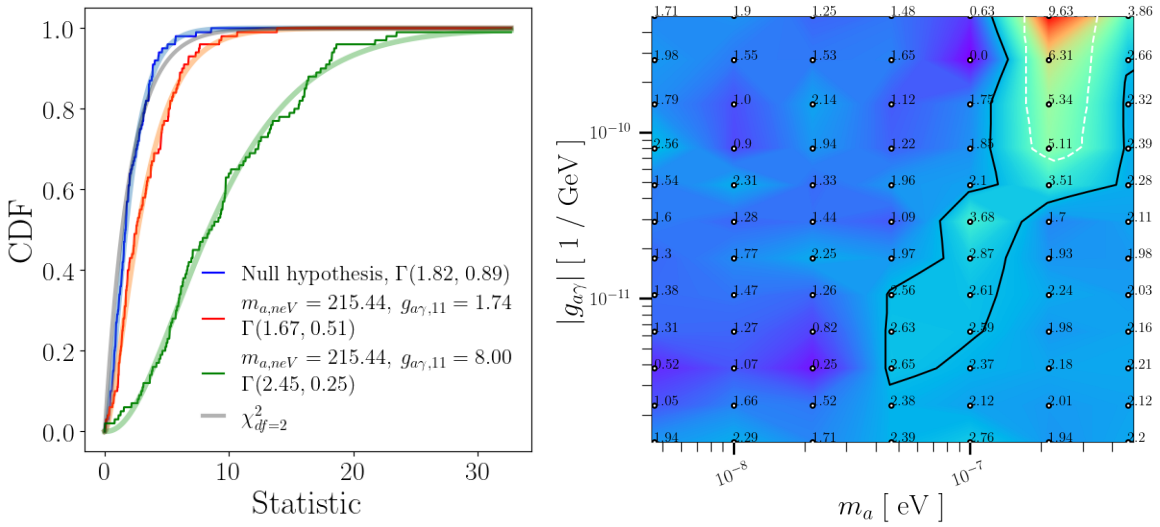

Figure 7.8: CDFs of the $\mathcal{TS}(m_a, g_{a\gamma})$ obtained from MC simulations for 3 different pairs of ALPs mass and coupling, and compared to the CDF of χ^2 distribution. Following the procedure of Abdalla et al. [160], the most conservative assumption, in this case the one with $g_{a\gamma} = 8.00 \times 10^{-11}\,\mathrm{GeV}^{-1}$ and $m_a = 215.44\,\mathrm{neV}$ (left plot). The comparison of 99% CLs yielded by a more conservative (white dashed line) and updated approach with computation of full coverage (black full line) (right plot) [232].

Target	State	Duration [h]	N_{on}	N_{off}	N_{exc}	$\mathcal{S}$
NGC 1275 (mock)	Flare	10	18154	12046	14138	129.0
	Baseline	252	201735	482674	40852	83.9
	Sum	262	219889	494720	54990	110.0

Table 7.4: The two datasets of mock NGC 1275 data used to cast our limits to compare them with Abdalla et al. [160]. For each dataset we report the status, the duration in hours, the global numbers N_{on} and N_{off} of events in the ON and OFF region, respectively, and the significance of the excess signal in the dataset $\mathcal{S}$. We do not report the spectral parameter for the null hypothesis (no ALP) as they correspond to those in Table 7.3 for the respective states.

We therefore adopt the same approach and recompute our limits as if we had taken 250 hours of baseline and 10 hours of flaring states. As done in [160], we neglect the post-flaring state of NGC 1275, see Table 7.4. To do so we are using the previously defined datasets where the observations are convoluted with the IRFs, ultimately giving us the predicted number of counts. To extend our flaring state and baseline to 10 hours and 252 hours respectively, we simulated with `gammapy` ~ 4 and ~ 7 times more total predicted counts in comparison to the original datasets of the flaring state and baseline used in the main part of this study.

The significance distribution is shown in Figure 7.9. We can clearly see that adding significantly more data allows to become sensitive to the parameter region with ALP masses around $1 - 10$ neV, in agreement with Abdalla et al. [160]. When comparing our findings with those from the CTA, it is essential to acknowledge that the CTA limits might be more conservative. This is due to their consideration of discrete step-wise variations in the effective area, which have been smoothed at the energy-resolution scale and were assumed to have an amplitude of ±5%. These variations were taken to occur at energies where one subsystem of telescopes begins to assume dominance in terms of point-source sensitivity. Therefore, a direct comparison should account for these methodological differences.

7.5.4 MAGIC sensitivity to spectral signatures of ALPs

In Figure. 7.10 we also report the corresponding $P_{\gamma\gamma}$ for a selection of 8 points in the parameter space. It is interesting to note the evolution of this probability: going from smaller to larger m_a, $P_{\gamma\gamma}$ in general becomes more oscillating; going from large to small $g_{a\gamma}$ the oscillations change pattern in an irregular way. This is also expected due to the

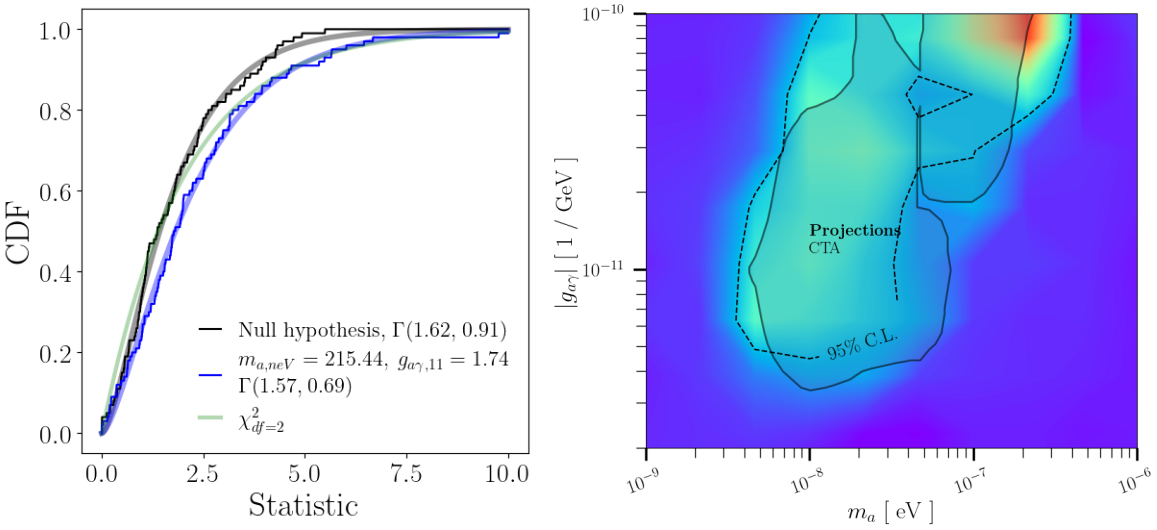

Figure 7.9: CDFs of the statistic $\mathcal{TS}(m_a, g_{a\gamma})$ obtained from MC simulations (10 hours of flare and 250 hours of NGC 1275 baseline) (left plot). Shown is one alternative hypothesis (one of the two plotted also in left side of Figure 7.8.) Since the aim of this approach is to stay conservative, we chose this ALP model, having a CDF distribution similar to the one of χ^2, and ultimately a similar $\mathcal{TS}(m_a, g_{a\gamma})(= 5.84)$. On the right, we show 95% CL exclusion region obtained with CTA projection from Abdalla et al. [160] (black line) compared to the projection of the MAGIC limits (dashed black line, 95% CL) obtained in this work, assuming a larger observation time of 262 hours corresponding to a global excess significance $\mathcal{S}_{\text{Li\&Ma}}$ of 110 as in Table 7.4. The background colour map shows the rejection significance expressed in number of standard deviations σ. The colour coding is the same of Figure 7.5 [232].

non-linear scaling of ALP-induced oscillations with the ALP parameters, the fact that the null hypothesis is independent on the magnetic field realisations and that the photon-ALP oscillations are degenerate in coupling and magnetic field. These are the same reasons for which Wilks' theorem cannot be considered valid for use in evaluation of our alternative hypotheses and setting the constraints in the ALPs parameter space.

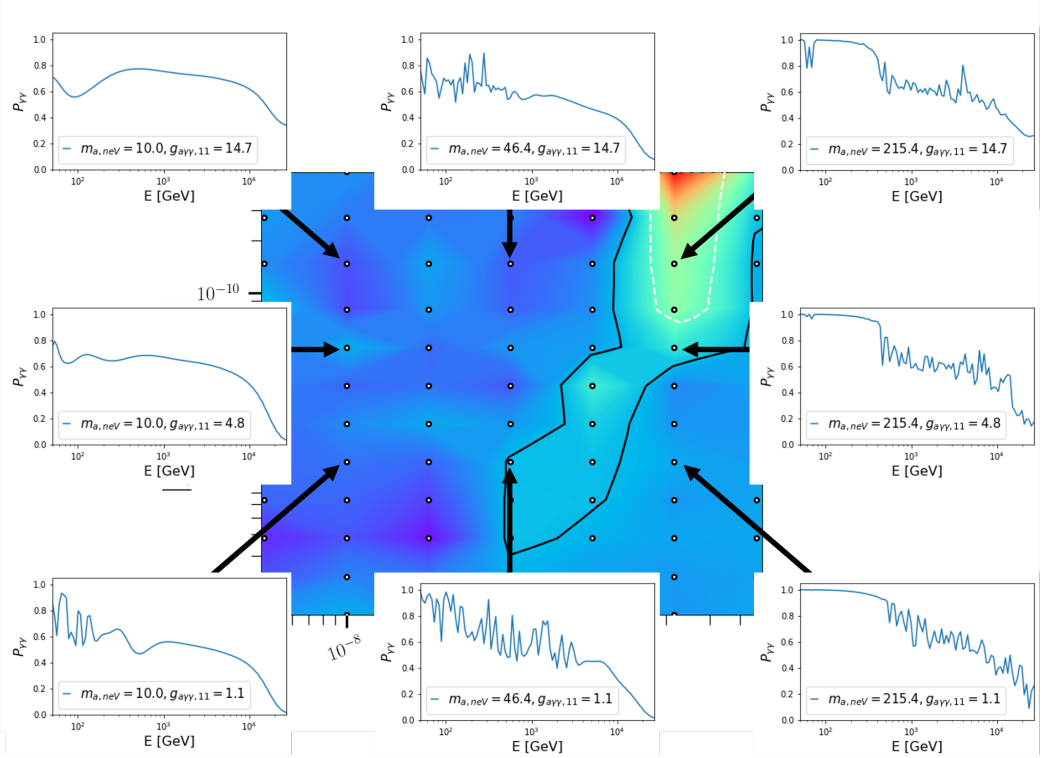

Figure 7.10: $P^a_{\gamma\gamma}$ for a selection of models in our scan of the parameter space. ALP mass (in neV) and coupling (in 10^{-11}GeV^{-1}) are displayed in the inlays. The background image is the significance distribution of Figure 7.5 with the addition of the 99% CL curve (dashed white line) obtained with the conservative coverage computation method of Abdalla et al. [160] (see also Section 7.5). The black solid line is the 99% CL curve obtained from the point-by-point coverage computation [232].

In Figure 7.10 we clearly see how the strongest constraints come from a region in which $P_{\gamma\gamma}$ *has sudden jumps rather than just wiggles*: compare e. g. the right column of $P_{\gamma\gamma}$ versus the central one. This follows from the fact that spectral jumps are more easily identified in the observed gamma-ray spectra, or alternatively that wiggles are too small to be detected due to the limited statistic and energy resolution of the instrument. This has important consequences in the search for ALP signatures with IACTs in previous publications that were focused specifically on searches for wiggles.

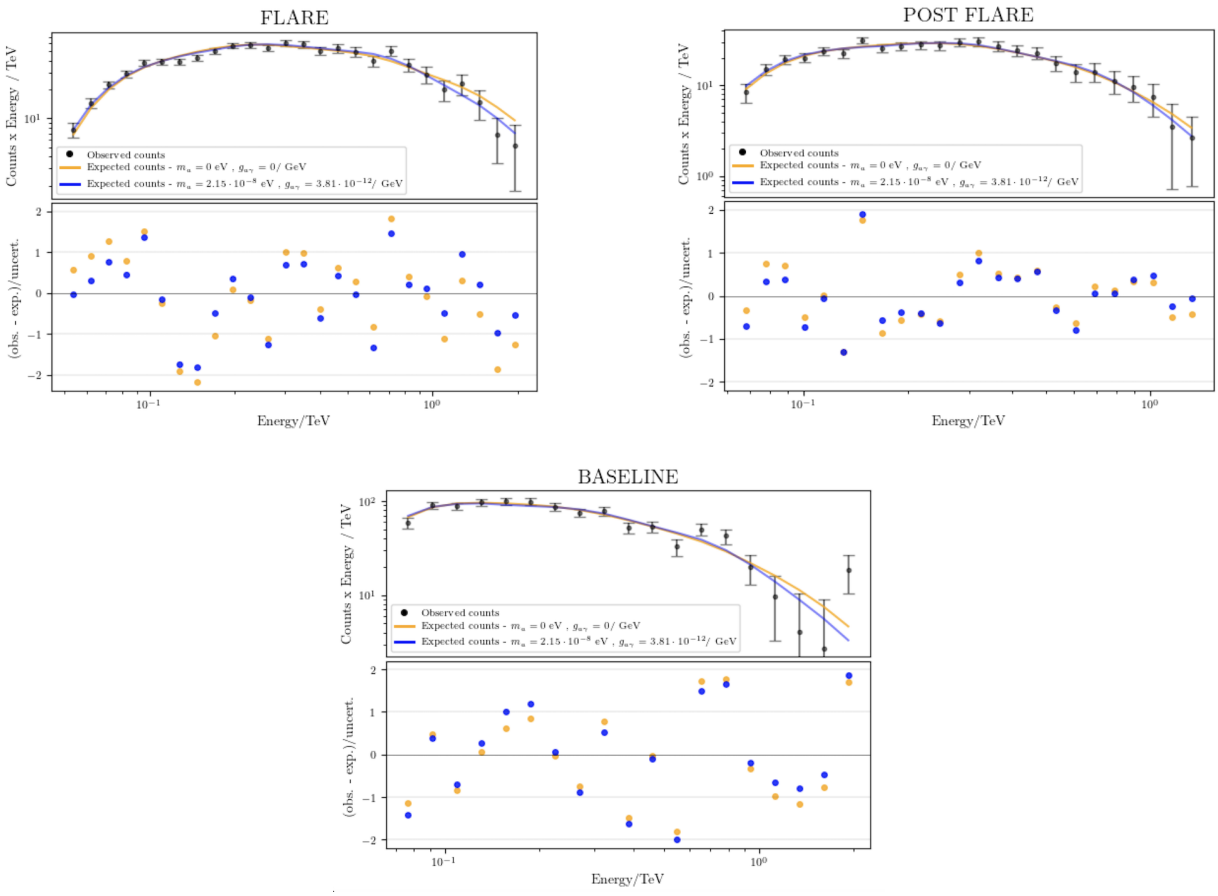

Figure 7.11: A comparison of observed excess counts per energy bin (multiplied by the centre value of the energy bin for visualisation purposes) with those expected from the null hypothesis model (orange line) and the best-fit ALP model (blue line). The expected counts are obtained by applying Equation 7.4, in which the SED parameters are fixed to the values maximising the likelihood. The observed counts are represented by black points. The bottom part of each plot highlights the relative distance between the observed and expected counts for all energy bins under both hypotheses. This is shown for all the three datasets in Table 7.3, here referred in the title of each plot as "FLARE", "POST FLARE", and "BASELINE", respectively [232].

7.5.5 Comparison of spectral counts between the null and alternative hypotheses

Figure 7.11 presents a comparison of the observed excess counts per energy bin (multiplied by the centre value of the energy bin for visualisation purposes) for the three datasets in this work (refer to Table 7.3) with those from the null hypothesis model and the best-fit ALP model. As discussed in Section 7.4, the latter corresponds to $m_a = 2.15 \times 10^{-8}$ eV and $g_{a\gamma} = 3.81 \times 10^{-12}\,\mathrm{GeV}^{-1}$. In the figure, one can observe how the expected counts from

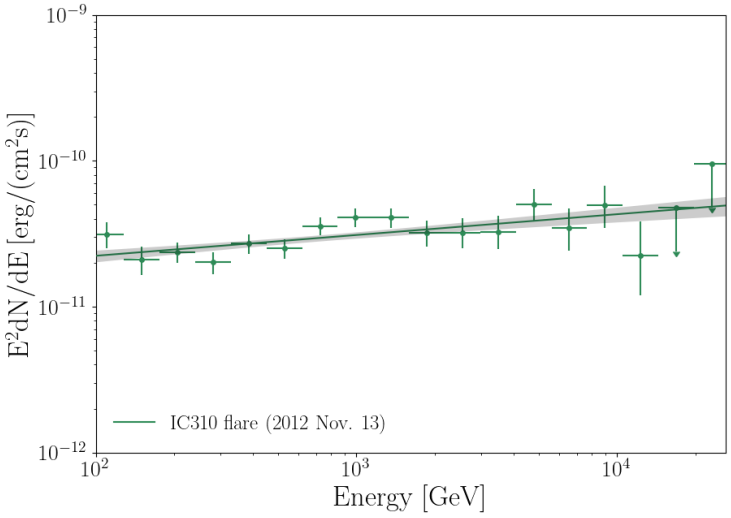

Figure 7.12: SED of IC 310 (flaring state) obtained with `gammapy` using the PWL fit.

the ALP hypothesis (blue line) show better agreement with the observed counts (black points) compared to the expected counts assuming the null hypothesis (orange line). Additionally, the flaring state appears to be the most constraining of the three datasets, as it is the only one in which the alternative hypothesis may be significantly favoured over the null hypothesis. These facts are emphasised in the bottom part of each of the three plots in Figure 7.11, where the relative distance between the observed and expected counts is displayed for all energy bins under both hypotheses, defined as $(N_{exc} - s)/\sigma_{N_{exc}}$. In this expression, $N_{exc} = N_{on} - \alpha N_{off}$, $\sigma_{N_{exc}} = \sqrt{N_{on} + \alpha^2 N_{off}}$, and s is given by Equation 7.4.

7.5.6 Additional flaring state of IC 310

A second bright head-tail radio galaxy located in Perseus, IC 310, is located at 0.6 deg off-centre and it was first detected in 2009 [309] due to its strong flaring activity in November 2012 [313]. The projected angular distance corresponds to about 750 kpc from the GC centre. The true distance is probably much larger considering the redshift of IC 310, estimated to be $z = 0.0189$, in comparison to the redshift of NGC 1275 of $z = 0.01759$. Even at its projected distance, the magnetic field appears to be reduced for about a factor 10 (see Figure 7.14), while at its true distance could be much smaller or vanishing. Our IC 310 dataset consists of 1.9 h taken on the November 13th, 2012 and it provided a detection of a strong fast flare with a sensitivity of 18 standard deviation off the residual background, globally less than that of NGC 1275 (see Table 7.5). SED of IC 310 for this dataset, fitted to a PWL model using `gammapy` is presented in Figure 7.12.
Considering the turbulent nature of the GC magnetic field, the $P_{\gamma\gamma}^{a,\mathrm{EBL}}$ for NGC 1275 and IC 310 should not strongly differ due to the different location only, but it would be affected by the magnetic field intensity as well. Before modelling the magnetic field in IC 310, we tried a naive combination of the two dataset *assuming the same* $P_{\gamma\gamma}^{a,\mathrm{EBL}}$ *for both targets.* In

Target	Date	Duration [h]	$N_{\rm on}$	$N_{\rm off}$	$N_{\rm exc}$	$\mathcal{S}$	Spectrum	Γ [$\rm cm^{-2}s^{-1}TeV^{-1}$]	$\Phi_0/10^{-10}$
IC 310	13 Nov '12	1.9	1469	2384	674	18.0	PWL	-1.86 ± 0.04	1.8 ± 0.1
Sum		43.2	41307	84090	13276	63.0	–	–	–

Table 7.5: The two datasets of mock NGC 1275 data used to cast our limits to compare them with Abdalla et al. [160]. For each dataset we report the status, the duration in hours, the global numbers $N_{\rm on}$ and $N_{\rm off}$ of events in the ON and OFF region, respectively, and the significance of the excess signal in the dataset $\mathcal{S}$. We do not report the spectral parameter for the null hypothesis (no ALP) as they correspond to those in Table 7.1 for the respective states.

Figure 7.13 one can see that IC 310 data are only weakly affecting the constraints obtained with NGC 1275 only. We therefore decided not to consider IC 310 in the final results presented above in Section 7.4.

7.6 Systematics

7.6.1 Relevance of magnetic field modelling

As discussed in Section 7.2.3, the modelling of the magnetic field in Perseus is still only fairly known up to date. To address this, the CTA Consortium recently conducted a detailed study comparing various magnetic field models available for Perseus [see 321, Figure 1]. For their study, they adopted a configuration based on Taylor et al. [283] with a reference magnetic field value $B_0 = 25\,\mu$G and $\eta = 2/3$. All remaining parameters of this modelling are reported in Table 7.6 and compared with our primary choice, based on [179].

	B_0 μG	η	n_0 $\rm cm^{-3}$	n_2 $\rm cm^{-3}$	$r_{\rm core}/r_{\rm core_2}$ kpc	β/β_2
B	10	0.5	$39 \cdot 10^{-3}$	$4.05 \cdot 10^{-3}$	80 / 280	1.2 / 0.58
B_{alt}	25	2/3	$46 \cdot 10^{-3}$	$3.60 \cdot 10^{-3}$	57 / 278	1.2 / 0.71

Table 7.6: The parameters used for the modelling of the Perseus magnetic field. B is representing the parameters used in the main analysis of this study [179]. B_{alt} are taken from [321].

A visual comparison of the $B(r)$ is reported in Figure 7.14. One can see that [321] displays a larger magnetic field toward the centre of the cluster without models in the region beyond 100 kpc. The effect on the choice of magnetic field on the upper limits is significant and is reported in Figure 7.15.

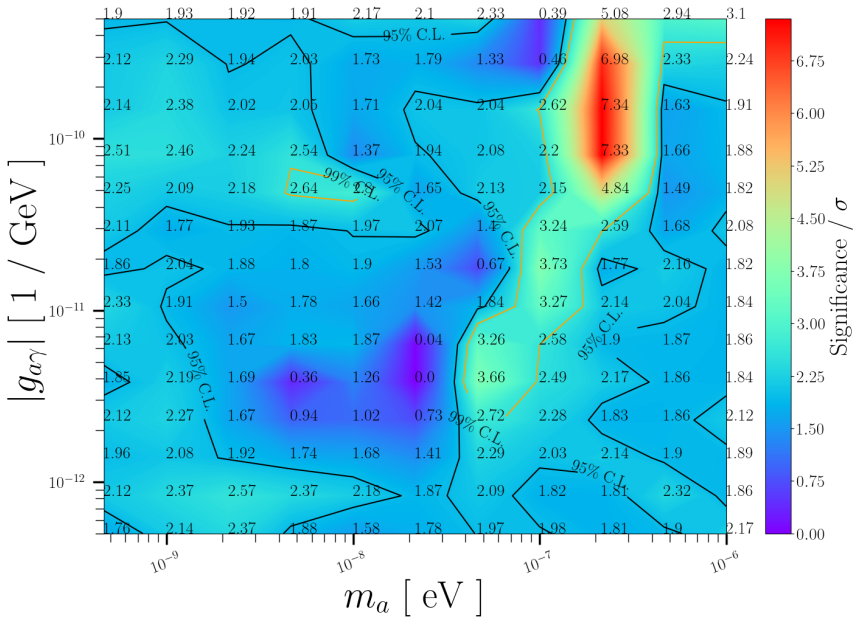

Figure 7.13: The likelihood-ratio statistic $\mathcal{TS}$ of Equation 7.7 is computed over 154 ALP points with m_a and $g_{a\gamma}$ using the data in Table 7.3. Computation process is the same as for Figure 7.5, only difference is that the dataset in this figure includes the flaring state of IC 310. The black dashed line shows a significance of 1.96 σ while the black solid one a significance of 2.58 (corresponding to a 95% and 99% confidence level, respectively) [232].

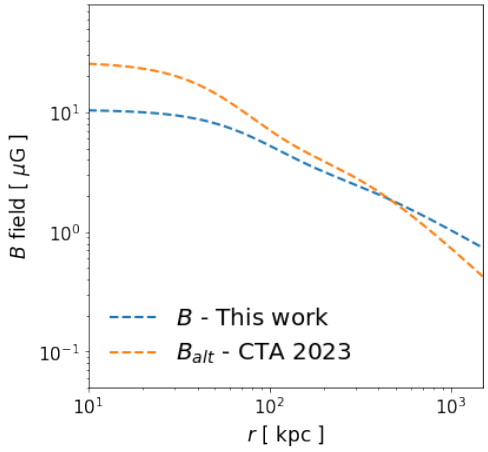

Figure 7.14: Comparison of magnetic field's radial profile. Blue dashed line is the reference model used in this work. Dashed orange line is the magnetic field model of [321].

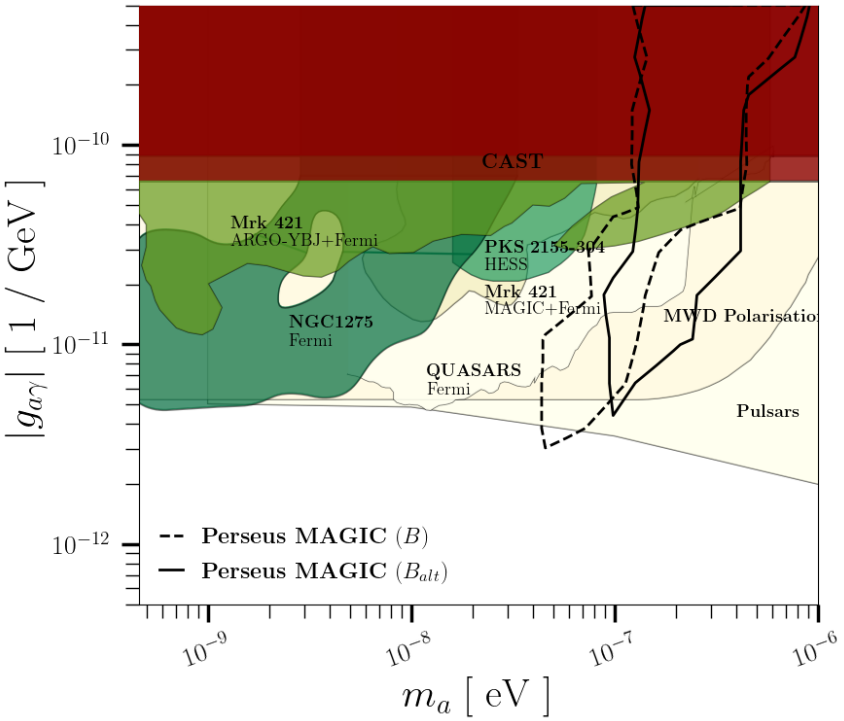

Figure 7.15: Comparison of the limits in the ALPs parameter space obtained with the Perseus cluster magnetic field from the main part of the study [232] with an alternative magnetic field model used in [321].

7.6.2 Energy resolution

The MAGIC telescopes reconstruct the energy with a precision of the order of $10-15\%$ depending on the energy, which is considered during data reconstruction and an irreducible

energy bias, which introduce energy scale uncertainties estimated to be around ±15% [248].

To evaluate this effect, we artificially scaled the ALP energy-dependent signatures in the spectra by ±15% and checked the effects on the bounds. The resulting discrepancies in the exclusion regions are shown in Figure 7.16. The effect is not negligible, but it does not alter our main conclusions. This uncertainty will be strongly reduced with upcoming IACT arrays, like CTA, whose energy scale systematics are expected to go down to ∼ 4% [327].

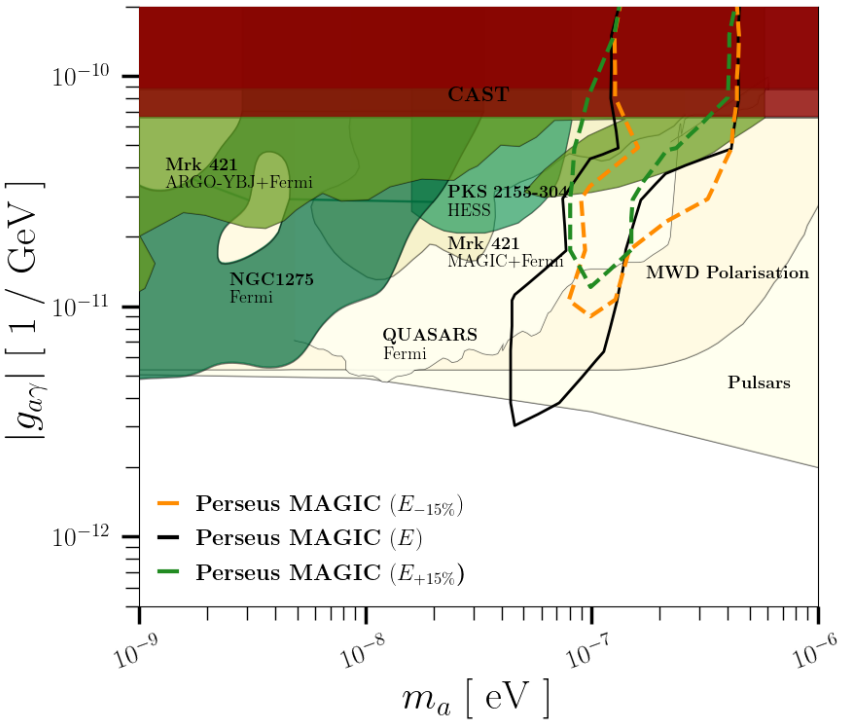

Figure 7.16: Discrepancies in the exclusion regions resulting from shifting the energy scale by −15% (dashed green) and +15% (dashed orange) in the ALP signatures in the spectra. For comparative purposes, we also depict in dashed black the exclusion regions obtained in this study, as presented in the main text in Figure 7.6 [232].

7.7 Summary and Conclusions

In this work we have analysed 41 hours of high-energy gamma-ray data coming from the direction of the Perseus GC in search for spectral irregularities induced by ALPs in the sub-μeV mass range. We have used gamma-ray beams of the radio galaxy in the centre of the cluster: NGC 1275, during its high emission state to have a significant detection. We have tested the alternative hypothesis (presence of ALP) on 154 points regularly selected in the ALP parameter space. For each model we have computed $P_{\gamma\gamma}$ over 100 realisations of the magnetic field around the target. The test statistic, once calibrated, does not provide significant detection, which allowed us to compute 99% CL exclusion upper limits in the ALP parameter space. These limits are shown in Figure 7.6 in comparison with other results and constrain ALP masses in the range $40 - 400\,\mathrm{neV}$. The excluded area matches that by earlier results and forecast for CTA. In particular in Figure 7.9 we show how larger observation times or significance of this target would allow to constrain also part of the parameter space at lower masses, around the neV.

In Figure 7.10 we have computed the significance point by point showing that this allows to improve the constraining power of the data with respect to vigorously conservative assumption on the coverage. In the same figure we have shown how IACTs are sensitive to ALP spectral induced jumps rather than wiggles, a fact which is usually not appreciated.

To date, these results offer the strongest constraints on ALP masses in the range of $40 - 90\,\mathrm{neV}$, with the greatest sensitivity for ALP masses of $m_a = 40\,\mathrm{neV}$, reaching the photon-axion coupling down to $g_{a\gamma} = 3.0 \times 10^{-12}\,\mathrm{GeV}^{-1}$.

Chapter 8

ALPs studies using the LST data of blazars

Contents

LST-1 is taking scientific data since November 2019. A significant fraction of the observed sources is constituted by AGNs, and particularly blazars. In case blazars are not located in galaxy cluster with strong (and widely spaced) magnetic fields, the magnetic field of the blazar ultra-relativistic jet plays a relevant role if the photon-ALP oscillation. However, the modelling of such fields is less known than that of galaxy clusters and must be modelled in details target by target. In this section, we will discuss the list of available sources, data selection, on-going development of the `lstchain` pipeline for data analysis and the preliminary results in search for oscillations in spectra of blazars observed with LST-1 caused by photon-ALP oscillations.

This will be complemented with study of the relevance of modelling of ultra-relativistic jet magnetic fields, modelled with the `gammaALPs` code, with global limits obtained with the `gammapy` code. Furthermore, using the same approach to the statistical analysis as in the ALPs study conducted with the Perseus data of MAGIC, we are going to present preliminary results in the context of the exclusions in the ALPs parameter space with LST-1 data.

8.1 Sources of interest - LST blazars pool

The LST-1 telescope is the first single mirror dish (23 m) IACT of four units for the future CTA. Several of the observed sources are blazars, jetted AGNs with their relativistic jets pointing towards us. This served as a motivation for expanding our search for ALPs on analysis of blazars' data. As pointed out in Section 6.1, the importance of the modelling of magnetic fields of relativistic jets becomes crucial in this case. Since the model of magnetic field of the relativistic jet with helical and tangled component developed by [193] is done using parameters of the SED modelling by Potter and Cotter [194], a first selection of the sources from the LST-1 dataset was performed in comparison to the respective available models in [194]. As a result, we have selected 5 different blazars for our study:

- Mrk 421, a high-synchrotron-peaked blazar at the redshift of $z = 0.031$.
- Mrk 501, a high-synchrotron-peaked blazar at the redshift of $z = 0.034$.
- BL Lac, an eponymous blazar usually classified as low peaked blazar at the redshift of $z = 0.069$.
- 1ES1959+650, a bright, high-frequency peaked blazar at the redshift of $z = 0.048$
- PG1553+113, a high-synchrotron-peaked blazar at the redshift of $z = 0.433$.

Mrk 421 and Mrk 501, as well as the BL Lac are long-term targets and objects with long legacy of observations of the MAGIC telescopes e. g. [328–331], motivating their observations with the LST-1 as well. The relative proximity of the listed targets, with the exception of PG1553+313, is suggesting low impact of EBL attenuation on the observed spectrum of the sources, an advantage that was also present in the study with Perseus data of MAGIC telescopes, discussed in Section 7. The preliminary results presented in this thesis include Mrk 421 only. Furthermore, we divided the available dataset based on the activity state of the source, which resulted in two sub-datasets, one presenting a flaring state detected in May 2022 and the other corresponding to a quiescent state of Mrk 421 spanning from December 2020 to February 2023.

8.2 Data selection

LST-1 data of the sources was selected after passing a set of conditions based on the quality and desired properties such as zenith range or angular distance of the pointing from the source position, important for reconstruction of the parameters for the shower reconstruction using the MC simulations. Remaining cuts are applied on data quality parameters, still not firmly determined generally, but rather dependent on the choice of source and observation conditions. At the moment, our approach was to apply cuts on each run individually, although cuts on level of subruns or even shorter time periods can be applied, as it will be standard practice with the upcoming CTA. At the moment, LST-1

data analysis pipeline and reconstruction in general are less stable than the MAGIC one, hence it requires more checks on the lowest levels. In the future, low level analysis will be automatised, and directly producing DL3 files for the high level analysis. We performed cuts on the night sky background counts, expected to change based on the position of the source relative to the centre of Milky Way, but also cuts on the cosmic rate, assumed to be completely dominated by protons and other nuclei creating the majority of atmospheric showers. Parameters that sustain "fixed" cut are the expected rates of "accident" triggers, caused by "noise-only" and uniform flashes, called "pedestal" and "flatfield" events, respectively. The remaining accidental triggers originate from fluctuations in the night sky's light, satellites, or light emitted from the vicinity of the telescopes, such as flashlights or car lights. After selection, we obtained two datasets of Mrk 421 data, presented in Table 8.1.

Target	Date	Observation time [h]	Zenith range [°]
Mrk 421	18 May 2022	0.9	18 – 29
	Dec 2020 - Feb 2023	63.9	9 – 57

Table 8.1: The datasets of Mrk 421 analysed in the study. For each dataset we report the observation date, the duration in hours and corresponding zenith range of observations.

8.3 Signal modelling - intrinsic and ALP spectrum

In Figure 8.1 we present two SEDs for the two analysed datasets of Mrk 421. Spectral points, red and blue for the flaring and low state respectively, are obtained using the analysis approach as in the case of NGC 1275 and IC 310 in 7.2.2. The difference is in the low-level analysis, where in this case we started from the DL1 level data and applying the `lstchain` tools for the source independent analysis and obtained DL3 files of Mrk 421 with incorporated IRFs. Solid lines are representing the best fit to the observed data, hence assuming the intrinsic spectrum of the source, free of ALPs effects, together with the corresponding shaded areas representing uncertainties of fit parameters. For both datasets, fitting with the EPWL function resulted with the best fit, reported in Table 8.2. We divided the datasets into energy bins for both ON and OFF regions. In this analysis, we used only one OFF region for background estimation. We determine the number of energy bins separately for both datasets, aiming to obtain a stable spectrum without significant oscillations due to systematic or analysis effects. Our analysis appears to be independent on the number of bins, since the results obtained with unbinned likelihood approach do not significantly differ from the ones obtained with the binned one. Nevertheless, the results presented in this chapter are preliminary, and the validity of this assumption is yet to be proven. In case of Mrk 421 at the redshift of $z = 0.031$, the EBL absorption in the intergalactic medium is expected to be relatively weak, but dependent on the energies of the incident gamma-ray, especially in the energy range of sensitivity of IACTs. Aside of the

best fit parameters, Table 8.2 reports the total number N_{on}, N_{off} and N_{exc} events for the flaring and low activity state, as well as the significance $\mathcal{S}$ of N_{exc} defined by Equation 5.4.

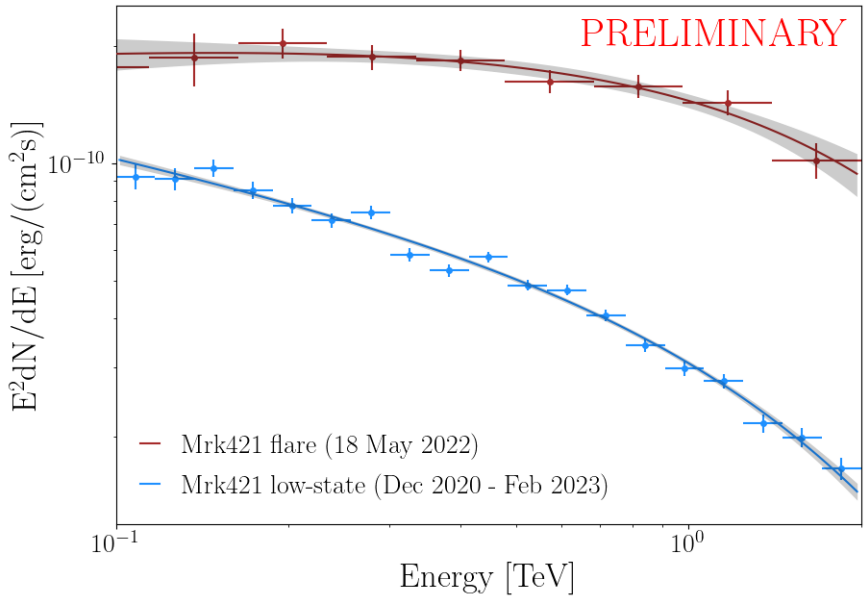

Figure 8.1: SEDs of two different activity states of Mrk 421 obtained with `gammapy`.

Target Mrk 421	Date	Duration [h]	N_{on}	N_{off}	N_{exc}	$\mathcal{S}$	Spectrum	Γ	$\Phi_0/10^{-10}$ [cm^{-2} s^{-1} TeV^{-1}]	E_k [TeV]
Flare	18 May 2022	0.9	56283	50455	5828	17.9	EPWL	-1.89 ± 0.11	15.3 ± 1.2	1.82 ± 0.19
Low state	Dec 2020 - Feb 2023	61.8	2676269	2530433	145836	63.9	EPWL	-2.29 ± 0.04	5.4 ± 0.2	1.75 ± 0.07
Total		62.7	2732507	2580888	151664	65.8	–	–	–	–

Table 8.2: Two datasets of Mrk 421 used in our study. Similarly as before, we report the observation date, the duration in hours, the global number of events in the ON and OFF region ($N_{\text{on}}, N_{\text{off}}$ respectively), number of excess events (N_{exc}), and the significance of the excess signal in the dataset $\mathcal{S}$ (Equation 5.4). We report the spectral features corresponding to the null hypothesis (no ALP), namely EPWL, including the photon index Γ, the normalisation flux Φ_0 computed at a normalisation energy $E_0 = 0.3\,\text{TeV}$ in all cases, and the cut-off energy E_k.

Modelling of magnetic fields in the ultra-relativistic jet and ALP effect For an ALP analysis or Mrk 421 data, we evaluated 90 combinations of equally logarithmically spaced values of ALP mass and coupling to photons, given in ranges of $1 - 1000\,\text{neV}$ and $0.02 - 5 \times 10^{-10}\,\text{GeV}^{-1}$, respectively. The ALP scenario for sources such as blazars introduces the importance of modelling of relativistic jets. The modelling of the magnetic field of the relativistic jets was discussed in Section 6.1, where the helical and tangled

components were presented. The two components are used to model the parabolic base and conical jet, as the field is developing from poloidal near the base, to helical down the jet. Motivated by the study of Davies et al. [193], we decided to use the same model for the relativistic jet, and adjusted it to our source, Mrk 421, using the parameters obtained by Potter and Cotter [194] and applied successfully to the SEDs of 38 Fermi blazars. In particular, as reported for Mrk 421 in [194], the length of the relativistic jet is 3×10^{21} m, with Lorentz factors $\gamma_{min} = 9$ and $\gamma_{max} = 12$, the initial jet power W $= 1.71 \times 10^{37}$ W, the radius of transition region R(t) $= 2.22 \times 10^{15}$ m, the magnetic field strength at the transition region B $= 2.91 \times 10^{-6}$ T and the effective black hole mass M $= 6.31 \times 10^{8}$ $M_{\odot}$. The complete list of remaining parameters can be found in [194].

Founding no claims that any of the GCs in which Mrk 421 is located are gas-rich, we believe that the magnetic field of the jet dominates over the GC magnetic field and we decided to neglect the effects of ICMF in the photon-ALP coupling. Similarly to NGC 1275 and for same reasons as in 7.2.3 (see also [232]), we neglected the effect of IGMF. Instead, we included the EBL absorption modelled with [320] for redshift $z = 0.034$. Finally, we include the possible ALP-photon conversion by including the magnetic field of the Milky Way, modelled as in our study with Perseus data of MAGIC, following the model of Jansson and Farrar [187].

8.4 Statistical analysis

The statistical analysis of Mrk 421 data and the evaluation of 90 ALP models was performed in the manner described in Section 7.3. We scanned the ALPs parameter space in range of $1 - 1000$ neV and $0.02 - 5 \times 10^{-10}$GeV^{-1} for ALP mass and coupling to photons, respectively. For each model, we defined a hypothesis including the configuration of magnetic fields in the jet axis: the magnetic field of the relativistic jet, EBL absorption in the intergalactic medium and the magnetic field of Milky Way. In comparison to earlier case with NGC 1275 [232], where the magnetic field of the cluster overpowered the jet magnetic field, we exclude the cluster magnetic field here, hence we had simply one domain of the jet magnetic field. This allowed us to avoid scanning over significant number of different magnetic field realisations needed in the case of magnetic fields such as the one of Perseus, extended over hundreds of kpc. In comparison, the magnetic field of relativistic jets is of the $\mathcal{O}(10)$ pc. Instead of profiling, we took one and only one magnetic field realisation and used the corresponding likelihood value. We did not profile over the uncertainties of the parameters of this specific magnetic field modelling because there is no continuous dependence over the parameters in question. In that case, only approximate solutions can be applied.

Furthermore, we are using Equation 7.7 to define the statistic. Due to the argumentation given in Section 7.3, using the Wilks' theorem to obtain the exclusion values for the 99% and 95% CLs would lead to wrong coverage. Instead, we performed 100 simulations of our dataset, and obtained the coverage from the distribution of the statistic $\mathcal{TS}(g_{a\gamma}, m_a)$. Finally, we converted the $\mathcal{TS}(g_{a\gamma}, m_a)$ into standard deviation of the corresponding Gaus-

sian: $\sigma = \sqrt{2}\,\mathrm{erf}^{-1}(\mathrm{CL})$, where erf^{-1} is the inverse of the error function and CL is the confidence level for excluding the hypothesis.

8.5 Preliminary constraints on the ALPs parameter space with the LST Mrk 421 data

In Figure 8.2 one can see exclusions in the ALPs parameter space obtained from two states of Mrk 421, as well as exclusions from the entire dataset. Dashed and solid black lines are representing 95% and 99% CL exclusions, respectively. We obtained them using the distribution of test statistic of 100 simulations of our dataset, defined as in Equation 7.7.

The difference in constraining power of the flaring, in comparison to low-activity state, shown in Figure 8.2, confirms the importance of flaring states in ALP studies, but also suggests the superiority and importance that high statistics has in overall exclusions. Although showing no strong activity of the source in the period, dataset marked as "low activity" state gives strong constraints in scanned part of the parameter space.

Having in mind that these results are preliminary, this is an important point to be studied. Conclusions of existing studies performed with IACTs data [159, 160, 179], and confirmed with our study with Perseus data of MAGIC discussed in Chapter 7, suggest the domination of flaring states over low activity states data in overall exclusions on ALPs. High photon flux has indeed been proven to give better sensitivity to measuring ALPs signatures in the spectra, but an exception could arise in the case of sources such as Markarians. Mrk 421 and Mrk 501 are one of the closest and brightest sources in the VHEs gamma-ray sky, observed in dedicated and extensive campaigns due to their particular behaviour exhibiting often (yearly and more frequent) flaring episodes e. g. [328–331]. As such, available datasets include hundreds of hours of observations, good part of which are taken during flaring states of the sources.

In comparison to previous constraints obtained in the part of ALPs parameter space shown in Figure 8.3, our analysis and dataset collected with LST-1 let us set the strongest preliminary constraints up to date. Figure 8.3 shows preliminary constraints obtained in our study using the data of Mrk 421 collected with LST-1, in particular the 99% CL, compared with current 95% CL limits obtained in existing studies.

8.6 Next steps and future prospects

Results presented in previous section are serving as a prelude to the complete analysis of entire LST-1 dataset of blazars. Motivated by preliminary constraints shown in Figure 8.3, our goal is to analyse the data of the remaining sources: Mrk 501, BL Lac, 1ES 1595+650 and PG 1553+113. Paying attention to individual configurations of magnetic fields along the line of sight, we aim to evaluate different models of ALPs in the available part of the ALPs parameter space. Furthermore, we plan to investigate the impact that energy

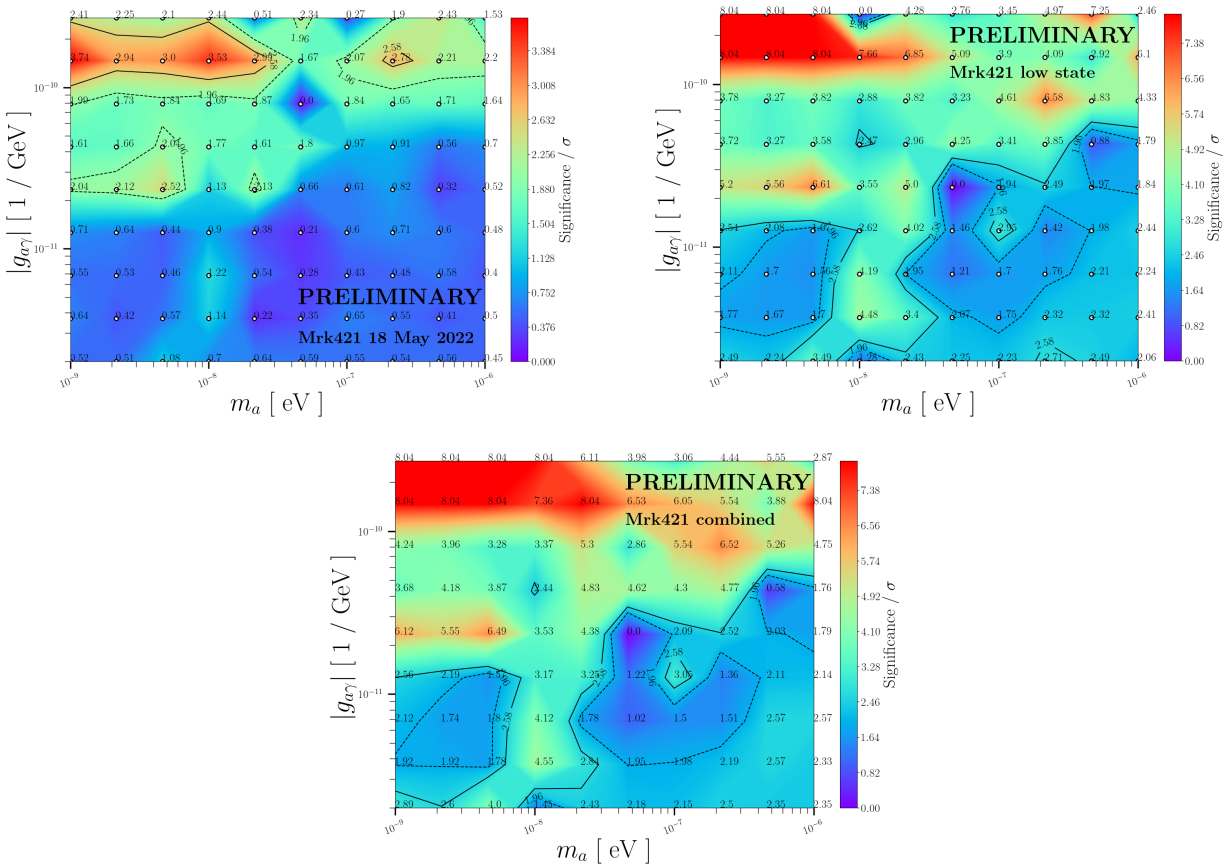

Figure 8.2: The likelihood-ratio statistic $\mathcal{TS}$ of Equation 7.7 is computed over 90 ALP points with m_a and $g_{a\gamma}$ using the data in Table 8.1. For each point, the obtained statistic is then compared to the distribution of $\mathcal{TS}$ one would get assuming the corresponding ALP hypothesis m_a and $g_{a\gamma}$ to be true. The obtained p-value is converted in the 1-dimensional-Gaussian equivalent standard deviations σ (also known as $z-$scores). Black dashed lines are showing a significance of 1.96 σ corresponding to a 95% CL, while black solid lines are representing 99% CL.

binning has on final results and how to optimise this choice for blazars from our selected group of sources.

Attention has to be given on modelling of magnetic fields of relativistic jets, in particular to test different values of parameters obtained in Potter and Cotter [194]. In case one decides to consider data of FSRQs, complete photon-photon dispersion within the relativistic jet is to be taken into account, as done in [195, 275]. This is an important point that has not been included in other studies up to date, but is to be considered since the dispersion off of other photon fields within the blazar can impact the total photon-ALP conversion. This includes photon fields produced by the accretion disk, the broad line region, the dust torus, starlight, and the synchrotron field [275].

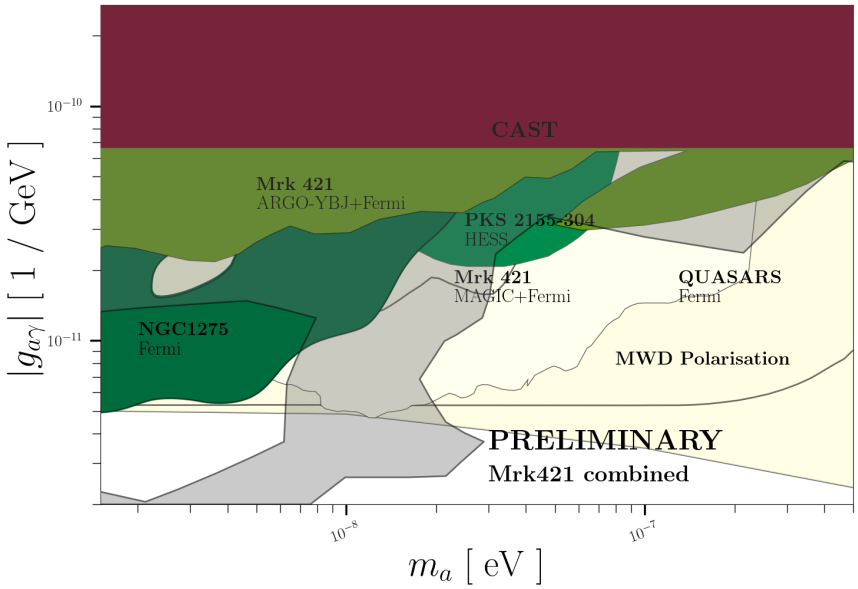

Figure 8.3: The 99% CL limits obtained with Mrk 421 data of LST-1 in comparison with current 95% CL limits in similar part of the parameter space, gathered in [86].

Once all the previous questions are addressed for each source individually, our goal is to combine the obtained constraints into total exclusion region that can be set using the blazars data collected with the LST-1.

Chapter 9

Conclusions

In this thesis, we offered insights into the state of the art of searches for ALPs, peculiar particles uniting the physics outside of SM with astroparticle physics of the entire EM spectrum. Emerging from the axion, a viable solution for the strong CP problem of QCD, ALPs are suggested to be produced in various theories unifying fundamental forces [75], string theories [76–78] and other extensions of SM. Most intriguing motivation in search for ALPs comes from their potential to unveil the nature of DM, serving as a viable candidate for its characterisation. As an introduction we outlined current initiatives and experiments searching for ALPs.

When travelling through magnetic fields, ALPs can convert to photons and back, leaving signatures in the observed photon signal. This phenomenon has been the main key in searching for ALPs. This is true for laboratory experiments in search for solar or DM axions, but also studies using indirect detection of ALPs in photon flux associated to VHE emission of astrophysical objects. In our case, we investigated VHE gamma-ray signal in which we searched for signatures called "wiggles", occurring due to the aforementioned mixing of photons and ALPs in astrophysical magnetic fields in the line of sight, on gamma ray's path from the emission site to the telescope. These oscillations are expected around critical energy E_{crit} related to the mass m_a and strength of ALPs coupling to photons $g_{a\gamma}$, but also the nature of the ambient magnetic field, and in the first place, its strength B.

In our study, we interconnected ALPs and studies of AGNs located in rich GCs. Datasets processed in this thesis were collected with IACTs, namely the MAGIC telescopes array and standalone LST-1. In the main study, we analysed the data of NGC 1275 in the centre of Perseus GC. In total, 43.1 hours of data, divided in three activity states, one flaring state, detected on 1st of January 2017, following post-flaring state observed during two days after the flare, and low activity state spanning from September of 2016 to February of 2017. Our data is analysed with MAGIC proprietary software MARS and processed with `magicDL3` [318], a MAGIC proprietary software that converts data files from MAGIC `ROOT` format into standardised data files [265]. Remaining analysis was performed with `gammapy` [1].

[1] https://gammapy.org/

To test the existence of ALPs and their impact on the observed spectrum of the source, we calculated the photon survival probability on its way through magnetic fields in the AGN site, Perseus GC, IGMF and the Milky Way, in which the final reconversion of ALPs back to photons is possible. The strength of the ambient magnetic field is found to be $(O) \sim \mu$G for astrophysical magnetic fields in galaxies and galaxy clusters, setting the E_{crit} in the GeV –TeV energy range for $m_a \sim$neV and $g_{a\gamma} \sim 10^{-11}\,\mathrm{GeV}^{-1}$, respectively. To evaluate the models of ALPs, we scanned the ALP parameter space defined by their mass and coupling to photons, and selected 154 combinations of parameters to compute and test the models. For computation of photon survival probability, we used `GammaALPs`, a python code that solves the equations of motion of the photon-ALP system based on the input parameters of ALPs and environments in the line of sight and at the emission site [2]. Once folded with the intrinsic model of our source, we compared the ALPs models with the observed spectrum and computed the test statistic from the simulations to obtain our results and exclusions in the parameter space. Novelty of our study is a new approach to the statistical evaluation of the models assuming the existence of ALPs signatures in the spectrum of NGC 1275, where for the first time a complete coverage was computed, yielding 95% and 99% confidence levels for projecting the exclusion regions in the ALPs parameter space. Despite finding no statistical evidence of ALP signatures, we were able to exclude ALP models in the sub-micro electronvolt range and establish the most stringent limits for ALPs with masses around 40 neV [232].

Apart from that, as a part of our study, we tested the sensitivity of VHE gamma-ray data observed with IACTs to signatures of ALPs. Investigating the models of ALPs that we claim to exclude, we compared the spectra obtained with the models in question with the intrinsic spectrum of the source and concluded that using our dataset and methodology, we were able to exclude models that manifest as "sudden" jumps in photon survival probability, rather than "wiggles" that we expected to constrain. This conclusion can be extended to similar studies performed up to date, most of which suggested to search for this signature in particular.

Furthermore, we expanded our analysis to data of blazars. In this case, we used data of another IACT, standalone LST-1 telescope, and initiated the research with the data from Mrk 421 blazar. Our dataset was divided into two subsets, based on the activity of the source, following which we had one dataset representing the flaring state detected on 18th of May 2022 and second one corresponding to a low activity state from December 2020 to February 2023, with the aforementioned flaring state excluded. In total, 64.8 hours of data. Data analysis was performed with the `lstchain` software developed for the analysis of LST-1 data, while the high level analysis was done as for the case of NGC 1275, using the `gammapy` software. Following the statistical approach as before, we tested 90 combinations of ALPs parameters by convoluting them within the intrinsic fit function that in this case corresponded to an EPWL. Results showed that the statistic of the data has a supremacy in setting the constraints, and that low activity state in this case can be used for setting stronger constraints than with only short flaring activity episodes.

[2]Hosted on GitHub (`https://github.com/me-manu/gammaALPs`) and archived on Zenodo [1]

Our intention is to explore the entire dataset of blazars observed with LST-1, including four other sources, Mrk 510, BL Lac, 1ES1959+650 and PG1553+113 namely. This said, we plan to test different models of blazar relativistic jets, along with magnetic fields in remaining environments in the line of sight. Finally, combination of constraints from all respective sources individually is to be performed, obtaining complete picture in the ALP parameter space using the LST-1 data of blazars.

In conclusion, this thesis gave an overview of the current search for ALPs along with the application of the ALP phenomenology in the field of astroparticle physics. We have demonstrated that the search for ALPs with the VHE gamma-ray data is not only feasible, but also competitive with the latest studies of ALPs, as it is seen from the results of our study conducted with the data of the Perseus galaxy cluster. Despite finding no statistical evidence of ALP signatures, we have shown the importance of the modelling of magnetic fields surrounding the target of interest and in the line of sight. From the analysis point of view, we developed an analysis approach able to compute complete coverage of the parameter space containing considered models of ALPs within reasonable time and available computational power. This is the first time that such analysis was performed, given that the previous approach, considering only few points in the parameter space, was already computationally demanding. Aside of the sources embedded in strong magnetic fields of galaxy clusters, we have studied sources with different magnetic field configurations, specifically blazars, in whose case the modelling of the magnetic field of the relativistic jet can dominate in the total photon-ALP conversion. Finally, we discussed a new approach to ALPs studies using the VHE gamma-ray data, suggesting that the full potential of this topic is yet to be discovered.

Bibliography

[1] M. Meyer, J. Davies, and J. Kuhlmann. gammalps, June 2021. URL https://doi.org/10.5281/zenodo.6344566.

[2] A. Pais and S. B. Treiman. How many charm quantum numbers are there? *Physical Review Letters*, 35:1556–1559, Dec 1975. doi: 10.1103/PhysRevLett.35.1556. URL https://link.aps.org/doi/10.1103/PhysRevLett.35.1556.

[3] A. G. Riess et al. Observational Evidence from Supernovae for an Accelerating Universe and a Cosmological Constant. *The Astronomical Journal*, 116(3):1009–1038, September 1998. URL https://ui.adsabs.harvard.edu/abs/1998AJ....116.1009R.

[4] S. Perlmutter and The Supernova Cosmology Project. Measurements of Ω and Λ from 42 High-Redshift Supernovae. *The Astrophysical Journal*, 517(2):565–586, June 1999. URL https://ui.adsabs.harvard.edu/abs/1999ApJ...517..565P.

[5] P. J. Peebles and B. Ratra. Cosmology with a Time-Variable Cosmological "Constant". *The Astrophysical Journal Letters*, 325:L17, February 1988. URL https://ui.adsabs.harvard.edu/abs/1988ApJ...325L..17P.

[6] S. Weinberg. The cosmological constant problem. *Reviews of Modern Physics*, 61 (1):1–23, January 1989. URL https://ui.adsabs.harvard.edu/abs/1989RvMP...61....1W.

[7] N. Aghanim et al. (Planck Collaboration). Planck 2018 results. VI. Cosmological parameters. *Astronomy & Astrophysics*, 641:A6, 2020. URL https://ui.adsabs.harvard.edu/abs/2020A&A...641A...6P. [Erratum: Astron.Astrophys. 652, C4 (2021)].

[8] R. D. Peccei and H. R. Quinn. CP conservation in the presence of pseudoparticles. *Physical Review Letters*, 38:1440–1443, Jun 1977. URL https://link.aps.org/doi/10.1103/PhysRevLett.38.1440.

[9] R. D. Peccei and H. R. Quinn. Constraints imposed by CP conservation in the presence of pseudoparticles. *Physical Review D*, 16:1791–1797, Sep 1977. URL https://link.aps.org/doi/10.1103/PhysRevD.16.1791.

[10] F. Zwicky. Die Rotverschiebung von extragalaktischen Nebeln. *Helvetica Physica Acta*, 6:110–127, January 1933. URL https://ui.adsabs.harvard.edu/abs/1933AcHPh...6..110Z.

[11] F. Zwicky. On the Masses of Nebulae and of Clusters of Nebulae. *The Astrophysical Journal*, 86:217, October 1937. URL https://ui.adsabs.harvard.edu/abs/1937ApJ....86..217Z.

[12] V. C. Rubin and W. K. Jr. Ford. Rotation of the Andromeda Nebula from a Spectroscopic Survey of Emission Regions. *The Astrophysical Journal*, 159:379, February 1970. URL https://ui.adsabs.harvard.edu/abs/1970ApJ...159..379R.

[13] B. Audren et al. Strongest model-independent bound on the lifetime of Dark Matter. *Journal of Cosmology and Astroparticle Physics*, 2014(12):028–028, December 2014. URL https://ui.adsabs.harvard.edu/abs/2014JCAP...12..028A.

[14] R. L. Workman et al. Review of Particle Physics. *PTEP*, 2022:083C01, 2022. URL https://doi.org/10.1093/ptep/ptac097.

[15] P. J. E. Peebles. *The large-scale structure of the universe*. Princeton University Press, 1980. URL https://ui.adsabs.harvard.edu/abs/1980lssu.book.....P.

[16] B. Paczynski. Gravitational Microlensing by the Galactic Halo. *The Astrophysical Journal*, 304:1, May 1986. doi: 10.1086/164140. URL https://ui.adsabs.harvard.edu/abs/1986ApJ...304....1P.

[17] K. Griest. Galactic Microlensing as a Method of Detecting Massive Compact Halo Objects. *The Astrophysical Journal*, 366:412, January 1991. URL https://ui.adsabs.harvard.edu/abs/1991ApJ...366..412G.

[18] C. Alcock et al. The MACHO Project: Microlensing Results from 5.7 Years of Large Magellanic Cloud Observations. *The Astrophysical Journal*, 542(1):281–307, October 2000. URL https://ui.adsabs.harvard.edu/abs/2000ApJ...542..281A.

[19] P. Tisserand et al. (EROS-2 Collaboration). Limits on the Macho content of the Galactic Halo from the EROS-2 Survey of the Magellanic Clouds. *Astronomy & Astrophysics*, 469(2):387–404, July 2007. URL https://ui.adsabs.harvard.edu/abs/2007A&A...469..387T.

[20] L. Wyrzykowski et al. The OGLE view of microlensing towards the Magellanic Clouds - I. A trickle of events in the OGLE-II LMC data. *Monthly Notices of the Royal Astronomical Society*, 397(3):1228–1242, August 2009. doi: 10.1111/j.1365-2966.2009.15029.x. URL https://ui.adsabs.harvard.edu/abs/2009MNRAS.397.1228W.

[21] G. Steigman et al. Dynamical interactions and astrophysical effects of stable heavy neutrinos. *The Astronomical Journal*, 83:1050–1061, September 1978. URL https://ui.adsabs.harvard.edu/abs/1978AJ.....83.1050S.

[22] S. Dodelson and L. M. Widrow. Sterile neutrinos as dark matter. *Physical Review Letters*, 72(1):17–20, January 1994. URL https://ui.adsabs.harvard.edu/abs/1994PhRvL..72...17D.

[23] B. Carr, f. Kühnel, and M. Sandstad. Primordial black holes as dark matter. *Physical Review D*, 94(8):083504, October 2016. URL https://ui.adsabs.harvard.edu/abs/2016PhRvD..94h3504C.

[24] F. Capela, M. Pshirkov, and P. Tinyakov. Constraints on primordial black holes as dark matter candidates from capture by neutron stars. *Physical Review D*, 87 (12):123524, June 2013. URL https://ui.adsabs.harvard.edu/abs/2013PhRvD..87l3524C.

[25] H. Niikura et al. Microlensing constraints on primordial black holes with Subaru/HSC Andromeda observations. *Nature Astronomy*, 3:524–534, April 2019. URL https://ui.adsabs.harvard.edu/abs/2019NatAs...3..524N.

[26] C. Boehm, T. A. Enßlin, and J. Silk. Can annihilating dark matter be lighter than a few GeVs? *Journal of Physics G Nuclear Physics*, 30(3):279–285, March 2004. URL https://ui.adsabs.harvard.edu/abs/2004JPhG...30..279B.

[27] K. Griest and M. Kamionkowski. Unitarity limits on the mass and radius of dark-matter particles. *Physical Review Letters*, 64:615–618, Feb 1990. URL https://link.aps.org/doi/10.1103/PhysRevLett.64.615.

[28] G. Jungman, M. Kamionkowski, and K. Griest. Supersymmetric dark matter. *Physics Reports*, 267:195–373, March 1996. URL https://ui.adsabs.harvard.edu/abs/1996PhR...267..195J.

[29] D. J. H. Chung, E. W. Kolb, and A. Riotto. Superheavy dark matter. *Physical Review D*, 59(2):023501, December 1998. URL https://ui.adsabs.harvard.edu/abs/1998PhRvD..59b3501C.

[30] V. A. Kuzmin and I. I. Tkachev. Ultrahigh-energy cosmic rays, superheavy long-lived particles, and matter creation after inflation. *Soviet Journal of Experimental and Theoretical Physics Letters*, 68(4):271–275, August 1998. URL https://ui.adsabs.harvard.edu/abs/1998JETPL..68..271K.

[31] V. A. Kuzmin and I. I. Tkachev. Ultra-high-energy cosmic rays and inflation relics. *Physics Reports*, 320(1):199–221, October 1999. URL https://ui.adsabs.harvard.edu/abs/1999PhR...320..199K.

[32] D. Tak, M. Baumgart Matthew, N. L. Rodd, and E. Pueschel. Current and Future γ-Ray Searches for Dark Matter Annihilation Beyond the Unitarity Limit. *The Astrophysical Journal Letters*, 938(1):L4, October 2022. URL https://ui.adsabs.harvard.edu/abs/2022ApJ...938L...4T.

[33] L. Roszkowski, E. M. Sessolo, and S. Trojanowski. WIMP dark matter candidates and searches—current status and future prospects. *Reports on Progress in Physics*, 81(6):066201, June 2018. URL https://ui.adsabs.harvard.edu/abs/2018RPPh..81f6201R.

[34] M. Doro, M. A. Sánchez-Conde, and M. Hütten. Fundamental Physics Searches with IACTs. *arXiv e-prints*, art. arXiv:2111.01198, November 2021. URL https://ui.adsabs.harvard.edu/abs/2021arXiv211101198D.

[35] P. Arias et al. WISPy cold dark matter. *Journal of Cosmology and Astroparticle Physics*, 2012(6):013, June 2012. URL https://ui.adsabs.harvard.edu/abs/2012JCAP...06..013A.

[36] R. D. Peccei. QCD, strong CP and axions. *Journal of the Korean Physical Society*, 29:S199–S208, September 1996. URL https://ui.adsabs.harvard.edu/abs/1996JKPS...29S.199P.

[37] N. Arkani-Hamed et al. A theory of dark matter. *Physical Review D*, 79(1):015014, January 2009. URL https://ui.adsabs.harvard.edu/abs/2009PhRvD..79a5014A.

[38] J. Khoury and A. Weltman. Chameleon cosmology. *Physical Review D*, 69:044026, Feb 2004. URL https://link.aps.org/doi/10.1103/PhysRevD.69.044026.

[39] L. Bergström and J. Kaplan. Gamma ray lines from TeV dark matter. *Astroparticle Physics*, 2(3):261–268, August 1994. URL https://ui.adsabs.harvard.edu/abs/1994APh.....2..261B.

[40] T. Bringmann, L. Bergström, and J. Edsjö. New gamma-ray contributions to supersymmetric dark matter annihilation. *Journal of High Energy Physics*, 2008(1):049, January 2008. URL https://ui.adsabs.harvard.edu/abs/2008JHEP...01..049B.

[41] T. C. Weekes et al. (VERITAS Collaboration). VERITAS: the Very Energetic Radiation Imaging Telescope Array System. *Astroparticle Physics*, 17(2):221–243, May 2002. URL https://ui.adsabs.harvard.edu/abs/2002APh....17..221W.

[42] J. A. Hinton et al. (HESS Collaboration). The status of the HESS project. *New Astronomy Reviews*, 48(5-6):331–337, April 2004. URL https://ui.adsabs.harvard.edu/abs/2004NewAR..48..331H.

[43] B. S. Acharya et al. The Cherenkov Telescope Array Consortium. *Science with the Cherenkov Telescope Array*. World Scientific, 2019. URL https://ui.adsabs.harvard.edu/abs/2019scta.book.....C.

[44] C. Deil et al. Gammapy - A prototype for the CTA science tools. In *35th International Cosmic Ray Conference (ICRC2017)*, volume 301 of *International Cosmic Ray Conference*, page 766, January 2017. URL https://ui.adsabs.harvard.edu/abs/2017ICRC...35..766D.

[45] A. Di Domenico. Testing cpt symmetry with neutral k mesons: A review. *Symmetry*, 12(12), 2020. ISSN 2073-8994. URL https://www.mdpi.com/2073-8994/12/12/2063.

[46] J. P. Lees et al. (The BABAR Collaboration). Observation of Time-Reversal Violation in the B^0 Meson System. *Physical Review Letters*, 109(21):211801, November 2012. URL https://ui.adsabs.harvard.edu/abs/2012PhRvL.109u1801L.

[47] M. E. Peskin and D. V. Schroeder. *An Introduction to Quantum Field Theory*. Addison-Wesley, Reading, USA, 1995. ISBN 978-0-201-50397-5. URL https://ui.adsabs.harvard.edu/abs/1995iqft.book.....P.

[48] M. D. Schwartz. *Quantum Field Theory and the Standard Model*. Cambridge University Press, 3 2014. ISBN 978-1-107-03473-0, 978-1-107-03473-0. URL https://ui.adsabs.harvard.edu/abs/2014qfts.book.....S.

[49] S. Weinberg. The u(1) problem. *Physical Review D*, 11:3583–3593, Jun 1975. URL https://link.aps.org/doi/10.1103/PhysRevD.11.3583.

[50] G. 't Hooft. Symmetry breaking through bell-jackiw anomalies. *Physical Review Letters*, 37:8–11, Jul 1976. URL https://link.aps.org/doi/10.1103/PhysRevLett.37.8.

[51] C.G. Callan, R.F. Dashen, and D.J. Gross. The structure of the gauge theory vacuum. *Physics Letters B*, 63(3):334–340, 1976. ISSN 0370-2693. URL https://www.sciencedirect.com/science/article/pii/037026937690277X.

[52] R. Jackiw and C. Rebbi. Vacuum periodicity in a yang-mills quantum theory. *Physical Review Letters*, 37:172–175, Jul 1976. URL https://link.aps.org/doi/10.1103/PhysRevLett.37.172.

[53] Alessandro A. de Angelis and M. Roncadelli G. Galanti. Relevance of axionlike particles for very-high-energy astrophysics. *Physical Review D*, 84(10):105030, November 2011. URL https://ui.adsabs.harvard.edu/abs/2011PhRvD..84j5030D.

[54] E. Wigner. Einige Folgerungen aus der Schrödingerschen Theorie für die Termstrukturen. *Zeitschrift fur Physik*, 43(9-10):624–652, September 1927. URL https://ui.adsabs.harvard.edu/abs/1927ZPhy...43..624W.

[55] C. Eckart. The application of group theory to the quantum dynamics of monatomic systems. *Reviews of Modern Physics*, 2:305–380, Jul 1930. URL https://link.aps.org/doi/10.1103/RevModPhys.2.305.

[56] C. Abel et al. Measurement of the permanent electric dipole moment of the neutron. *Physical Review Letters*, 124:081803, Feb 2020. URL https://link.aps.org/doi/10.1103/PhysRevLett.124.081803.

[57] A. E. Nelson. Naturally Weak CP Violation. *Physics Letters B*, 136:387–391, 1984. URL https://doi.org/10.1016/0370-2693(84)92025-2.

[58] S. M. Barr. Solving the Strong CP Problem Without the Peccei-Quinn Symmetry. *Physical Review Letters*, 53:329, 1984. URL https://doi.org/10.1103/PhysRevLett.53.329.

[59] S. M. Barr. Natural class of non-peccei-quinn models. *Physical Review D*, 30:1805–1811, Oct 1984. URL https://link.aps.org/doi/10.1103/PhysRevD.30.1805.

[60] Hai-Yang Cheng. Low-energy interactions of scalar and pseudoscalar higgs bosons with baryons. *Physics Letters B*, 219(2):347–353, 1989. ISSN 0370-2693. URL https://www.sciencedirect.com/science/article/pii/0370269389904024.

[61] S. Weinberg. A new light boson? *Physical Review Letters*, 40:223–226, Jan 1978. URL https://link.aps.org/doi/10.1103/PhysRevLett.40.223.

[62] F. Wilczek. Problem of strong p and t invariance in the presence of instantons. *Physical Review Letters*, 40:279–282, Jan 1978. URL https://link.aps.org/doi/10.1103/PhysRevLett.40.279.

[63] C. Edwards et al. Upper limit for $\frac{J}{\Psi} \to \gamma + axion$. *Physical Review Letters*, 48:903–906, Apr 1982. URL https://link.aps.org/doi/10.1103/PhysRevLett.48.903.

[64] M. Sivertz et al. Upper limit for axion production in radiative Υ decay. *Physical Review D*, 26:717–719, Aug 1982. URL https://link.aps.org/doi/10.1103/PhysRevD.26.717.

[65] M. S. Alam et al. Search for axion production in Υ decay. *Physical Review D*, 27:1665–1667, Apr 1983. URL https://link.aps.org/doi/10.1103/PhysRevD.27.1665.

[66] J. E. Kim. Light Pseudoscalars, Particle Physics and Cosmology. *Physics Reports*, 150:1–177, 1987. URL https://doi.org/10.1016/0370-1573(87)90017-2.

[67] J.E. Kim. Weak-interaction singlet and strong CP invariance. *Physical Review Letters*, 43:103–107, Jul 1979. URL https://link.aps.org/doi/10.1103/PhysRevLett.43.103.

[68] M. A. Shifman, A. I. Vainshtein, and V. I. Zakharov. Can confinement ensure natural CP invariance of strong interactions? *Nuclear Physics B*, 166(3):493–506, April 1980. URL https://ui.adsabs.harvard.edu/abs/1980NuPhB.166..493S.

[69] M. Dine, W. Fischler, and M. Srednicki. A simple solution to the strong cp problem with a harmless axion. *Physics Letters B*, 104(3):199–202, aug 1981. URL https://ui.adsabs.harvard.edu/abs/1981PhLB..104..199D.

[70] A. R. Zhitnitsky. Possible suppression of axion-hadron interactions. *Soviet ournal of Nuclear Physics (Engl. Transl.); (United States)*, 31:2, 2 1980. URL https://www.osti.gov/biblio/7063072.

[71] H. Primakoff. Photo-Production of Neutral Mesons in Nuclear Electric Fields and the Mean Life of the Neutral Meson. *Physical Review*, 81(5):899–899, March 1951. URL https://ui.adsabs.harvard.edu/abs/1951PhRv...81..899P.

[72] P. Sikivie. Experimental Tests of the Invisible Axion. *Physical Review Letters*, 51: 1415–1417, 1983. URL https://doi.org/10.1103/PhysRevLett.51.1415. [Erratum: Phys.Rev.Lett. 52, 695 (1984)].

[73] G. Raffelt and L. Stodolsky. Mixing of the Photon with Low Mass Particles. *Physical Review D*, 37:1237, 1988. URL https://doi.org/10.1103/PhysRevD.37.1237.

[74] N. Turok. Almost Goldstone bosons from extra dimensional gauge theories. *Physical Review Letters*, 76:1015–1018, 1996. URL https://doi.org/10.1103/PhysRevLett.76.1015.

[75] S. Chang, S. Tazawa, and M. Yamaguchi. Axion model in extra dimensions with TeV scale gravity. *Physical Review D*, 61:084005, 2000. URL https://doi.org/10.1103/PhysRevD.61.084005.

[76] E. Witten. Some Properties of O(32) Superstrings. *Physics Letters B*, 149:351–356, 1984. URL https://doi.org/10.1016/0370-2693(84)90422-2.

[77] P. Svrcek and E. Witten. Axions In String Theory. *Journal of High Energy Physics*, 06:051, 2006. URL https://doi.org/10.1088/1126-6708/2006/06/051.

[78] J. P. Conlon. The QCD axion and moduli stabilisation. *Journal of High Energy Physics*, 05:078, 2006. URL https://doi.org/10.1088/1126-6708/2006/05/078.

[79] J. Jaeckel and A. Ringwald. The Low-Energy Frontier of Particle Physics. *Ann. Rev. Nucl. Part. Sci.*, 60:405–437, 2010. URL https://doi.org/10.1146/annurev.nucl.012809.104433.

[80] K. K. van Bibber, P. M. McIntyre, D. E. Morris, and G. G. Raffelt. Design for a practical laboratory detector for solar axions. *Physical Review D*, 39:2089–2099, Apr 1989. URL https://link.aps.org/doi/10.1103/PhysRevD.39.2089.

[81] D. M. Lazarus et al. Search for solar axions. *Physical Review Letters*, 69:2333–2336, Oct 1992. URL https://link.aps.org/doi/10.1103/PhysRevLett.69.2333.

[82] S. Moriyama et al. Direct search for solar axions by using strong magnetic field and x-ray detectors. *Physics Letters B*, 434:147, 1998. URL https://doi.org/10.1016/S0370-2693(98)00766-7.

[83] R. D. Peccei. *in 'CP Violation' ed. by C. Jarlskog*. World Scientific Publ., 1989. URL https://doi.org/10.1142/9789814503280_0013.

[84] G. Raffelt and L. Stodolsky. Mixing of the photon with low-mass particles. *Physical Review D*, 37(5):1237–1249, March 1988. URL https://ui.adsabs.harvard.edu/abs/1988PhRvD..37.1237R.

[85] A. Mirizzi, G. G. Raffelt, and P. D. Serpico. Photon-axion conversion in intergalactic magnetic fields and cosmological consequences. *Lecture Notes in Physics*, 741:115–134, 2008. URL https://doi.org/10.1007/978-3-540-73518-2_7.

[86] C. O'HARE. cajohare/axionlimits: Axionlimits, July 2020. URL https://doi.org/10.5281/zenodo.3932430.

[87] K. Zioutas et al. First results from the CERN Axion Solar Telescope (CAST). *Physical Review Letters*, 94:121301, 2005. URL https://doi.org/10.1103/PhysRevLett.94.121301.

[88] V. et al. (CAST Collaboration) V. Anastassopoulos. New CAST limit on the axion-photon interaction. *Nature Physics*, 13(6):584–590, June 2017. URL https://ui.adsabs.harvard.edu/abs/2017NatPh..13..584A.

[89] E. Armengaud et al. Physics potential of the International Axion Observatory (IAXO). *Journal of Cosmology and Astroparticle Physics*, 06:047, 2019. URL https://doi.org/10.1088/1475-7516/2019/06/047.

[90] A. Abeln et al. Conceptual design of BabyIAXO, the intermediate stage towards the International Axion Observatory. *Journal of High Energy Physics*, 05:137, 2021. URL https://doi.org/10.1007/JHEP05(2021)137.

[91] M. Giannotti et al. Stellar Recipes for Axion Hunters. *Journal of Cosmology and Astroparticle Physics*, 10:010, 2017. URL https://doi.org/10.1088/1475-7516/2017/10/010.

[92] S. Cebrian et al. Prospects of solar axion searches with crystal detectors. *Astroparticle Physics*, 10:397–404, 1999. URL https://doi.org/10.1016/S0927-6505(98)00069-3.

[93] F.T. III Avignone et al. (SOLAX Collaboration). Experimental search for solar axions via coherent Primakoff conversion in a germanium spectrometer. *Physical Review Letters*, 81:5068–5071, 1998. URL https://doi.org/10.1103/PhysRevLett.81.5068.

[94] R. Bernabei et al. (DAMA Collaboration). Search for solar axions by primakoff effect in nai crystals. *Physics Letters B*, 515(1):6–12, 2001. ISSN 0370-2693. doi: https://doi.org/10.1016/S0370-2693(01)00840-1. URL https://www.sciencedirect.com/science/article/pii/S0370269301008401.

[95] A. Morales et al. (COSME Collaboration). Particle dark matter and solar axion searches with a small germanium detector at the Canfranc Underground Laboratory. *Astroparticle Physics*, 16:325–332, 2002. URL https://doi.org/10.1016/S0927-6505(01)00117-7.

[96] Z. Ahmed et al. (CDMS Collaboration). Search for Axions with the CDMS Experiment. *Physical Review Letters*, 103:141802, 2009. URL https://doi.org/10.1103/PhysRevLett.103.141802.

[97] R. Ruoso et al. (BFRT Experiment). Limits on light scalar and pseudoscalar particles from a photon regeneration experiment. *Zeitschrift für Physik*, 56:505–508, 1992. URL https://doi.org/10.1007/BF01474722.

[98] R. Cameron et al. Search for nearly massless, weakly coupled particles by optical techniques. *Physical Review D*, 47:3707–3725, May 1993. URL https://link.aps.org/doi/10.1103/PhysRevD.47.3707.

[99] R. Ballou et al. (OSQAR Collaboration). New exclusion limits on scalar and pseudoscalar axionlike particles from light shining through a wall. *Physical Review D*, 92:092002, Nov 2015. URL https://link.aps.org/doi/10.1103/PhysRevD.92.092002.

[100] F. Hoogeveen and T. Ziegenhagen. Production and detection of light bosons using optical resonators. *Nuclear Physics B*, 358(1):3–26, 1991. ISSN 0550-3213. URL https://www.sciencedirect.com/science/article/pii/0550321391905286.

[101] P. Sikivie et al. Resonantly enhanced axion-photon regeneration. *Physical Review Letters*, 98:172002, Apr 2007. URL https://link.aps.org/doi/10.1103/PhysRevLett.98.172002.

[102] G. Mueller et al. Detailed design of a resonantly enhanced axion-photon regeneration experiment. *Physical Review D*, 80:072004, Oct 2009. URL https://link.aps.org/doi/10.1103/PhysRevD.80.072004.

[103] R. Bähre et al. Any light particle search II —Technical Design Report. *JINST*, 8: T09001, 2013. URL https://doi.org/10.1088/1748-0221/8/09/T09001.

[104] K. Ehret et al. New ALPS Results on Hidden-Sector Lightweights. *Physics Letters B*, 689:149–155, 2010. URL https://doi.org/10.1016/j.physletb.2010.04.066.

[105] L. Maiani et al. Effects of Nearly Massless, Spin Zero Particles on Light Propagation in a Magnetic Field. *Physics Letters B*, 175:359–363, 1986. URL https://doi.org/10.1016/0370-2693(86)90869-5.

[106] E. Zavattini. Experimental Observation of Optical Rotation Generated in Vacuum by a Magnetic Field. *Physical Review Letters*, 96(11):110406, March 2006. URL https://ui.adsabs.harvard.edu/abs/2006PhRvL..96k0406Z.

[107] E. et al. (PVLAS Collaboration) Zavattini. New PVLAS results and limits on magnetically induced optical rotation and ellipticity in vacuum. *Physical Review D*, 77: 032006, 2008. URL https://doi.org/10.1103/PhysRevD.77.032006.

[108] W. H. Press and P. Schechter. Formation of Galaxies and Clusters of Galaxies by Self-Similar Gravitational Condensation. *The Astrophysical Journal*, 187:425–438, February 1974. URL https://ui.adsabs.harvard.edu/abs/1974ApJ...187..425P.

[109] W. Giaré, E. Di Valentino, A. Melchiorri, and O. Mena. New cosmological bounds on hot relics: axions and neutrinos. *Monthly Notices of the Royal Astronomical Society*, 505(2):2703–2711, August 2021. URL https://ui.adsabs.harvard.edu/abs/2021MNRAS.505.2703G.

[110] D. Cadamuro and J. Redondo. Cosmological bounds on pseudo Nambu-Goldstone bosons. *Journal of Cosmology and Astroparticle Physics*, 02:032, 2012. URL https://doi.org/10.1088/1475-7516/2012/02/032.

[111] P. F. Depta, M. Hufnagel, and K. Schmidt-Hoberg. Robust cosmological constraints on axion-like particles. *Journal of Cosmology and Astroparticle Physics*, 05:009, 2020. URL https://doi.org/10.1088/1475-7516/2020/05/009.

[112] P. Arias et al. WISPy cold dark matter. *Journal of Cosmology and Astroparticle Physics*, 2012(6):013, June 2012. URL https://ui.adsabs.harvard.edu/abs/2012JCAP...06..013A.

[113] Pierre Sikivie. Axion searches. *Nuclear Physics B - Proceedings Supplements*, 87: 41–52, 2000. URL https://doi.org/10.1016/S0920-5632(00)00628-9.

[114] A.D. Linde. Generation of isothermal density perturbations in the inflationary universe. *Physics Letters B*, 158(5):375–380, 1985. ISSN 0370-2693. URL https://www.sciencedirect.com/science/article/pii/0370269385904368.

[115] C. Hagmann and P. Sikivie. Computer simulations of the motion and decay of global strings. *Nuclear Physics B*, 363(1):247–280, 1991. ISSN 0550-3213. URL https://www.sciencedirect.com/science/article/pii/055032139190243Q.

[116] S. Chang, C. Hagmann, and P. Sikivie. Studies of the motion and decay of axion walls bounded by strings. *Physical Review D*, 59:023505, 1999. URL https://doi.org/10.1103/PhysRevD.59.023505.

[117] T. Hiramatsu, Masahiro M. Kawasaki, and K. Saikawa. Gravitational Waves from Collapsing Domain Walls. *Journal of Cosmology and Astroparticle Physics*, 05:032, 2010. URL https://doi.org/10.1088/1475-7516/2010/05/032.

[118] A. Ringwald and K. Saikawa. Axion dark matter in the post-inflationary Peccei-Quinn symmetry breaking scenario. *Physical Review D*, 93(8):085031, 2016. URL https://doi.org/10.1103/PhysRevD.93.085031. [Addendum: Phys.Rev.D 94, 049908 (2016)].

[119] V. B. Klaer and G. D. Moore. The dark-matter axion mass. *Journal of Cosmology and Astroparticle Physics*, 2017(11):049, November 2017. URL https://ui.adsabs.harvard.edu/abs/2017JCAP...11..049K.

[120] M. Gorghetto, E. Hardy, and G. Villadoro. More axions from strings. *SciPost Physics*, 10(2):050, 2021. URL https://doi.org/10.21468/SciPostPhys.10.2.050.

[121] P. Sikivie. Invisible Axion Search Methods. *Reviews of Modern Physics*, 93(1):015004, 2021. URL https://doi.org/10.1103/RevModPhys.93.015004.

[122] S. DePanfilis et al. Limits on the abundance and coupling of cosmic axions at 4.5 $m_a; 5.0 \mu ev$. *Physical Review Letters*, 59:839–842, Aug 1987. URL https://link.aps.org/doi/10.1103/PhysRevLett.59.839.

[123] C. Hagmann et al. Results from a search for cosmic axions. *Physical Review D*, 42: 1297–1300, Aug 1990. URL https://link.aps.org/doi/10.1103/PhysRevD.42.1297.

[124] R. Khatiwada et al. (ADMX Collaboration). Axion Dark Matter Experiment: Detailed design and operations. *Rev. Sci. Instrum.*, 92(12):124502, 2021. URL https://doi.org/10.1063/5.0037857.

[125] C. Bartram et al. (ADMX Collaboration). Search for invisible axion dark matter in the $3.3 - -4.2$ μeV mass range. *Physical Review Letters*, 127:261803, Dec 2021. URL https://link.aps.org/doi/10.1103/PhysRevLett.127.261803.

[126] C. Boutan et al. (ADMX Collaboration). Piezoelectrically tuned multimode cavity search for axion dark matter. *Physical Review Letters*, 121:261302, Dec 2018. URL https://link.aps.org/doi/10.1103/PhysRevLett.121.261302.

[127] L. et al. (HAYSTAC Collaboration) Zhong. Results from phase 1 of the HAYSTAC microwave cavity axion experiment. *Physical Review D*, 97(9):092001, 2018. URL https://doi.org/10.1103/PhysRevD.97.092001.

[128] S. Lee et al. Axion dark matter search around 6.7 μeV. *Physical Review Letters*, 124:101802, Mar 2020. URL https://link.aps.org/doi/10.1103/PhysRevLett.124.101802.

[129] J. Jeong et al. Search for Invisible Axion Dark Matter with a Multiple-Cell Haloscope. *Physical Review Letters*, 125(22):221302, 2020. URL https://doi.org/10.1103/PhysRevLett.125.221302.

[130] A. K. Yi et al. Search for the Sagittarius tidal stream of axion dark matter around 4.55 μeV. *Physical Review D*, 108(2):L021304, 2023. URL https://doi.org/10.1103/PhysRevD.108.L021304.

[131] D. Alesini et al. Search for invisible axion dark matter of mass $m_a = 43$ μeV with the QUAX–$a\gamma$ experiment. *Physical Review D*, 103(10):102004, 2021. URL https://doi.org/10.1103/PhysRevD.103.102004.

[132] D. et al. Alesini. Search for Galactic axions with a high-Q dielectric cavity. *Physical Review D*, 106(5):052007, 2022. URL https://doi.org/10.1103/PhysRevD.106.052007.

[133] B. T. McAllister et al. The ORGAN Experiment: An axion haloscope above 15 GHz. *Physics of the Dark Universe*, 18:67–72, 2017. URL https://doi.org/10.1016/j.dark.2017.09.010.

[134] A. P. Quiskamp. Direct search for dark matter axions excluding ALP cogenesis in the 63- to 67-μeV range with the ORGAN experiment. *Sci. Adv.*, 8(27):abq3765, 2022. URL https://doi.org/10.1126/sciadv.abq3765.

[135] P. Brun et al. (MADMAX Collaboration). A new experimental approach to probe QCD axion dark matter in the mass range above 40 μeV. *The European Physical Journal C*, 79(3):186, 2019. URL https://doi.org/10.1140/epjc/s10052-019-6683-x.

[136] J. L. Ouellet et al. First Results from ABRACADABRA-10 cm: A Search for Sub-μeV Axion Dark Matter. *Physical Review Letters*, 122(12):121802, 2019. URL https://doi.org/10.1103/PhysRevLett.122.121802.

[137] A. V. Gramolin et al. Search for axion-like dark matter with ferromagnets. *Nature Physics*, 17(1):79–84, 2021. URL https://doi.org/10.1038/s41567-020-1006-6.

[138] D. A. Dicus et al. Astrophysical bounds on the masses of axions and higgs particles. *Physical Review D*, 18:1829–1834, Sep 1978. URL https://link.aps.org/doi/10.1103/PhysRevD.18.1829.

[139] G. G. Raffelt. Astrophysical axion bounds. *Lecture Notes in Physics*, 741:51–71, 2008. URL https://doi.org/0.1007/978-3-540-73518-2_3.

[140] A. Weissand H. Schlattl and G. Raffelt. Helioseismological constraint on solar axion emission. *Astroparticle Physics*, 10:353–359, 1999. URL https://doi.org/10.1016/S0927-6505(98)00063-2.

[141] N. Vinyoles et al. New axion and hidden photon constraints from a solar data global fit. *Journal of Cosmology and Astroparticle Physics*, 2015(10):015, oct 2015. URL https://doi.org/10.1088/1475-7516/2015/10/015.

[142] E. Hertzsprung. Über die Sterne der Unterabteilungen c und ac nach der Spektralklassifikation von Antonia C. Maury. *Astronomische Nachrichten*, 179(24):373, January 1909. URL https://ui.adsabs.harvard.edu/abs/1909AN....179..373H.

[143] A. Ayala et al. Revisiting the bound on axion-photon coupling from Globular Clusters. *Physical Review Letters*, 113(19):191302, 2014. URL https://doi.org/10.1103/PhysRevLett.113.191302.

[144] I. G. Irastorza et al., editor. *Proceedings, 11th Patras Workshop on Axions, WIMPs and WISPs (Axion-WIMP 2015): Zaragoza, Spain, June 22-26, 2015*, Hamburg, 2015. DESY. URL https://doi.org/10.3204/DESY-PROC-2015-02.

[145] F. Capozzi and G. G. Raffelt. Axion and neutrino bounds improved with new calibrations of the tip of the red-giant branch using geometric distance determinations. *Physical Review D*, 102:083007, Oct 2020. URL https://link.aps.org/doi/10.1103/PhysRevD.102.083007.

[146] M. Bertolami et al. Revisiting the axion bounds from the Galactic white dwarf luminosity function. *Journal of Cosmology and Astroparticle Physics*, 10:069, 2014. URL https://doi.org/10.1088/1475-7516/2014/10/069.

[147] G. G. Raffeltand D. Seckel. Bounds on exotic-particle interactions from SN 1987A. *Physical Review Letters*, 60(18):1793–1796, January 1988. URL https://ui.adsabs.harvard.edu/abs/1988PhRvL..60R1793R.

[148] A. de Angelis, M. Roncadelli, and O. Mansutti. Evidence for a new light spin-zero boson from cosmological gamma-ray propagation? *Physical Review D*, 76(12):121301, December 2007. URL https://ui.adsabs.harvard.edu/abs/2007PhRvD..76l1301D.

[149] M. Simet et al. Milky Way as a kiloparsec-scale axionscope. *Physical Review D*, 77(6):063001, March 2008. URL https://ui.adsabs.harvard.edu/abs/2008PhRvD..77f3001S.

[150] M. A. Sánchez-Conde et al. Hints of the existence of axionlike particles from the gamma-ray spectra of cosmological sources. *Physical Review D*, 79(12):123511, June 2009. URL https://ui.adsabs.harvard.edu/abs/2009PhRvD..79l3511S.

[151] D. Horns et al. Hardening of TeV gamma spectrum of active galactic nuclei in galaxy clusters by conversions of photons into axionlike particles. *Physical Review D*, 86(7): 075024, October 2012. URL https://ui.adsabs.harvard.edu/abs/2012PhRvD..86g5024H.

[152] A. Dobrynina, A. Kartavtsev, and G. Raffelt. Photon-photon dispersion of TeV gamma rays and its role for photon-ALP conversion. *Physical Review D]*, 91 (8):083003, April 2015. URL https://ui.adsabs.harvard.edu/abs/2015PhRvD..91h3003D.

[153] R. J. Protheroe and H. Meyer. An infrared background-TeV gamma-ray crisis? *Physics Letters B*, 493(1-2):1–6, November 2000. URL https://ui.adsabs.harvard.edu/abs/2000PhLB..493....1P.

[154] A. Mirizzi, G. G. Raffelt, and P. D. Serpico. Signatures of axionlike particles in the spectra of TeV gamma-ray sources. *Physical Review D*, 76(2):023001, July 2007. URL https://ui.adsabs.harvard.edu/abs/2007PhRvD..76b3001M.

[155] D. Hooper and P. D. Serpico. Detecting Axionlike Particles with Gamma Ray Telescopes. *Physical Review Letters*, 99(23):231102, December 2007. URL https://ui.adsabs.harvard.edu/abs/2007PhRvL..99w1102H.

[156] A. de Angelis, O. Mansutti, M. Persic, and M. Roncadelli. Photon propagation and the very high energy γ-ray spectra of blazars: how transparent is the Universe? *Monthly Notices of the Royal Astronomical Society*, 394(1):L21–L25, March 2009. URL https://ui.adsabs.harvard.edu/abs/2009MNRAS.394L..21D.

[157] F. Tavecchio et al. Evidence for an axion-like particle from PKS 1222+216? *Physical Review D*, 86(8):085036, October 2012. URL https://ui.adsabs.harvard.edu/abs/2012PhRvD..86h5036T.

[158] G. Galanti, M. Roncadelli, A. De Angelis, and G. F. Bignami. Hint at an axion-like particle from the redshift dependence of blazar spectra. *Monthly Notices of the Royal Astronomical Society*, 493(2):1553–1564, April 2020. URL https://ui.adsabs.harvard.edu/abs/2020MNRAS.493.1553G.

[159] A. Abramowski et al. (HESS Collaboration). Constraints on axionlike particles with H.E.S.S. from the irregularity of the PKS 2155-304 energy spectrum. *Physical Review D*, 88(10):102003, November 2013. URL https://ui.adsabs.harvard.edu/abs/2013PhRvD..88j2003A.

[160] H. Abdalla et al. (The Cherenkov Telescope Array Consortium). Sensitivity of the Cherenkov Telescope Array for probing cosmology and fundamental physics with gamma-ray propagation. *Journal of Cosmology and Astroparticle Physics*, 2021(02): 048–048, feb 2021. doi: 10.1088/1475-7516/2021/02/048. URL https://doi.org/10.1088/1475-7516/2021/02/048.

[161] L. Anchordoqui et al. Ultrahigh-energy cosmic rays: The State of the art before the Auger Observatory. *International Journal of Modern Physics A*, 18:2229–2366, 2003. URL https://doi.org/10.1142/S0217751X03013879.

[162] J. W. Brockway, E. D. Carlson, and G. G. Raffelt. SN 1987A gamma-ray limits on the conversion of pseudoscalars. *Physics Letters B*, 383:439–443, February 1996. URL https://ui.adsabs.harvard.edu/abs/1996PhLB..383..439B.

[163] J. A. Grifols, E. Massó, and R. Toldrà. Gamma Rays from SN 1987A due to Pseudoscalar Conversion. *Physical Review Letters*, 77(12):2372–2375, September 1996. URL https://ui.adsabs.harvard.edu/abs/1996PhRvL..77.2372G.

[164] A. Payez et al. Revisiting the SN1987A gamma-ray limit on ultralight axion-like particles. *Journal of Cosmology and Astroparticle Physics*, 2015(2):006, February 2015. URL https://ui.adsabs.harvard.edu/abs/2015JCAP...02..006P.

[165] G. G. Raffelt. *Stars as laboratories for fundamental physics : the astrophysics of neutrinos, axions, and other weakly interacting particles*. The University of Chicago Press, 1996. URL https://ui.adsabs.harvard.edu/abs/1996slfp.book.....R.

[166] G. G. Raffelt. *Astrophysical Axion Bounds*, volume 741, page 51. Springer-Verlag Berlin Heidelberg, 2008. URL https://ui.adsabs.harvard.edu/abs/2008LNP...741...51R.

[167] B. Berenji, J. Gaskins, and M. Meyer. Constraints on axions and axionlike particles from Fermi Large Area Telescope observations of neutron stars. *Physical Review D*, 93(4):045019, February 2016. URL https://ui.adsabs.harvard.edu/abs/2016PhRvD..93d5019B.

[168] D. E. Morris. Axion mass limits may be improved by pulsar x-ray measurements. *Physical Review D*, 34:843–848, Aug 1986. URL https://link.aps.org/doi/10.1103/PhysRevD.34.843.

[169] M. Giannotti, L. D. Duffy, and R. Nita. New constraints for heavy axion-like particles from supernovae. *Journal of Cosmology and Astroparticle Physics*, 2011(1):015, January 2011. URL https://ui.adsabs.harvard.edu/abs/2011JCAP...01..015G.

[170] A. de Angelis et al. Axion-like particles, cosmic magnetic fields and gamma-ray astrophysics. *Physics Letters B*, 659(5):847–855, February 2008. URL https://ui.adsabs.harvard.edu/abs/2008PhLB..659..847D.

[171] A. M. Hillas. The Origin of Ultra-High-Energy Cosmic Rays. *Annual Review of Astronomy and Astrophysics*, 22:425–444, January 1984. URL https://ui.adsabs.harvard.edu/abs/1984ARA&A..22..425H.

[172] J. Linsley. Evidence for a Primary Cosmic-Ray Particle with Energy 10^{20} eV. *Physical Review Letters*, 10(4):146–148, February 1963. URL https://ui.adsabs.harvard.edu/abs/1963PhRvL..10..146L.

[173] J. Albert et al. (MAGIC Collaboration). Very-High-Energy gamma rays from a Distant Quasar: How Transparent Is the Universe? *Science*, 320(5884):1752, June 2008. URL https://ui.adsabs.harvard.edu/abs/2008Sci...320.1752M.

[174] J. Aleksić et al. (MAGIC Collaboration). MAGIC Discovery of Very High Energy Emission from the FSRQ PKS 1222+21. *The Astrophysical Journal*, 730(1):L8, March 2011. URL https://ui.adsabs.harvard.edu/abs/2011ApJ...730L...8A.

[175] T. Terzić, D. Kerszberg, and J. Strišković. Probing quantum gravity with imaging atmospheric cherenkov telescopes. *Universe*, 7(9):345, September 2021. URL https://ui.adsabs.harvard.edu/abs/2021Univ....7..345T.

[176] K. Katarzyński et al. The multifrequency emission of Mrk 501. From radio to TeV gamma-rays. *Astronomy & Astrophysics*, 367:809–825, March 2001. URL https://ui.adsabs.harvard.edu/abs/2001A&A...367..809K.

[177] D. Wouters and P. Brun. Irregularity in gamma ray source spectra as a signature of axionlike particles. *Physical Review D*, 86(4):043005, August 2012. URL https://ui.adsabs.harvard.edu/abs/2012PhRvD..86d3005W.

[178] J.G. Cheng et al. Revisiting the analysis of axion-like particles with the Fermi-LAT gamma-ray observation of NGC1275PhysRevLett.40.279. *arXiv e-prints*, art. arXiv:2010.12396, October 2020. URL https://ui.adsabs.harvard.edu/abs/2020arXiv201012396C.

[179] M. Ajello et al. (Fermi-LAT Collaboration). Search for Spectral Irregularities due to Photon-Axionlike-Particle Oscillations with the Fermi Large Area Telescope. *Physical Review Letters*, 116(16):161101, April 2016. URL https://ui.adsabs.harvard.edu/abs/2016PhRvL.116p1101A.

[180] C. Zhang et al. New bounds on axionlike particles from the Fermi Large Area Telescope observation of PKS 2155 -304. *Physical Review D*, 97(6):063009, March 2018. URL https://ui.adsabs.harvard.edu/abs/2018PhRvD..97f3009Z.

[181] Y. Liang et al. Constraints on axion-like particle properties with TeV gamma-ray observations of Galactic sources. *Journal of Cosmology and Astroparticle Physics*, 2019(6):042, June 2019. URL https://ui.adsabs.harvard.edu/abs/2019JCAP...06..042L.

[182] D. Malyshev et al. Improved limit on axion-like particles from gamma-ray data on Perseus cluster. *arXiv e-prints*, art. arXiv:1805.04388, May 2018. URL https://ui.adsabs.harvard.edu/abs/2018arXiv180504388M.

[183] J. Guo et al. The implications of the axion like particle from the Fermi-LAT and H.E.S.S. observations of PG 1553+113 and PKS 2155-304. *arXiv e-prints*, art. arXiv:2002.07571, February 2020. URL https://ui.adsabs.harvard.edu/abs/2020arXiv200207571G.

[184] D. A. Sanchez et al. Evidence for a cosmological effect in γ-ray spectra of BL Lacertae. *Astronomy & Astrophysics*, 554:A75, June 2013. URL https://ui.adsabs.harvard.edu/abs/2013A&A...554A..75S.

[185] O. Mena Olga and S. Razzaque. fparticle mixing in the GeV gamma-ray blazar data? *Journal of Cosmology and Astroparticle Physics*, 2013(11):023, November 2013. URL https://ui.adsabs.harvard.edu/abs/2013JCAP...11..023M.

[186] G. Galanti et al. Blazar VHE spectral alterations induced by photon-ALP oscillations. *Monthly Notices of the Royal Astronomical Society*, 487(1):123–132, July 2019. URL https://ui.adsabs.harvard.edu/abs/2019MNRAS.487..123G.

[187] R. Jansson and G. R. Farrar. The Galactic Magnetic Field. *The Astrophysical Journal Letters*, 761(1):L11, December 2012. URL https://ui.adsabs.harvard.edu/abs/2012ApJ...761L..11J.

[188] M. S. Pshirkov et al. Deriving the Global Structure of the Galactic Magnetic Field from Faraday Rotation Measures of Extragalactic Sources. *The Astrophysical Journal*, 738(2):192, September 2011. URL https://ui.adsabs.harvard.edu/abs/2011ApJ...738..192P.

[189] Z. Xia et al. Searching for spectral oscillations due to photon-axionlike particle conversion using the Fermi-LAT observations of bright supernova remnants. *Physical Review D*, 97(6):063003, March 2018. URL https://ui.adsabs.harvard.edu/abs/2018PhRvD..97f3003X.

[190] Z. Xia et al. Searching for the possible signal of the photon-axionlike particle oscillation in the combined GeV and TeV spectra of supernova remnants. *Physical Review D*, 100(12):123004, December 2019. URL https://ui.adsabs.harvard.edu/abs/2019PhRvD.100l3004X.

[191] M. Meyer, D. Montanino, and J. Conrad. On detecting oscillations of gamma rays into axion-like particles in turbulent and coherent magnetic fields. *Journal of Cosmology and Astroparticle Physics*, 2014(9):003, September 2014. URL https://ui.adsabs.harvard.edu/abs/2014JCAP...09..003M.

[192] R. Jansson and G. R. Farrar. A New Model of the Galactic Magnetic Field. *The Astrophysical Journal*, 757(1):14, September 2012. URL https://ui.adsabs.harvard.edu/abs/2012ApJ...757...14J.

[193] J. Davies, Manuel M. Meyer, and G. Cotter. Relevance of jet magnetic field structure for blazar axionlike particle searches. *Physical Review D*, 103(2):023008, 2021. URL https://doi.org/10.1103/PhysRevD.103.023008.

[194] W. J. Potter and G. Cotter. New constraints on the structure and dynamics of black hole jets. *Monthly Notices of the Royal Astronomical Society*, 453(4):4070–4088, 2015. URL https://doi.org/10.1093/mnras/stv1657.

[195] J. Davies, Manuel M. Meyer, and G. Cotter. Constraints on axionlike particles from a combined analysis of three flaring Fermi flat-spectrum radio quasars. *Physical Review D*, 107(8):083027, 2023. URL https://doi.org/10.1103/PhysRevD.107.083027.

[196] G. Long, S. Chen, Xu, and H. Zhang. Probing μeV ALPs with future LHAASO observation of AGN γ-ray spectra. *arXiv e-prints*, art. arXiv:2101.10270, January 2021. URL https://ui.adsabs.harvard.edu/abs/2021arXiv210110270L.

[197] G. Sinnis, Andy A. Smith, and J. E. McEnery. Hawc:. a Next Generation All-Sky VHE Gamma-Ray Telescope. In *The Tenth Marcel Grossmann Meeting. On recent developments in theoretical and experimental general relativity, gravitation and relativistic field theories*, page 1068, February 2006. URL https://ui.adsabs.harvard.edu/abs/2006tmgm.meet.1068S.

[198] Z. Cao et al. (LHAASO Collaboration). The Large High Altitude Air Shower Observatory (LHAASO) Science Book (2021 Edition). *arXiv e-prints*, art. arXiv:1905.02773, May 2019. URL https://ui.adsabs.harvard.edu/abs/2019arXiv190502773C.

[199] U. Barres de Almeida et al. (SWGO Collaboration). The southern wide-field gamma-ray observatory. *Astronomische Nachrichten*, 342(1-2):431–437, 2021. URL https://onlinelibrary.wiley.com/doi/abs/10.1002/asna.202113946.

[200] T. Wulf. Observations on the radiation of high penetration power on the eiffel tower. *Physikalische Zeitschrift*, 11:811, 1910.

[201] D. Pacini. La radiazione penetrante alla superficie ed in seno alle acque. *Il Nuovo Cimento*, 3(1):93–100, December 1912. URL https://ui.adsabs.harvard.edu/abs/1912NCim....3...93P.

[202] A. Gockel. Luftelektrische Beobachtungen bei einer Ballonfahrt. *Physikalische Zeitschrift*, 11:280–282, 1910.

[203] A. Gockel. Messungen der durchdringendern Strahlung bei Ballonfahrten. *Physikalische Zeitschrift*, 12:595–597, 1911.

[204] V. F. Hess. Über Beobachtungen der durchdringenden Strahlung bei sieben Freiballonfahrten. *Physikalische Zeitschrift*, 13:1084–1091, 1912.

[205] V. F. Hess. On the Observations of the Penetrating Radiation during Seven Balloon Flights. *arXiv e-prints*, art. arXiv:1808.02927, July 2018. URL https://ui.adsabs.harvard.edu/abs/2018arXiv180802927H.

[206] Alessandro A. De Angelis and M. Pimenta. *Introduction to Particle and Astroparticle Physics*. 2018. URL https://ui.adsabs.harvard.edu/abs/2018ipap.book.....D.

[207] C. Evoli. The cosmic-ray energy spectrum, December 2020. URL https://doi.org/10.5281/zenodo.4396125.

[208] R. Alves Batista et al. Open Questions in Cosmic-Ray Research at Ultrahigh Energies. *Frontiers in Astronomy and Space Sciences*, 6:23, June 2019. URL https://ui.adsabs.harvard.edu/abs/2019FrASS...6...23B.

[209] M. S. Longair. *High Energy Astrophysics*. 2011. URL https://ui.adsabs.harvard.edu/abs/2011hea..book.....L.

[210] B. T. Zhang and K. Murase. Ultrahigh-energy cosmic-ray nuclei and neutrinos from engine-driven supernovae. *Physical Review D*, 100(10):103004, November 2019. URL https://ui.adsabs.harvard.edu/abs/2019PhRvD.100j3004Z.

[211] K. Fang, K.Kotera, and A. V. Olinto. Ultrahigh energy cosmic ray nuclei from extragalactic pulsars and the effect of their Galactic counterparts. *Journal of Cosmology and Astroparticle Physics*, 2013(3):010, March 2013. URL https://ui.adsabs.harvard.edu/abs/2013JCAP...03..010F.

[212] S. S. Kimura, K. Murase, and P. Mészáros. Super-knee Cosmic Rays from Galactic Neutron Star Merger Remnants. *The Astrophysical Journal*, 866(1):51, October 2018. URL https://ui.adsabs.harvard.edu/abs/2018ApJ...866...51K.

[213] K. Greisen. End to the Cosmic-Ray Spectrum? *Physical Review Letter*, 16(17): 748–750, April 1966. URL https://ui.adsabs.harvard.edu/abs/1966PhRvL..16..748G.

[214] G. T. Zatsepin G. T. and Kuz'min. Upper Limit of the Spectrum of Cosmic Rays. *Soviet Journal of Experimental and Theoretical Physics Letters*, 4:78, August 1966. URL https://ui.adsabs.harvard.edu/abs/1966JETPL...4...78Z.

[215] M. Apel and The KASCADE-Grande Collaboration. KASCADE-Grande measurements of energy spectra for elemental groups of cosmic rays. *arXiv e-prints*, art. arXiv:1306.6283, June 2013. URL https://ui.adsabs.harvard.edu/abs/2013arXiv1306.6283T.

[216] A. Abdul Halim and Pierre Auger Collaboration. Constraining the sources of ultra-high-energy cosmic rays across and above the ankle with the spectrum and composition data measured at the Pierre Auger Observatory. *Journal of Cosmology and*

Astroparticle Physics, 2023(5):024, May 2023. URL https://ui.adsabs.harvard.edu/abs/2023JCAP...05..024A.

[217] A. Abdul Halim and Pierre Auger Collaboration. Constraining models for the origin of ultra-high-energy cosmic rays with a novel combined analysis of arrival directions, spectrum, and composition data measured at the Pierre Auger Observatory. *Journal of Cosmology and Astroparticle Physics*, 2024(1):022, January 2024. URL https://ui.adsabs.harvard.edu/abs/2024JCAP...01..022A.

[218] Y. Tsunesada et al. Energy Spectrum of Ultra-High-Energy Cosmic Rays Measured by The Telescope Array. In *35th International Cosmic Ray Conference (ICRC2017)*, volume 301 of *International Cosmic Ray Conference*, page 535, July 2017. URL https://ui.adsabs.harvard.edu/abs/2017ICRC...35..535T.

[219] E. Fermi. On the Origin of the Cosmic Radiation. *Physical Review*, 75(8):1169–1174, April 1949. URL https://ui.adsabs.harvard.edu/abs/1949PhRv...75.1169F.

[220] A. Cooray. Extragalactic background light measurements and applications. *arXiv*, 2016. URL http://dx.doi.org/10.1098/rsos.150555.

[221] M. Ackermann et al. (Fermi-LAT Collaboration). Resolving the Extragalactic γ -Ray Background above 50 GeV with the Fermi Large Area Telescope. *Physical Review Letters*, 116(15):151105, April 2016. URL https://ui.adsabs.harvard.edu/abs/2016PhRvL.116o1105A.

[222] M. Ackermann et al. (Fermi-LAT Collaboration). The Spectrum of Isotropic Diffuse Gamma-Ray Emission between 100 MeV and 820 GeV. *The Astrophysical Journal*, 799(1):86, January 2015. URL https://ui.adsabs.harvard.edu/abs/2015ApJ...799...86A.

[223] M. Fornasa and M. A. Sánchez-Conde. The nature of the Diffuse Gamma-Ray Background. *Physics Reports*, 598:1–58, October 2015. URL https://ui.adsabs.harvard.edu/abs/2015PhR...598....1F.

[224] M. Persic and Y. Rephaeli. Starburst galaxies and the X-ray background. *Astronomy & Astrophysics*, 399:9–17, February 2003. URL https://ui.adsabs.harvard.edu/abs/2003A&A...399....9P.

[225] W. Xiang-Ping Wu and X. Yan-Jie. The x-ray background from groups and clusters of galaxies. *The Astrophysical Journal*, 560(2):544, oct 2001. URL https://dx.doi.org/10.1086/322961.

[226] V. A. Acciari et al. (MAGIC Collaboration). Measurement of the extragalactic background light using MAGIC and Fermi-LAT gamma-ray observations of blazars up to z = 1. *Monthly Notices of the Royal Astronomical Society*, 486(3):4233–4251, July 2019. URL https://ui.adsabs.harvard.edu/abs/2019MNRAS.486.4233A.

[227] H. Abdalla et al. (H. E. S. S. Collaboration). Measurement of the EBL spectral energy distribution using the VHE γ-ray spectra of H.E.S.S. blazars. *Astronomy & Astrophysics*, 606:A59, October 2017. URL https://ui.adsabs.harvard.edu/abs/2017A&A...606A..59H.

[228] A. Franceschini. Photon–photon interactions and the opacity of the universe in gamma rays. *Universe*, 7(5), 2021. ISSN 2218-1997. URL https://www.mdpi.com/2218-1997/7/5/146.

[229] S. P. Wakely and D. Horan. TeVCat: An online catalog for Very High Energy Gamma-Ray Astronomy. *International Cosmic Ray Conference*, 3:1341–1344, 2008. URL http://adsabs.harvard.edu/abs/2008ICRC....3.1341W.

[230] V. Schoenfelder et al. Instrument Description and Performance of the Imaging Gamma-Ray Telescope COMPTEL aboard the Compton Gamma-Ray Observatory. *The Astrophysical Journal Supplement Series*, 86:657, June 1993. URL https://ui.adsabs.harvard.edu/abs/1993ApJS...86..657S.

[231] W. B. Atwood et al. The Large Area Telescope on the Fermi Gamma-Ray Space Telescope Mission. *The Astrophysical Journal*, 697(2):1071–1102, June 2009. URL https://ui.adsabs.harvard.edu/abs/2009ApJ...697.1071A.

[232] H. Abe et al. (MAGIC Collaboration). Constraints on axion-like particles with the perseus galaxy cluster with magic. *Physics of the Dark Universe*, 44:101425, 2024. ISSN 2212-6864. doi: https://doi.org/10.1016/j.dark.2024.101425. URL https://www.sciencedirect.com/science/article/pii/S2212686424000074.

[233] P. Auger et al. Extensive cosmic-ray showers. *Reviews of Modern Physics*, 11:288–291, Jul 1939. URL https://link.aps.org/doi/10.1103/RevModPhys.11.288.

[234] A. López-Oramas. *Multi-year campaign of the gamma-ray binary LS I +61° 303 and search for VHE emission from gamma-ray binary candidates with the MAGIC telescopes*. PhD thesis, Autonomous University of Barcelona, Spain, September 2014. URL https://ui.adsabs.harvard.edu/abs/2014PhDT.......351L.

[235] W. Heitler. *The quantum theory of radiation*, volume 5 of *International Series of Monographs on Physics*. Oxford University Press, Oxford, 1936.

[236] P. A. Čerenkov. Visible Radiation Produced by Electrons Moving in a Medium with Velocities Exceeding that of Light. *Physical Review*, 52(4):378–379, August 1937. URL https://ui.adsabs.harvard.edu/abs/1937PhRv...52..378C.

[237] T. M. Shaffer, E. C. Pratt, and J. Grimm. Utilizing the power of Cerenkov light with nanotechnology. *Nature Nanotechnology*, 12(2):106–117, February 2017. URL https://ui.adsabs.harvard.edu/abs/2017NatNa..12..106S.

[238] M. de Naurois and D. Mazin. Ground-based detectors in very-high-energy gamma-ray astronomy. *Comptes Rendus Physique*, 16(6-7):610–627, August 2015. URL https://ui.adsabs.harvard.edu/abs/2015CRPhy..16..610D.

[239] A. M. Hillas. Cerenkov Light Images of EAS Produced by Primary Gamma Rays and by Nuclei. In *19th International Cosmic Ray Conference (ICRC19), Volume 3*, volume 3 of *International Cosmic Ray Conference*, page 445, August 1985. URL https://ui.adsabs.harvard.edu/abs/1985ICRC....3..445H.

[240] A. M. Hillas. Evolution of ground-based gamma-ray astronomy from the early days to the cherenkov telescope arrays. *The Astrophysical Journal*, 43:19–43, 2013. ISSN 0927-6505. URL https://doi.org/10.1016/j.astropartphys.2012.06.002.

[241] E. Lorenz et al. (MAGIC Collaboration). Status of the 17 m diameter Magic telescope. In *International Cosmic Ray Conference*, volume 7 of *International Cosmic Ray Conference*, page 2789, August 2001. URL https://ui.adsabs.harvard.edu/abs/2001ICRC....7.2789L.

[242] J. Aleksić et al. (MAGIC Collaboration). Measurement of the Crab Nebula spectrum over three decades in energy with the MAGIC telescopes. *Journal of High Energy Astrophysics*, 5:30–38, March 2015. URL https://ui.adsabs.harvard.edu/abs/2015JHEAp...5...30A.

[243] K. A. Hochmuth and G. Sigl. Effects of axion-photon mixing on gamma-ray spectra from magnetized astrophysical sources. *Physical Review D*, 76(12):123011, December 2007. URL https://ui.adsabs.harvard.edu/abs/2007PhRvD..76l3011H.

[244] A. Mirizzi and D.Montanino. Stochastic conversions of TeV photons into axion-like particles in extragalactic magnetic fields. *Journal of Cosmology and Astroparticle Physics*, 2009(12):004, December 2009. URL https://ui.adsabs.harvard.edu/abs/2009JCAP...12..004M.

[245] X. Ma et al. Chapter 1 LHAASO Instruments and Detector technology. *Chinese Physics C*, 46(3):030001, March 2022. doi: 10.1088/1674-1137/ac3fa6. URL https://ui.adsabs.harvard.edu/abs/2022ChPhC..46c0001M.

[246] N. Park et al. (VERITAS Collaboration). Performance of the VERITAS experiment. In *34th International Cosmic Ray Conference (ICRC2015)*, volume 34 of *International Cosmic Ray Conference*, page 771, July 2015. URL https://ui.adsabs.harvard.edu/abs/2015ICRC...34..771P.

[247] M. Holler et al. Observations of the Crab Nebula with H.E.S.S. Phase II. *arXiv e-prints*, art. arXiv:1509.02902, September 2015. URL https://ui.adsabs.harvard.edu/abs/2015arXiv150902902H.

[248] J. Aleksić et al. (MAGIC Collaboration). The major upgrade of the MAGIC telescopes, Part II: A performance study using observations of the Crab Nebula. *Astroparticle Physics*, 72:76–94, January 2016. URL https://ui.adsabs.harvard.edu/abs/2016APh....72...76A.

[249] A. U. Abeysekara et al. (HAWC Collaboration). Observation of the Crab Nebula with the HAWC Gamma-Ray Observatory. *The Astrophysical Journa*, 843(1):39, July 2017. URL https://ui.adsabs.harvard.edu/abs/2017ApJ...843...39A.

[250] A. Albert et al. Science Case for a Wide Field-of-View Very-High-Energy Gamma-Ray Observatory in the Southern Hemisphere. *arXiv e-prints*, art. arXiv:1902.08429, February 2019. URL https://ui.adsabs.harvard.edu/abs/2019arXiv190208429A.

[251] P. Bruel et al. Fermi-LAT improved Pass~8 event selection. *arXiv e-prints*, art. arXiv:1810.11394, October 2018. URL https://ui.adsabs.harvard.edu/abs/2018arXiv181011394B.

[252] A. Haungs et al. The KASCADE Cosmic-ray Data Centre KCDC: granting open access to astroparticle physics research data. *European Physical Journal C*, 78(9): 741, September 2018. URL https://ui.adsabs.harvard.edu/abs/2018EPJC...78..741H.

[253] R. U. Abbasi et al. (Telescope Array Collaboration). An extremely energetic cosmic ray observed by a surface detector array. *Science*, 382(6673):903–907, November 2023. URL https://ui.adsabs.harvard.edu/abs/2023Sci...382..903T.

[254] F. Di Pierro et al. (MAGIC Collaboration). Performance of joint gamma-ray observations with MAGIC and LST-1 telescopes. *PoS*, ICRC2023:636, 2023. URL https://doi.org/10.22323/1.444.0636.

[255] J. Aleksić et al. (MAGIC Collaboration). The major upgrade of the MAGIC telescopes, Part I: The hardware improvements and the commissioning of the system. *Astroparticle Physics*, 72:61–75, January 2016. URL https://ui.adsabs.harvard.edu/abs/2016APh....72...61A.

[256] J. et al. (CTA-LST Project) Cortina. Status of the Large Size Telescopes of the Cherenkov Telescope Array. In *36th International Cosmic Ray Conference (ICRC2019)*, volume 36 of *International Cosmic Ray Conference*, page 653, July 2019. URL https://ui.adsabs.harvard.edu/abs/2019ICRC...36..653C.

[257] A. Biland et al. The Active Mirror Control of the MAGIC Telescopes. In *International Cosmic Ray Conference*, volume 3 of *International Cosmic Ray Conference*, pages 1353–1356, January 2008. URL https://ui.adsabs.harvard.edu/abs/2008ICRC...3.1353B.

[258] C. Fruck et al. A novel LIDAR-based Atmospheric Calibration Method for Improving the Data Analysis of MAGIC. *arXiv e-prints*, art. arXiv:1403.3591, March 2014. URL https://ui.adsabs.harvard.edu/abs/2014arXiv1403.3591F.

[259] V.P. Fomin et al. New methods of atmospheric cherenkov imaging for gamma-ray astronomy. i. the false source method. *Astroparticle Physics*, 2(2):137–150, 1994. ISSN 0927-6505. URL https://www.sciencedirect.com/science/article/pii/0927650594900361.

[260] R. López-Coto. *Very-high-energy Gamma-ray Observations of Pulsar Wind Nebulae and Cataclysmic Variable Stars with MAGIC and Development of Trigger Systems for IACTs*. Springer Theses, 01 2017. ISBN 978-3-319-44750-6. URL https://doi.org/10.1007/978-3-319-44751-3.

[261] R. Zanin. MARS, the MAGIC analysis and reconstruction software. In *33rd International Cosmic Ray Conference*, page 0773, 2013.

[262] R. Lopez-Coto et al. cta-observatory/cta-lstchain: v0.9.14 – 2023-09-25, September 2023. URL https://doi.org/10.5281/zenodo.8377093.

[263] M. Noethe et al. (The Cherenkov Telescope Array Consortium). Prototype Open Event Reconstruction Pipeline for the Cherenkov Telescope Array. In *37th International Cosmic Ray Conference*, page 744, March 2022. URL https://ui.adsabs.harvard.edu/abs/2022icrc.confE.744N.

[264] J. L. Contreras et al. (The Cherenkov Telescope Array Consortium). Data model issues in the Cherenkov Telescope Array project. *PoS*, ICRC2015:960, 2016. URL https://doi.org/10.22323/1.236.0960.

[265] C. Nigro, T. Hassan, and L. Olivera-Nieto. Evolution of data formats in very-high-energy gamma-ray astronomy. *Universe*, 7(10), 2021. ISSN 2218-1997. URL https://www.mdpi.com/2218-1997/7/10/374.

[266] D. Heck et al. CORSIKA: A Monte Carlo code to simulate extensive air showers. 2 1998.

[267] T. Vuillaume et al. (CTA-LST Project). Analysis of the Cherenkov Telescope Array first Large-Sized Telescope real data using convolutional neural networks. *arXiv e-prints*, art. arXiv:2108.04130, August 2021. URL https://ui.adsabs.harvard.edu/abs/2021arXiv210804130V.

[268] H. Abe et al. (CTA-LST Project). Observations of the Crab Nebula and Pulsar with the Large-Sized Telescope Prototype of the Cherenkov Telescope Array. *arXiv e-prints*, art. arXiv:2306.12960, June 2023. URL https://ui.adsabs.harvard.edu/abs/2023arXiv230612960P.

[269] T. P. Li and Y. Q. Ma. Analysis methods for results in gamma-ray astronomy. *The Astrophysical Journal*, 272:317–324, 1983. URL https://doi.org/10.1086/161295.

[270] J. Albert et al. Unfolding of differential energy spectra in the MAGIC experiment. *Nuclear Instruments and Methods in Physics Research A*, 583(2-3):494–506, December 2007. URL https://ui.adsabs.harvard.edu/abs/2007NIMPA.583..494A.

[271] E. J. Summerlin and M.G. Baring. Diffusive Acceleration of Particles at Oblique, Relativistic, Magnetohydrodynamic Shocks. *The Astrophysical Journal*, 745(1):63, January 2012. URL https://ui.adsabs.harvard.edu/abs/2012ApJ...745...63S.

[272] B. Cerutti et al. Beaming and Rapid Variability of High-energy Radiation from Relativistic Pair Plasma Reconnection. *The Astrophysical Journal Letters*, 754(2): L33, August 2012. URL https://ui.adsabs.harvard.edu/abs/2012ApJ...754L..33C.

[273] K.-I. Nishikawa et al. Relativistic Jet Simulations of the Weibel Instability in the Slab Model to Cylindrical Jets with Helical Magnetic Fields. *Galaxies*, 7(1):29, January 2019. URL https://ui.adsabs.harvard.edu/abs/2019Galax...7...29N.

[274] P. Padovani et al. Active galactic nuclei: what's in a name? *Astronomy and Astrophysics Reviews*, 25(1):2, August 2017. URL https://ui.adsabs.harvard.edu/abs/2017A&ARv..25....2P.

[275] J. Davies, M. Meyer, and G. Cotter. Relevance of photon-photon dispersion within the jet for blazar axionlike particle searches. *Physical Review D*, 105(2):023017, 2022. URL https://doi.org/10.1103/PhysRevD.105.023017.

[276] J. C. McKinney. General relativistic magnetohydrodynamic simulations of the jet formation and large-scale propagation from black hole accretion systems. *Monthly Notices of the Royal Astronomical Society*, 368(4):1561–1582, June 2006. URL https://ui.adsabs.harvard.edu/abs/2006MNRAS.368.1561M.

[277] F. Govoni and L. Feretti. Magnetic Fields in Clusters of Galaxies. *International Journal of Modern Physics D*, 13(8):1549–1594, January 2004. URL https://ui.adsabs.harvard.edu/abs/2004IJMPD..13.1549G.

[278] D. Grasso and H. R. Rubinstein. Magnetic fields in the early universe. *Physics Reports*, 348:163–266, 2001. URL https://doi.org/10.1016/S0370-1573(00)00110-1.

[279] P. P. Kronberg, H. Lesch, and U. Hopp. Magnetization of the Intergalactic Medium by Primeval Galaxies. *The Astrophysical Journal*, 511(1):56–64, January 1999. URL https://ui.adsabs.harvard.edu/abs/1999ApJ...511...56K.

[280] K. Roettiger, J. M. Stone, and J. O. Burn. Magnetic Field Evolution in Merging Clusters of Galaxies. *The Astrophysical Journal*, 518(2):594–602, June 1999. URL https://ui.adsabs.harvard.edu/abs/1999ApJ...518..594R.

[281] F. Feretti et al. Clusters of galaxies: observational properties of the diffuse radio emission. *The Astronomy and Astrophysics Review*, 20:54, May 2012. URL https://ui.adsabs.harvard.edu/abs/2012A&ARv..20...54F.

[282] E. Churazov et al. XMM-Newton Observations of the Perseus Cluster. I. The Temperature and Surface Brightness Structure. *The Astrophysical Journa*, 590(1):225–237, June 2003. URL https://ui.adsabs.harvard.edu/abs/2003ApJ...590..225C.

[283] G. B. Taylor et al. Magnetic fields in the centre of the Perseus cluster. *Monthly Notices of the Royal Astronomical Society*, 368(4):1500–1506, June 2006. URL https://ui.adsabs.harvard.edu/abs/2006MNRAS.368.1500T.

[284] J. Aleksić et al. (MAGIC Collaboration). Constraining cosmic rays and magnetic fields in the Perseus galaxy cluster with TeV observations by the MAGIC telescopes. *Astronomy & Astrophysics*, 541:A99, May 2012. URL https://ui.adsabs.harvard.edu/abs/2012A&A...541A..99A.

[285] R. Alves Batista and A. Saveliev. The Gamma-ray Window to Intergalactic Magnetism. *Universe*, 7(7):223, 2021. URL https://doi.org/10.3390/universe7070223.

[286] A. Neronov, D. Semikoz, and M. Banafsheh. Magnetic Fields in the Large Scale Structure from Faraday Rotation measurements. *arXiv e-prints*, art. arXiv:1305.1450, May 2013. URL https://ui.adsabs.harvard.edu/abs/2013arXiv1305.1450N.

[287] M. S. Pshirkov, P. G. Tinyakov, and F. R. Urban. New limits on extragalactic magnetic fields from rotation measures. *Physical Review Letters*, 116(19):191302, 2016. URL https://doi.org/10.1103/PhysRevLett.116.191302.

[288] K. Jedamzik and A. Saveliev. Stringent Limit on Primordial Magnetic Fields from the Cosmic Microwave Background Radiation. *Physical Review Letters*, 123(2):021301, July 2019. URL https://ui.adsabs.harvard.edu/abs/2019PhRvL.123b1301J.

[289] A. Neronov, A. M. Taylor, C. Tchernin, and I. Vovk. Measuring the correlation length of intergalactic magnetic fields from observations of gamma-ray induced cascades. *Astronomy & Astrophysics*, 554:A31, June 2013. URL https://ui.adsabs.harvard.edu/abs/2013A&A...554A..31N.

[290] R. Alves Batista and A. Saveliev. Multimessenger Constraints on Intergalactic Magnetic Fields from the Flare of TXS 0506+056. *The Astrophysical Journal Letters*, 902(1):L11, October 2020. URL https://ui.adsabs.harvard.edu/abs/2020ApJ...902L..11A.

[291] P. A. R. Ade et al. (Planck Collaboration). Planck 2013 results. XVI. Cosmological parameters. *Astronomy & Astrophysics*, 571:A16, November 2014. doi: 10.1051/0004-6361/201321591. URL https://ui.adsabs.harvard.edu/abs/2014A&A...571A..16P.

[292] R. Durrer and A. Neronov. Cosmological magnetic fields: their generation, evolution and observation. *The Astronomy and Astrophysics Review*, 21:62, June 2013. URL https://ui.adsabs.harvard.edu/abs/2013A&ARv..21...62D.

[293] A. Abramowski and H. E. S. S. Collaboration. Search for extended γ-ray emission around AGN with H.E.S.S. and Fermi-LAT. *Astronomy & Astrophysics*, 562: A145, February 2014. URL https://ui.adsabs.harvard.edu/abs/2014A&A...562A.145H.

[294] S. Archambault et al. Search for Magnetically Broadened Cascade Emission from Blazars with VERITAS. *The Astrophysical Journal*, 835(2):288, February 2017. URL https://ui.adsabs.harvard.edu/abs/2017ApJ...835..288A.

[295] M. Ackermann and Fermi-LAT Collaboration. The Search for Spatial Extension in High-latitude Sources Detected by the Fermi Large Area Telescope. *The Astrophysical Journal Supplement Series*, 237(2):32, August 2018. URL https://ui.adsabs.harvard.edu/abs/2018ApJS..237...32A.

[296] F. Aharonian et al. (Fermi-LAT Collaboration). Constraints on the Intergalactic Magnetic Field Using Fermi-LAT and H.E.S.S. Blazar Observations. *The Astrophysical Journal Letters*, 950(2):L16, June 2023. URL https://ui.adsabs.harvard.edu/abs/2023ApJ...950L..16A.

[297] M. Meyer, D. Horns, and M. Raue. First lower limits on the photon-axion-like particle coupling from very high energy gamma-ray observations. *Physical Review D*, 87(3): 035027, February 2013. URL https://ui.adsabs.harvard.edu/abs/2013PhRvD..87c5027M.

[298] X. H. Sun et al. Radio observational constraints on Galactic 3D-emission models. *Astronomy & Astrophysics*, 477:573, 2008. URL https://doi.org/10.1051/0004-6361:20078671.

[299] S. Xiao-Hui and W. Reich. The galactic halo magnetic field revisited. *Research in Astronomy and Astrophysics*, 10(12):1287, dec 2010. URL https://dx.doi.org/10.1088/1674-4527/10/12/009.

[300] T. R. Jaffe et al. Modelling the Galactic magnetic field on the plane in two dimensions. *Monthly Notices of the Royal Astronomical Society*, 401(2):1013–1028, 01 2010. URL https://doi.org/10.1111/j.1365-2966.2009.15745.x.

[301] B. M. Gaensler and S. Johnston. The pulsar/supernova remnant connection. *Monthly Notices of the Royal Astronomical Society*, 277(4):1243–1253, 12 1995. URL https://ui.adsabs.harvard.edu/abs/1995MNRAS.277.1243G.

[302] M. Haverkorn et al. The outer scale of turbulence in the magnetoionized galactic interstellar medium. *The Astrophysical Journal*, 680(1):362, jun 2008. URL https://dx.doi.org/10.1086/587165.

[303] R. Adam et al. (Planck Collaboration). Planck intermediate results. XLII. Large-scale Galactic magnetic fields. *Astronomy & Astrophysics*, 596:A103, December 2016. URL https://ui.adsabs.harvard.edu/abs/2016A&A...596A.103P.

[304] M. Unger Michael and G. Farrar. Progress in the Global Modeling of the Galactic Magnetic Field. In *European Physical Journal Web of Conferences*, volume 210 of *European Physical Journal Web of Conferences*, page 04005, October 2019. URL https://ui.adsabs.harvard.edu/abs/2019EPJWC.21004005U.

[305] J. Kleimann, T. Schorlepp, L. Merten, and J. Becker Tjus. Solenoidal Improvements for the JF12 Galactic Magnetic Field Model. *The Astrophysical Journal*, 877(2):76, June 2019. URL https://ui.adsabs.harvard.edu/abs/2019ApJ...877...76K.

[306] M. Unger and G. R. Farrar. The Coherent Magnetic Field of the Milky Way. *arXiv e-prints*, art. arXiv:2311.12120, November 2023. URL https://ui.adsabs.harvard.edu/abs/2023arXiv231112120U.

[307] M. Guenduez et al. A novel analytical model of the magnetic field configuration in the Galactic center. *Astronomy & Astrophysics*, 644:A71, December 2020. URL https://ui.adsabs.harvard.edu/abs/2020A&A...644A..71G.

[308] J. et al. (MAGIC Collaboration) Aleksić. MAGIC Gamma-Ray Telescope Observation of the Perseus Cluster of Galaxies: Implications for Cosmic Rays, Dark Matter and NGC 1275. *The Astrophysical Journal*, 710:634–647, 2010. URL https://doi.org/10.1088/0004-637X/710/1/634.

[309] J. et al. (MAGIC Collaboration) Aleksić. Detection of very high energy gamma-ray emission from the Perseus cluster head-tail galaxy IC 310 by the MAGIC telescopes. *The Astrophysical Journal Letters*, 723:L207, 2010. URL https://doi.org/10.1088/2041-8205/723/2/L207.

[310] J. et al. (MAGIC Collaboration) Aleksić. Detection of very high energy gamma-ray emission from NGC 1275 by the MAGIC telescopes. *Astronomy & Astrophysics*, 539: L2, 2012. URL https://doi.org/10.1051/0004-6361/201118668.

[311] J. et al. (MAGIC Collaboration) Aleksić. Constraining Cosmic Rays and Magnetic Fields in the Perseus Galaxy Cluster with TeV observations by the MAGIC telescopes. *Astronomy & Astrophysics*, 541:A99, 2012. URL https://doi.org/10.1051/0004-6361/201118502.

[312] J. et al. (MAGIC Collaboration) Aleksić. Contemporaneous observations of the radio galaxy NGC 1275 from radio to very high energy γ-rays. *Astronomy & Astrophysics*, 564:A5, 2014. URL https://doi.org/10.1051/0004-6361/201322951.

[313] J. et al. (MAGIC Collaboration) Aleksić. Black hole lightning due to particle acceleration at subhorizon scales. *Science*, 346(6213):1080–1084, nov 2014. URL https://doi.org/10.1126/science.1256183.

[314] M. L. Ahnen et al. (MAGIC Collaboration). Deep observation of the NGC 1275 region with MAGIC: search of diffuse γ-ray emission from cosmic rays in the Perseus cluster. *Astronomy & Astrophysics*, 589:A33, 2016. URL https://doi.org/10.1051/0004-6361/201527846.

[315] S. Ansoldi et al. (MAGIC Collaboration). Gamma-ray flaring activity of NGC1275 in 2016–2017 measured by MAGIC. *Astronomy & Astrophysics*, 617:A91, 2018. URL https://doi.org/10.1051/0004-6361/201832895.

[316] V. A. Acciari et al. (MAGIC Collaboration). Constraining Dark Matter lifetime with a deep gamma-ray survey of the Perseus Galaxy Cluster with MAGIC. *Physics of the Dark Universe*, 22:38–47, 2018. URL https://doi.org/10.1016/j.dark.2018.08.002.

[317] Y. Fujita and H. Nagai. Discovery of a new subparsec counterjet in NGC 1275: the inclination angle and the environment. *Monthly Notices of the Royal Astronomical Society*, 465(1):L94–L98, 11 2016. URL https://doi.org/10.1093/mnrasl/slw217.

[318] N. Cosimo. Establishing the MAGIC data legacy: adopting standardised data formats and open-source analysis tools. In *Proceedings of 7th Heidelberg International Symposium on High-Energy Gamma-Ray Astronomy — PoS(Gamma2022)*, volume 417, page 122, 2023. URL https://doi.org/10.22323/1.417.0122.

[319] A. Franceschini and G. Rodighiero. The extragalactic background light revisited and the cosmic photon-photon opacity. *Astronomy & Astrophysics*, 603:A34, 2017. URL https://doi.org/10.1051/0004-6361/201629684.

[320] A. Dominguez et al. Extragalactic Background Light Inferred from AEGIS Galaxy SED-type Fractions. *Monthly Notices of the Royal Astronomical Society*, 410:2556, 2011. URL https://doi.org/10.1111/j.1365-2966.2010.17631.x.

[321] K. Abe et al. (The Cherenkov Telescope Array Consortium). Prospects for γ-ray observations of the Perseus galaxy cluster with the Cherenkov Telescope Array. *arXiv e-prints*, art. arXiv:2309.03712, September 2023. URL https://ui.adsabs.harvard.edu/abs/2023arXiv230903712C.

[322] V. Vacca et al. The intracluster magnetic field power spectrum in A2199. *Astronomy & Astrophysics*, 540:A38, 2012. URL https://doi.org/10.1051/0004-6361/201116622.

[323] V. A. Acciari et al. (MAGIC Collaboration). A lower bound on intergalactic magnetic fields from time variability of 1ES 0229+200 from MAGIC and Fermi/LAT observations. *Astronomy & Astrophysics*, 670:A145, 2023. URL https://doi.org/10.1051/0004-6361/202244126.

[324] W. A. Rolke et al. Limits and confidence intervals in the presence of nuisance parameters. *Nucl. Instrum. Meth. A*, 551:493–503, 2005. URL https://doi.org/10.1016/j.nima.2005.05.068.

[325] J. Neyman et al. Ix. on the problem of the most efficient tests of statistical hypotheses. *Philosophical Transactions of the Royal Society of London. Series A, Containing Papers of a Mathematical or Physical Character*, 231(694-706):289–337, 1933. URL https://royalsocietypublishing.org/doi/abs/10.1098/rsta.1933.0009.

[326] S. S. Wilks. The Large-Sample Distribution of the Likelihood Ratio for Testing Composite Hypotheses. *The Annals of Mathematical Statistics*, 9(1):60 – 62, 1938. URL https://doi.org/10.1214/aoms/1177732360.

[327] M. Gaug et al. Using muon rings for the calibration of the cherenkov telescope array: A systematic review of the method and its potential accuracy. *The Astrophysical Journal Supplement Series*, 243(1):11, jul 2019. URL https://doi.org/10.3847/1538-4365/ab2123.

[328] J. et al. (MAGIC Collaboration) Aleksić. Search for an extended VHE γ-ray emission from Mrk 421 and Mrk 501 with the MAGIC Telescope. *Astronomy & Astrophysics*, 524:A77, December 2010. URL https://ui.adsabs.harvard.edu/abs/2010A&A...524A..77A.

[329] M. L. Ahnen et al. Long-term multi-wavelength variability and correlation study of Markarian 421 from 2007 to 2009. *Astronomy & Astrophysics*, 593:A91, September 2016. URL https://ui.adsabs.harvard.edu/abs/2016A&A...593A..91A.

[330] V. A. Acciari et al. (MAGIC Collaboration). Unraveling the Complex Behavior of Mrk 421 with Simultaneous X-Ray and VHE Observations during an Extreme Flaring Activity in 2013 April. *The Astrophysical Journal Supplement Series*, 248(2):29, jun 2020. URL https://dx.doi.org/10.3847/1538-4365/ab89b5.

[331] V. A. Acciari et al. (MAGIC Collaboration). Multiwavelength variability and correlation studies of Mrk 421 during historically low X-ray and γ-ray activity in 2015–2016. *Monthly Notices of the Royal Astronomical Society*, 504(1):1427–1451, 12 2020. ISSN 0035-8711. URL https://doi.org/10.1093/mnras/staa3727.

List of acronyms

AGN Active Galactic Nucleus.

ALP Axion-like particle.

AMC Active Mirror Control.

BL Lac BL Lacertae.

CH Counting House.

CMB Cosmic Microwave Background.

COMPTEL Imaging COMPton TELescope.

CORSIKA COsmic Ray Simulations for KAscade.

CP Conjugation-Parity.

CR Cosmic Ray.

CTA Cherenkov Telescope Array.

DAQ Data AcQuisition.

DISP Distance between the Image centroid and the Source Position.

DM Dark Matter.

DRS4 Domino Ring Sampler 4.

DT Discrimination Threshold.

EAS Extensive Air Shower.

EBL Extragalactic Background Light.

EM Electromagnetic.

EPWL Power-Law with an Exponential Cut-off.

FADC Flash Analog-to-Digital Counts.

Fermi-LAT Fermi Large Area Telescope.

FoV Field of View.

FR-I Fanaroff-Riley type-I.

FR-II Fanaroff-Riley type-II.

FSRQ Flat Spectrum Radio Quazars.

GC Galaxy Cluster.

GMF Galactic magnetic field.

GRB Gamma Ray Burst.

H.E.S.S. High Energy Stereoscopic System.

HAWC High Altitude Water Cherenkov.

HV High Voltage.

IACT Imaging Atmospheric Cherenkov Telescope.

ICMF Instracluster magnetic field.

IGMF Intergalactic magnetic field.

IR Infrared.

IRF Instrument Response Function.

KASCADE KASCADE Cosmic Ray Data Centre.

L0 Level 0 Trigger.

L1 Level 1 Trigger.

L3 Level 3 Trigger.

LC Light Curve.

LHAASO Large High Altitude Air Shower Observatory.

LIDAR LIght Detection And Ranging.

LIV Lorentz Invariance Violation.

LST Large-sized telescope.

LST-1 Large-sized telescope.

LUT Look Up Tables.

M1 MAGIC I.

M2 MAGIC II.

MACHO MAssive Compact Halo Objects.

MAGIC Major Atmospheric Gamma Imaging Cherenkov.

MARS MAGIC Analysis and Reconstruction Software.

MC Monte Carlo.

MST Medium-Sized Telescope.

MW Milky Way.

NSB Night Sky Background.

PBH Primordial Black Hole.

PMT Photomultiplier Tube.

PSF Point Spread Function.

PWL Power-Law.

QCD Quantum Chromodynamics.

RF Random Forest.

RM Rotation Measure.

SED Spectral Energy Distribution.

SM Standard Model.

SST Small-Sized Telescope.

SWGO The Southern Wide-field Gamma-ray Observatory.

TA Telescope Array.

TNG Telescopio Nazionale Galileo.

UV Ultraviolet.

VERITAS Very Energetic Radiation Imaging Telescope Array System.

VHE Very High Energy.

WIMP Weakly Interacting Massive Particle.

WISP Weakly Interacting Slim Particles.

List of Figures

List of Tables

Acknowledgements

"Time flies when you're having fun", they say, and the past three years have definitely proven me that. During my Ph.D. I have met many people, now my dear friends and colleagues. Those that have been with me through my whole journey, my family, longtime friends, and all the others that had passed through my life in the past three years.

I'd like to thank all of you.

First of all, I'd like to thank the best supervisor I could've wished for, Prof. Michele Doro, who had led me all these years and supported my advancement and helped me to become not only a better scientist, but also a better person. I'd like to thank him for his trust, advice and opportunities, all that made a student proud to call him my mentor and a friend.
My longtime supervisor and co-supervisor of this thesis, Prof. Marina Manganaro, who thought me to love astrophysics, showed me what it means and introduced me to academia, supported and followed me through it all, being more than just a supervisor, being a friend.
Thanks to my whole Padova group, who had accepted and supported me through beautiful and difficult times, laugh and tears. People that I met and I hope to keep as my dear friends, Marine, Giuseppe, Ilaria, Davide, and everyone else.
To the whole MAGIC and LST collaborations, for all the unforgettable collaboration meetings and great times, help, comments, and opportunity to learn and share my knowledge with all of them. I'd like to particularly thank Cosimo, for all the help and patience during my first year of Ph.D., all replied messages and questions, and for always giving an advice and a nice word. Giacomo D'Amico, who had welcomed me in beautiful Bergen, and showed me the beauty of statistics, made me love and appreciate it more. Thanks for all the explanations, solutions to my doubts and the knowledge he have shared with me.
Thanks to Miguel Ángel for inviting me to Madrid and welcoming me in his group, helping and supporting me in my growth as a scientist.
During these years, I have been given the opportunity to visit MAGIC and LST telescopes for several times. Alongside these beautiful telescopes that I had the honour to operate, I brought back the best memories of my co-shifters during the P236, P044, P249 and P261 shifts. Long, sleepless nights, both in front of a computer screen in the counting house and the container, but also TV screen in apartment 6. Every single moment with all of you has been a blast and full of memories that I will always keep. Thank you for all of them.

Finally, I'd like to thank to all my friends, Marah, who I have met in Padova, and who had followed me down this whole path, from the first moments we met over a zoom call in a meeting of Ph.D. students, to the celebration of the thesis submission, not the last, but just one more out of many celebrations that I hope we'll do together.
I'd like to thank my friends back home (and in some distant places), Lucija, Paulina, Lorena and Lucijana, four of them that had followed me since I was just a child and with whom I had shared all the most important moments and events in my life, including this one.
Lastly, there are no words of gratitude that I can use to express my feelings for my family, my mother and father, who selflessly supported me in all that I did, who are generals of my army, standing strong and still holding my back, loving me with a purest and strongest form of love. I thank my brother, sister, and my brother and sister in law, for staying home and supporting my parents, giving them all the help they needed, being the pillars while I am away, full of understanding and proud of my achievements. Finally, I want to thank the most little ones, my nieces and nephew who had been my motivation, a reason to always push to be the best version of myself and (trying to be) their role model: Rafaela, Anamaria, Fran and Magdalena, who probably did not understand a lot of my work, but the spark in their eyes and a hug that they'd give me every time I returned home, was a wind in my wings to always keep going.

Thank you all, for good and for bad, for learned and forgotten, finishing one chapter of life and starting the next, but remembering a most important lesson that I learned; "do everything in love".